KATHOLIEKE UNIVERSITEIT
LEUVEN

Arenberg Doctoral School of Science, Engineering & Technology
Faculty of Sciences
Department of Physics and Astronomy

MASS SPECTROMETRIC DEVELOPMENTS AND A STUDY OF LITHIUM DOPED SILICON AND GERMANIUM CLUSTERS

Jorg DE HAECK

Promotor:
Prof. Dr. P. Lievens

Leden van de examencommissie:
Prof. Dr. M. Nguyen, voorzitter
Prof. Dr. P. Lievens, promotor
Prof. Dr. R. Silverans, assessor
Prof. Dr. N. Severijns, assessor
Dr. E. Janssens, secretaris
Prof. Dr. Sara Bals (Universiteit Antwerpen)
Dr. Martin Schmidt (Laboratoire Aimé Cotton, CNRS)

Proefschrift voorgedragen tot
het behalen van de graad van
Doctor in de Wetenschappen

November 2011

ISBN 978-90-8649-459-0
Legal Depot D/2011/10.705/77

Voor mijn schatjes.

Παντα ρει

- Herakleitos of Ephesios (500 BC)

Summary

Clusters, consisting of a few up to several thousands of atoms, exhibit size-dependent physical and chemical properties linking the nanoscale to bulk matter in a non-trivial way. The careful design of clusters of two different elements (binary clusters) allows the synthesis of particularly stable species with tailored properties that eventually could be used as building blocks for novel nanomaterials. However, the continuation of our experimental research of binary clusters in the gas phase often is hampered by the limited mass resolution of the mass spectrometer. Beside the investigation of lithium doped silicon and germanium clusters a novel mass spectrometer has been designed and constructed, dividing this thesis into two distinct parts:

Part I: High resolution tandem time-of-flight mass spectrometer

One of the problems with the mass spectrometric investigation of binary clusters is the need of a resolution high enough to identify clusters unambiguously. Therefore a novel instrument was designed and constructed in the framework of this thesis. It consists of a binary cluster source and a high resolution tandem time-of-flight mass spectrometer (HRTTOF). Analytical calculations and extensive simulations were performed to understand and optimize the mass resolution of the system. The orthogonal extraction optic implements a new design with incorporated deflection which offers an extended mass range for simultaneous detection and which leaves the vertical velocity component of the incoming ions unaltered. The TOF chamber contains two dual-stage reflectrons and a chevron-type multichannel plate (MCP) detector. The detector operates in positive or negative ion mode with up to 5 kV post acceleration and can be coupled to a 0.25 ns time-to-digital convertor (TDC), ensuring high resolution in the full mass range of the clusters produced. Due to the tandem design an intermediate time focal point can be accessed, which can be employed for mass selected photofragmentation spectroscopy. A mass resolution close to 10 000 and a mass selectivity of 1/400 has been demonstrated for small silicon clusters. Peak analysis software and a new deconvolution method were developed to improve data analysis.

Part II: Properties of lithium doped silicon and germanium clusters

Photofragmentation spectroscopy shows that germanium and silicon agglomerates are composed of stable building blocks with six to eleven atoms. These building blocks are dianionic deltahedra, reminiscent of borane and carborane, which follow Wade's rules rather than the spherical shell model for metals. The units can be stacked, functionalized with organo-metallic groups, or doped with interstitial atoms to tailor the chemical and physical properties of what can be conceived as promising nanomaterials.

We report on a combined experimental and theoretical study of the geometric and electronic structure, stability, and ionization potentials of lithium doped silicon and germanium clusters. Mass spectra for doped silicon and doped germanium reveal a striking similarity and show enhanced abundances for particular sizes that relate to the building blocks of larger agglomerates. The structures of those stable sizes are further studied with density functional theory. The stability of bare and doped silicon and germanium is determined both by electronic and geometric motifs, which are strongly intertwined. We confirm the high stability of Ge_5^{2-}, Si_5^{2-}, Ge_9^{4-} and Si_9^{4-} units, previously synthesized in solution, in the gas phase by analysis of mass abundance spectra of lithium doped silicon and germanium cations after laser fragmentation. Together with neutral Si_7, Ge_7, Si_{10} and Ge_{10}, which are favoured in dissociation experiments, they form a set of highly stable structures. Each structure has a deltahedral geometry with highly

regular bond lengths and an associated optimal charge state. There is a clear distinction between the electronic s-band and p-band in these clusters. A new model is proposed to explain the stability of the (lithium doped) silicon and germanium clusters. In short, the shell closing in the former determines the geometry, while a shell closing in the latter determines the optimal charge state for the stable structures.

Splitting this thesis into two separate parts risks to imply that technological innovation and fundamental cluster science are distinct topics. This is strongly contradicted by the daily reality in the research lab. That both topics are intertwined can be illustrated by the new instrumentation that was readily developed for the ionization energy measurements, while the new mass spectrometer was build with the complicated isotope patterns and interesting fragmentation patterns of silicon and germanium clusters in mind.

Outline of the thesis

Chapter 1 offers a comprehensive theoretical background on the design of the high resolution instrument, mainly based on original work. First the need for a new instrument is illustrated by a number of examples. The main requirements for the new instrument are a high resolution and an intermediate focal point, while being compatible with our cluster source. A short discussion of existing instruments is given. The core of this chapter however is aimed at a quantitative understanding of how to reach a high resolution, clearly identifying the different sources of inaccuracy. These insights are further supported by extensive ion trajectory simulations. In the end, specific design guidelines are extracted.

The next chapter gives a technical and detailed overview of the HRTTOF. The instrument was built in-house, which comprises a substantial part of this thesis project. The chapter starts with an overview of the vacuum components and a discussion on pumping requirements. Next the source is described, followed by a discussion on the effect of the source parameters on the velocity and internal energy of the clusters. After that, the time-of-flight mass spectrometer is detailed with emphasis on the novel 'curved field' extraction and the detection system. The chapter closes with new developments in the data analysis procedure, which improve and extend existing methods.

The final chapter of the first part reports on the preliminary tests performed with the HRTTOF. The performance is illustrated regarding mass range, high resolution, and mass selection. The instrument is currently used for mass selective photofragmentation experiments, making use of the additional intermediate focal point.

Chapter 4 is the first chapter of the second part and gives a broad background of experimental and theoretical results regarding bare and metal doped silicon and germanium clusters. Larger clusters are composed of what appears to be stable building blocks. Smaller clusters are discussed in function of differences in their charge state. An extensive overview of experiments on (alkali metal) doped silicon and germanium clusters is presented to support these findings.

Chapter 5 gives an overview of experiments conducted strictly within the framework of this doctoral research project. It starts with the lithium doped germanium atom, which shows subsequent filling of atomic orbitals by electrons donated by the highly ionic lithium atoms. Results on mass abundance spectra of neutral lithium doped silicon and germanium clusters are combined with the derived ionization energies. The last section investigates the fragmentation mass abundance spectra of bare and lithium doped silicon and germanium cations giving direct information on stability features.

The final chapter of part II gives a deeper insight in the stability patterns for bare and doped silicon and germanium clusters. It starts with a short overview of existing models that help understand stability features. After identifying the most stable systems based on experimental evidence and theoretical predictions, we investigate their density of states more closely. This is concluded in a proposed model explaining the structure and charge state of these systems.

Samenvatting

Clusters zijn systemen bestaande uit een paar tot enkele duizenden atomen die een brug slaan tussen de nanowereld van atomen en moleculen en de wereld van de bulk materie. Ze vertonen sterk grootte-afhankelijke fysische en chemische eigenschappen. Het zorgvuldige ontwerp van clusters van twee verschillende elementen (binaire clusters) maakt de synthese mogelijk van stabiele nanomaterialen met specifieke eigenschappen. De continuïteit van het experimenteel onderzoek naar binaire clusters wordt bedreigd door de resolutie van de massaspectrometer. Daarom werd binen het kader van deze thesis, naast het onderzoek van lithium gedoteerde silicium en germanium clusters, een nieuwe massaspectrometer ontwikkeld. Dit verdeeld dit proefschrift in twee afzonderlijke stukken:

Deel I: Hoge resolutie tandem vluchttijd massaspectrometer

Een probleem dat opduikt bij massaspectrometrisch onderzoek van binaire clusters is dat de resolutie hoog genoeg moet zijn om ondubbelzinnig clusters te kunnen identificeren. Als antwoord hierop werd een nieuw instrument ontwikkeld en gebouwd, bestaande uit een binaire cluster bron en een hoge resolutie tandem vluchttijd massaspectrometer (HRTTOF). Aan de hand van analytische berekeningen en uitgebreide simulaties werd het optimaliseren van de resolutie onder de loep genomen. De orthogonale extractie optiek implementeert een nieuw ontwerp met geïntegreerde deflectie. Het laat een toe een uniek massabereik te detecteren, zonder de resolutie te verminderen en zonder de verticale snelheidscomponent van de ionen te wijzigen. De belangrijkste vacuümkamer bevat twee reflectrons en een detector van het type chevron MCP. De detector kan zowel positieve als negatieve ionen opmeten en gebruik maken van een extra 5 kV post acceleratie. Door de detector te koppelen aan een 0.25 ns time-to-digital convertor (TDC), kan een optimale resoluie verkregen worden over het volledige massa gebied van de geproduceerde clusters. Door het tandem design ontstaat er een intermediair focuspunt, wat nodig is voor massa geselecteerde foto-fragmentatie spectroscopie. Karakterisatie van het toestel aan de hand van silicium clusters toont een massa resolutie in de buurt van 10.000 en een massa selectiviteit van 1/400. Specifieke software en een nieuwe deconvolutie methode werden ontwikkeld om de data analyse te verbeteren.

Deel II: De stabiliteit van lithium gedoteerde silicium en germanium clusters

Foto-fragmentatie spectroscopie toont aan dat germanium en silicium clusters zijn samengesteld uit stabiele bouwstenen met zes tot elf atomen. Deze bouwstenen zijn veelal deltahedra met een negatieve lading, die doen denken aan de structuren van boraan en carboraan. Deze volgen eerder ‘Wade's rules’ dan het elektronische schillen model voor metaalclusters. Deze bouwblokken kunnen worden gecombineerd, gefunctionaliseerd met organo-metallische groepen of gedoteerd met interstitiële atomen naargelang de gewenste chemische en fysische eigenschappen, wat hen veelbelovende nanomaterialen maakt.

Dit werk bespreekt de resultaten van een experimentele en theoretische studie van de structuur, de stabiliteit, en de ionisatie-energie van lithium gedoteerde silicium en germanium clusters. Massa spectra voor silicium en germanium onthullen een opvallende gelijkenis en tonen verhoogde abundanties voor bepaalde groottes die gerelateerd zijn aan de hierboven beschreven bouwstenen. De structuur van de meest stabiele groottes is verder onderzocht aan de hand van dichtheids functionaal theorie. De stabiliteit van zuivere en gedoteerde silicium en germanium clusters wordt zowel bepaald door

elektronische als geometrische motieven, die sterk verweven zijn. We bevestigen de hoge stabiliteit van Ge_5^{2-}, Si_5^{2-}, Ge_9^{4-} and Si_9^{4-} (eerder gesynthetiseerd in oplossing) in de gasfase door analyse van de massa spectra van lithium gedoteerd silicium en germanium kationen na laser fragmentatie. Samen met de neutrale Si_7, Ge_7, Si_{10} and Ge_{10} clusters, dominant in dissociatie experimenten, vormen ze een set van zeer stabiele structuren. Elke structuur heeft een deltahedrale geometrie met zeer regelmatige interatomaire afstanden en een bijbehorende optimale ladingstoestand. Er is een duidelijk onderscheid tussen de elektronische s-band en p-band voor deze clusters. Een nieuw model is uitgewerkt om de stabilitieit van (lithium gedoteerde) silicium en germanium clusters te verklaren. In het kort: de schilsluiting in de s-band bepaalt de geometrie, terwijl een schilssluiting in de p-band de optimale ladingstoestand voor verhoogde stabiliteit bepaalt.

Dit proefschrift in twee afzonderlijke delen splitsen, suggereert dat technologische innovatie en fundamenteel onderzoek naar clusters twee volledig verschillende onderwerpen zijn. Dit is in tegenspraak met de dagelijkse realiteit in het onderzoekslabo. Beide onderwerpen zijn in feite sterk met elkaar verweven. Dit kan geïllustreerd worden door enerzijds de nieuwe instrumentatie die op tijd ontwikkeld moest worden voor de meting van de ionisatie-energiën, en anderzijds de nieuwe massaspectrometer die werd gebouwd met de ingewikkelde isotopenpatronen en interessante fragmentatie eigenschappen van silicium en germanium clusters in het achterhoofd.

Nomenclature

Symbols

A	atomic mass [amu]
ΔV	potential difference [V]
E_k	kinetic energy [eV]
M	molecular mass [amu]
m_m	molar mass [kg/kmol]
p	pressure [Pa]
q	charge [C]
t	time [µs]
T	temperature [K]
V	volume [m³]

Constants

k_B	1.3806504(24) 10^{-23} J/K
k_B	8.617343(15) 10^{-5} eV/K
R	8314.472(15) J/K.kmol
e/u	96.485 10^{6} C/kg
$m_{m,He}$	4.002602 kg/kmol
γ_{He}	5/3

Abbreviations

AIE	adiabatic ionization energy
CID	collision induced dissociation
DFT	density functional theory
EA	electron affinity
ESI	electro spray ionization
FTMS	fourier transform mass spectrometer
FWHM	full width at half maximum
HOMO	highest occupied molecular orbital
HRTTOF	high resolution tandem time-of-flight mass spectrometer
IR-MPD	infrared multiple photon dissociation
LUMO	lowest unoccupied molecular orbital
MALDI	matrix assisted laser desorption and ionization
MCP	multichannel plate (detector)
MR	mass resolution

PES	photoelectron spectroscopy
PES	potential energy surface
PID	photoinduced dissociation
PIE	photoionization efficiency (curve)
PSV	pulsed supersonic gas valve
RTOF	reflectron time-of-flight mass spectrometer
S	silicon - germanium
SOMO	singly (highest) occupied molecular orbital
TOF	time-of-flight
TR	time resolution
TTP	tricapped-trigonal-prism
UPS	ultraviolet photoelectron spectroscopy
VIE	vertical ionization energy

Table of contents

Part I: High resolution tandem time-of-flight mass spectrometer

Part I of this thesis records the development of a novel high resolution tandem time-of-flight mass spectrometer (HRTTOF) for the K.U.Leuven cluster laboratory. While this part is divided in three distinct chapters (describing the design of the instrument, its realization, and the first results) the actual process was more complex and even took a few dead ends.

With the laboratory's benchmark achievements in the field of binary clusters in mind, there was a growing awareness that the mass resolution of our equipment might become a bottleneck. As illustrated in section 1.1.2 and 1.1.3 progress in science also depends on progress in technology. Section 1.1.4 gives an introduction to mass spectrometers used in the research field of nanoclusters. A good reference instrument is the high resolution time-of-flight mass spectrometer built by Thorald Bergmann. Unfortunately, this design is quite complex and would require the manufacturing of many mechanical and electronical parts with high tolerances. The first goal in this project was to simplify this design without losing too much of its performance. A simulation program was used for this task which culminated in the design of the 'curved field extraction' described in section 2.4.1. The same simulaton software was used later on for modeling the entire mass spectrometer and to check the analytical formulae (section 1.2.3). In this stage, clear specifications were set forward regarding mass resolution and mass range. Also the requirement for mass selection was added (section 1.1.1). To support the design of the HRTTOF quantitatively the concept of high resolution was studied extensively. Due to the limited and scattered material published on this topic, the theory was redeveloped from scratch and significantly extended to incorporate a full set of sources that might affect loss of resolution. The result can be found in section 1.2. These calculations had a direct impact on the design choices of the instrument (section 1.3.2) and the optimalization of the resolution (section 1.3.1).

Initially there was no intent to build this instrument 'in-house'. Unfortunately in the limited market of custom-made mass spectrometers we found no company willing to engineer our custom design. After a market study and a budgetary analysis the decision was taken to develop the instrument ourselves. Wherever possible the instrument standardized components were incorporated to lower the cost, to improve the reliability, and to offer a better platform for future optimization. The mechanical design started with the two reflectrons, custom made but with standard outer dimensions (section 2.4.2), and the first challenge was to design a chamber to house them (section 2.2.1) and connect to the extraction optics and detector. The extraction optic (section 2.4.1) was built in house but the motion system was bought, and the chamber was adapted to them. With the main vacuum chambers defined, appropriate vacuum pumps were selected (section 2.2.3) and the support tables with slides were configured (section 2.2.2). The mass selector was reused from our existing setup and just needed a new feedthrough and recabling (section 2.4.3). Most of the electronics had been bought or (re)developed. The main detection system was bought as a whole, but other detection systems were assembled later on (section 2.5.2-2.5.4).

First tests on the HRTTOF were hampered by an initial failure of the detection system and the absence of an adequate cluster source. The source chamber was designed later, together with the skimmer and it holds the existing transportable binary cluster source. Failure to attain stable production lead to a theoretical study of the cluster production and beam dynamics as well as fast ion gauge measurements (section 2.3). After improvements in the cluster production the testing stage (chapter 3) soon evolved into mass selected photofragmentation measurements.

While all stages within the development of the HRTTOF fell within the framework of this doctoral research project, there was significant support from a number of different sources: technical support from S. Piessens and the mechanical workshops within the department, scientific and general support by prof. P. Lievens and other team members of the K.U.Leuven cluster laboratory, a valuable introduction to the simulation software by dr. D. Ievlev, electronic support by the electronic workshop of the department, and support from the purchase department. The development of this instrument was also strongly influenced by the pioneering work of Thorhald Bergmann.

1 Design

While chapter 2 will provide a technical overview of the new instrument, this chapter offers a comprehensive theoretical background on the design of the high resolution tandem time-of-flight mass spectrometer (HRTTOF), which is mainly based on original work. First, the need for a new instrument is illustrated by a number of examples. The main requirements for the new instrument are a high resolution and an additional focal point, while being compatible with our cluster source and research methods. A short discussion of existing instruments is given. The core of this chapter is aimed at a quantitative understanding of how to reach a high resolution, through identification of all different sources of inaccuracy. These insights are supported by extensive ion trajectory simulations. In the end, specific design guidelines are extracted.

1.1 Introduction

1.1.1 Objectives

From the development of the first telescope at the beginning of the 17th century to the large hadron collider in the 21st century, progress in science is driven by technological innovation. One of the problems with the mass spectrometric investigation of mixed clusters, especially if elements with more than one stable isotope are involved, is the need of a resolution high enough to identify complicated cluster systems unambiguously.

The ongoing trend towards miniaturization of electronic components has motivated the search for new nanomaterials. Our ongoing study of clusters, species consisting of a few up to several thousands of atoms, offers a unique bottom-up approach in understanding and developing new nanoscaled building blocks. While many people are still thrilled by the beautiful symmetry of the carbon fullerenes and similar cage-like structures, others envisage applications in catalysis, photoluminescence, cancer treatment, hydrogen storage, nanodevices, and so on. Clusters are compatible to other organic and inorganic nanosystems and can be tailored by doping with proper elements. In the research group Clusters and Laser Spectroscopy of the Laboratory of Solid State Physics and Magnetism fundamental research of binary clusters is an important research theme since quite some time. For diverse elements we have studied which mechanisms control the growth and the size specific properties of small clusters. Information on the cluster structure is not directly obtained, but is elegantly reached by confronting the experimental observables with the results of computational studies. By establishing the cluster structure, also other computed properties are validated, such as electronic structure, charge distribution, chemical bonds, etc. However, these experiments are limited by the increasing

complexity of the mass spectrum, something which becomes inevitable for doped clusters. In order to broaden the scope of our research and stay competitive on an international level, state-of-the-art equipment and continuous development are mandatory. In the framework of this thesis a novel high resolution tandem time-of-flight mass spectrometer (HRTTOF) was designed and implemented. This instrument consists of a binary cluster source and a tandem time-of-flight mass spectrometer. The objectives of the new instrument can be summarized as:

- An enhanced mass resolution ($m/\Delta m > 10\,000$)
- A secondary focal point for mass selected experiments
- Compatible with the existing binary cluster source
- A broad mass window (up to 100 000 amu)

1.1.2 A need for higher resolution

Below are three examples that illustrate the limitations of the original K.U.Leuven time-of-flight mass spectrometer used for the investigation of binary clusters in the gas phase. This experimental setup is well described in the theses of Peter Thoen and Wim Bouwen.[1,2] The two first examples below illustrate the need for enhanced resolution in binary cluster research. One shows the complexity when introducing many different atomic species into the TOF mass spectrometer. The other elucidates the problems that occur when studying elements with isotopes. A third example addresses the need for mass selective experiments.

Reactivity measurements

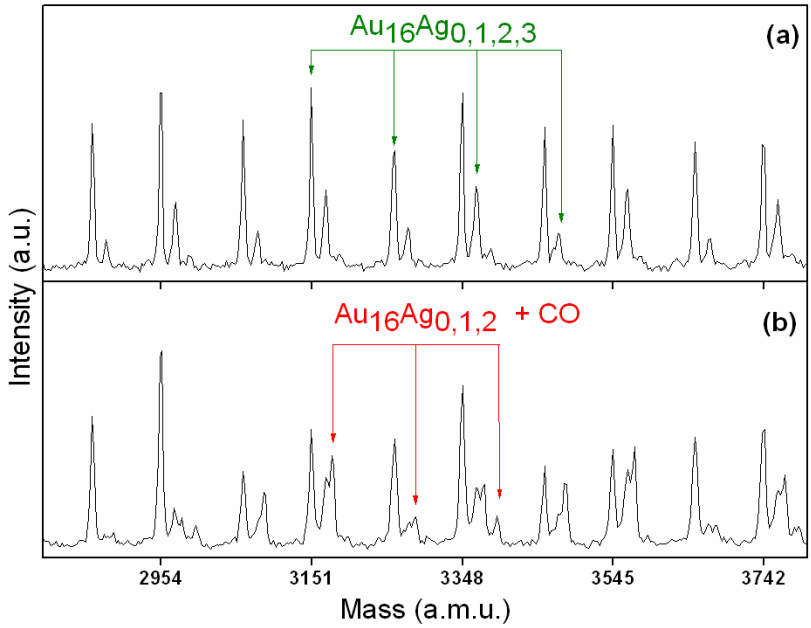

Figure 1-1: Mass abundance spectra of neutral Au_nAg_m clusters (n = 15-19) after passage through the reaction cell and photoionization with 7.89 eV photons. The upper spectrum (a) is recorded without CO gas in the cell. The lower spectrum (b) is recorded with 0.15 Pa CO in the cell. [from J. De Haeck and coworkers (2011)[3]]

Before the construction of the new HRTTOF, reactivity measurements were performed in a TOF mass spectrometer with a standard mass resolution of 600-800.[3] A selection of the mass spectra for silver doped gold clusters, illustrating the experimental output, is shown in Figure 1-1 for around size 16. The upper spectrum has been recorded without CO. The

production parameters were optimized to achieve a high content of singly doped Au_nAg clusters, but also multiple doped Au_nAg_{2-5} clusters are present. The lower spectrum has been recorded for a high amount of CO attachment, and reveals a higher CO content in the spectrum. Because the mass difference between AuCO and Ag_2 is only 9 amu, at a certain size deconvolution of the two peaks becomes very difficult. With a mass resolution of 600, at 5400 amu the FWHM of the peaks becomes comparable with the distance between the peaks. This means that from Au_{27} on, it is difficult to identify the intensity of each peak. It is clear that for another choice of elements the distance between the peaks can even be smaller than 9 amu, limiting the choice of experimental systems drastically with this available mass resolution.

Isotope patterns

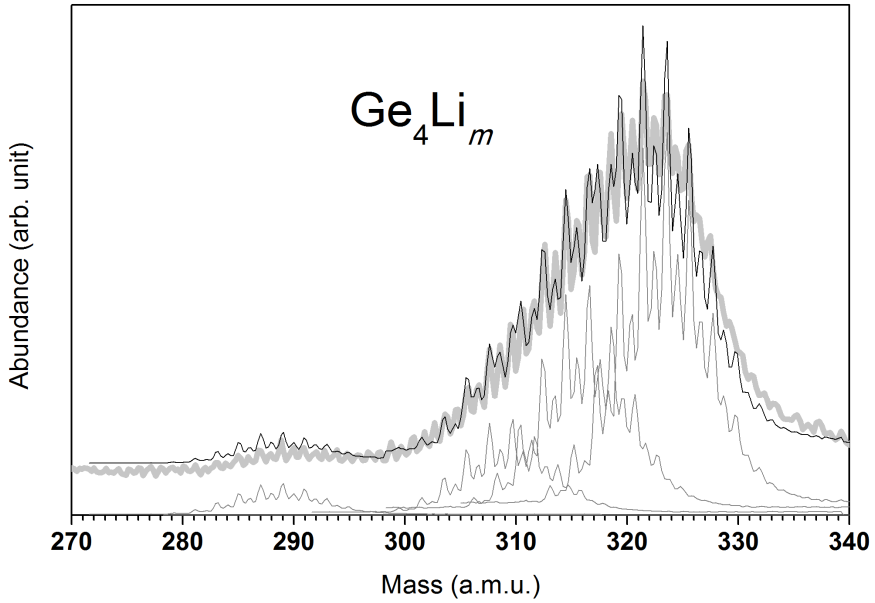

Figure 1-2: The mass spectrum around Ge_4Li_m (thick grey line) is fitted (black line) using the isotope pattern of Ge_4 from a pure germanium spectrum. Significant contributions are found present for Ge_4Li_0, Ge_4Li_3, Ge_4Li_4 and Ge_4Li_5 (grey lines at the bottom). [from G. Gopakumar and coworkers (2009)[4]]

An example of a system incorporating many isotopes is a lithium doped germanium cluster as both elements have distinct isotope patterns.[4] Because the mass of lithium is only 7 amu, which is smaller than the width of the isotope pattern for basically all germanium clusters, overlap of the patterns for different stoichiometries of Ge_nLi_m cannot be avoided and deconvolution is needed. To determine the precise stoichiometry for the most abundant clusters, each conglomerate of peaks was fitted with the isotope pattern for the corresponding bare germanium cluster. The isotope patterns are taken from a reference spectrum at the same experimental conditions as the doped spectrum. This is illustrated in Figure 1-2, which shows the contribution of Ge_4Li_3, Ge_4Li_4, and Ge_4Li_5 to the mass peak of Ge_4Li_m. This approach becomes however impossible when individual peaks in the isotope pattern can no longer be distinguished, because then the mass calibration needed for deconvolution fails. With a mass resolution of 800 and a peak distance of 1 amu this happens at 800 amu, which corresponds to $Ge_{11}Li_m$.

1.1.3 A need for mass selective experiments

Gold fragmentation

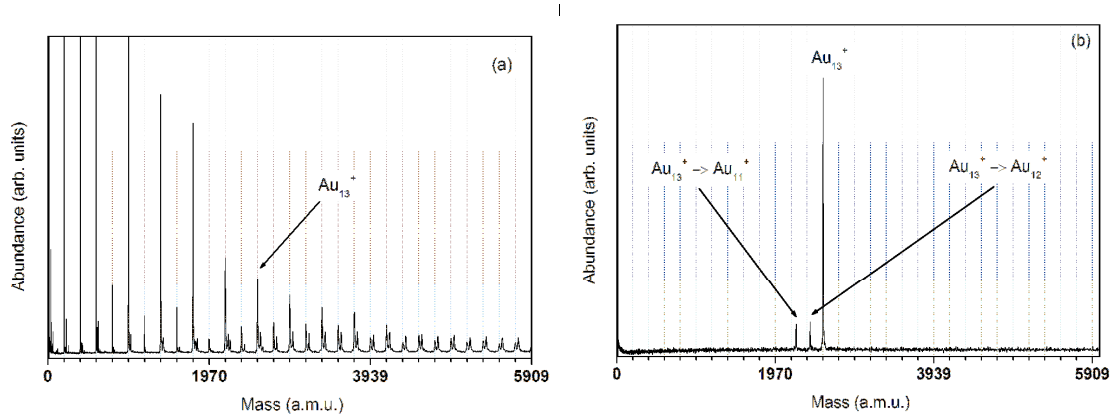

Figure 1-3: (a) Mass abundance spectrum of photofragmented Au_n^+ clusters for n= 1–30. The grid lines mark the bare Au_n^+ clusters. Small peaks at the right side of the bare cluster peaks correspond to metastable fragments stemming from one size up. (b) Mass selected mass abundance spectrum showing metastable fragmentation of Au_{13}^+. The grid lines mark the bare Au_n^+ clusters. [after N. Veldeman and coworkers (2008)[5]]

When clusters interact with high fluence laser light, they are heated by multiphoton absorption. Cooling occurs through fast sequential evaporation of atoms and larger fragments. The photofragmentation spectrum for Au_n^+ (Figure 1-3 (a)) shows small peaks that appear at the right side of the bare cluster peaks. They correspond to metastable fragments stemming from one size up. This becomes much more clear when a mass gate is used which blocks all sizes, except one, from reaching the detector (Figure 1-3 (b)). The delayed fragmentation of mass selected Au_{13}^+ shows a prominent peak, corresponding to the selected cluster, and less intense peaks with a shorter flight time corresponding to metastable fragmentation. The preferred fragmentation channel is found to be size dependent. This type of experiment tells a lot about the stability of clusters.[5] By fragmenting the clusters after size selection instead of before, as was done in this case, more and quantitative information could be obtained. This is certainly of interest for silicon and germanium clusters which dissociate into larger fragments that can be conceived as stable building blocks.

1.1.4 Mass spectrometers

High resolution

In the past two decades, the mass spectroscopy market has known a tremendous boom. The noble prize winning concepts of Electro Spray Ionization (ESI)[6] and Matrix Assisted Laser Desorption/Ionization (MALDI)[7] have stimulated the development of instruments for gas phase ion chemistry and a growing number of clinical and biological applications.[8] From this perspective the apparent solution for an instrument with a high mass resolution would be to just check the market and pick out the most appropriate model. However, most well advertised end-user products emphasize on high efficiency, accuracy, and resolution but have a limited mass range, not meeting the requirement to study clusters with sizes exceeding m/z 200 000. In addition, and more important, they are not compatible with a cluster source that produces clusters with a mass independent velocity of 1000 m/s.[9] Mass spectrometers that allow investigating large clusters are only provided by a limited number of small-scale companies. As a result, many of the instruments used in the cluster research community are at least partially home-made. The

challenging specifications listed in section 1.1.1 could only be met by implementing a design which was not commercially available.

There exist different types of mass analyzers. A popular mass spectrometer, because of its compact size and versatility, is the quadrupole.[10] It uses oscillating electrical fields to selectively stabilize or destabilize ions. Fourier transform mass spectrometers[11] and the more recent Orbitrap™ technology[12,13] detect mirror currents due to cycling ions of all masses at once and reach very high resolution. The sector instrument uses magnetic and electrostatic deflection to split ion beams into mass dependant angles. Time-of-flight (TOF) mass spectrometers make use of the velocity difference for different masses after acceleration in an electrostatic field. Often an ion mirror (reflectron)[14] is used to enhance the resolution, culminating in the design of multiple reflection TOF mass spectrometers.[15,16] In contrast to other types of mass analyzers, there is no fundamental limit on the mass range of a TOF mass spectrometer. For this reason, we opted to build a TOF mass spectrometer.

High resolution TOF mass spectrometers are far from exceptional these days.[17] Though setups with a mass resolution of 20 000 and more are available, they usually are connected to sources that produce low speed ions (such as a MALDI source) or they have a limited mass range. Both the high velocity and the significant velocity spread with which the clusters leave a laser vaporization source pose serious restrictions on the design. One approach is to use a collisional ion guide to thermalize the ions. The most obvious solution to bypass the velocity spread is the use of orthogonal extraction, i.e., have independent (orthogonal) axes for ion generation and mass analysis.[18,17] The reduction of the spread of the velocity in the TOF direction improves the resolving power. The average velocity in the TOF direction is zero, which makes the mass calibration easier. This layout also improves the extraction volume and the sampling speed, favoring the efficiency. There is however a severe drawback for ion beams involving supersonic expansion because they tend to have constant ion velocity rather than constant ion energy. Consequently, ions with different masses will be extracted under different angles. Most often, deflection electrodes are used to steer the ions along the TOF axis. Unfortunately, a deflection mechanism jeopardizes the mass resolution and the mass range of the system. Only the 'Cluster-TOF' made by T. Bergmann two decades ago,[19,20,21,22,23] achieves a mass resolution of 40 000 in combination with a decent mass range and being compatible with a laser vaporization cluster source. The main drawback of this system is a low efficiency.

A high efficiency TOF mass spectrometer, compatible to a laser vaporization cluster source, has been implemented by W.A. de Heer.[24] It has a straightforward design that consists of an orthogonal three stage extraction optic and a detector. Both the ionization volume and the detector have a large area, resulting in good efficiency. Extensive manipulation of the ion beam before entering the TOF enhances the resolution and the mass range of the instrument significantly. Though the mass resolution of 10 000 and the high mass range fulfill our requirements, the minimized flight path leaves no room to study mass selected clusters.

Tandem mass spectrometers

Tandem mass spectrometry is a popular tool in biochemistry and in the pharmaceutical sector. Multiple stages of mass analysis can either be separated in time or in space. By doing tandem mass spectrometry in time, the separation is accomplished by trapping ions at the same place and multiple separation steps take place over time. A quadrupole ion trap or Fourier Transform Mass Spectrometer (FTMS) can be used for such an analysis.

In tandem mass spectrometry in space, the separation elements are physically separated. These elements can be magnetic or static electric sectors, energy selective transmission quadrupoles, or the time selective time-of-flight mass filters. The resolving power for the sector element is relatively low and the quadrupole tends to have low mass range. This is why we chose for the last option. Two TOF elements are coupled together: mass selection or dissociation takes place in the focal point of the first TOF while a detector is placed in the focal point of the second TOF. For mass selection an electrostatic gate can be used: it opens during a small time interval, allowing only ions in a small mass window to travel further. Alternatively, a lateral time-of-flight mass selector for cluster deposition was developed by B. von Issendorff and R.E. Palmer.[25] The basic idea is to use time-limited high voltage pulses to displace laterally a preaccelerated ion beam, without changing its direction or shape. The design offers a mass resolution of 20–50 and a transmission of about 50%.

To fragment mass selected gas-phase ions tandem mass spectrometry is essential and the fragmentation should occur between different stages of mass analysis. There are many approaches to fragment ions, of which the most common are collision induced dissociation (CID)[27] and photon induced dissociation (PID). Often, the ionization process is sufficiently violent to leave the resulting ions with sufficient internal energy to fragment within the mass spectrometer. If the product ions persist in their non-equilibrium state for a moderate amount of time before auto-dissociation this process is called metastable fragmentation. Tandem TOF mass spectrometry combines very well with photon induced dissociation because of the possibility to have a high temporal and spatial overlap of the cluster beam and the laser beam. There is however a drawback in using tandem TOF mass spectrometers: because the fragments receive only part of the parent ion's energy they will not be focused correctly by a standard two stage reflectron in the second part of the mass spectrometer. The larger the mass difference between the parent and daughter, the larger will be the energy difference and the lower the resolution. In the case of monomer and dimer evaporation the effect is small and it can be ignored. But for dissociation of larger fragments the effect can become severe. There are three solutions for this problem: scan the reflectron voltages, use a curved field reflectron or use an accelerating-decelerating unit. The curved field reflectron has a non linear field that serves to compensate for the time discrepancy that results from field-free flight of isomass ions of varying energy.[26] A linear field reflectron has a limited bandwidth that cannot accommodate the entire range of energies. Alternatively, by decelerating the ions prior to collision and then reaccelerating the product ions, the kinetic energy range of the daughter ions is reduced to the decelerated energy.[27] Before using tandem TOF mass spectrometers, different attempts were made to incorporate mass selection in a single TOF mass spectrometer. An easily implemented method involves firing the dissociation laser across the ion path at the back of the reflectron, where the ions are almost stationary.[28] The product ions are accelerated and separated in the second part of the reflectron. Although the ions are easy to hit, the time spread is huge, severely lowering efficiency and resolving power. Another straightforward method is to fire the dissociation laser at the focal point immediately following the ion extraction region.[29] Due to the very short flight time, ion separation will however be very poor.

A number of tandem TOF mass spectrometers for photofragmentation have been constructed.[30,31] G. Enke was among the first to construct a tandem TOF mass spectrometer for photodissociation of small molecules.[30,32] His system included a retardation-acceleration region, an ion deflection gate, and a curved field reflectron. The field free regions are at a constant negative value because the instrument uses an energy lift before the ions enter the curved field reflectron. This reduces the relative kinetic

energy range of the product ions from nearly 100% to 25%. Fragmentation efficiencies of up to 79% have been obtained together with unit mass resolution to at least 300 for all components of the tandem TOF mass spectrometer. While this design, using two TOF mass spectrometers which are linearly coupled, is most often been copied, instruments consisting of two separate analyzers placed orthogonally also exist.[33,34] But extraction into the second analyzer is difficult in this case, due to the high energy.

1.2 How to achieve enhanced resolution?

1.2.1 Resolution in one dimension: an analytical model

Defining resolution

The possibility to differentiate two species with slightly different masses by mass spectrometry does not only depend on their mass difference but also the width of each peak. The mass resolution (MR) is defined as the mass of a peak *(m)* divided by the full width at half maximum (FWHM) *(Δm)* of the peak:

$$MR = \frac{m}{\Delta m} \tag{1.1}$$

The time resolution (TR) is defined as the arrival time of a peak *(t)* divided by the FWHM *(Δt)* of the peak:

$$TR = \frac{t}{\Delta t} \tag{1.2}$$

Mass resolution and time resolution are straightforwardly related with each other. Further on it will be shown (equations (1.5) and (1.6)) that:

$$t \cong c\sqrt{m} \tag{1.3}$$

Differentiating the time towards the mass gives:

$$\frac{dt}{dm} \cong \frac{t}{2m} \Leftrightarrow MR \cong \frac{TR}{2} \tag{1.4}$$

This shows that to change from time resolution to mass resolution, one just has to divide by two. For a large mass range the mass resolution can be considered constant, making it a property of the instrument more than a property of a single peak.

By adjusting the voltages of the different components of the mass spectrometer the resolution of the instrument can be optimized. The highest resolution is achieved when all particles of the same mass and charge arrive at the same time at the detector. The resolution depends on the starting position and the starting velocity of the clusters in the extraction region, but also on the deflection through grids, general beam broadening, the quality of the electrostatic fields, the detection cycle, the alignment of the different components...

Total flight time

To predict the resolution of a given design, a combination of simulations and approximations is needed. Useful qualitative and even quantitative information can

already be gained by a one dimensional model consisting of only linear field potentials. Although similar models exist in literature, we opted to derive our own set of formulas. Instead of relying on numeric calculations our approach gives concise analytic results, incorporating any number of components. It is possible to extend this method to any order of focusing, but for clarity the formulas only go up to second order focusing, which is more than enough in practice. To clarify the formalism used below a typical layout of a reflectron TOF mass spectrometer is shown in Figure 1-4. It consists of a double stage extraction, a double stage reflectron and a detector. The long arrow illustrates the flight path of the clusters in the TOF, while the small, thick arrow illustrates the flight direction from the cluster source into the TOF in the case of orthogonal extraction. The vertical lines depict transparent grids, whose voltage manipulates the velocity and the beam path of the clusters.

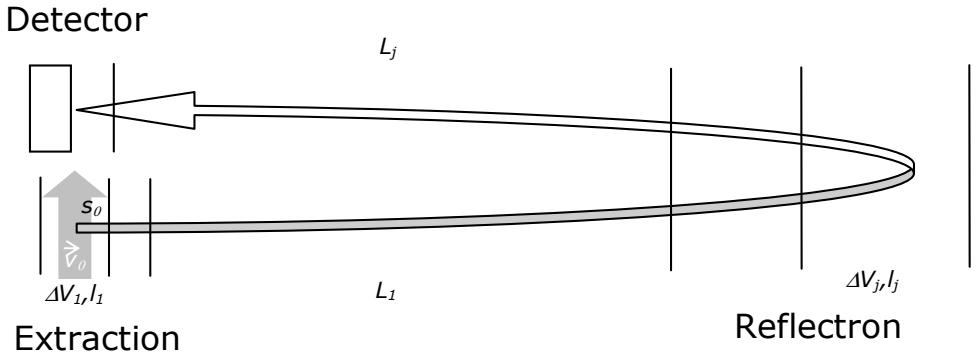

Figure 1-4: Schematic overview of a TOF mass spectrometer consisting of a double stage extraction, a double stage reflectron and a detector. The long arrow illustrates the flight path of the clusters in the TOF, while the small, thick arrow illustrates the flight direction from the cluster source into the TOF in the case of orthogonal extraction. The vertical lines depict transparent grids, whose voltage manipulates the velocity and the beam path of the clusters.

To make quantitative predictions regarding the resolution of a system, one first has to derive a general formula for the total flight time between extraction and detection. Hereto, the system is divided in different stages *j*, where each stage is defined by a length l_j and a potential difference ΔV_j. A negative potential difference concurs with a positive (negative) acceleration a_j for a positive (negative) charge q. The time t_j spent in a non-zero linear field is:

$$t_j = \frac{v_j - v_{j-1}}{a_j} = \frac{\sqrt{\frac{2E_{k,j}}{m}} - \sqrt{\frac{2E_{k,j-1}}{m}}}{-\frac{q\Delta V_j}{ml_j}} = \frac{\sqrt{2m}}{q}\frac{l_j}{\Delta V_j}\left(\sqrt{E_{k,j-1}} - \sqrt{E_{k,j}}\right) \tag{1.5}$$

and the time spent in a field-free stage is:

$$t_j = \frac{L_j}{v_{j-1}} = \sqrt{\frac{m}{2}}\frac{L_j}{\sqrt{E_{k,j-1}}} \tag{1.6}$$

The capital L is used to explicitly refer to a field free stage, and v_j is the velocity at the end of stage *j*. The kinetic energy $E_{k,j}$ at the end of each stage *j* is defined by the kinetic energy at the end of the first stage, $E_{k,1}$, and the negative of the sum of the potential differences of the traversed stages:

$$E_{k,j} = E_{k,1} - q\sum_{i=2}^{j} \Delta V_i \tag{1.7}$$

An exception is the reflectron, where the clusters do not pass through but reach a turning point where the kinetic energy becomes zero: $E_{k,j} = 0$. Special attention is needed to describe the kinetic energy upon leaving the first stage, $E_{k,1}$. It equals the sum of the kinetic and potential energy the cluster obtained at its starting conditions:

$$E_{k,1} = E_{k,0} + E_{p,0} = \frac{1}{2} m v_0^2 - \frac{q\Delta V_1}{l_1} s_0 \tag{1.8}$$

The variable s_0 describes the starting position in the extraction relative to the next grid and v_0 the starting velocity in the extraction in the direction of the TOF: they are determined either by creation of the ion following ionization or by switching on the field when the ion is in the extraction region.

Of course, the total flight time t_{total} of a charged particle in the TOF spectrometer is:

$$t_{total} = \sum_j t_j \tag{1.9}$$

Through the kinetic energy $E_{k,0}$ a complex mass dependence is introduced in the total flight time, which is important when calibrating a spectrum. Notice that t_1, in contrast to all other times, explicitly depends on the sign of the starting velocity v_0:

$$t_1 = \frac{\sqrt{2m}}{q} \frac{l_1}{\Delta V_1} \left[v_0 \sqrt{\frac{m}{2}} - \sqrt{E_{k,1}} \right] \tag{1.10}$$

Dispersion curve

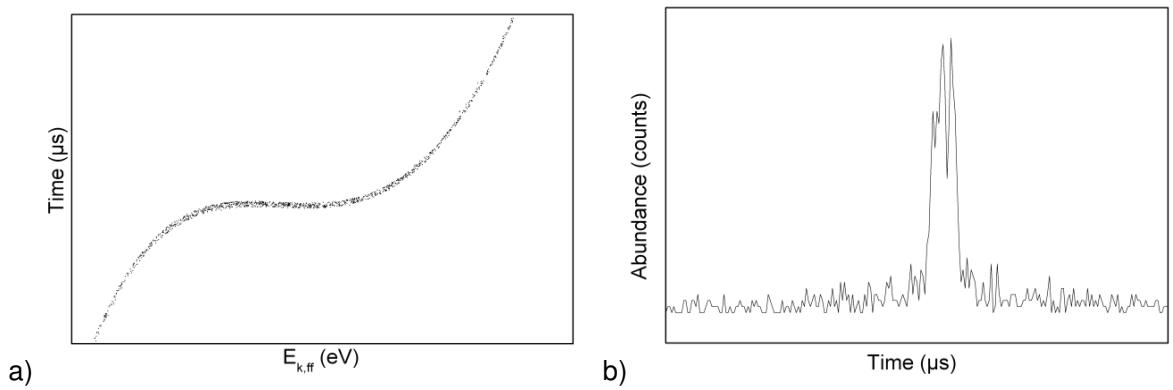

Figure 1-5: (a) Dispersion curve and (b) the according peak profile for a given mass.

To monitor the resolution at any give position along the flight path, the 'dispersion curve' $t(E_k)$ can be used, which is the plot of the flight time against the kinetic energy for all clusters of a given mass. The spread on this relationship determines the resolution, because the peak shape can be constructed as the histogram of the inverse plot. Figure 1-5 shows the dispersion curve and the according histogram. Ideally the dispersion curve is a horizontal line, which means all clusters of the same mass arrive at the same time at the detector, disregarding differences in kinetic energy. The mathematical translation is that all derivatives of $t(E_k)$ vanish:

$$\frac{d^i t}{dE_k^i} = 0, \quad i = 1...\infty \tag{1.11}$$

In practice, only i number of these equations will be met, where i will be called the order of focusing. Ignoring higher order terms and using a Taylor expansion one can determine the time delay of species arriving at the detector relative to species with energy E_k.

$$\Delta t = \frac{d^{(i+1)} t}{dE_k^{(i+1)}} \frac{\Delta E_k^{(i+1)}}{(i+1)!} \tag{1.12}$$

In practice a dual stage reflectron is most often used. For second order focusing the time spread at the detector which limits the resolution can readily be calculated using equations (A.2) and (A.3) in appendix A.1:

$$\Delta t = \frac{\Delta E_k^3}{16} \sqrt{\frac{m}{2}} \left[-5 L_{ff} \left(E_{k,ff} \right)^{-\frac{7}{2}} + 2 \sum_j \frac{l_j}{q \Delta V_j} \left(\left(E_{k,j-1} \right)^{-\frac{5}{2}} - \left(E_{k,j} \right)^{-\frac{5}{2}} \right)^* \right] \tag{1.13}$$

The star (*) means that in the formula each term including $E_{k,j} = 0$ needs to be removed. This is the case for i=0 in case of a zero starting velocity and for the terms corresponding to the final stage of a reflectron. If the actual energy distribution ΔE_k is known, in principle the resolution can be predicted, based on this formula.[35] However, simulations show that this contribution to the resolution is very small compared to other factors (section 1.2.3). In the case of second order focusing, the resolution of the system is determined by the broadening of the dispersion curve more than by its shape.

Kinetic and potential energy focusing

While plotting the dispersion curve, each ion is only labeled by its kinetic energy. However, the kinetic energy of an ion with a given mass is characterized by both the starting position s_0 and the starting velocity v_0. This dependence was already explicit in formulas (1.7) and (1.8): upon varying s_0 the starting potential energy changes, while v_0 sets the starting kinetic energy. Other parameters depend on the TOF and not on the ion. The derivative towards both should vanish in order to remove the time spread at the detector for a given mass. This will happen when they appear together as in $E_{k,1}$. However, the derivative of t_1 is different for $E_{k,0}$ and $E_{p,0}$ and using equation (1.10) one finds:

$$\frac{dt}{dE_{k,0}} = \frac{dt}{dE_{p,0}} + \frac{l_1}{q \Delta V_1 v_0} \tag{1.14}$$

Even for an ideal one dimensional design, perfect first order focusing is inherently impossible if the time spread due to the starting position and starting velocity are uncorrelated. Setting the derivative to the kinetic (potential) energy to zero will be referred to as kinetic (potential) energy focusing. Both derivatives can be zero simultaneously for an infinite starting velocity (v_0) or infinite extraction field (V_1/l_1). These requirements are trivial, as they remove either the spread in the starting velocity or in the starting position.

An important remark has to be made. Once the ions leave the extraction stage, their flight time seems to depend only on their kinetic energy. This suggests that perfect focusing up

to a given order should be possible. Imagine an initial position along the flight path. It is now possible to construct a reflectron that makes all ions have the same flight time from this position on, regardless of their energy and up to a given order depending on the number of stages of the reflectron. However, not all ions will cross the initial position at the same time, and the time delay they have in that point will be exactly the same as the difference in arrival time at the detector. This means that the dispersion curve at one point can be copied towards any other point without any change, up to the order corresponding to the number of stages of the reflectron. A reflectron truly is an ion mirror: the image it mirrors is the dispersion curve.

If kinetic energy focusing and potential energy focusing cannot be achieved simultaneously, it is valuable to make a choice between them based on the residual time spread. This spread is visualized by broadening of the dispersion curve. For potential energy focusing the derivative of t towards the potential energy is zero and the time spread due to the initial velocity spread is:

$$\Delta t_v = \int \frac{dt}{dE_{k,0}} dE_{k,0} = \int \left(\frac{dt}{dE_{p,0}} + \frac{l_1}{q\Delta V_1 v_0} \right) dE_{k,0} = \int \frac{m l_1}{q\Delta V_1} dv_0 = \frac{\Delta v_0}{a_0} \tag{1.15}$$

This result is often referred to as the 'turn-around time' in the case of orthogonal extraction: it is the time difference of arriving on the detector between a cluster with velocity $-v$ and a similar cluster with the opposite velocity v. Because both clusters have the same kinetic energy throughout the flight path, their difference in t_{total}, only depends on their difference in t_1. Alternatively for kinetic energy focusing, the time spread due to the initial position spread is:

$$\Delta t_s = \int \frac{dt}{dE_{p,0}} dE_{p,0} = \int \left(\frac{dt}{dE_{k,0}} - \frac{l_1}{q\Delta V_1 v_0} \right) dE_{p,0} = \int \frac{1}{v_0} ds_0 = \frac{\Delta s_0}{v_0} \tag{1.16}$$

An estimate of the mass resolution for potential energy focusing, MR_p, and for the mass resolution for kinetic energy focusing, MR_k, is given by:

$$\begin{cases} MR_p = \dfrac{t}{2\Delta t_v} = \dfrac{a_0}{2\Delta v_0} t \\ MR_k = \dfrac{t}{2\Delta t_s} = \dfrac{v_0}{2\Delta s_0} t \end{cases} \tag{1.17}$$

This implies that MR_p can be enhanced by increasing the flight time, by increasing the accelerating field, and by lowering the velocity spread. The velocity spread can be reduced by applying orthogonal extraction: the perpendicular velocity components of an ion beam are smaller than the distribution in the axial component. On the other hand, MR_k is enhanced by increasing the flight time and the initial velocity and by lowering the range in the initial positions. By directly extracting the ions from a sample surface one can keep this last distribution small, contributing to the success of MALDI. The effect of increasing mass is different in the two cases: while the resolution is improved for larger ions in the case of kinetic energy focusing, the opposite is true for potential energy focusing.

Table 1-1: Prediction of the resolution based on a 1D model for the K.U.Leuven gas phase cluster setups.

	TOF	HRTTOF
MR_p	$\frac{19.10^3}{\sqrt{n_{Au}}}$	$> \frac{270 \cdot 10^3}{\sqrt{n_{Au}}}$
MR_k	$2\sqrt{n_{Au}}$	$< 0.063\sqrt{n_{Au}}$

Table 1-1 compares the MR_p and MR_k for the newly developed HRTTOF and the RTOF the laboratory was using before. The mass dependence of the resolution is expressed by numbers of gold atoms (n_{Au}). For both setups, potential energy focusing is the most useful approach. For the RTOF, kinetic energy focusing becomes interesting for large sizes corresponding to more than 1000 gold atoms. Comparing potential energy focusing for the two systems, the HRTTOF has at least a ten times better resolution. The main reasons are a doubling of the flight time, a tripling of the extraction field and a reduction of the velocity spread (Δv_0) by the orthogonal extraction. Details of the calculations can be found in appendix A.2. Notice that for the HRTTOF the time spread due to starting position and starting velocity are correlated and the resolution can still be enhanced as described later in this chapter. From the absolute values in Table 1-1 it is clear that the one dimensional model is not sufficient to predict the resolution of a real instrument, which is much lower in both cases.

Calculating electrode voltages

The introduction of the reflectron was a major breakthrough in enhancing the resolution of time-of-flight mass spectrometers.[14] It increases the total flight time, basically without changing the time spread at the detector. The reflectrons used in the HRTTOF consist of two segments with highly homogeneous electric fields (ΔV_{R2} or ΔV_{R1}), separated by wire meshes. Ions with higher velocity penetrate deeper into the reflectron. This time delay can be used to compensate for the shorter time the faster ions spend in the field free region. Exact, analytic solutions for an electric field inside a one-dimensional reflectron allow achieving infinite order kinetic energy focusing.[36,37] The required field can be realized approximately in a curved field reflectron. However, the field inside also has a curvature in a transverse direction, which limits the angular aperture of such a reflectron, resulting in divergent ions with different kinetic energy and a lower mass resolution. A dual stage reflectron can be used to achieve second order, potential energy focusing.[14] The optimal settings for ΔV_{R2} and ΔV_{R1} are derived in appendix A.1 as equations (A.8) and (A.9). The result for potential energy focusing up to second order is:

$$\begin{cases} \Delta V_{R1} = \dfrac{2E_{k,ff}}{3q} \dfrac{L_{ff} + \sum_j \lambda_j + 2l_{R1}}{L_{ff} + \sum_j \kappa_j} \\ \Delta V_{R2} = \Delta V_{R1} \dfrac{2l_{R2}}{2l_{R1} + \left[L_{ff} + \sum_j \lambda_j \right] \left(1 - \dfrac{q\Delta V_{R1}}{E_{k,ff}} \right)^{\frac{3}{2}}} \end{cases} \tag{1.18}$$

with the abbreviations:

$$\begin{cases} \lambda_j = \dfrac{l_j}{q\Delta V_j}\left(\left(E_{k,ff} - E_{k,j}\right)\left(\dfrac{E_{k,j}}{E_{k,ff}}\right)^{-\frac{3}{2}} - \left(E_{k,ff} - E_{k,j-1}\right)\left(\dfrac{E_{k,j-1}}{E_{k,ff}}\right)^{-\frac{3}{2}} \right)^* \\ \kappa_j = \dfrac{2l_j}{3q\Delta V_j}\left(E_{k,ff}\left(\dfrac{E_{k,j}}{E_{k,ff}}\right)^{-\frac{3}{2}} - E_{k,ff}\left(\dfrac{E_{k,j-1}}{E_{k,ff}}\right)^{-\frac{3}{2}} \right)^* \end{cases} \tag{1.19}$$

With $E_{k,ff}$ the kinetic energy and L_{ff} the total length, the same for all field free regions. The star (*) means that in the formula each term including $E_{k,j} = 0$ needs to be removed. This is the case for i=0 in case of a zero starting velocity and for the terms corresponding to the final stage of a reflectron. Through λ_i and κ_i one can introduce as many components as needed. The parameters λ_i and κ_i can be considered as first and second order effective lengths of the components. Indeed, when no voltages are applied, the effective length is equal to the real length of the stage. The value becomes bigger for retarding fields and smaller for accelerating fields. Here follow some examples for λ_j and κ_j in the case of orthogonal extraction, more details can be found in appendix A.1:

- For double stage extraction and no initial velocity:

$$\begin{cases} \lambda_{EXT} = \lambda_{E1} + \lambda_{E2} = \Delta V_{E2}\left(\dfrac{l_{E1}}{\Delta V_{E1}} - \dfrac{l_{E2}}{\Delta V_{E2}}\right)\left(1 + \dfrac{q\Delta V_{E2}}{E_{k,ff}}\right)^{-\frac{3}{2}} \\ \kappa_{EXT} = \kappa_{E1} + \kappa_{E2} = \dfrac{2E_{k,ff}}{3q}\dfrac{\left(l_{E2} + \lambda_{EXT}\right)}{\Delta V_{E2}} \end{cases} \tag{1.20}$$

- For a single stage extraction and no initial velocity:

$$\begin{cases} \lambda_{EXT} = 0 \\ \kappa_{EXT} = \dfrac{2E_{k,ff}}{3q}\dfrac{l_E}{\Delta V_E} \end{cases} \tag{1.21}$$

- For a zero stage extraction (see below):

$$\begin{cases} \lambda_{EXT} = 0 \\ \kappa_{EXT} = 0 \end{cases} \tag{1.22}$$

If we implement a second reflectron, additional terms for λ and κ can be introduced. If the first reflectron is used to create an intermediate focal point (for mass selective experiments), it is better to split up the problem. For the first part between extraction and the intermediate focal point, the equations can be solved for the first reflectron. For the second part between the intermediate focal point and the detector, the equations have to be solved again, now for the second reflectron. In this second part the ions start from a single point, or 'zero stage extraction' and perfect focusing up to second order is possible using the values of (1.22). The reflectron works as a perfect ion mirror and the dispersion

curve is copied from the intermediate focal point towards the detector without deterioration.

- For a detector:

$$\begin{cases} \lambda_D = l_D \left(1 - \dfrac{q\Delta V_D}{E_{k,ff}}\right)^{-\frac{3}{2}} \\ \kappa_D = -\dfrac{2E_{k,ff}}{3q\Delta V_D}\left(l_D + \lambda_D\right) \end{cases} \tag{1.23}$$

In a multichannel plate (MCP) detector an ion first gets accelerated before actually hitting the detector. The reason is that after hitting the MCP plate the secondary electrons need to be accelerated. The voltage between the grounded entrance grid and the MCP (ΔV_D) is of the order of -2kV.

A reflectron is not always required for ion focusing. The first time-of-flight mass spectrometers made use of a three grid extraction optic without a reflectron: the Wiley-McLaren configuration. The three grids define two stages: an extraction stage with a shallow field and an acceleration stage with a high electrostatic field. The optimal settings for ΔV_{E1} and ΔV_{E2} are similar to equation (1.18):

$$\begin{cases} \Delta V_{E2} = -\dfrac{2E_{k,ff}}{3q} \dfrac{L_{ff} + \sum_j \lambda_j + l_{E2}}{L_{ff} + \sum_j \kappa_j} \\ \Delta V_{E1} = \Delta V_{E2} \dfrac{l_{E1}}{l_{E2} + \left[L_{ff} + \sum_j \lambda_j\right]\left(1 + \dfrac{q\Delta V_{E2}}{E_{k,ff}}\right)^{\frac{3}{2}}} \end{cases} \tag{1.24}$$

However, ΔV_{E1} and ΔV_{E2} are not free parameters as they also determine the kinetic energy $E_{k,ff}$. This introduces a third equation to be met and a third parameter is needed to ensure second order focusing. This yields the following geometric condition (see appendix A.1):

$$\left(\frac{L_{ff} - 2l_{E2}}{2L_{ff} + 2l_{E2}}\right)\left[1 + \frac{L_{ff}}{l_{E2}}\left(\frac{L_{ff} - 2l_{E2}}{3L_{ff}}\right)^{\frac{3}{2}}\right] = \frac{s_0}{l_{E2}} \tag{1.25}$$

which was previously derived for MALDI, where $s_0 = l_{E1}$. Applying this equation to realistic values shows that second order focusing only works for very short field free lengths. The easiest improvement is to use a triple stage extraction. With this configuration the effective field free length can be modified electronically.

1.2.2 Corrections to the analytical model

The formulas derived in the previous section only apply to a one dimensional system. In reality the extraction, the reflectron and the detector are on different angles changing the focusing conditions significantly. In a first approximation the flight path together with the detector and the extraction optic simply make an angle α relative to the reflectron as illustrated in Figure 1-6.

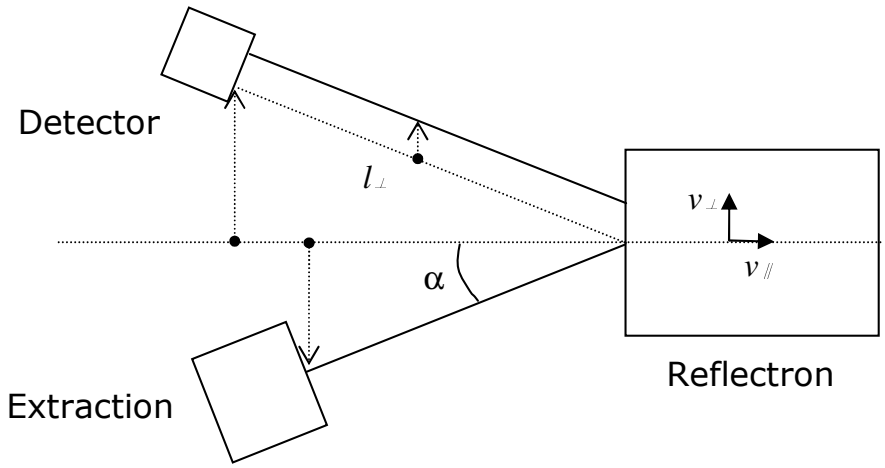

Figure 1-6: Simplified representation of a reflectron on an exaggerated angle α compared to the flight path, in line with the extraction and detection optics.

When the ion enters the reflectron the velocity of the ion can be split into a component parallel to the reflectron axis, $v_{//}$, and a component perpendicular to the reflectron axis $v_\perp$, both depending on the angle α. The electrostatic field of the reflectron only affects the velocity component parallel to its axis. Due to the perpendicular component the ion will exit the reflectron at a different point than where it entered. The reduction of the effective ion velocity can be incorporated by applying effective stage lengths and potential differences inside the reflectron:

$$\begin{cases} l_i \rightarrow \dfrac{l_i}{|\cos\alpha|} \\ \Delta V_i \rightarrow \dfrac{\Delta V_i}{\cos^2\alpha} \end{cases} \tag{1.26}$$

Changing the angle α will also affect the total field free path. By changing the geometry of the system the path simply becomes longer:

$$L_{FF} \rightarrow \frac{L_{FF}}{\cos\alpha} \tag{1.27}$$

However, the ion velocity component perpendicular to the reflectron axis, results in an additional reduction of the total free field length. While the ions are inside the reflectron they exhibit a motion perpendicular to the reflectron axis. The displacement between the entrance and the exit point, $l_\perp$, depends on the perpendicular velocity component and the time spent in the reflectron. This displacement results in a change of flight path: the larger the displacement, the smaller the flight path towards the detector becomes. It is however more convenient to express this correction as a change in time:

$$\Delta t_\alpha = \frac{\Delta L_{FF}}{v} = -\frac{l_\perp \sin\alpha}{v} = -\frac{t_{Ref} v_\perp \sin\alpha}{v} = -t_{Ref} \sin^2\alpha \tag{1.28}$$

which adjusts the original time inside the reflectron:

$$t_{Ref} \rightarrow t_{Ref}\left(1-\sin^2\alpha\right) = t_{Ref}\cos^2\alpha \tag{1.29}$$

Because the time in the reflectron is linearly dependant on the stage lengths, this correction can also be expressed as an apparent change in dimension. This way, we can combine equation (1.26) and (1.29) and introduce the angle α in equation (1.18) through the following simple transformations:

$$\begin{cases} l_j \rightarrow l_j \dfrac{1-\sin^2\alpha}{|\cos\alpha|} = l_j |\cos\alpha| \\ \Delta V_j \rightarrow \dfrac{\Delta V_j}{\cos^2\alpha} \end{cases} \tag{1.30}$$

The formulas derived above take into account a two dimensional view of the flight trajectory but still treat the cluster beam one dimensionally. However, the three dimensional nature of the cluster beam itself turns out to be a determining factor on the mass resolution. Section 1.2.1 discussed the effect of the spread in the starting position and the spread in the starting velocity parallel to the extraction axis: when both are uncorrelated, loss in resolution occurs. A real ion beam also has a spread in the position and the velocity perpendicular to the extraction optic axis. Both of these perpendicular spreads lead to changes in the total flight time. Firstly, due to the spread on the initial velocities of the clusters, the cluster beam is diverging when entering the reflectrons. This results in a time spread at the detector. The derivation of this time spread is similar to equation (1.28): the time difference Δt_ϕ between an ion on the flight axis and an ion on an angle ϕ is given by:

$$\Delta t_\varphi = \frac{-t_{ref}\sin\alpha_D}{v} v_\varphi = -t_{ref}\sin\alpha_D \sin\varphi \tag{1.31}$$

In this equation, α_D is the angle between the detector and the reflectron. The divergence of the cluster beam can be substantial, but the effect on the time spread is limited by the acceptance angle of the detector. For a detector with diameter d_D the measured time spread is limited to:

$$\Delta t_\varphi < t \sin\alpha_D \frac{d_D}{L_{ff}} \tag{1.32}$$

As the angle ϕ depends on the initial conditions of the ion beam and cannot be changed, the apparent approach to cancel this malicious effect would be to change the angle of the detector and set α_D to zero. In that case, the extraction optic and the detector are no longer on the same angle, which introduces a new problem as the time difference Δt_y between an ion on the flight axis and an ion at a perpendicular distance y is now given by:

$$\Delta t_y = \frac{y}{v} tg\left(\alpha_D - \alpha_E\right) \tag{1.33}$$

In this equation, α_E is the angle between the extraction and the reflectron. The detector angle plays an analogous role for the perpendicular components as the reflectron voltages for the parallel components for kinetic and potential energy focusing. In practice, the detector angle α_D has to be a compromise between Δt_ϕ and Δt_y for a given beam divergence $\Delta\phi$ and beam width Δy.

1.2.3 Resolution in an ideal three dimensional system: simulations

Simion 3D

The performance of the instrument was further simulated with SIMION 3D™ 7.0[38]. This is a Windows PC based ion optic simulation program designed to study and analyze ion optics in either two or three dimensions. Electrostatic and magnetic potential arrays (.PA file) can be studied with this software to determine their effect on ion trajectories. The potentials at points outside electrodes and poles are determined by solving the Laplace equation by finite difference methods. An ion optics workbench (.IOB file) strategy allows to size, orient, and position up to 200 of these potential arrays. This way, entire instruments can be modeled. Ions, flown singly or in groups through the created geometry, are displayed as lines or flying dots.

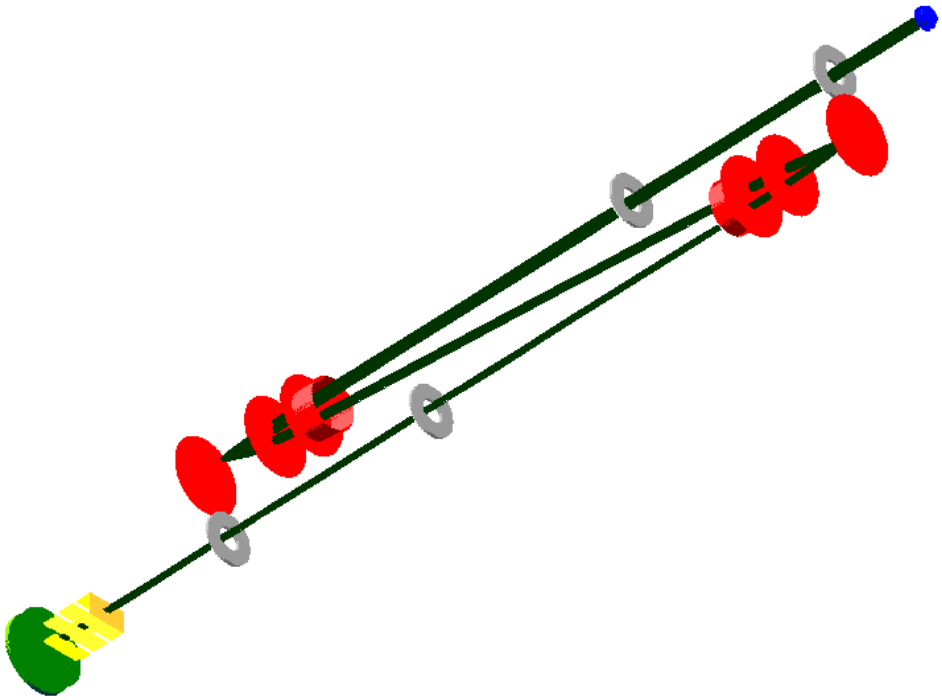

Figure 1-7: Simion ion optical bench representing the HRTTOF mass spectrometer. The ion optical components comprise: a two stage extraction (green), a flat lens (yellow), two reflectrons (red) and a detector (blue). The liners are simplified by only their entrance and exit apertures (grey). The flight path is shown in black. It starts from a 25 mm³ extraction volume and is optimized by the angles and voltages of the different instances. [SIMION 3D™ software]

All instances were constructed by using Simion geometry files (.GEM file). A geometry file uses 3D solid modeling language to define the desired electrode array geometry. The instances used in the ion optical bench do not accurately mimic the actual ion optics in the real instrument. In case accurate models were used, each instance would take over a

gigabyte in memory and the program would not be able to run properly. To keep the file size sufficiently low, cylindrical and planar symmetry was implemented and the effective grain size was limited to 1mm³. On the workbench however, the instances can be positioned with higher accuracy. The simulation also deviates from reality in other aspects:

- All grids are idealized by an infinitely thin, transparent metal sheet.
- The simulation does not account for inhomogeneities in the fields due to mechanical errors or the limitations in the precision of monitoring the actual dimensions and positions of all parts. These dimensions are not even fixed, because precise lengths of the bellows in the real system change while optimizing the system.
- Electronic effects in the extraction and detection of the ions are not taken into account.

Although the simulations give qualitative and even quantitative insight in the performance of the real system, it cannot accurately predict actual values or peak shapes. For this the real instrument has to be calibrated, which is common practice for commercial instruments. In the design phase, ion optics were investigated by instances at a higher accuracy.

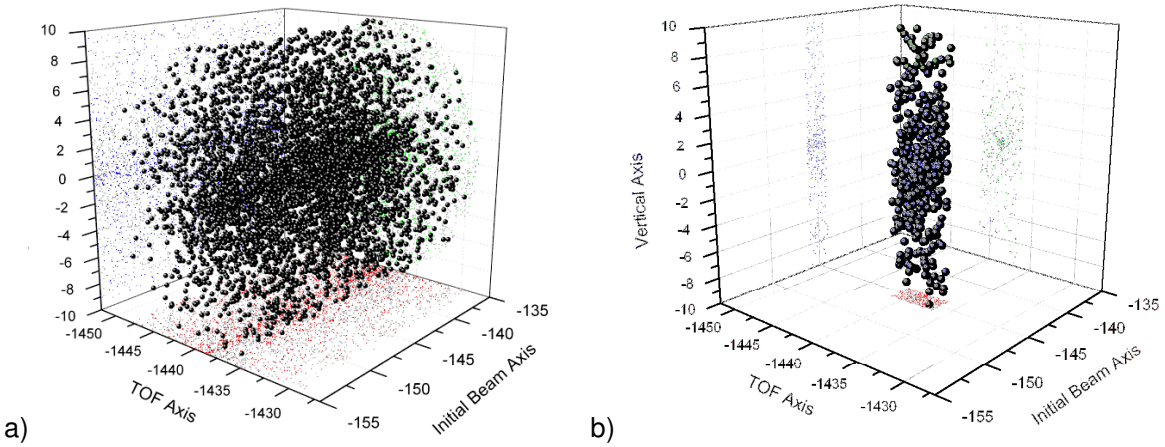

Figure 1-8: (a) Starting positions of the clusters for a cone angle of 0.7° and a radius of 10mm. (b) Reduced volume by a rectangular cut of 5 mm x 2 mm.

Great care was taken to mimic the real starting conditions of the clusters by using Simion user programming (.PRG file). A Simion user program is written in an HP RPN calculator style language and is associated with precisely one potential array. As an ion flies within that array instance, Simion calls each program segment to allow it to control how the ion flies. The program segments can dynamically change electrodes, electrostatic fields, velocities, masses … It is also possible to initialize the values of any predefined variable through the Adjustable Variables Screen prior to flying the clusters. A user program associated with the extraction optic was written to define the starting positions, mass, and velocities of the clusters.

Figure 1-8 (a) shows a typical cylindrical starting volume. This volume is determined by the radius and the cone angle of the cluster beam. The experimentally determined values of 0.7° for the cone angle and 10 mm for the radius were often used, though these values depend on the precise geometry of the cluster source and the beam shaping elements (skimmer, slits…). Figure 1-8 (b) shows the same volume but now with a rectangular cut

of 5 mm x 2 mm in the horizontal plane, which mimics a rectangular laser beam along the vertical axis ionizing a volume of neutral clusters.

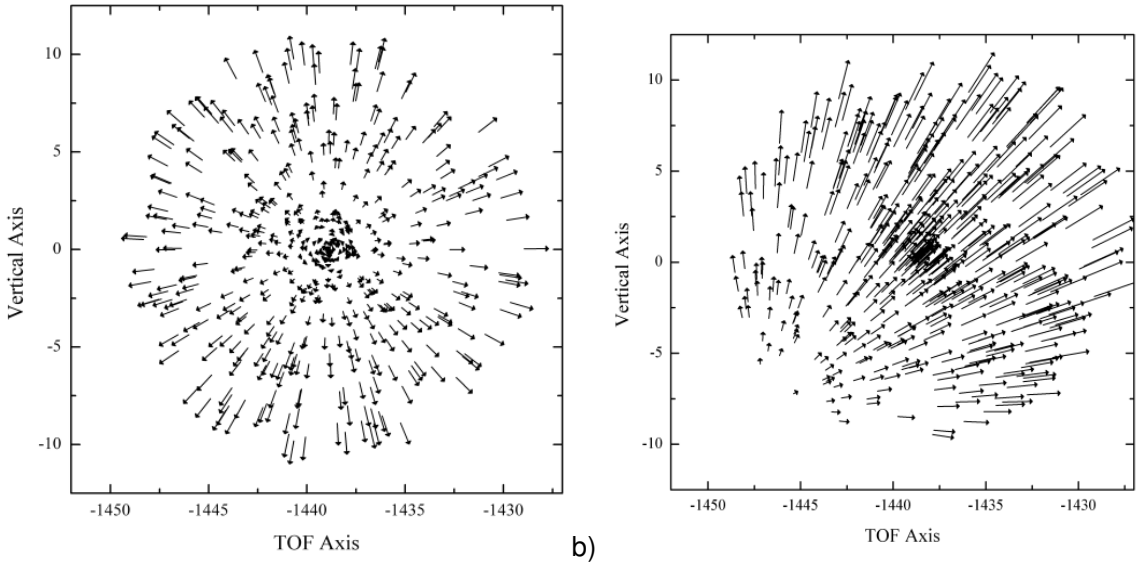

Figure 1-9: (a) Initial cluster positions and velocities in the plane perpendicular to the initial beam direction. The length of the velocity vectors roughly corresponds to the distance traveled in 100µs. (b) The beam undergoes a global deflection upwards and sidewise of 10m/s.

The effect of the cone angle appears in the velocity plot shown in Figure 1-9 (a). The plot shows the starting positions and velocities in the plane perpendicular to the initial flight direction. As can be expected from a diverging beam, the fastest clusters are located at the outside. The length of the velocity vector corresponds roughly with a distance traveled in 100 µs. It is also possible to initialize a cluster beam which is on an angle with regard to the optimal flight axis. Figure 1-9 (b) shows the same plot as (a) but now with global non zero velocity components in the directions perpendicular to the initial cluster beam axis. This corresponds to a cluster beam which is not aligned with the extraction optics. The velocity component perpendicular to the TOF axis needs to be compensated for or else the cluster will fly under the wrong angle and never reach the detector. The component along the TOF axis modifies the starting energy of the cluster. Both effects are mass dependent as they depend on the kinetic energy rather than on the velocity itself. For this reason the mass of the clusters is also an important variable, and its value is implemented by the mass of the element and the number of atoms. During all simulations gold clusters have been used as probe in a range of 0.01 to over 1000 atoms. Apart from the initialization in the extraction instance, user programming also appeared in the reflectron instances when fragmentation was simulated and when many electrode configurations were used.

To analyze the simulation three approaches were followed:

i) The most general approach is investigating the ion trajectories in the ion optics workbench. The ion optics workbench is an imaginary 3D rectangular volume of space which contains all array instances. Ions can be flown within the workbench volume and their trajectories change by the interaction of the array instances. Simion supports the concept of multiple nested 2D and 3D zooms and extended cutaway view options to track the ion flight path inside the array instances. To get a visual impression of the quality of the resolution, time information is tracked by using ‘time markers’. This feature draws points for every ion at user defined time steps giving a visual progression of the focal condition.

ii) A second qualitative approach to judge the effect of the ion optical components on the clusters flight path is using the Potential Energy (PE) view. The PE view displays the potential energy surface along a specific plane of the current 3D volume. The potential energy surface has real physical significance for electrostatic instances and it is the analogue of a miniature golf course for a golf ball representing the ion. It provides an important level of insight on the trajectories and plays a vital role in the design of the extraction optics (see Chapter 2).

iii) The quantitative approach in assessing the performance of the system is using the data recording options that allow recording specific data, occurring at specified events, in a designated format. The main data elements chosen are the time and the kinetic energy recorded at different events, often, but not exclusively, the arrival at the detector. This allows drawing dispersion curves and calculating the resolution. Also position information can be recorded, for instance to track the influence of the angle of the detector. Excel® spreadsheet software[39] was used for data analysis, such as histograms to explore the peak shape and resolution. Origin® scientific graphing and data analysis software[40] was used for graphing.

Simulation of the configuration with single stage extraction

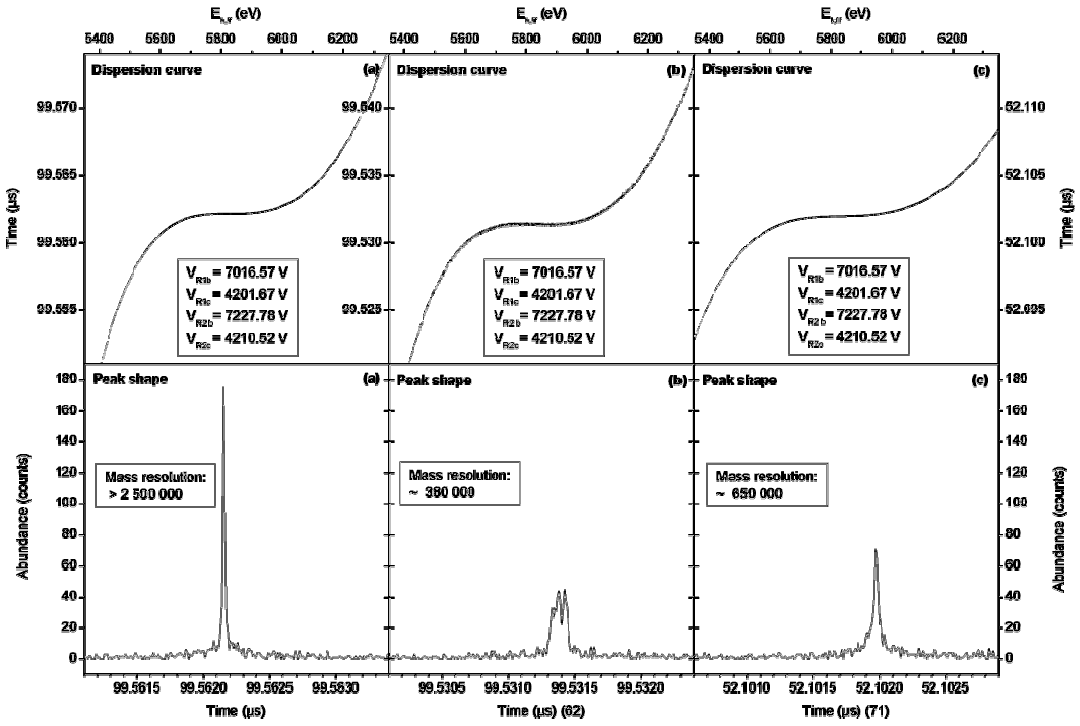

Figure 1-10: Dispersion curve and peak shape for the simulated configuration consisting of a single stage extraction, two reflectrons and a detector and idealized starting conditions. The reflectron voltages were calculated by the one dimensional analytical formulas including corrections for the angles of the reflectrons: the left pane (a) shows the result at the final detector for ideal starting conditions, while the middle pane (b) shows the result at the final detector for more realistic starting conditions where only the spread on the initial velocity is reduced to zero. The right pane (c) shows the result at the intermediate detector for the case were both the spread on the starting velocity and on the position are idealized.

The first configuration which was simulated consists of single stage extraction, two reflectrons and a detector. The single stage configuration allows for direct comparison with the one dimensional analytical formulas derived above. The first run uses idealized starting conditions: the initial cluster beam has a radius of 10 mm and zero divergence. The ionization volume is limited in the direction of the cluster beam axis to only 0.1 mm

and in the direction of the TOF axis to 5 mm. The starting velocity of the clusters is zero. Figure 1-10 (a) shows the dispersion curve and peak shape from this simulation, after calculations of the reflectron voltages including the two dimensional corrections for the reflectron angle (α=1.64°). The calculation of the reflectron voltages seems to be successful, certainly when applying the two dimensional corrections: the dispersion curve becomes completely flat and the peak shape sharp. The presented mass resolution is calculated with a bin width of 0.01 ns limiting the resolution to 2 500 000. A more realistic bin width of 1 ns would further limit the resolution to 50 000, and the resolution in this configuration is well above this value. Without the two dimensional correction discussed in section 1.2.2 the resolution drops to 100 000. In that case the dispersion curve has two local extrema, which correspond to two subpeaks in the peak shape (not shown). Figure 1-10 (b) shows the result for more realistic starting conditions: the initial cluster beam has a radius of 10 mm and a divergence of 0.7°. The ionization volume is limited in the direction of the cluster beam axis to 20 mm and in the direction of the TOF axis to 5 mm. The initial velocity of the clusters is 1000 m/s. Only the spread on this velocity is set to zero. The mass resolution for this simulation is now 380 000, which is more than the value of 270 000 predicted using equation (1.17). Taking into account the actual radial distribution of the starting velocities instead of an artificial linear distribution drastically enhances this prediction. The limiting factor in the simulation is actually the width of the extraction volume and not the velocity spread due to the divergence. Figure 1-10 (c) shows a result for the intermediate focal point. The settings are the same as for Figure 1-10 (b) except for the width of the ionization volume, which again is idealized to 0.1 mm. The mass resolution of 650 000 is very close to half of the 1 250 000 mass resolution at the final detector for the same configuration (not shown). This is a clear example that doubling the flight time doubles the resolution.

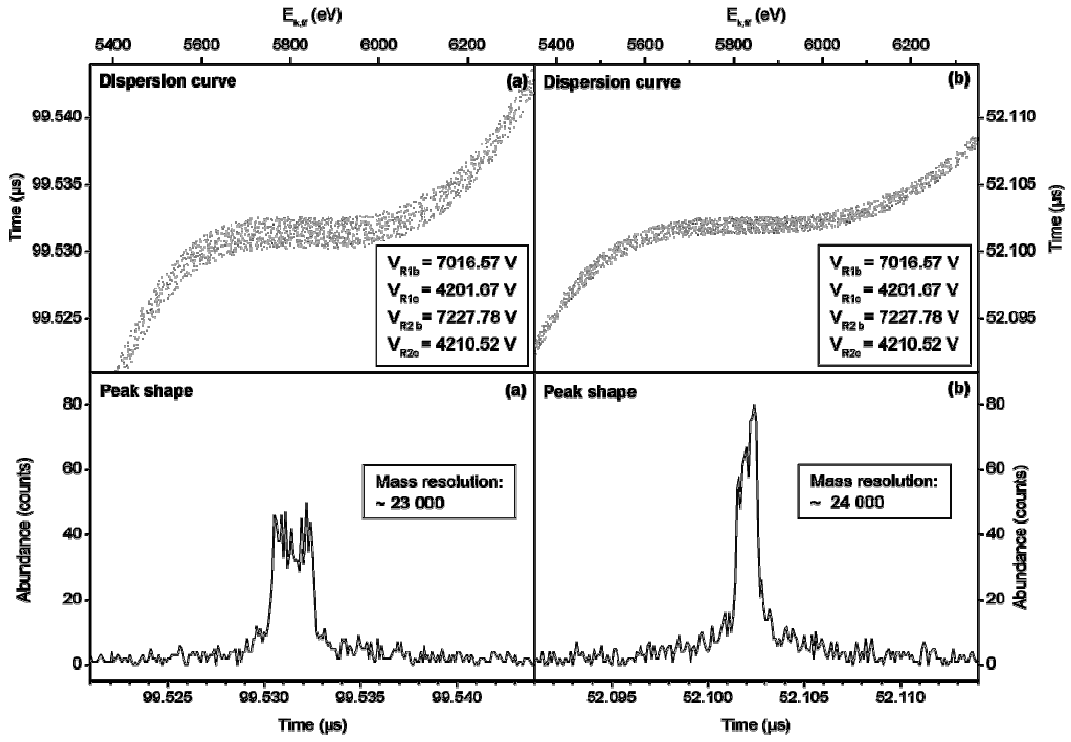

Figure 1-11: Dispersion curve and peak shape for the simulated configuration consisting of a single stage extraction, two reflectrons and a detector. The reflectron voltages were calculated by the one dimensional analytical formulas, including corrections for the angles of the reflectrons. The most realistic starting conditions were applied. The left (a) panel shows the result for the final detector. The right panel (b) shows the result for the intermediate detector.

Due to their idealizations, these results give insight in the different limiting factors on the mass resolution but don't have much predictive value concerning the real resolution of the mass spectrometer. Figure 1-11 shows the result of the simulation with the most realistic starting conditions: the initial cluster beam has a radius of 10 mm and a divergence of 0.7°. The ionization volume is limited in the direction of the cluster beam axis to 20 mm and in the direction of the TOF axis to 5 mm. The initial velocity of the clusters is 1000 m/s with a spread of +/- 3%. By introducing the spread in the starting velocities, the mass resolution drops dramatically. Figure 1-11 (a) and (b) show a mass resolution of 23 000 and 24 000 at the final detector and the intermediate detector, respectively. The spread on the initial velocities of the clusters has a strong negative effect on the resolution. This effect can clearly be seen as a broadening in the dispersion curves. In this case the doubling in resolution due to a doubling in flight time is offset by the time spread induced at the second reflectron and the mass resolution at the two detectors is nearly the same. The sharp drop in resolution can also be predicted quantitatively by equation (1.31).

Simulation of the configuration with curved field extraction

The HRTTOF relies on curved field extraction, which is described in section 2.4.1, instead of single stage extraction to cover a broad mass range. Because the curved field extraction is not build from stages with constant electrostatic field, the derived analytical formulas are not readily applicable. Based on the dispersion curve upon leaving the extraction it is possible to approximate the curved field extraction by an extraction optic with linear potential fields. Since the reflectrons consist of two stages, it is viable to use two stage extraction as a best approximation. From equations (1.15) and (1.17) follows:

$$t_{ext}\left(E_{k,ff}\right)=\frac{\sqrt{2m}}{q}\left[\frac{l_1}{\Delta V_1}\left(v_0\sqrt{\frac{m}{2}}-\sqrt{E_{k,ff}+q\Delta V_2}\right)+\frac{l_2}{\Delta V_2}\left(\sqrt{E_{k,ff}+q\Delta V_2}-\sqrt{E_{k,ff}}\right)\right] \quad (1.34)$$

This was fitted to a dispersion curve by optimizing the potential differences and lengths of the two virtual stages. For reasons of comparison the sum of the length of the virtual stages $l_1 + l_2$ was set equal to the actual length of the extraction optics.

Figure 1-12 shows the result for the simulation of the most realistic starting conditions: an initial cluster beam with a radius of 10 mm and a divergence of 0.7°. The ionization volume is limited in the direction of the cluster beam axis to 20 mm and in the direction of the TOF axis to 5 mm. The initial velocity of the clusters is 1000 m/s with a spread of +/- 3%. Figure 1-12 (a) and 1.9 (b) show a mass resolution of 380 000 and 390 000 at the final detector and the intermediate detector, respectively. These values are exceptionally high and are achieved only by optimizing the detector angle. Without adjusting the angle of the detector, the mass resolution is only 4000. As discussed in section 1.2.2, both the spread in starting position and the velocity spread along the initial cluster beam axis, generate a time spread at the detector. Both can be compensated by adjusting the detector angle. To compensate for the spread in starting position, the angle of the detector must be the same as the angle of the extraction optic. To compensate for the spread in velocity the angle of the detector should be the same as the reflectron. In practice, the chosen angle should be a compromise between these two. In the case of curved field extraction the optimized angle is only 0.03° from the reflectron angle and a huge gain in resolution is possible. This value is very close to zero. The reason is that right after curved field extraction all clusters pass through a spatial focal point, rendering the spatial and velocity spread in the perpendicular direction highly correlated. Both calculations and simulations

clearly indicate that a one dimensional treatment of the ions starting position and velocity is not sufficient in optimizing and predicting the mass resolution.

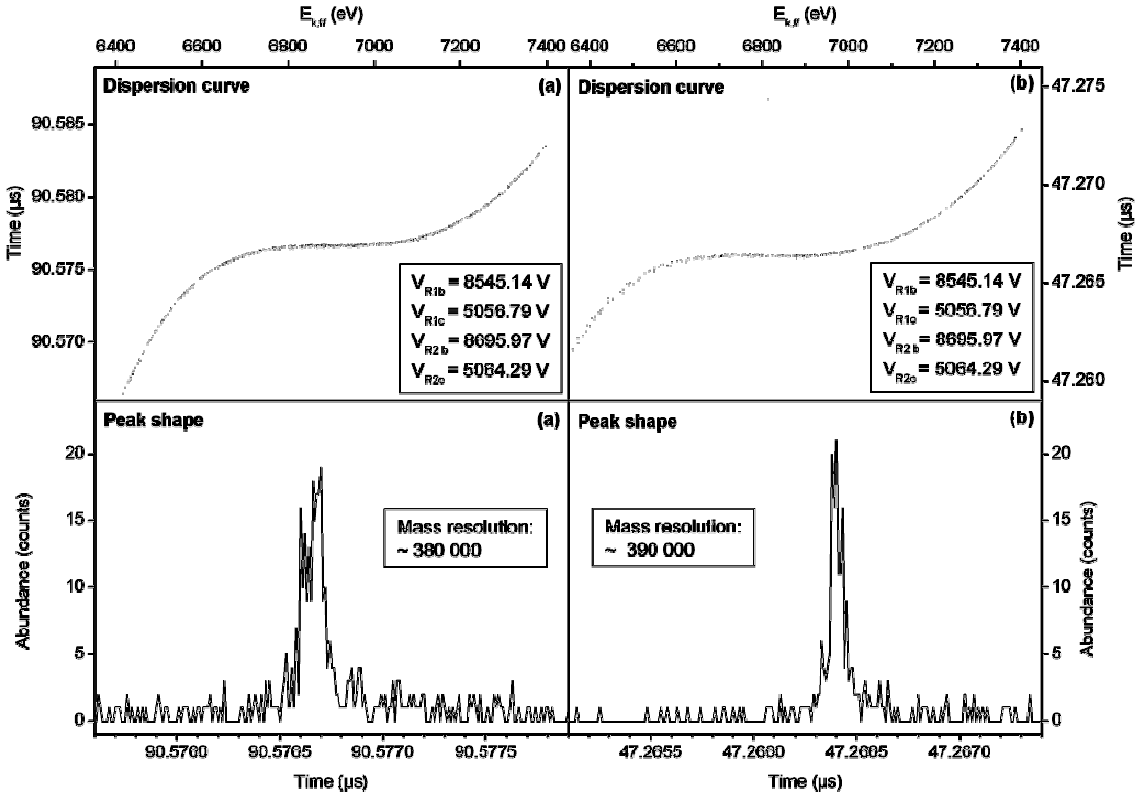

Figure 1-12: Dispersion curve and peak shape for the simulated configuration consisting of a curved field extraction, two reflectrons and a detector. The reflectron voltages were calculated by the one dimensional analytical formulas, with corrections as discussed in the text. The most realistic starting conditions were applied. The left (a) panel shows the result for the final detector. The right panel (b) shows the result for the intermediate detector.

1.2.4 Corrections to the ideal case

Grids

The presence of grids has an important influence on the resolution of a TOF mass spectrometer. When ions pass through a grid, each grid hole acts as a little lens, deflecting the ions and changing their axial kinetic energy. This induces a spread in the arrival time at the detector. Different numerical[41,42] and analytical[20,43] approaches exist in literature to determine the resolution limitation due to the grids. Below a general formula is derived to calculate the time error of a cluster beam induced by passing through a grid, closely following the approach of T. Bergmann.[20] Based on this formula, the total effect of grids on the resolution has been calculated using data from Simion 3D.

Similar to any electrostatic lens, near the surface of a grid, significant perpendicular components of the electric field exist, which induce in-plane acceleration $a_\perp$ of ions passing through. If the axis of the grid lies on the x-direction, ions receive an increase in perpendicular velocity $\Delta v_\perp(r,\theta)$ given by:

$$\Delta v_\perp(r,\theta) = \int a_\perp(r,\theta)dt = \frac{1}{v_{//}}\int a_\perp(r,\theta)\mathrm{dx} \tag{1.35}$$

with $v_{//}$ the axial velocity component and r and θ polar coordinates to describe the position of the ion inside a unit cell of the grid. Because the integral scales with the difference in acceleration at both sides of the grid Δa and with the grid pitch g, we can rewrite this as

$$\Delta v_{\perp}(r,\theta) = \frac{\Delta a}{v_{//}} g G(r,\theta) \tag{1.36}$$

where $G(r,\theta)$ can further be determined theoretically or experimentally. The distribution of $\Delta v_{//}$ depends on the precise position of the cluster between the grids. When traveling through a grid, clusters decelerate. One way to look at this is to interpret the cluster as being on his original time path but with a changed energy, influencing the future path. A different viewpoint is to see the cluster with its new energy, and to assign a certain time difference compared to clusters with the same energy. So every time a cluster goes through a grid it is conceived as a cluster with unchanged energy but with a shift in time. If we know the slope of the dispersion curve in our energy region of interest, we can calculate the time delay for each ion:

$$\Delta t(r,\theta) = \frac{\partial t}{\partial E_{k,//}} \Delta E_{k,//}(r,\theta) \approx \frac{\partial t}{\partial E_{k,//}} q\Delta E \frac{\left(2v_{\perp} + \Delta v_{\perp}\right)}{2v_{//}} g G(r,\theta) \tag{1.37}$$

Here we used

$$\Delta E_{k,//}(r,\theta) = -\Delta E_{k,\perp}(r,\theta) = -m\left(v_{\perp} + \frac{\Delta v_{\perp}(r,\theta)}{2}\right)\Delta v_{\perp}(r,\theta) \tag{1.38}$$

with $E_{k,//}$ and $E_{k,\perp}$ the axial and perpendicular components of the kinetic energy, and

$$\Delta a = -\frac{q}{m}\Delta E \tag{1.39}$$

with ΔE the difference in electric field at both sides of the grid. An estimate of the error on the time distribution is given by:

$$\Delta t_{FWHM} \approx \sqrt{\overline{\Delta t^2(r,\vartheta)}} \approx G_{rms}\, g \cdot \left|q\Delta E\right| \cdot \frac{\partial t}{\partial E_{k,//}} \cdot \frac{v_{\perp}}{v_{//}} \tag{1.40}$$

taking into account $v_{\perp} > 40\Delta v_{\perp}$ for all grids in the HRTTOF. The parameters affecting the grid's performance can easily be distinguished:

- The first factor is the pseudo constant G and the grid pitch g. The pseudo constant depends on the type of grid, but only slightly. On the market, there is a whole range of pitch values: lowering the pitch means a reduced lens effect, but it also means lower transparency and a trade off needs to be made.
- The second factor is the difference in electrical field at a grid ΔE. Strong fields can have large effects. By enhancing the length of the first reflectron stage, a larger grid pitch can be used without losing resolution. The strong field at the curved field or single stage extraction optics can become problematic.

- The third factor is the slope of the dispersion curve. As the slope becomes smaller near a focal point, a grid close to a focal point isn't very harmful: when using curved field or single stage extraction instead of double stage extraction the demands on the grid pitch can lower significantly because there is a focal point right after the exit grid of the single stage or curved field extraction.
- The fourth factor gives information on the angle and amplitude of the velocity of the cluster beam. If the cluster is slowing down as is the case inside a reflectron, this factor becomes larger.

Values of G_{rms} and $\overline{G}$ are obtained from literature. S. Colby used SIMION 3D v.6.0 to simulate the flight of ions through individual grid holes for a number of wire densities.[44] To compare his data with the previous formulas we divide equation (1.36) by $v_{//}$ to get:

$$\frac{\Delta v_{\perp}(r,\theta)}{v_{//}} = \frac{\Delta a_{//}}{v_{//}^2} gG(r,\theta) = \frac{q|\Delta E|\, g}{m v_{//}^2} G(r,\theta) = \frac{q|\Delta E|\, g}{2E_{k,//}} G(r,\theta) \tag{1.41}$$

For the simple case where an ion goes from a single acceleration stage to the free field region this results in:

$$\overline{G} = \frac{\overline{\Delta v_{\perp}}}{v_{//}} \frac{2l}{g} \tag{1.42}$$

with l the length of the accelerating field. Based on the data of Colby for the 'high field' starting region, this corresponds to a value of $\overline{G} = 0.15$. Based on Bergmann's analytical approach[20] the following formula can be identified:

$$G(r) = \frac{1}{4} - \frac{r}{2g} \tag{1.43}$$

This corresponds to $\overline{G} = 0.125$ and $G_{rms} = \frac{1}{4\sqrt{3}} \approx 0.144$. A computational study has been carried out by D. Williams on 4 different types of mesh[41]. For welded mesh with a transparency of 95% the following values can immediately be derived based on the presented data: $\overline{G} = 0.124$ and $G_{rms} \approx 0.134$. By using information from Simion a very accurate calculation can be performed of the grid resolution. At each grid ΔE, $v_{\perp}$, $v_{//}$ and $E_{k,//}$ are obtained. The contributions from different grids need to be convoluted. The results are discussed in section 1.3.1.

Grids not only have an effect on resolution, they also affect efficiency. Though transmission loss is the most important factor it is also important to look at beam divergence. Following equation (1.41) the maximum deviation becomes:

$$\Delta v_{\perp,\max} = G_{\max} g \frac{|q\Delta E|}{m v_{//}} \tag{1.44}$$

To check whether all ions hit the detector, equation (1.44) can be multiplied by the flight time towards the detector and compared with the ratio of the detector. For large flight distances, the divergence can cause a severe deviation on the detector. This can cause

loss of signal, but the broadening can also cause loss of resolution as discussed in paragraph 1.2.2.

Electronics

During detection and extraction, the limitations of the electronics can lead to broadening of the measured peak width. While many MCP detectors have time resolutions better than 1 ns, the amplifiers that follow are generally not as fast and also the matching oscilloscope needs to have an appropriate bandwidth. One solution is to use a timing amplifier which is faster but loses linearity towards the peak height by differentiating the signal. In single ion detection mode it can be used to record very precise timings. For most modern detection systems, the time spread induced is smaller than the time spread induced during extraction.

To accelerate charged clusters a fast electronic switch is needed to pulse the high voltage on the extraction plates. Typical values of rise times are between 30 and 100 ns. The result is a Gaussian type of distribution of the time spread at the detector with FWHM of about 1/40 of the rise time. To accelerate neutral clusters a constant field can be used in which the clusters get ionized by a short laser pulse (typical 6-10 ns). The resulting time spread at the detector is the same. Even detection and extraction systems that induce only small time spreads can limit the time resolution for very small ions, which have the shortest flight times. With the modern standards in equipment, decrementing of resolution due to electronic effects should in general not be a major concern.

Inhomogeneous fields

The inhomogeneous fields that are produced by grids are discussed above. Other sources of inhomogeneous fields are due to mechanical inaccuracies in the construction or assembling of various parts. Existing fields can also get modified over time by deposited material, dirt or charging effects. Stray fields of neighboring components have to be shielded, which is a design concern. Looking at the electronic requirements, electrostatic fields can only be stable as long as the high voltage supplies that support them are stable, without long and short time fluctuations.

For the reflectron, both the precision of the resistors in the resistor chain and the relative position of the grids can induce non ideal fields. To limit unwanted effects due to inhomogeneous fields, the number of electrodes in the HRTTOF design was limited to an absolute minimum.

Inhomogeneous fields can also be induced on purpose by using deflection plates. Trajectory calculations indicate that deflection fields placed after orthogonal extraction optics distort the ion packet and degrade the mass resolution to values around 450-1200.[45] In such case, changing reflectron voltages or the detector angle to optimize the position and velocity spread in one or two dimensions becomes quite futile.

1.3 Conclusion

1.3.1 Predicting the resolution

In the previous paragraphs a broad number of limitations to the resolution were discussed. In this paragraph follows a quantitative overview of the different contributions aiming to derive an estimate for the experimental mass resolution.[46] Such overview is currently lacking in literature, mainly because the contribution of the position and velocity spread perpendicular to the flight path is often overlooked. Below, all ions are

considered to have the same mass and charge. Calculations of numeric values can be found in appendix A.2.

If the ions do not start at one point in the extraction region, they will arrive at different times at the detector. By using potential energy focusing this spread can be corrected for. Similarly, if the ions have different initial velocities, kinetic energy focusing can compensate for the spread in flight time. However, it is not possible to compensate for both distributions at the same time as discussed in section 1.2.1. Simulations are in agreement with the calculations: the second order focusing is very successful and there is no significant contribution to the resolution expected at lower masses. For an effective velocity spread of 5 m/s we obtain:

$$MR_p = \frac{a_0 t}{2\Delta v_0} \approx \frac{1350 \cdot 10^3}{\sqrt{n_{Au}}} \tag{1.45}$$

The clusters in the extraction volume also have a position and velocity spread in the plane perpendicular to the flight axis. When the cluster beam passes through a reflectron the resolution can drop significantly. To compensate for the position spread, the detector must be aligned to the extraction optics. To compensate for the velocity spread, the detector must be aligned to the reflectron. When the reflectron is not aligned with the extraction optics, a compromise has to be found for the detector axis as discussed in section 1.2.2. Following equations (1.31) and (1.33) the mass resolution for the position spread (MR_y) and the velocity spread (MR_ϕ) can be estimated by:

$$\begin{aligned} MR_\varphi &= \frac{t^2 v}{2 t_{Ref} \sin\alpha_D d_D} \approx 540 \cdot 10^3 \\ MR_y &= \frac{t}{2\Delta t_y} = \frac{vt}{2\Delta y.tg\left(\left|\alpha_E - \alpha_D\right|\right)} \approx 540 \cdot 10^3 \end{aligned} \tag{1.46}$$

The combination of these two effects yields a resolution of $380 \cdot 10^3$ in perfect agreement with the simulated value of section 1.2.3. This value is extremely high, which is due to the spatial focal point of the curved field extraction. For the single stage extraction a resolution around $25 \cdot 10^3$ was found, which is reduced to $10 \cdot 10^3$ for larger masses.

Not only do the starting conditions of the clusters determine the resolution, but also the specifications of the instrument itself. This was discussed in more detail in section 1.2.4. Every grid will induce a change in the dispersion curve and the divergence of the beam. The magnitudes of these effects depend on the location, the electric field strength, the velocity and the quality of the grid.

$$\begin{aligned} MR_g &= \frac{v_{//} t}{2 G_{rms} g \left|q\Delta E\right| \dfrac{\partial t}{\partial E_{k,//}} v_\perp} \approx 62 \cdot 10^3 \\ MR_{g'} &\approx \frac{E_k t}{G_{rms} g \left|q\Delta E\right| t_{Ref} \sin\alpha_D} \approx 83 \cdot 10^3 \end{aligned} \tag{1.47}$$

The above values are convoluted values for all passages through all grids. MR_g is the contribution due to changes in the kinetic energy when passing through the grid following equation (1.40), while $MR_{g'}$ is the contribution due to changes in the flight

angle following equation (1.44). Both effects need to be convoluted. The effects of inhomogeneous fields and misalignment can partially be traced by variation of parameters in the simulations. Deflection electrodes can lower the mass resolution to 1000.

Both the limited resolution of the detection system Δt_{det} and the duration of the extraction process Δt_{ext} result in a mass dependant spread as discussed in section 1.2.4. The mass resolution contributions are given by:

$$MR_{ext} = \frac{t}{2\Delta t_{ext}} \approx 50 \cdot 10^3 \sqrt{n_{Au}}$$
$$MR_{\det} = \frac{t}{2\Delta t_{\det}} \approx 25 \cdot 10^3 \sqrt{n_{Au}} \qquad (1.48)$$

All contributions to the mass resolutions due to independent origins have to be convoluted to predict the experimental mass resolution:

$$\frac{1}{MR_t} = \sqrt{\sum_i \left(\frac{1}{MR_i}\right)^2} \qquad (1.49)$$

The result cannot be given by a single number but is mass dependant and is presented in Figure 1-13.

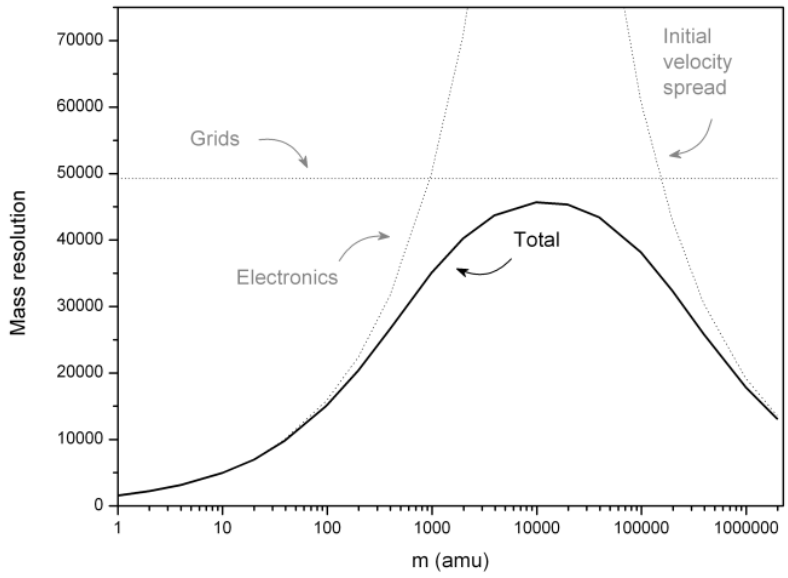

Figure 1-13: Estimated maximum mass resolutions (black) and the main contributions of the grids, electronics and initial velocity spread (grey).

Great care was taken in the design to balance the effect of all grids evenly and the total effect of the grids can be limited to $50 \cdot 10^3$. The effect of the position and velocity spread perpendicular to the TOF axis in principle also contributes to this constant value, but the effect is insignificant. The contribution of the electronics limits the resolution for the smaller masses. The curve in this graph is determined by a 1 ns rise time of the extraction pulse and a 2 ns detection time. On the high mass side the resolution is limited by the initial velocity spread along the TOF axis. This spread is because we opted for orthogonal extraction. Without orthogonal extraction the predicted mass resolution curve would show a maximum of $25 \cdot 10^3$ around mass 1000.

1.3.2 Design of the HRTTOF

Very few commercial mass spectrometers are compatible with the K.U.Leuven laser vaporization cluster source. To be able to perform high resolution mass spectrometry, photofragmentation spectrometry and photoionization spectrometry over a large mass range a new instrument was required. The rather high and mass independent velocity of the clusters limits the design possibilities of a new mass spectrometer significantly. To be able to detect clusters above 20 000 amu, a time-of-flight (TOF) mass spectrometer is the only viable option. Both the high velocity and the velocity spread with which the clusters leave the source form serious limitations for the resolution. The obvious solution to bypass the velocity spread is to use orthogonal extraction. However, this introduces a serious drawback: because different masses enter the extraction region with different energy, a deflection mechanism is required to steer all masses onto the detector. In the current instrument, an improved extraction optic, 'curved field extraction' has been designed and implemented. Though this design is beneficial for both resolution and mass range, it lowers the efficiency of the system by a factor of 10 compared to conventional single or double stage extraction schemes.

To perform mass selected photofragmentation experiments, an intermediate focal point in a dual reflectron scheme was designed. Mass selection takes place in the focal point of the first TOF while a detector is placed in the focal point of the second TOF. A mass gate opens only during a small time interval, allowing only ions in a small mass window to travel further. Tandem TOF mass spectrometry combines very well with photon induced dissociation because of the possibility to have a high temporal and spatial overlap of the cluster beam and the laser beam. This leads to a high dissociation efficiency and mass selectivity. Fragments receive only part of the parent ion's energy and they are not perfectly well focused by a standard two stage reflectron. Because many clusters only fragment by dimer or monomer evaporation a two stage reflectron is still sufficient.

Great care was taken in the design to balance the effect of all grids evenly to limit the effect of the grids on the mass resolution. Both calculations and simulations clearly indicate that a one dimensional treatment of the ions position and velocity is not sufficient in optimizing the mass resolution. For this reason, the detector, the reflectrons and the extraction optics have flexible angles. The contribution of the electronics limits the resolution only for very small masses, where mass resolution is less of an issue.

This design meets all requirements for the new mass spectrometer:

- An enhanced resolution (> 10 000)
- A secondary focal point for mass selected experiments
- Compatible with the K.U.Leuven binary cluster source
- Broad mass window (up to 100 000 amu)

2 Realization

While the first chapter gave a more theoretical background, this chapter gives a technical and detailed overview of the novel instrument. The instrument was built in-house, which comprises a substantial part of this thesis project. The chapter starts with an overview of vacuum components and a discussion on pumping requirements. Next the source is described, followed by a discussion on the effect of the source parameters on the velocity and internal energy of the clusters. After that, the time-of-flight mass spectrometer is detailed with emphasis on the novel 'curved field' extraction and the detection system. The chapter closes with new developments in the data analysis procedure, which improve and extend existing methods.

2.1 Introduction

To be able to perform high resolution mass spectrometry, photofragmentation spectrometry and photoionization spectrometry over a large mass range the implementation of a new instrument was required. The rather high and mass independent velocity of the clusters produced in the existing laser vaporization source limits the design possibilities of a new mass spectrometer significantly. This has been discussed in detail in chapter 1. In short, to be able to detect clusters up to a size of 500 gold atoms (Au_{500}), nearly 100 000 amu, a time-of-flight mass spectrometer is the only viable option. To overcome the velocity spread of the initial cluster beam and to reach a resolution higher than 10 000, orthogonal extraction is required. An improved extraction optic is designed to obtain both high resolution and maintain a high mass range. To achieve high resolution mass selection a tandem reflectron TOF is the obvious choice. We have chosen for a straightforward design to keep options for future modifications open.

A drawing of the high resolution time-of-flight mass spectrometer (HRTTOF) is shown in Figure 2-1. The system can be separated in three vessels: source chamber, extraction chamber, and the flight chamber, vacated by a total of four turbo molecular pumps. In the first, cubic vacuum chamber a dual-laser dual-target vaporization cluster source is installed. Two rectangular targets of different materials are placed beside each other and are moved in a closed-loop pattern under computer control. The targets are exposed to the focused 532 nm laser light of two pulsed Nd:YAG lasers. Synchronous with the ablation of the target surfaces, helium gas is injected into the source by a pulsed supersonic valve, with a maximal backing pressure of 10 bar. Cluster formation is initiated by collisions between atoms, dimers and trimers of the vaporized material and inert-gas atoms. The mixture of atoms, clusters, and inert gas undergoes a supersonic expansion into a vacuum chamber through a suitable nozzle. The isentropic expansion reduces the temperature of the cluster beam and because of the rapidly decreasing

density, ends the cluster-growth process. A conical skimmer with an aperture of 3 mm selects the central part of the cluster beam. This way, both ionic and neutral clusters are produced. The cationic clusters (direct ions) are studied directly by the HRTTOF, while for the study of neutral clusters, additional laser ionization is needed. In this case ionic clusters, produced in the source, are eliminated from the beam by electrostatic deflection before entering the mass spectrometer. Excimer lasers (6.42 eV and 7.89 eV) or a tunable laser provide the necessary laser light.

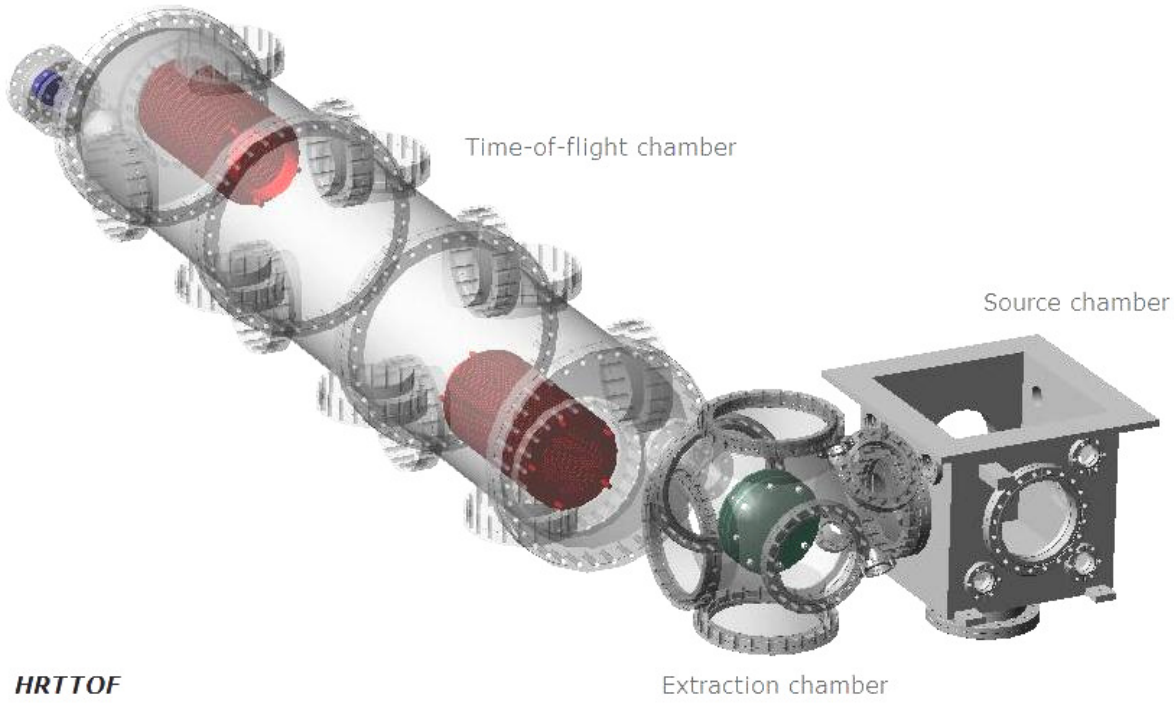

Figure 2-1: Schematic overview of the HRTTOF. The system can be separated in three vacuum vessels: source chamber, extraction chamber, and time-of-flight chamber. The main electrostatic components are highlighted in colour: extraction optics (green), reflectrons (red) and the MCP detector (blue). [made with Alibre Design^{TM} software]

In the extraction chamber the clusters are accelerated perpendicular to their initial velocity into the dual reflectron mass spectrometer through a 'curved field' extraction optic. The extraction chamber is coupled to a large cylindrical flight chamber, which contains two dual stage reflectrons. Alongside the reflectrons are cylindrical liners to screen the cluster beam from the high voltage. In the center of the chamber a wire type mass gate is installed for mass selection in the intermediate focal point. At each side of the mass gate there is a glass window to enable mass selected photofragmentation. The clusters are reflected twice before hitting a chevron type MCP detector. The detector is coupled capacitively to a fast preamplifier. A single ion counter and an oscilloscope can be used simultaneously for data collection.

2.2 Vacuum housing

2.2.1 Vacuum chambers

The most commonly used material for high vacuum and UHV chambers is a 300-series stainless steel, most frequently 304L, which is available in sheet, tube, bar, plate, and forged forms. This steel has desirable vacuum chamber properties: mechanically strong, machinable, weldable; magnetic permeability close to one; resistance to atmospheric corrosion; takes a high polish; and can be effectively outgassed by baking. Grade 316L stainless steel has better overall corrosion resistant properties and has been used for the source chamber. Although a great number of standard chambers and components can readily be purchased on the market, modern CNC mills and lathes facilities make modified or custom parts accessible even at a low cost. Appendix A.3 gives an overview of custom purchased vacuum components. All custom chambers or parts were designed using Alibre Design™ Xpress 9.2 SP1.[47] Alibre Design is a parametric 3D CAD suite that provides powerful 3D model creation and documentation capabilities. The software is comprised of several integrated modules that allow the creation of parts, unfoldable sheet metal parts, assemblies, and 2D drawings.

The source chamber is a cubic box with a hinged lid for maximal accessibility, which facilitates the regular maintenance of the source. The hinged lid contains a DN-160 viewport to inspect the target holder position and motion during operation. One of the main ports at the side of the box is 30 mm off center to allow mounting of a cold finger close to the source. A total of 10 DN-40 ports are added for flexibility in mounting feedthroughs and other auxiliary components. The connection towards the extraction chamber is a DN-160 double sided flange with 100 mm aperture and tapped holes to mount the skimmer.

The extraction chamber is based on a DN-200 six-cross. One of the ports has a reduced size DN-160 to fit a turbo pump. Another DN-160 port has an extension to hold a DN-100 port and 3 DN-40 auxiliary ports. This extension can hold small devices to manipulate the cluster beam or to perform experiments: for instance apertures, deflectors or a reaction shell. This design significantly reduces the distance between source and extraction, compared to mounting an intermediate vacuum component to host the same devices. The extraction chamber also has a DN-200 viewport to monitor the positioning of the extraction optic. Opposite to the source chamber is a reducer flange, which holds a DN-63 MgF_2 laser window for optimal transmission of 157 nm laser light and a mechanical shutter.

The connection towards the flight chamber consists of a reducer flange, which also mounts a flat ‘Einzel’ lens followed by a flexible DN-63 15 cm long hose. This hose allows for some flexibility in the angle between the extraction and flight chamber. It also absorbs the mechanical stress between these two parts. The source and extraction chambers are separated from the flight chamber by a manual gate valve. The flight chamber consists of three 600 mm long cylindrical tubes. The DN-350 size is the smallest size to contain the tandem configuration. Each tube is mounted on a separate gliding table for ease of maintenance. The middle chamber has two DN-63 UV grade quartz viewports on reduction flanges for photofragmentation experiments. It also has a custom DN-160 flange with feedthroughs for the associated mass gate. The main tube is closed on both sides by identical flanges. Each flange has a small port that connects either to the extraction optics or the detector and a large port on a 1° angle that allows for the mounting of one of the reflectrons. To further accommodate the alignment of the

cluster beam, the reflectrons are mounted on bellows with a three point adjustment spider.

2.2.2 Support Tables

The entire setup is mounted on two identical support tables built of high-tensile aluminium profiles: one supporting the flight chamber and the other supporting the source and extraction chambers. All profiles are anodized and are produced with modular dimensions and they are compatible with a broad stock of building components. Each table has 3 gliding frames, which allows manual movement of all vacuum chambers. Aluminum stands connect the vacuum chambers to the gliding frames. The level of the tables can be adjusted with screws at the feet and wheels can be used for sporadic transport of the table.

2.2.3 Vacuum pumps and pressure measurement

Vacuum pumps

A vacuum pump acts like a one-way road for gas molecules allowing them to travel out of the chamber but not back into it. The way this is accomplished very much depends on the required pressure. Pushing volumes of gas from inside the chamber to the outside by compressing them along the way is what rotary vane pumps and other mechanical pump designs do. Given this method of pushing molecules out of a chamber, it is quite natural to define a pump's ability to remove gas in terms of its pumping speed S_p [l/s]. The pressure of the gas inside the chamber then determines how many gas molecules actually reside inside. A rotary vane pump has a good pumping speed all the way up to atmospheric pressure, but it has difficulty pumping under high vacuum conditions. The efficiency of a turbo molecular pump, on the other hand, is rapidly decreasing as the pressure goes above about 10^{-2} mbar. Turbo molecular pumps are not nearly so efficient at pumping when the pressure is large because the gas load slows down the pump vanes. For this reason, rotary vane pumps and turbo molecular pumps are often used in conjunction to pump a chamber down from atmospheric pressure to ultra high vacuum.

When talking about gases, it is no longer worthwhile to simply keep track of the volume being moved by a pump, instead one must discuss the quantity of gas molecules being moved by that pump. This is represented by the gas throughput Q_g [W]:

$$Q_g = \frac{d(pV)}{dt} \tag{2.1}$$

Consequently, the amount of mass flowing through the system is called the mass flow Q [kg/s]:

$$Q = \frac{m_m}{RT} Q_g \tag{2.2}$$

The symbol m_m represents the molar mass. The amount of mass flowing into the vacuum system equals the amount "flowing" out provided the pressure is constant.

Achieving a low pressure is not only a matter of choosing the correct pumping system but as well designing the correct chamber geometry. The factor which accounts for the geometry is called conductance C [l/s]. For short round orifices (A) and the pressure being in the molecular flow regime, the conductance can be modeled as:

$$C = \frac{A}{4}\sqrt{\frac{8RT}{\pi m_m}} \tag{2.3}$$

Another common situation is pumping through long tubes. When the pressure is low so that molecular flow conditions prevail inside the tube the conductance is given by:

$$C = \frac{\pi d^3}{12l}\sqrt{\frac{8RT}{\pi m_m}} \tag{2.4}$$

Here d is the tube diameter and l is the tube length. This equation strongly indicates that the length of the line is not nearly as important as the diameter of the vacuum line and that increasing the diameter of vacuum piping makes a large difference in the conductance. When there are several different elements of a vacuum system placed in series or in parallel, the overall system conductance is found in a similar fashion as the overall capacitance in an electrical network.

Finally, the relationship between the gas throughput Q_g, the conductance C, the pumping speed S_p and the chamber pressure p and volume V is set by the following equation:

$$\frac{dp}{dt} = \frac{Q_g}{V} - \frac{p}{V}\left(\frac{1}{S_p} + \frac{1}{C}\right)^{-1} \tag{2.5}$$

The final pressure also greatly depends on the nature of the gas: for instance, the pumping speed for helium is about 30% slower than for argon gas. In most cases it is the base throughput from degassing and leaks that will eventually determine the base pressure.

The vacuum pumps used for our system are four air cooled Leybold Turbovac 600C turbomolecular pumps mounted on DN-160 flanges and controlled by Leybold TD20 Turbo Drives. The turbo pumps have a documented pumping speed of 600 l/s for helium gas and an ultimate pressure of below 10^{-10} mbar. Taking into account the conductance of the DN-160 ports by equations (2.3) and (2.4), the effective pumping speed drops to a value of around 475 l/s for air. According to equation (2.5) the turbo pump can vacate the vacuum chambers in a matter of seconds. This is much shorter than the 3 minutes required for the pump blades to reach their maximum speed. The backing pumps are four Leybold Trivac D 25B rotary vane pumps, delivering 5.10^{-3} mbar of forevacuum and a documented pumping speed of 7.2 l/s. Taking into account the conductance of the 1m KF25 hose connecting the backing pump with the turbo pump, the effective pumping speed is reduced to 3.0 l/s and it takes around 3 minutes to pump down to the required forevacuum. In practice, the system can indeed pump down in only 5 minutes, but the base pressure will only be reached at much longer timescales due to microleaks and degassing. Degassing depends on the area and the quality of the inner surface of the vessel. Venting with argon instead of air clearly reduces the time to reach a working pressure. Base pressures below 10^{-9} mbar were recorded in the flight chamber.

Pressure measurement

Three pressures gauges are used to measure the pressure in the different vacuum chambers: each of them is a Leybold PenningVac PTR90 all-range pressure gauge, measuring from pressures of 5.10^{-9} up to 1000 mbar for air by combining a Pirani (> 5.10^{-4} mbar) and a cold cathode system for the lower range. The gauges are controlled by a single channel vacuum gauge controller, the Leybold Center one, for the flight chamber and a Leybold Display Two multichannel vacuum gauge controller for the source and extraction chambers. The control connector of the Center one is connected with the safety switch of the detector high voltage supply. If for some reason the pressure goes above 5.10^{-6} mbar, the detector voltages will be switched off to avoid damage. For gasses other than air, the pressure reading has to be multiplied by a correction constant. In the case of helium, which is used as a carrier gas and determines the pressure during operation, the pressure readout has to be multiplied by a factor of 5.9 to get the correct value.

2.3 Cluster production

2.3.1 Laser ablation cluster source

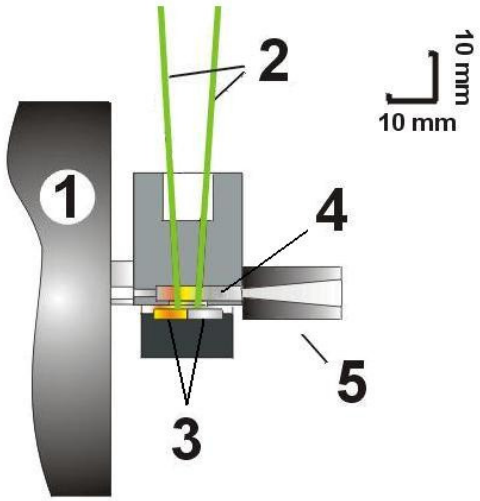

Figure 2-2: Schematic of the laser ablation cluster source: (1) pulsed supersonic valve (PSV), (2) 532 nm laser beams, (3) target plates, (4) cluster formation chamber, and (5) nozzle.

Source

A schematic of the cluster source is shown in Figure 2-2 indicating its main components. The actual cluster formation chamber (4) is a cylindrical channel with a diameter of 3 mm and a length of 15 mm inside a larger stainless steel source block. Clusters composed of two different types of atoms can be made by separate laser (2) ablation of two target plates (3). Synchronous with the ablation of the targets, helium gas is injected into the source by a pulsed supersonic gas valve (PSV) (1). The helium backing gas is more than just a carrier gas. Cluster formation is initiated by three body collisions because a third (helium) atom is needed to take away the binding energy of each newly formed dimer. Moreover, while clusters increase in size the helium atoms keep them in thermal equilibrium with the source block walls. By cooling the source, the internal energy of the clusters will be lowered accordingly. The cluster source is thermally and electronically insulated from the surroundings (pulsed valve, target holder and nozzle (5)) by Macor and Teflon parts.

Target motion system

To achieve stable cluster production, laser ablation takes place by moving the target plates in a constant and reproducible way. Hereto, two UHV compatible stepper motors, Arun Microelectronics Ltd. C17.2, are employed: one for the horizontal motion and one for vertical motion. Together they cover a rectangular area of about 2x10 mm². The stepmotor controllers (09P06) are made in the electronic workshop of the department. By physically changing a set of jumpers, the motors can be operated either in full step mode or in 1/2, 1/4, and 1/8 fractional step mode. This allows for smoother laser ablation, but at the cost of torque and precision. Communication with the stepmotor controllers is established trough a Labview virtual instrument.

The targets are two 7 x 24 mm² rectangular plates mounted next to each other in a brass target holder. A Teflon ring is used to ensure the seal with the source block. The target holder is connected to the target motion system by three small rods that contain springs to press the target holder against the source block. The combination of low friction coefficient and relatively high elasticity of Teflon, allow for a good seal and smooth translation. The quality of the Teflon is of the utmost importance. If for some reason the Teflon sealing shows a leak, the pressure inside the formation chamber changes and the production becomes unstable. The existence of leaks can be confirmed by visual inspection of the target surface. Without a leak there is a symmetric spot of deposited material around the ablation spot. A leak will extend this spot, preferentially in one direction.

Cooling system

To effectively cool the source or the nozzle, these parts have to be insulated from their environment. Heat transfer from the surrounding towards these parts will hamper the cooling efficiency and will increase the attainable temperature. Qualitative information can be found in appendix A.2. To start with, the effect of radiation is limited. The Stefan-Boltzmann law shows that the power of energy radiated from the walls of the source chamber to the source block, mainly depends on the total surface of the source block. For source block temperatures below 200 K the power is 3-4 W. Intuitively, one might think that the ablation lasers significantly heat up the source block, but this is not the case. Even using relatively high laser powers, the laser induced heat transfer is limited to 0.5 W. There is also some convection taking place from the PSV to the source by the helium gas. This value can be estimated using the molar heat capacity of helium and is limited to 0.01 W. The most important form of heat transfer is conduction. The source is mounted on the PSV, which has an operational temperature of 50 °C or more. The heat load due to conduction depends on the geometry of the connection, the materials used, and the final temperature. Not only does Teflon have a very low friction coefficient, its thermal conductivity is only 0.25 W/m.K.

Figure 2-3 shows three possible mounting configurations. In the first configuration the source block is simply connected to the PSV by four 10 mm long stainless steel studs. For a stud diameter of 3 mm and a temperature difference of 300 K this results in a heat conductance of about 14 W. When Macor insulation is used (b) this value doesn't change much. The Macor itself is a poor insulator due to the large contact area. A lower heat conductance can be achieved by placing a Teflon block in between the PSV and the source. Both parts are screwed into the Teflon leaving at least 5 mm of Teflon insulation. The heat conductance now depends almost linearly on the contact area of the Teflon block with the PSV and the source block. For a relatively large contact area of 2 x 9 cm² the heat conductance is 10 W.

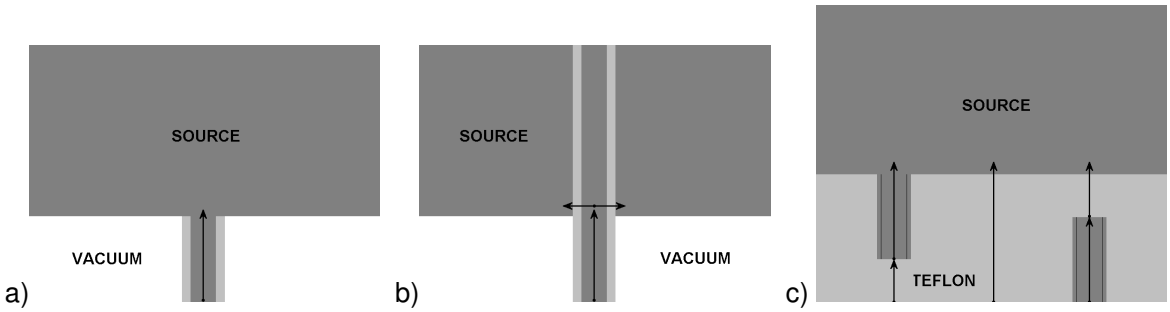

Figure 2-3: Three possible mounting configurations of the source on the PSV. The arrows indicate the main paths for the heat transfer. a) 4 stainless steel studs are screwed directly into the source block (one stud surrounded by Macor is shown), b) using Macor isolation between the stainless steel studs and the source (one stud surrounded by Macor is shown) and c) using a Teflon block between the PSV and the source, four studs mount the Teflon block onto the PSV while four other studs connect the source to the Teflon block (one stud from each side is shown).

Thus, depending on the actual configuration, a total heat loss of below 10 W can be achieved. Any cooling system that delivers a cooling power of more than 10 W can then cool down the system. However, at least double the power is needed to cool the system down efficiently as the effective cooling power P_c', the cooling power of the cooling system minus the heat loss, determines the cool down time Δt_c of the system:

$$\Delta t_c \approx \frac{c \rho V_s \Delta T}{P_c'} \tag{2.6}$$

The cool down time depends on the volume V_s and on the material of the source block by its specific heat capacity c and its density ρ. A total cooling power of 20 W should be sufficient to cool down a stainless steel source in less than one hour. A copper source will take 15% less time and an aluminum source even 40% less.

The cooling system used in our lab uses liquid nitrogen, which flows from a cryogenic vessel towards a heat exchanger made of copper and fastened to the nozzle. The cooling power depends on the flow which can be controlled by the pressure of the nitrogen gas in the cryogenic vessel. The temperature of the source block is measured with a thermocouple. A final temperature close to liquid nitrogen temperature (77 K) can be achieved within half an hour. To reach lower temperatures a cold finger coupled to a closed cycle refrigerator can be used. Commercial Gifford McMahon closed cycle refrigerators are standard available and achieve temperatures below 10 K for 6.7 W of heat load. They allow for additional cooling of a radiation shield which will partly reduce the 3 W of radiation.

Pulsed supersonic valve

Short helium carrier gas pulses are introduced into the formation chamber by using a Pulsed Supersonic Valve (PSV) from Jordan TOF Products, Inc. The valve is composed of a gold-plated beryllium-copper top spring, which is clamped over a viton O-ring to seal the nozzle exit towards the cluster formation chamber. The spring is mounted on top of a faceplate and electrically connected at one side. The PSV power supply passes a current pulse of up to 5 kA and 20 µs duration through the spring and faceplate configuration. Because the current passes in opposite directions through the adjacent conductors a magnetic field will lift up the top spring from the viton O-ring seal. This injects helium gas pulses of approximately 60 µs pulse length by supersonic expansion into the cluster formation chamber. The PSV inlet tube is connected to a gas cylinder containing high purity helium gas. The valve can operate with carrier gas pressures up to

10 bar. The outlet tube is connected to a vacuum pump to purge the lines. While using plastic tubes, the spectrum was heavily contaminated with water. After installing stainless steel tubes, the water trace completely disappeared. The valve does not respond immediately to an input signal and has an adjustable delay of 200 up to 4500 µs. The delay of the PSV was matched with the delay of the Q-switch of the vaporization lasers.

The gas pulse shape was monitored by a fast ionization gauge (FIG) from Jordan TOF Products, Inc. This gauge is a Bayard Alpert type high vacuum gauge on which the grid dimensions have been reduced to increase speed of response. It can be used to observe the time profile of a short duration pulsed molecular beam. The FIG was installed on a special designed flange mounted on the side of the source chamber and aligned to the center of the source nozzle. The distance to the nozzle could be varied with the insertion depth of the PSV and was set to 1.5 cm. Both the FIG voltage and current were operated in a low range: I = 5 mA and V = 150 V, not to saturate the signal. Figure 2-4 shows the variation of the time profile of the helium pulse with the PSV current for two different inlet pressures of helium gas. For both pressures saturation of the signal takes place at higher PSV currents. This is due to choking, which will be explained below. For Figure 2-4 (a) the backing pressure is 5.0 bar and the pulse duration is up to 130 µs. For Figure 2-4 (b) the backing pressure is 7.5 bar and the maximal pulse duration decreases to 110 µs. The maximal signal increases by 20%, due to the higher backing pressure during the choked flow. The gas exerts a higher force on the top spring for a higher inlet pressure, hence a higher current is needed for the same effect. These measured results are very similar to the result documented in the PSV manual.

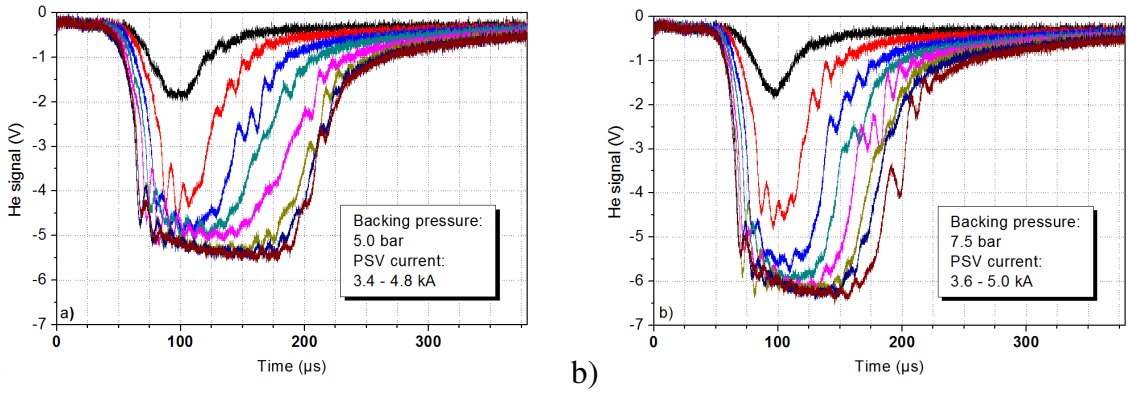

Figure 2-4: He signal measured with a fast ionization gauge as function of the PSV current (3.4 – 5 kA) at two different inlet pressures: a) 5.0 bar and b) 7.5 bar.

Both the helium signal measured with the FIG and the background pressure measured in the source chamber decrease after starting the PSV. As can be seen in Figure 2-5 it takes about one hour for the pressures to reach their saturation values. The most probable reason for this decrease is the increase in PSV temperature. Due to the high current, the PSV valve and body slowly heat up. The temperature gradient in the helium gas is compensated by a lowering of the density towards the valve aperture. This means less atoms are pulsed into the formation chamber and after temperature equilibration the pressure will be lower than before heating up of the PSV. Therefore, stable cluster production cannot be reached within the first hour.

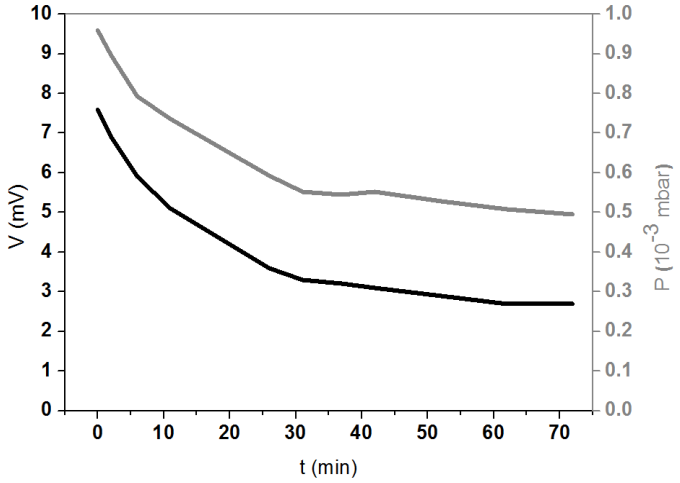

Figure 2-5: Background pressure in the source chamber (grey) and fast ionization gauge He signal (black) as function of the operation time of the PSV.

The vaporization lasers

The vaporization lasers used for cluster production are two Q-switched Nd:YAG lasers (Quanta Ray Indi-series, Spectra Physics) equipped with a 2nd harmonic generator option. After pumping with a flash lamp, whose output matches principle absorption bands in the red and near infrared, the most probable lasing transition emits a photon at 1064 nm. Because the upper level of the transition has a long lifetime, a large population of excited neodymium ions can build up in the YAG rod. Therefore the lasers are equipped with an electro-optic device (Q-switch), which prevents oscillation while the population inversion builds up, and allows for subsequent quick release of the stored energy resulting in a short, intense pulse of laser light. The 1064 nm Nd:YAG fundamental wavelength interacts with a nonlinear crystal to produce a secondary wave with half the fundamental wavelength. After frequency doubling the resulting 532 nm wavelength has pulse energies of about 240 mJ. The pulse width is 5-8 ns and the lasers operate at a repetition frequency of 10 Hz. The beam diameter is about 7 mm, which is focused to about 1 mm when vaporizing the target material. The 532 nm laser light is preferred over an infrared 1064 nm beam for efficiency, alignment and for safety reasons.

Since the energy density on the insert glass and the viewport should be low and a high energy density is needed on the target, a plano convex lens with a short focal distance of 40-50 cm is used. The focal point is a couple of centimeters behind the target surface. To reach the targets, the laser beams pass through two separate laser channels. These laser channels are drilled in an insert that is fixed with screws in the source block. Instead of using two lasers it is, in specific cases such as for the production of doped clusters, also possible to use a beamsplitter (Edmund 532 nm Laser Non-Polarizing Plate Beamsplitter 25 mm Dia) and an attenuator. The attenuator makes it possible to lower the power of the laser used for the dopant material relative to the energy of the main element laser. The attenuator allows for much higher precision than the knob of the control panel of the lasers.

2.3.2 Cluster beam characterization

A laser vaporization cluster source allows production of a large variety of single element and mixed clusters in a very controllable way. The amount of ionized clusters is a few orders of magnitude smaller than the amount of neutral clusters. The velocity and the velocity distribution of these clusters are important for the mass range and mass resolution of the HRTTOF as discussed in the previous chapter. Another important property is the internal energy of the cluster, which gets influenced by the supersonic expansion upon leaving the nozzle. Understanding how the properties of the clusters are influenced in the source and in the region before extraction is important both for fundamental science and for the practical operation of the instrument.

Isentropic flow relations

When a gas flow is forced through a tube, the gas molecules are confined by the walls of the tube. If the gas flow is very gradually compressed and then gradually expanded, the flow conditions return to their original values and the process is reversible. From a consideration of the second law of thermodynamics, a reversible flow maintains a constant value of entropy. Isentropic flow occurs when the changes in flow variables is small and gradual, such as the ideal flow through a nozzle.

The derivation of the isentropic flow equations first starts with the introduction of the Mach number *M*: the Mach number *M* is the ratio of the speed of the flow *v* to the local speed of sound *c*.[48]

$$M = \frac{v}{c} = v\sqrt{\frac{m_m}{\gamma RT}} \tag{2.7}$$

The local speed of sound, in turn, depends on the temperature *T*, the specific heat ratio γ, the universal gas constant *R* and the molar mass m_m. The speed of sound in helium at room temperature is about 1000 m/s. From the entropy equations for a gas, it can be shown that the pressure and density of an isentropic flow are related as follows:

$$\frac{p}{\rho^{\gamma}} = cte \tag{2.8}$$

The value of the constant can be defined by the upstream conditions (subscript ‘u’). Using the equation of state and the conservation of mass, momentum, and energy in combination with and the definition of total enthalpy in the flow, results in the following isentropic flow relations:

$$\frac{p}{p_u} = \left(\frac{\rho}{\rho_u}\right)^{\gamma} = \left(\frac{n}{n_u}\right)^{\gamma} = \left(\frac{T}{T_u}\right)^{\frac{\gamma}{\gamma-1}} = \left(1+(\gamma-1)\frac{M^2}{2}\right)^{-\left(\frac{\gamma}{\gamma-1}\right)} \tag{2.9}$$

From equation (2.7) a similar relation can be determined for the velocity:

$$v = M\sqrt{\frac{\gamma RT}{m_m}} = \sqrt{\frac{RT_u}{m_m}\frac{\gamma}{\frac{\gamma-1}{2}+\frac{1}{M^2}}} \tag{2.10}$$

If the Mach number of the flow is determined, all of the other flow relations can be determined. Similarly, determining any flow relation will fix the Mach number and set all the other flow conditions.

Mass flow rate

The conservation of mass tells us that the mass flow rate Q through a tube is a constant and equal to the product of the density ρ , velocity v, and flow area A:

$$Q = \rho v A \tag{2.11}$$

Considering the mass flow rate equation, it appears that for a given area and a fixed density, the mass flow rate can be increased indefinitely by simply increasing the velocity. If the speed of the gas is much less than the speed of sound of the gas, the density of the gas remains constant and the velocity of the flow increases. However, as the speed of the flow approaches the speed of sound, compressibility effects on the gas have to be taken into account. Now the density of the gas varies from one location to the next.

By combining the mass flow rate equation with the isentropic flow relations and the equation of state, a compressible form of the mass flow rate can be derived:

$$Q = CAMP_u \sqrt{\frac{\gamma m_m}{ZRT_u}\left(1+(\gamma-1)\frac{M^2}{2}\right)^{-\left(\frac{\gamma+1}{\gamma-1}\right)}} \tag{2.12}$$

Two corrections are made to take into account realistic settings: the discharge coefficient C (~ 0.9) which incorporates the effective nozzle geometry and the gas compressibility factor Z.

At the throat of the convergent-divergent nozzle the flow can choke, which means the Mach number has become 1.[49,50] The choked flow of gases is useful because the mass flow rate becomes independent of the downstream pressure. It is important to note that the mass flow rate can still be increased by increasing the upstream stagnation pressure, or by decreasing the upstream stagnation temperature. A nozzle will only choke at the throat if the pressure and mass flow through the nozzle are sufficient to reach sonic speed, otherwise no supersonic flow is achieved. In addition, the downstream pressure of the gas at the exit of the expansion portion of the exhaust of a nozzle must not be too high. Because pressure cannot travel upstream through the supersonic flow, the exit pressure of the gas can be significantly below the background pressure it exhausts into, but if it is too far below ambient, then the flow will cease to be supersonic or become unstable. In practice the background pressure has to be at least two times smaller than the pressure in the supersonic gas at the exit for supersonic flow to leave the nozzle. In our instrument this factor is even several decades lower.[51]

The flow conditions at the nozzle throat can easily be calculated from the isentropic flow relations by setting M=1, e.g.:

$$\frac{p_u}{p_t} = \left(\frac{\gamma+1}{2}\right)^{\frac{\gamma}{\gamma-1}} \tag{2.13}$$

Also the mass flow rate can be calculated:

$$Q = CAp_u \sqrt{\frac{\gamma m_m}{ZRT_u}\left(\frac{2}{\gamma+1}\right)^{\frac{\gamma+1}{\gamma-1}}} \tag{2.14}$$

With the mass flow rate known, the Mach number at the exit of the nozzle can be approximated roughly based on the area of the orifice (A) and subsequently the flow conditions at the exit of the nozzle can be estimated.

$$\frac{A_{exit}}{A} = \frac{1}{M}\sqrt{\left(\frac{(\gamma-1)M^2+2}{\gamma+1}\right)^{\left(\frac{\gamma+1}{\gamma-1}\right)}} \tag{2.15}$$

Helium pressure in the formation chamber

The pressure of the helium gas in the formation chamber of our pulsed source is clearly not constant. In the first step the source gets filled with helium introduced by the PSV. From Figure 2-4 it is clear that this flow is choked and the mass flow rate Q_1 is almost constant during the time t_{psv} when the valve is opened. This time is about 100 µs. During and after this step the gas leaves the source through the nozzle and the corresponding mass flow rate Q_2 is time dependant:

$$\begin{cases} \dfrac{dm(t)}{dt} = \left(Q_1 - \dfrac{m(t)}{\tau_2}\right) & t < t_{PSV} \\ \dfrac{dm(t)}{dt} = \dfrac{m(t)}{\tau_2} & t > t_{PSV} \end{cases} \qquad \frac{1}{\tau_2} = \frac{Q_2(t)}{m(t)} = C\frac{A_n}{V_s}\sqrt{\frac{\gamma RT_u}{m_m}\left(\frac{2}{\gamma+1}\right)^{\frac{\gamma+1}{\gamma-1}}} \tag{2.16}$$

For values below 10 bar, the value of Z is already well within 0.01 of 1, and Z will be set to 1 throughout these calculations.[52] Solving both equations for the mass of helium yields:

$$\begin{cases} m(t) = Q_1\tau_2\left(1 - \mathrm{e}^{-\frac{t}{\tau_2}}\right) & t < t_{PSV} \\ m(t) = m(t_{PSV})\,\mathrm{e}^{-\frac{(t-t_{PSV})}{\tau_2}} & t > t_{PSV} \end{cases} \tag{2.17}$$

These results can easily be translated to mass flow rate or formation chamber pressure through the linear dependences:

$$Q_2(t) = \frac{m(t)}{\tau_2}, \quad p_s(t) = \frac{RT_u}{m_m V_s}m(t) \tag{2.18}$$

A realistic value for the helium temperature is about 320 K and a common pressure of the backing gas might be 8 bar. The radii of the orifice of the valve and the formation chamber are respectively 0.35 mm and 1.44 mm, while the volume of the formation chamber is about 190 mm³. The mass flow rate of the pulsed supersonic valve Q_1 then has a value of about 64 mg/s following equation (2.14) and the half life time of the nozzle mass flow rate τ_2 becomes 155 µs following equation (2.16). The maximal

amount of He inside the source corresponds to a mass flow rate Q_2 of 21 mg/s and a maximal pressure in the formation chamber p_s of about 160 mbar.

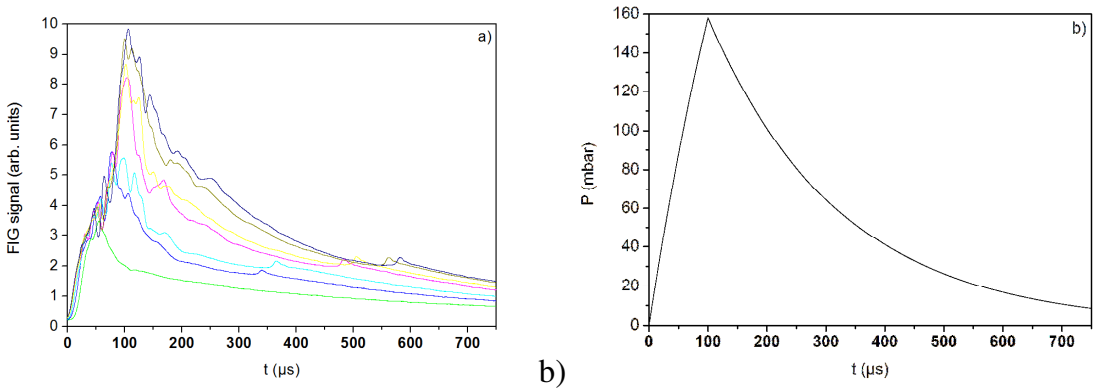

Figure 2-6: (a): Helium signal measured with the FIG for a conical nozzle, a backing pressure of 7.5 bar and various PSV currents. (b): Calculated helium signal pressure in formation chamber as function of time.pressure

Figure 2-6 (b) shows the result from the equations (2.16) to (2.18). During the time the PSV is open, the pressure in the source is building up. This results in the rising edge of the pressure inside the source. When the PSV is closed, the gas will slowly expand into the vacuum chamber, leading to the elongated time profile observed. This results in the falling edge of the helium pressure in the source. The half-life time of the pressure decay is longer for larger formation chambers, smaller apertures and lower temperatures. The time profile of the carrier gas pulse can also be measured experimentally by a fast ionization gauge.[1] Figure 2-6 (a) shows the time profile for a conical nozzle and a backing pressure of 7.5 bar at different currents between 3.5 and 5.0 kA. The signal has been smoothed to remove the noise on the FIG measurement and inverted for comparison. The remaining features are probably due to real turbulences in the helium pulse. The results are in agreement with the work of Peter Thoen and with the results calculated above.[1] Figure 2-4 showed that an increase of the PSV current also increased the pulse duration of the PSV. This correspondence is also clear in this measurement: as the current increases, the peak becomes higher and shifts further in time. Measurements with an insert nozzle and a plate nozzle gave similar profiles and the increase of the half-life time with the increasing volume of the formation chamber is clearly observed. The profile for the copper nozzle is more complicated, which might be due to its complicated design incorporating several orifices.

Understanding the pressure dynamics inside the formation chamber is important because it has an effect on the cluster production. In a simple model, cluster growth is only determined by the helium pressure and the residence time of the clusters. From the quantitative analysis above it can be concluded that the helium backing pressure, the current of the PSV, the temperature of the PSV and the ablation time all probe the pressure of the helium gas in the formation chamber is well understood.

As a consistency check, the effect of the helium pulse on the vacuum chamber pressure can be estimated. The actual value is around $4 - 5 \cdot 10^{-4}$ mbar for a 6.5 bar helium pressure and 5 kV PSV current. Applying equation (2.5) yields a source chamber pressure of $6.3 \cdot 10^{-4}$ mbar for similar settings. The difference might be attributed to the helium loss through the skimmer, the temperature drop after the expansion, a clogged orifice of the PSV or an underestimation of the effective pumping speed. Taking into account these factors, the correspondence is quite well.

Cluster temperature and velocity

While the pressure inside the formation chamber is important during the clustering process, the velocities and the internal energies are the important properties once the clusters left the source. They are determined by the conditions in the formation chamber, but also strongly by the supersonic expansion upon leaving the source. As pointed out before, from equations (2.7) and (2.9) it is easy to calculate the velocity and the temperature of a gas, as long as the Mach number is known. In practice, the Mach number should be derived from a measurable quantity. For example, the following phenomenological relation links the Mach number to the distance (x) from the nozzle, as derived for the three dimensional axisymmetric expansion of helium gas:[53]

$$\frac{x}{d} > 0.5: \quad M = \left(\frac{x}{d}\right)^{\gamma-1}\left[3.232 - \frac{0.7563}{\left(\frac{x}{d}\right)} + \frac{0.3937}{\left(\frac{x}{d}\right)^2} - \frac{0.0729}{\left(\frac{x}{d}\right)^3}\right] \tag{2.19}$$

As the flow leaves the nozzle, at a certain point the collision frequency cannot maintain continuum flow and a transition to molecular flow occurs. This transition region is referred to as the freezing or quitting region because properties are frozen-in in the absence of further collisions. Translational relaxation ends when the number of two-body collisions drops below 1, and clustering ends for three-body collisions below 1. Curves for the number of two-body (Z_2) and three-body (Z_3) collisions remaining in an axisymmetric expansion versus the distance from the nozzle aperture were derived for source conditions at p_0d = 10 torr.cm, T_0 = 300 K and d = 0.0025 cm.[53] Because hard-sphere two-body collisions scale as p_0d/T_0 and three body collisions as p_0^2d/T_0^2, these qualitative results can be scaled to other source conditions. For a source temperature of 300 K, a backing gas pressure of 8 bar and a nozzle diameter of 1.44 mm cluster formation will stop within 1 mm behind the aperture of the nozzle at the peak of the helium pulse. The freezing point is found at around 20 mm. This relates to a Mach number of around 18.5. The knowledge of the Mach number allows determination of the thermodynamic variables by application of the isentropic flow relations. For instance, at the freezing point the temperature drops to 0.8% of the helium temperature in the source. The terminal velocity becomes about 1760 m/s. When lowering the source temperature by 50%, the temperature now drops to 0.75% and the terminal velocity decreases to 1240 m/s. When reducing the pressure by 50%, the temperature only drops to 1.4% and the terminal velocity decreases to 1750 m/s.

Some care must be taken with the interpretation of these temperatures. First, the calculated temperatures are the temperatures of the helium gas. For a gas consisting of only clusters or a mixed gas, the values are higher. Secondly, this ‘temperature’ does not correspond to the internal energy of the cluster. The vibrational modes in the cluster are frozen much earlier in the expansion than the translational modes and correspond to a much higher ‘temperature’. The larger the cluster, the larger the number of vibrational modes and the closer the cluster ‘temperature’ will be towards the source temperature.

While the temperature of the clusters is a very important quantity for our research it cannot be measured directly, but some important remarks can be made. First, the temperature in the source affects the Mach number only weakly. Hence, the temperature drop is almost constant and the absolute temperature of the helium gas depends quasi linearly on the source temperature. Second, the cooling due to the supersonic expansion

is severe and cannot be neglected, which means that the internal energy of the cluster also depends on variables like formation pressure and nozzle geometry. Even more, the temperature in the formation chamber is a priori unknown. The falling edge of the helium pulse corresponds to a period of equilibrium in the formation chamber where the temperature of the helium gas is dominated by thermalization with the walls of the formation chamber and the temperature of the helium gas is assumed to be equal to the temperature set by the cooling system. For the rising edge the supersonic expansion from the PSV cannot be neglected and this will affect the temperature and the velocity of the helium gas in this time interval.

The velocity of the clusters is easier to observe in practice. A rough estimate of the velocity comes from dividing the time between laser ablation and extraction by the distance between the source and the extraction region. The accuracy is very low, because the width of the cluster pulse is more than 100 µs. There is a clear dependence of the velocity on the source pressure and temperature. When decreasing the pressure of the helium backing gas or the PSV current, the optimal extraction time decreases. As suggested by Figure 2-6, the timing of ablation should also probe the pressure in the formation chamber. Indeed, clusters which are ablated later in the helium pulse are clearly slower. A strong temperature effect is also observed. When going from room temperature to a source temperature of about 160 K, the clusters become almost 40% slower. For more precise information a fast ion gauge can be used. Figure 2-7 shows the measurement of the helium pulse (grey) and the signal of the gold cations (black). The helium pulse is measured with the filament of the FIG on and the ablation laser off, and the gold cation pulse is measured with the reverse settings. The small feature at the front is a pickup signal of the PSV high current pulse, which actuates the valve. The time of the gold pulse when crossing the FIG is clear from this graph and the time of extraction can be read out from the delay generator, within a range of 20-30 µs. This gives a flight time of 85 µs over a distance of 150 mm. The velocity of the gold cations in this case is very close to 1760 m/s. The velocity is measured on the rising edge of the helium pulse, which means the residence time of the clusters in the source is minimal. For the falling edge, the residence time is longer and the correct velocity cannot easily be derived.

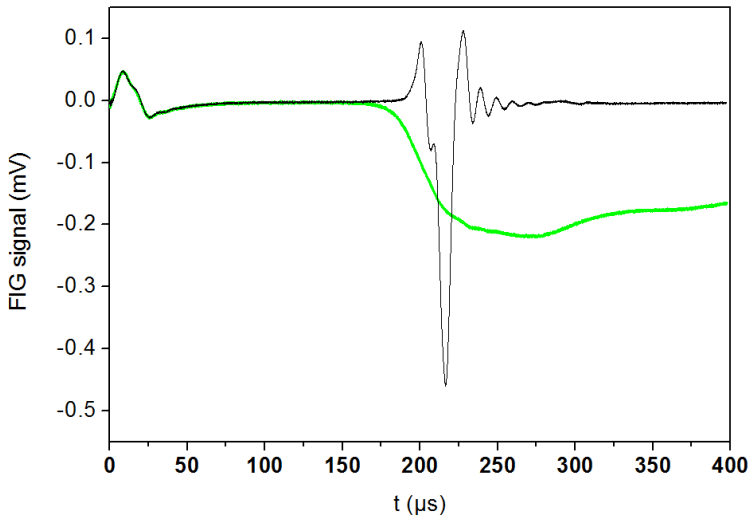

Figure 2-7: Measurement of the helium pulse (grey) and the signal of the gold cations (black) by a fast ion gauge.

The cluster beam

After leaving the formation chamber through the nozzle, the clusters form a beam of independent particles. The properties of this beam are important for the extraction into the time-of-flight mass spectrometer, as explained in chapter 1.

Often it is desirable to shape the cluster beam to improve its properties. This can be done by slits, collisional cooling, trapping, mass selection, magnetic deflection, electrostatic deflection… There is sufficient room on the support tables to implement the necessary components. In the current configuration, the main component in the path of the cluster beam is the skimmer. The skimmer is a conical structure with a hole in the middle at the exit of the source chamber. The outer diameter is about 2 cm and the entrance diameter between 2 and 4 mm. The first purpose of the skimmer is differential pumping. During operation the pressure in the source is high because of the helium gas load, but should be as low as possible in the time-of-flight chamber to improve the detection. The skimmer achieves a drop in pressure by a factor of thousand, with the cluster source chamber having a pressure close to 10^{-4} mbar and the extraction being close to 10^{-7} mbar. The skimmer only selects the center part of the cluster beam which contains the heavier clusters. The helium gas comes out very divergent from the nozzle and it will mainly remain in the source chamber.

A skimmer also is often used to avoid mach shockwaves. Shock waves provide a mechanism to reduce the Mach number to subsonic values where the flow can adjust to the downstream boundary conditions. The skimmer has to be put before the place where the shock wave occurs or where the beam becomes turbulent. The distance of the Mach disk x_M, a shock wave normal to the beam centerline, can be calculated through:[53]

$$\frac{x_M}{d} = 0.67\sqrt{\frac{p_0}{p_b}} \tag{2.20}$$

with d the diameter of the nozzle. It is often stated that a shock wave is absent for low load pulsed sources in high vacuum chambers. Indeed, taking into account a chamber pressure in the range of 10^{-4} mbar, the distance of the shock wave is in the order of 50 cm, far beyond the freezing point, which implies no practical constraints to the position of the skimmer: a continuum shock structure is absent and there is a smooth transition from continuum to free-molecular drift. Experience and results from FIG measurements seem to contradict this. Indeed, the chamber pressure above is only an average value which does not take into account the pulsed nature of the helium load: the maximal pressure in the source chamber can be as high as 0.3 mbar. At the peak of the pulse the distance of the Mach disk reduces to only a couple of cm, clearly restricting the position of the skimmer.

The specific conical shape of the skimmer is also designed to suppress the negative effects of deposition of charged clusters. Due to the substantial divergence of the cluster beam, the area around the aperture of the skimmer will be coated. If the clusters itself are insulating, charge can build up on the skimmer and cause an electrostatic field that blocks or deviates the incoming clusters. By using a conical shape instead of an aperture in a flat surface, the unwanted field is mainly directed away from the skimmer opening. The charging problem is not limited to the skimmer only, and in general it is necessary to dissipate deposited charge as much as possible. For this reason, the skimmer, nozzle, source block and other contact areas have to be grounded properly. Often, tightening nuts by hand is not sufficient and it is recommended to measure whether the resistance is low

enough (<1 Ω). When producing insulating materials like silicon, the charge might not dissipate and has to be repelled by using short electrostatic pulses.

While charging effects can strongly reduce the acquisition of charged clusters, a low signal also for neutral clusters is often caused by misalignment of the cluster beam. It is important to make sure the cluster beam is not obstructed by the skimmer or any other object. This can be done either by checking with a laser pointer or a theodolite, mounted on a translation and rotation stage. The direction of the cluster beam is determined by the angle of the nozzle, but the exit and entrance of the nozzle are too close to each other for determination of the cluster beam's axis. If the source block is tightened sufficiently onto the PSV, an optical axis can be established between the PSV hole and the nozzle aperture. In the perfect case this optical axis should be aligned with the axis of the extraction chamber. However, the PSV is fixed with a rubber ring to the source chamber allowing for some freedom, and similarly, the source block is mounted to the PSV on a disk which can pivot on a rubber O-ring. Using a laser pointer it is quite easy to set an optical axis between the PSV hole and the nozzle exit, and align the skimmer on this optical axis. Alternatively, by putting intense light on the Teflon near the exit of the PSV, the PSV hole can directly be observed with the theodolite. The optical axis is reached when this hole is concentric with the nozzle aperture. The large diameter of the laser beam, makes using the theodolite a more cumbersome, but more precise technique. The quality of the alignment can be checked experimentally, as the skimmer, and other parts of the setup get coated by deposited material indicating the real beam path. From this deposition spot one can also estimate the angle of the beam broadening ϕ for the cluster beam:

$$\varphi = arctg\left(\frac{\Delta r}{\Delta x}\right) \tag{2.21}$$

With Δr the radius of the deposition spot compensated for the skimmer radius and Δx the distance between the skimmer and the deposition spot. For a typical nozzle and for gold clusters this results in an angle of ± 0.7°. For an axial velocity of 1000 m/s this results in a perpendicular velocity of about 12.5 m/s, two orders of magnitude lower. However, the angular distribution of the clusters depends on the square root of the mass: the smaller the cluster, the bigger the spread. For instance, the divergence of the helium carrier gas is huge, adding to the success of the differential pumping.

2.4 Time-of-flight Mass Spectrometer

2.4.1 Extraction optics

Mass Range

One of the main advantages of a time-of-flight mass spectrometer is the theoretically unlimited mass range it can accept. If the extraction is along the same axis as the initial particle velocity vector, the mass range of the instrument is indeed virtually unlimited. This is no longer true for orthogonal extraction. Due to the original velocity component, the velocity acquired after acceleration will make an angle with the acceleration field. This angle depends on the initial energy and not on the initial velocity. If all ions in the original ion beam travel with equal energy, the angle after acceleration will be fixed. If all ions in the original ion beam travel with equal velocity, the angle after acceleration will become larger for larger masses. This has dramatic consequences for the design of a

time-of-flight mass spectrometer. In the first case, no compensation is needed for the ions to travel to the reflectron. But in the second, most prevalent case, some kind of deflection is needed to bend the paths of the heavier ions into the direction of the reflectron or detector. The most common method is to use deflection electrodes.[45,21] In most cases the deflection electrodes are introduced after extraction where the clusters already deviated significantly from the ideal direction. This will limit the angle of acceptance and accordingly the mass range.

Extraction optics

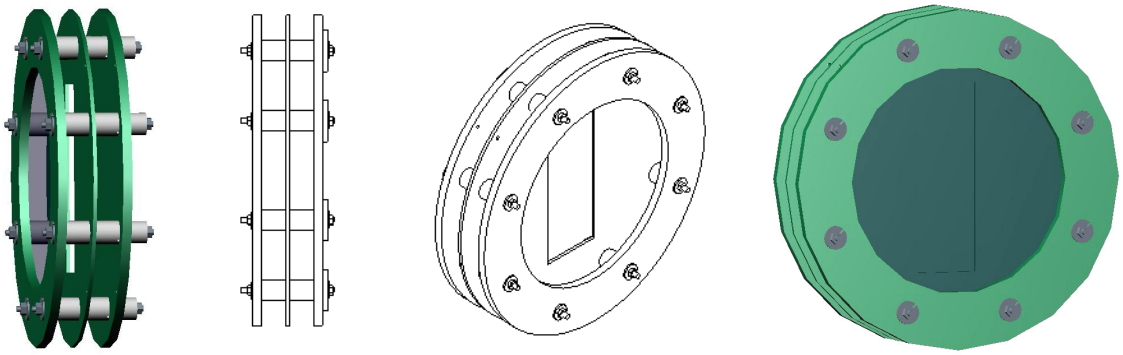

Figure 2-8: Curved field extraction optic [Alibre Design™]

To accommodate the problem of the limited mass range upon orthogonal acceleration, a new design of extraction optics was implemented. Figure 2-8 illustrates the extraction optics, which is home-build in K.U.Leuven and which consists of three parallel, disk shaped plates with a diameter of 180 mm. The large size of these plates is to minimize the effect of penetrating external fields. The back plate is pulsed from zero up to 10 kV by means of an ultrafast high voltage push-pull switch. The second plate has a thickness of 2 mm and is placed 14 mm away from the both the front and the back plates. It has a rectangular hole of 32 x 110 mm² and is pulsed to the same voltage as the back plate. The front plate has a grid of bonded nickel mesh with a pitch of 112 µm (Precision Eforming, 200LPI) and a transparency of 78%. This grid is kept at ground. The middle plate can be removed after disassembly and the extraction can be used as single stage extraction.

The stack of plates can be tilted by an elaborate motion manipulation system mounted on top of a CF160 flange custom made by Kore Technology Ltd.[54] The suspension of the extraction optic allows movement in the x- and y-direction to optimize the starting parameters and horizontal and vertical tilting to align the exiting cluster beam with the desired axis for the TOF. The flange has two external linear motion drives. On the vacuum side of the flange, the forward motion of the linear motion drives is converted to lateral motion using translation levers. Each linear motion drive is adjusted manually in a range of 20 mm. The readout of the linear drives has been calibrated: the back plate crosses the center of the chamber between 23 and 18 mm and the middle plate crosses the center from 4 mm downwards. A good setting to have the cluster beam in the center between the back plate and the middle plate is to set the manipulator to 11 mm. For the other axis, the center is more or less at 15 mm. Built onto this XY- stage is a precision tilting device. The extraction optic can pivot in the centre and can be tilted in the two axes of the vertical plane using stepper motors. These motors are of UHV construction and have a 3 mm range with a 5 µm resolution. This motion is converted to a maximal tilt of ± 1.5° tilt. The internal stepmotors are driven by a separate controller. Motor 1 provides the vertical tilt and motor 2 provides the horizontal tilt. The effect of motor 1 is to aim the cluster beam towards the detector. As both reflectrons are aligned carefully on

the horizontal plane, the same has to be done with the extraction plates. Due to the long flight path, a small change in angle already has a substantial effect, and the response upon moving this motor is clear. Careful control of this motor is possible through a simple DOS computer program (SMD2). This program, in combination with in-vacuum limit switches, allows for calibration of the position. Changing motor 2 gives no measurable effect in the case of 'curved field extraction' as one basically probes different locations for the extraction volume. This is different when using the single stage extraction: turning the plates is essential in scanning through subsequent mass windows. Unfortunately, the range that can be probed is limited to the ± 1.5° tilt and it might be necessary to move the whole support table to expand the range.

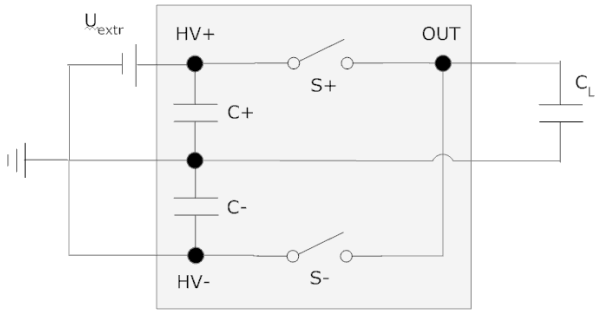

Figure 2-9: Electronic diagram of the Behlke switch.

To accelerate cations, the backplate and the middle plate are pulsed synchronously by a Behlke HTS-03-GSM high voltage switch. The HV supply is a 12.5 kV FUG HCP 14-12500. Although it uses HS21 feedthroughs, the coax cable and the SHV10 connector to the setup are rated to only 10 kV. Figure 2-9 shows a simplified electronic diagram of the Behlke switch. In the off-state, S+ is open and S- is closed, and the external HV supply will recharge C+ while the load is connected to ground. When the Behlke switch receives an on-pulse, S+ will close and S- will open. Now a current up to 30 A will flow from C+ charging the capacitive load. The front plate of the extraction optics needs to be grounded properly or the extraction will not work. The capacitive load for the switch C_L, which is determined by the total capacitance of the plates, has been measured both directly and indirectly. Direct measurement with the multimeter between the HV cable unplugged at the Behlke switch, but still connected to the extraction optics, and ground gave C_L = 0.160 nF. An indirect measurement comes from the conservation of charge: all the charge that gets pulsed has to come from the HV supply. In between two pulses the HV supply has to regenerate the capacitors of the Behlke switch. The saturation current I_{sat} is the current when the HV supply is continuously refilling these condensators. This current has been probed by increasing the frequency of the pulses. If the frequency becomes too high, the HV supply cannot follow and the voltage it delivers will start to drop.

$$C_L.V_{extr} = Q = \frac{I_{sat}}{f} \tag{2.22}$$

Requiring a voltage of 9 kV, the current saturates to 1 A for a frequency of 750 Hz. This results in a load C_L = 0.159 nF in perfect agreement with the direct measurement. The internal capacitance of the Behlke is set to C+ = 2.5 nF, which is in between 10 and 100 times C_L, which is recommended for fastest transition times. The transition time for this load and voltage can be estimated to be around 30 ns. The limitation on the FWHM of the recorded peaks is then around 0.5 ns.

To accelerate neutral clusters, light from an ionization laser is used which overlaps with the cluster beam in between the charged extraction plates. An F_2 excimer laser (Lambda Physik Optex) provides 5-10 ns pulses of 157 nm (7.89 eV) photons with maximum pulse energy of 1.2 mJpp. An ArF excimer laser (Lambda Physik Compex 102) providing 20 ns pulses of 193 nm (6.42 eV) photons with a maximum pulse energy of 200 mJpp is also available in the lab. The laser light enters through a MgF_2 glass which is sucked against a rubber ring and fastened by a cover ring. A removable shield protects this glass from coating by the part of the cluster beam that is not extracted into the TOF.

Curved Field Extraction

A new design of extraction electrodes has been developed improving the mass range significantly compared to tilted extraction plates. The concept of this new design is related to the curved field reflectron, which is a many electrode reflectron with a curved electrostatic field that is optimized for a broad energy range of incoming ions.[26] The principle of the 'curved field' extraction is straight forward. Consider a range of particles of different mass near the center of the extraction optics when they get accelerated. To leave the extraction on the same, orthogonal angle, the velocity component in the original direction has to be negated. Because ions of higher mass need a larger force to decelerate than lighter ones, they require a steeper potential. This can be realized by using a position dependant potential gradient and allowing the heavier clusters to travel or start a bit deeper into this potential. In the novel extraction optic design the rectangular cut in the middle plate creates the necessary sink potential, which is illustrated in Figure 2-10. Because the deflection takes place inside the extraction, the displacement of the different masses is about 1 cm for a mass range from 1 up to 200 000 amu. This shift is still acceptable given a 40 mm diameter detector. In practice, there is no significant influence of the mass range on the position along the initial axis. The extraction volume is large and ions can be extracted from different positions leading to the same exit position and angle even for different masses.

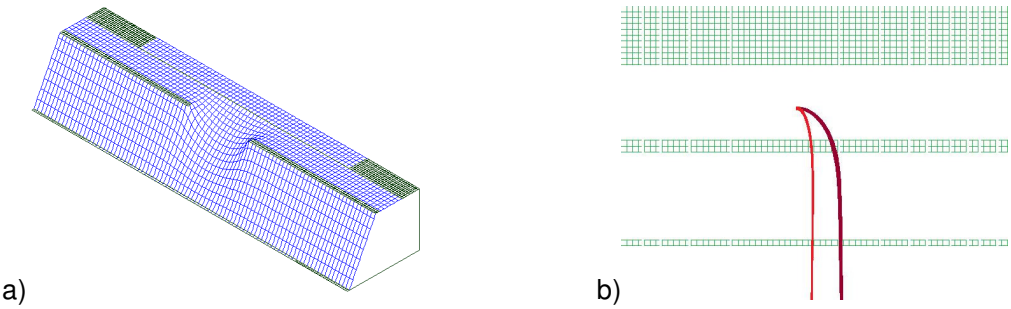

Figure 2-10: (a) Potential landscape of the curved field extraction optic (b) Path of a light (light grey) and a heavier ion (dark grey) after switching on the extraction field and starting from the same position. [Simion 3D™]

The compensation of the initial velocity depends on the precise starting position, giving rise to an extracted cluster beam that is highly divergent. The impact on the efficiency is significant, lowering it by a factor of 10-20 compared to a collimated beam.

Compared to systems with deflection electrodes, the curved field extraction has its deflection inside the acceleration region and uses an axial symmetric field (sink potential). The mass range when using deflection plates is limited by the angle upon which the clusters hit the deflection plates. This suggests implementing the deflection plates as close as possible to the acceleration region. Increasing the distance of the plates, requires increasing the applied voltages. The design of T. Bergmann can also be conceived as curved field extraction. In this design a sink potential is artificially created

in between two electrodes by the use of an orthogonally set of electrodes, effectively forming a quadrupole design.[23] However, this compromises the z-component of the field, and a second quadrupole is needed to compensate. The efficiency of this system is also low. The efficiency is not improved in the K.U.Leuven design, however, the deflection takes place even earlier in the acceleration, and clusters, even with constant initial velocity, can be extracted orthogonally in an energy range of 10 up to 1000 eV. Moreover, the z-component of the cluster velocity remains unchanged.

Single stage Extraction

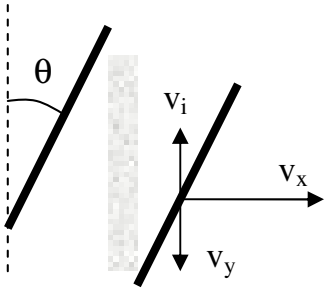

Figure 2-11: Schematic of tilted single stage extraction. The two bold lines depict the back plate and grid that make up the single stage. The broad line depicts the path of the cluster beam coming from the source.

Instead of using deflection electrodes, the angle of the flight path can also be corrected by tilting the extraction plates.[55] After dismounting the curved field extraction optics the middle plate can be removed and a single stage extraction design remains which can be used without further adaptations. To extract orthogonally, into the x-direction, the following equation is valid:

$$v_i = \sqrt{\frac{2E_p}{m}} \sin\vartheta = \sqrt{\frac{2E_{k,ff}}{m}} tg\vartheta \qquad (2.23)$$

With v_i the initial velocity, which is more or less the same for all sizes of clusters, θ the tilt angle and E_p the potential energy related to the starting position s_0 in the extraction region. From equation (2.23) it is clear that for different masses and similar starting positions and potentials, the angle has to be changed, to probe different mass windows in the mass spectrum. Inside a given mass window, which corresponds with a given angle, different masses need to have different kinetic energy. However, the reflectron settings for the optimal mass resolution depend on the kinetic energy. This effect can also be seen in the dispersion curve. While the mass resolution is never a constant of mass, after tilting the single stage extraction plates one can expect larger changes in mass resolution throughout the selected mass window.

Flat 'Einzel' lens

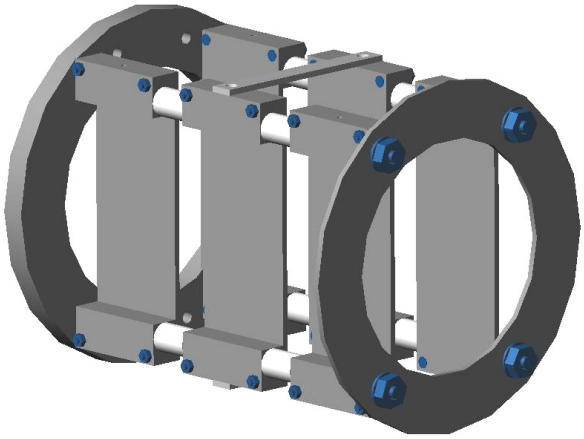

Figure 2-12: Flat 'Einzel' lens [Alibre Design™]

To recover part of the diverging cluster beam, a flat lens is mounted after the extraction optics. The design of the lens consists of three sets of parallel plates, each with a flat, rectangular surface of 37.5 mm by 98 mm. The middle plates are both on the same voltage, between 0 and 6 kV, fed by a 12.5 kV FUG HCP 14-12500. The other two pairs of plates are grounded, much like a conventional cylindrical 'Einzel' lens. However, this lens only acts on the horizontal velocity component of the clusters and leaves the vertical component unaltered, due to the large surface and a set of small compensation bars. The distance to the extraction optics is minimized, but the use of the lens still implies a loss in resolution. Another drawback is that different masses leave the extraction optic parallel to each other. Though this does not result in considerable loss at the detector, the flat lens works best for clusters traveling near its axis. As a solution, the position of the extraction optic can be optimized relative to the lens by an external motion manipulation system. This way, the 'flat' lens can be used for a chosen mass window. The use of the lens implies a compromise between mass resolution and mass efficiency, which depends on the nature of the experiment.

2.4.2 Reflectrons

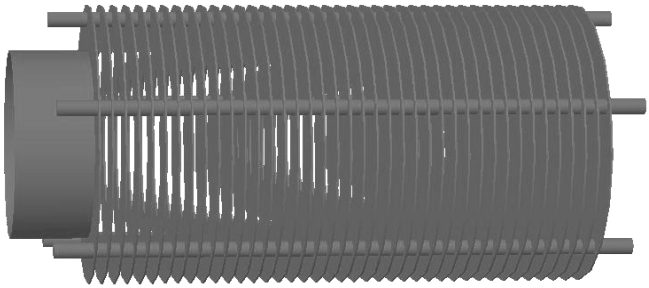

Figure 2-13: Reflectron (simplified model) [Alibre Design™]

The use of a reflectron increases the resolution of the instrument as is discussed in chapter 1. The second reflectron allows for interaction with the clusters in an intermediate focal point. Both reflectrons in the HRTTOF are identical and were custom made by Kore Technology Ltd. They consist of a stack of rings with an inner diameter of 120 mm and a thickness of 1.2 mm, with grids separating the reflectron in two stages. The rings are stacked by highly uniform 7 mm spacers on 5 stainless steel rods and

connected by 1 MΩ (±1%) resistors. The first, decelerating stage has a length of 106.6 mm and the second stage has a length of 205 mm. The length of the first stage is mainly determined by equation (1.40) to balance the effect of the grids on the mass resolution. The length of the second stage is determined by the maximal applied extraction voltage: if the energy of the cluster is too high it flies through the reflectron instead of being turned around. The grids have a parallel mesh of high strength 18 µm tungsten wires at a pitch of 250 µm, giving a transmission of 92%. Parallel wires have better properties regarding transmission, and also reduce the negative effects due to the lens effect.[56] The correct positioning of the grids is not straightforward. The length of the spacers at the grids is optimized to match the field of the rings to avoid lens effects. This is not only a mechanical issue: when a conducting partially-transparent mesh is used to separate two regions of different electrostatic field strength, there are also changes to the field and potential distributions in the vicinity of the mesh.[43] Of particular relevance are the average potentials ϕ_1 and ϕ_2 at the two planes that touch the two surfaces of the mesh. Their value depends only on the wire diameter *d,* the pitch *s* and on the field strengths E_1 and E_2 on the two sides of the mesh:

$$\phi_{1,2} = (E_1 - E_2)\, s\chi_m \pm (E_1 + E_2)\, s\chi_d \tag{2.24}$$

With the semi empirical formula:

$$\begin{cases} \chi_m = 0.25\left(\dfrac{d}{s}\right) + \left(\dfrac{1}{2\pi}\right)\ln\left(\dfrac{s}{\pi d}\right) \\ \chi_d = 0.25\left(\dfrac{d}{s}\right) - 0.36\left(\dfrac{d}{s}\right)^2 \end{cases} \tag{2.25}$$

To accommodate this potential offset, which is of the order of 1-4 V, the grids have to be repositioned accordingly. Although the change is only 0.05-0.1mm, this is taken into account when building these reflectrons. Behind the back grid, an additional grid is placed to keep out the penetrating field. Fields penetrating from the side, lower the active diameter to 100 mm, as estimated from simulations. Alongside the reflectrons are cylindrical liners that effectively screen the cluster beam from the high voltage of the reflectron chain. The liners are 60 mm diameter cylindrical stainless steel tubes with a length of 60 cm. They are mounted at one side in the small tube of the TOF chamber custom flanges and at the other side clamped at the inside of the main chamber at a distance of 64.7 ± 0.1 mm from the outer edge in correspondence with the cluster beam flight path. The liners are screening sufficiently: while a linear detector was placed behind the first reflectron, switching on or off the second reflectron had no effect on the signal.

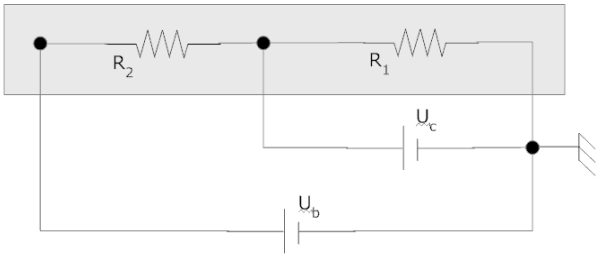

Figure 2-14: Simplified electronic diagram of the reflectron.

Figure 2-14 shows the electronic configuration of the reflectron. Electronically, the reflectron is a stack of ring electrodes with a resistor chain R_1 between the front and the middle grid and another resistor chain R_2 between the middle and the end grid. The front grid is grounded while the other grids are connected to two independent 12.5 kV FUG HCP 14-12500 high voltage supplies U_c and U_b. The measured values of the resistor chain are about 25 MΩ for R_2 and about 13 MΩ for R_1. This implies that U_c has to dissipate current if its value is roughly below one third of U_b. Although the operation value is above two third of U_b, the HV supplies are capable of dissipating each other's current.

The steering of the reflectron is achieved by a bellow assembly. The two flanges of a standard edge welded bellow are connected by a three-point adjustment spider. The bellows length of 16.4 mm is deliberately short, but permits steering angles of 5°, which is adequate. The three point spider has one leg in the horizontal plane and the other two legs symmetric to this plane, allowing for easy angle optimization in the horizontal plane. Internal flat faces of the bellows assembly are mechanically polished to minimize risk of electron emission between the grounded walls and the rear reflectron electrodes, which are at the highest voltage. The flanges on which the bellows are mounted already have an angle of 1°. To achieve an angle of 0.4°, used in the simulations, the length of the horizontal leg is 2.35 mm shorter than the vertical legs, measured at the outer edge.

2.4.3 Mass selected photofragmentation

Mass selector

The new instrument has a dual reflectron design combined with an intermediate ion deflection gate for mass selective ionization and fragmentation experiments.[26] A first reflectron is used for temporal focusing in the gate and a second reflectron is implemented to focus the mass selected beam onto the detector. The result is a Z-shaped beam path. There is enough space between the two outer legs of the beam path to put a constrained mass selective component into the beam path of the middle leg.

The pulsed mass gate consists of a plane of parallel wire segments formed by two electrically isolated sets of wires.[57] There are a total of 26 wire segments with a 1 mm pitch, 22 are exposed to the cluster beam through a circular aperture in the surrounding metal shield. If the two wire sets are held at the potential of the field free region, the ion beam, traveling through the plane of wire segments, is unaffected. Applying opposite voltages of equal magnitude (250 V) on the set of wires results in an electrical field that will deflects the ions, but only at short range. By holding the gate closed until an ion packet of interest is about to reach the selector and then pulse the opening of the gate for the duration of the passage time, mass selective ion transmission is obtained.

The mass selectivity is determined by the planarity of the electrostatic field of the parallel wire system, the rise and fall times of the pulsed field and the quality of the intermediate focal point. In practice, at opening times shorter than 500 ns, signal loss becomes significant. This is clearly not due to the rise and fall time of the switch: pulsed voltage switches with a short rise and fall time of 15 ns are used (Behlke HS 21-03). Clusters inside the range Δx_f of the electric field between the wires will be deviated. The corresponding time of flight Δt_f can be calculated from:

$$\Delta t_f = \sqrt{\frac{m}{2E_{k,ff}}}\Delta x_f \tag{2.26}$$

For a kinetic energy of 8000 V and a mass of 200 amu, a range of 1 cm corresponds to 100 ns. The same cluster at the same kinetic energy travels about 100µs to reach the detector. The time spread due to the limited mass resolution can be calculated by equation (1.4) and gives a value of 100 ns for a mass resolution of 420.

Photofragmentation

Hitting the cluster beam at the intermediate focal point is not straightforward as the clusters fly with high velocity. An estimate for the laser timing precision for photofragmentation can be calculated from the cluster velocity:

$$\frac{(l_l - l_c)}{v} < \Delta t < \frac{(l_l + l_c)}{v} \tag{2.27}$$

The lower limit is for total overlap between the laser beam diameter (l_l) and the length of the package of focused clusters (l_c), the higher limit is for zero overlap. In the optimal case, the resolution is maximal and l_c is minimal and the two values become similar. For l_l = 10 mm and ΔV = 9500V the precision for Au_1 becomes 0.1 µs. This is an order smaller than the accuracy of the simulations, so further calibration of the system is needed. Based on the timings for mass selection and knowledge of the velocity from simulations a crude estimate can be found for the timing of the photofragmentation. The effect of the pulse width of the laser is neglected as it is only 6 ns.

From the time difference between the mother and the daughter peak in the mass spectrum, the mass of the daughter can be derived. The flight time of the daughter peak is the same as the flight time of the mother peak outside the reflectrons, because they have the same velocity. The flight time of the daughter inside the first reflectron is the same as the flight time of the mother because no fragmentation has taken place yet. However, the flight time in the second reflectron for the daughter becomes:

$$t_{ref,D} = \sqrt{2m_D}\,\frac{l_{R1}}{q\Delta V_{R1}}\left(\sqrt{\frac{m_D}{m_M}E_k} - \sqrt{\frac{m_D}{m_M}E_k - q\Delta V_{R1}}\right) + \sqrt{2m_D}\,\frac{l_{R2}}{q\Delta V_{R2}}\sqrt{\frac{m_D}{m_M}E_k - q\Delta V_{R1}} \tag{2.28}$$

Because the potentials and the dimensions of the reflectron are well known, this formula is directly applicable as soon as the kinetic energy of the clusters is known. The kinetic energy can be derived from the total flight time. Knowledge of the kinetic energy is also useful to calculate the time difference between mass selection and the laser interaction.

A problem when fragmenting clusters in this configuration is the resolution upon detection. The energy of the fragments depends on the mass ratio of the fragment and parent cluster and might vary a lot. A standard double stage reflectron is optimized for a specific energy and cannot optimally focus all fragments. Because the error becomes larger with the energy difference, it is needed to make sure that all fragments have a limited energy window. A straightforward way to do this is to implement a decelerating-accelerating unit. The retarding field reduces the total energy window, next photofragmentation takes place, and then the accelerating field lifts the energy of all fragments to match the second stage of the reflectron.[27] A second purpose of such decelerating-accelerating unit is to slow down the clusters to enhance the interaction time with the laser pulse. The effect on the velocity however is limited to a factor of five because there is a significant spread on the velocities due to the dimensions of the ionization volume. In practice however, there is no big problem in hitting clusters at this

high velocity. Another problem is to combine this unit with the mass gate, because both need to be close to a focal point to be effective. The biggest drawback of course is the reduction of resolution and efficiency by introducing a number of grids and sharp fields. Probably the better solution is the use of a curved field reflectron. Of course, in the case of monomer and dimer evaporation, the whole focusing problem becomes less important and a standard reflectron is sufficient.

2.5 Data acquisition system

2.5.1 Efficiency

The strength of the signal that comes out of the instrument depends on many factors. First of all, the yield of the source determines the amount of material that can enter the time-of-flight mass spectrometer. This signal strength also depends on the charge state. For the current laser ablation source, the amount of neutral clusters is orders of magnitude larger than the amount of charged clusters (1-5%). Because the extraction of the ions into the time-of-flight is not a continuous process, in-between the detection cycles material gets lost. A possible solution is to trap ions and carefully time the sampling of these ions. Also important for the design of the time-of-flight is the size of the ionization volume. The length in the axial direction determines the position distribution of the accelerated ions. Ions from the ionization volume that reach the detector but not contribute to the peak, will add to the background. The ionization volume can be quite large for a double stage (WM) extraction, even without compromising resolution. Orthogonal extraction can also enhance the extraction volume. However, beam broadening in the time-of-flight mass spectrometer can make the cluster beam too wide to pass through the reflectrons or hit the detector completely. The width of the beam can be calculated based on the velocity spread perpendicular to the beam. For the vertical direction (z) only the initial velocity component will act throughout the flight, and the beam broadening can easily be calculated:

$$\Delta z = 2\Delta v_{z,0} t \tag{2.29}$$

A cluster beam traveling for 2 ms still only broadens by 25 mm, which is small compared to the 40 mm MCP diameter. In the horizontal direction the beam broadening becomes more problematic when using orthogonal extraction. Using deflection electrodes will seriously disrupt the velocity components perpendicular to the flight path. Trying to compensate by using correction electrodes is difficult and will often compromise the resolution. Grids, and other components, do not only induce an energy distribution in the axial direction, they will also result in severe beam broadening that can harm the efficiency. Last, it is needless to say that also the size and quality of the detector determine the efficiency of the instrument to a great extend.

2.5.2 MCP detector

Electron multipliers all rely on the phenomenon called secondary electron emission. When an electron with energy of more than about 100 eV strikes a surface, various processes can give rise to the emission of secondary electrons. Where the average number of electrons emitted is greater than one, there is gain. An electron multiplier detector is constructed using a material with a high secondary electron coefficient such as SiO_2 in the case of the micro channel plate (MCP). In the case of the MCP, electrons travel down a long thin microtube which has a voltage gradient down its length. The

secondary electrons accelerate down the tube, but strike the opposite wall of the tube periodically to give gain. In one MCP detector there are typically many thousands of such tubes packed together in the form of a plate. It should be noted that the multiplication process is not exactly the same for each ion strike. The gain will have a well defined average, but individual pulses have quite a large amplitude variation.

The Kore MCP detector assembly has a large active area (40 mm diameter) which gives high sensitivity and large field of view for the long flight path. The ability to operate with the anode floated away from ground allows both negative and positive ions to be detected with good efficiency. Burle Long-Life™ dual channel plates are employed to achieve good time resolution together with high gain to allow for ion counting applications and long lifetime. The complete assembly is bolted on to a standard Conflat vacuum flange and is bakeable. It is important that there is no stray electric field from the detector assembly, either for ions passing close by or for ions that are approaching the detector. To achieve this aim the detector is fitted with an earthed grid. A second grid is fitted after the earthed entrance grid and before the front face of the channel plate set. A connection brought out to the flange allows this grid to be used as an energy filter, for example to reject low energy secondary electrons in negative ion mode.

The dual MCP detector is operated in ion counting mode. That means the gain is set sufficiently high that a single ion input creates an output pulse high enough to be recorded by the data system. Like all detectors that operate by electron multiplication the MCP undergoes an ageing process as it is used. To maintain the gain required for efficient ion counting, the detector excitation is therefore periodically increased. The useful life of the detector lasts until the excitation has been increased to its maximum permitted value.

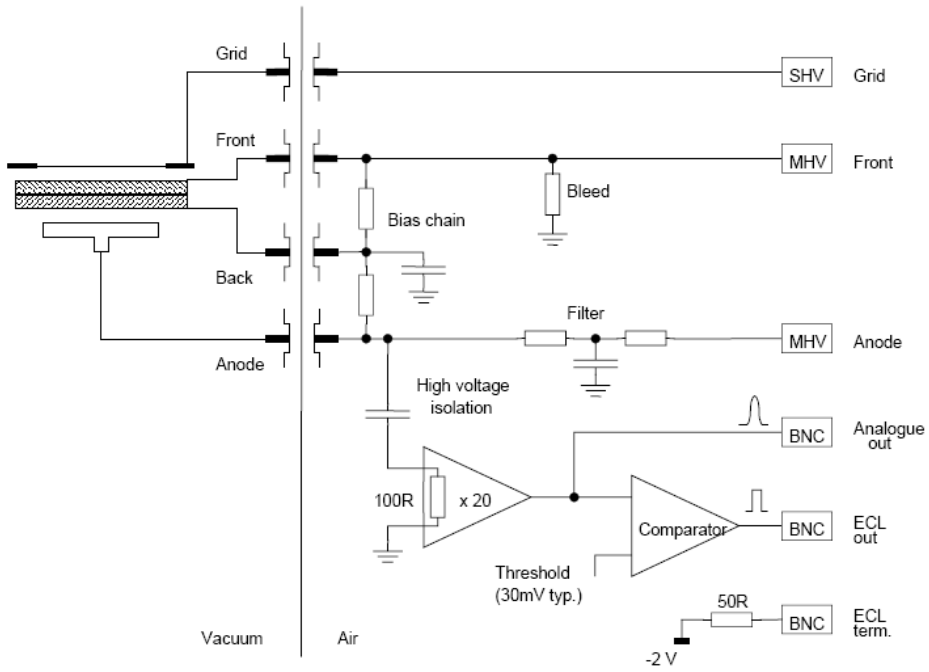

Figure 2-15: MCP with pre-amplifier block diagram. [From Kore Technology Ltd[54]].

This detector assembly has been designed to allow post-acceleration of both positive and negative ions, and secondary electron suppression. The front of the MCP is floated to negative high voltage for positive ions and to positive high voltage for negative ions. In either case 'Rear' is always positive with respect to 'Front'. Any one feedthrough is only able to stand a maximum of 5 kV, and since the maximum possible excitation for a

standard MCP is 3 kV, the post-acceleration is limited to +2 kV for negative ions and –5 kV for positive ions. With the ions having a flight energy of ± 10 kV, this results in impact energies of 12 kV for negative ions and 15 kV for positive ions. In all cases the anode is a couple of hundred volts more positive than the rear plate of the MCP. Unfortunately, the post acceleration induced sparks during testing, which destroyed some of the amplifier components.

The linear MCP detector (Jordan TOF Products) assembly has a smaller active area (20 mm diameter) than the main MCP detector, doesn't have as many features as the main detector and is used for testing purposes. The detector assembly is not floating. This means that the 'Front' connection to the micro-channel plates is held at a negative voltage of about -2.2 kV and the rear is at a negative voltage of about -0.2 kV. The anode is grounded through the amplifier and collects the negative charge.

2.5.3 Pre-amplifier

Most oscilloscopes are not able to process the tiny signal that is measured with the MCP detector directly, and the signal needs the appropriate pre-amplification. The Kore pre-amplifier is designed to mount directly to the flange of the floatable large area detector and provide signal amplification and 50 Ω output. The connections are made via push on connectors and captive screws to allow fast disassembly from the flange for baking. Two high voltage sockets (MHV) accept the front and rear excitation voltages from an external supply. The pre-amplifier input is coupled to the detector anode via a high voltage capacitor so that signals may be gathered with the anode up to 5 kV away from ground. It includes a high speed analogue gain stage (20 x, rise time <1.5 nsec) capable of driving a 50 Ω cable. However, the capacitive coupling results in count rate effects due to non DC balanced pulse trains and the corresponding coupling capacitor charging. This leads to deformations of the baseline and non-linearity of the peaks. The reason for the AC analogue amplification stage is that it is followed by a fast comparator stage that can provide digital output pulses to drive the Fast-Comtec P7887 TDC. The ECL voltages are attenuated to fall within the acceptable range of the Fast-Comtec, which should have its threshold adjusted to -0.7 V. This is a single ion counter and it only works properly in this regime. To maintain linearity in the peak heights, very slow acquisitions are needed. Other pre-amplifiers (Fast-Comtec TA1800 and the older Ortec 9305) were used for the linear MCP, which also present an alternative for the main MCP when using higher count rates.

A measure of protection is provided at the input of the amplifier by a very fast diode, primarily to speed up the recovery from excessively large input signals that often occur in a time-of-flight experiment. However, inevitably with research equipment, unusual experiments may lead to unintended high voltage flash-overs. Perfect protection from these is incompatible with very high speed performance so to minimise the pain associated with such events the semiconductor components on the pre-amplifier board are mounted in ultra low profile sockets and can therefore be changed relatively easily.

A good check in practice is the pickup signal from the extraction pulsing: for a working amplifier the pickup signal of 9 kV is 1 V on the oscilloscope. If it drops to around 0.5 V or lower one of the components is wearing out. The most critical components are the 2 amplifiers Intersil HFA1100IP and the diode D1 (0.62 V in one direction, overlimit in the other). The comparator Maxim MAX9691 never broke down. The break down of the other components is probably due to sparking. To avoid this, the detector has to be ramped slowly before switching on or off. The post acceleration feature seems to give more signal at lower detector voltages. However, it wears out the amplifiers very fast.

2.5.4 Data collection

For ion timing a Fast-Comtec 0.25 ns time-to-digital converter (TDC) with a deep FIFO is used. This is installed in a PCI slot in the instrument PC. The P7887 PCI board is one of the fastest commercially available multiple event time digitizers. Burst/peak count rates of up to 4 GHz can be handled with no deadtime between time bins. A proprietary input logic securely prevents double counting. The exceptionally dynamic range of up to 38 bit enables sweeps for 68.7 seconds with a time resolution of 250 ps. A crystal stabilized PLL oscillator assures a resolution of typically <400 ps FWHM at a full scale time range of 100 µs. Full 4 GHz bursts can be buffered for at least 2 µs. The first 127 deep multi event FIFO buffers incoming events at a maximum countrate of 4 GHz. A second 16k deep FIFO is filled at over 12 MHz and buffers the subsequent data transfer over the PCI bus. Data reduction is performed by recording inside a preselected time window. For experiments requiring repetitive sweeps, the spectral data obtained from each sweep can be summed in the PC enabling extremely high sweep repetition rates. The TDC P7887 only accepts signals with amplitude smaller than 1 V. This means one cannot use TTL pulses and the output of this channel is set to inverted NIM.

There are three major components to the software: the MCDWIN graphical user interface, the GRAMS/AI spectral processing suite and the Kore Spectral acquisition extensions. MCDWIN - the MS-WINDOWS based operating software - provides a powerful graphical user interface for setup, data transfer and spectral data display. Some of MCDWIN´s features are high-resolution graphics displays with zoom, linear and logarithmic (auto)scaling, ROIs… GRAMS/AI is a Windows based software package for spectroscopic and chromatographic processing, plotting and viewing. It has extensive facilities and is capable of exchanging and organizing information used with other packages, e.g., reports. The Kore spectral acquisition extensions integrate data collection using the Kore TDC into GRAMS/AI. All collection parameters are set up via standard Windows style dialogue boxes.

As mentioned before, the single ion counter only works well in single ion mode: for multiple hits the resolution goes down and the shape and position of the peaks starts to deform. It's important to adapt the voltage over the detector to keep the detection rate low enough. An example: imagine measuring two peaks with a height ratio of 10. To have enough statistics the smaller peak should have at least 100 counts. This means the higher peak will have 1000 counts. For 10 Hz and a low enough detection rate of 1 hit every 10 cycles, 1000 counts take 1000 seconds to acquire, which is more than 15 minutes. The dynamic range of the oscilloscope is better, though the AC coupling here also results in deformations of the baseline and non linearity in the peak heights. The oscilloscope used is a 500 MHz Tektronix TDS 3054. This corresponds roughly to a resolution of 2 ns when using full bandwidth.

2.5.5 Data analysis

MSA

A new Java™ application[58], called 'Data Handler', was developed using Borland® JBuilder® visual development tools[59] to facilitate spectrum analysis. It is able to find peaks, smooth the spectrum, subtract a baseline and calculate integrals from the peaks automatically. Conversion from time to mass is done by using a third order polynomial.

This program has recently been upgraded substantially under the name Mass Spectrum Analyzer (MSA).[60] This sophisticated program offers three approaches to determine the baseline. The standard method is to automatically construct a baseline: the implemented

algorithm removes all data points that stick out of the background noise and constructs a baseline through the remaining points. Optionally, a polynomial can be used to fit this automatic baseline. When peaks start to overlap with each other, the baseline for an isolated spectrum becomes arbitrary. As a solution, MSA allows to reuse a baseline from another (reference) spectrum. MSA offers two distinct strategies to search the peak locations. The more traditional algorithm finds peaks depending on features sticking out in the spectrum. However, this approach is not very successful over an extended dynamic range. This 'first search, then identify' algorithm can be reversed. Once a spectrum is well calibrated, the analyzer can check for peaks around given positions. The search intervals depend on the mass dependant errors of the calibration. This way, small intensities can still be recorded. The method is further optimized by defining the smaller peaks relative to the bigger ones, as the relative position of a peak is much more accurate compared to the absolute position.

Discrete deconvolution

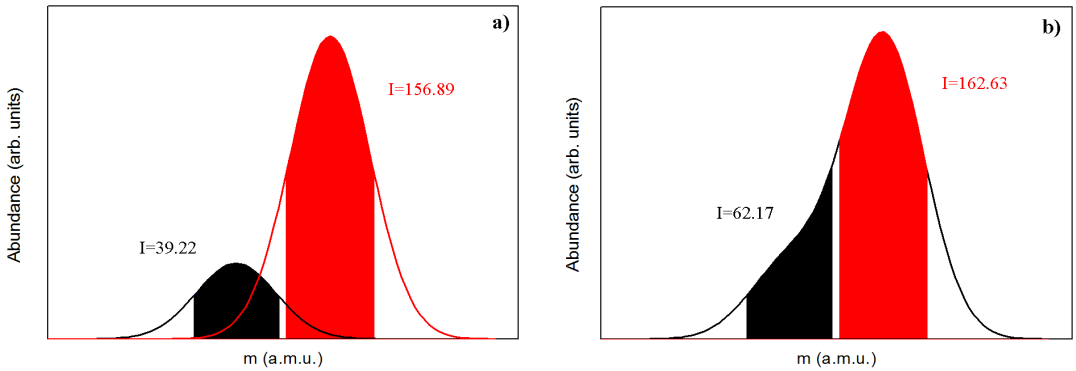

Figure 2-16: Illustration of convolution of two Gaussian peaks. (a) Two seperate peaks with considerable overlap. The individual integrals are shown, without overlap. (b) The same peaks, but now after convolution. The integrals over the same interval as in a) are now higher due to the overlap. In practice, the convoluted peaks are measured and by discrete deconvolution the original integrals are approximated.

To analyse the mass abundance of the clusters in the measured time-of-flight mass spectrum, their peaks are integrated. The integral is a better measure for the mass abundance than the peak height as it corresponds to a higher number of hits on the MCP, and as such has better statistics. Unfortunately, the measured time-of-flight spectra need to be corrected for the overlap between neighboring peaks. Most common, deconvolution is performed by fitting Gaussian functions onto a measured mass spectrum. For this work, a straightforward and discrete method has been developed. First, the spectrum is described by a sum of Gaussian functions superposed on a fixed baseline:

$$f(t) = \sum_i A_i e^{-\frac{(t-t_i)^2}{2\sigma_i^2}} \tag{2.30}$$

To obtain the intensity of each peak a selection of 8 peaks closest to this peak is considered. Instead of integrating over the 8 single peaks (which is impossible because they partially overlap), integrals I_j, are taken over 8 time intervals with width Δt. This is illustrated in Figure 2-16 in the case of two peaks only. The deconvoluted integrals I^d_j, are related to the convoluted integrals I_i, by the following relation:

$$I_j^d = C_{jj} \sum_i I_i C'_{ij} \tag{2.31}$$

With:

$$C_{ij} = FWHM_i \left[erf\left(2\sqrt{\ln 2}\,\frac{t_j - t_i + \Delta t}{FWHM_i} \right) - erf\left(2\sqrt{\ln 2}\,\frac{t_j - t_i - \Delta t}{FWHM_i} \right) \right] \tag{2.32}$$

herein *erf* is the error function:

$$erf(x) = \frac{2}{\sqrt{\pi}} \int_0^x e^{-t^2} dt \tag{2.33}$$

More details can be found in appendix A.3.

The integration interval Δt, the time interval between the individual peaks t_j-t_i and the average $FWHM_i$ are all known parameters. The error on the algorithm itself only depends on the accuracy of the computations: deconvolution of the peak integrals in Figure 2-16 by the above method results in values of 39.19 and 156.89, which are very close to the true values of 39.22 and 156.89 indicated in the figure. In practice, the error will be due to the Gaussian approximation of the peak shape and signal to noise. Accurate results indirectly depend on the exact knowledge of the position of the baseline as well.

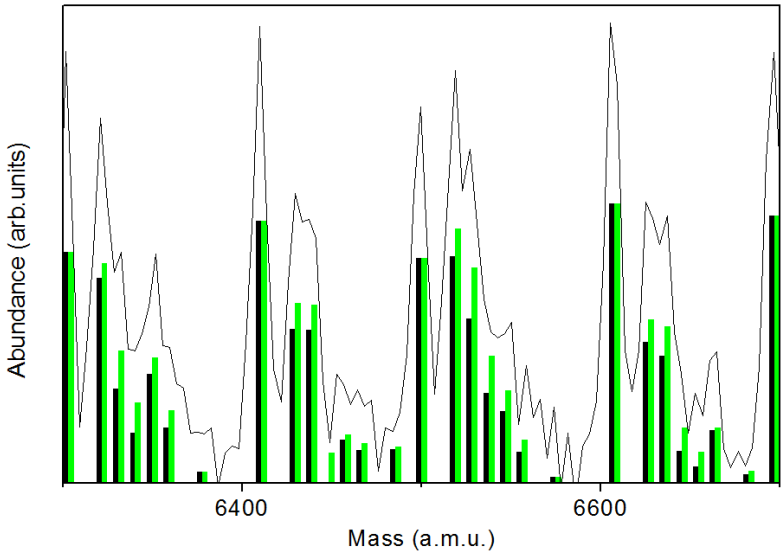

Figure 2-17: Part of a typical spectrum of silver doped gold clusters reacted with CO. The full line is the baseline corrected spectrum. The grey bars are the integrals corresponding to the different stoichiometries before, and the black bars after deconvolution. In between 6400 and 6600 a.m.u. 14 species have been accounted for: $Au_{32}Ag$, $Au_{31}Ag_3$, $Au_{32}Ag(CO)$, $Au_{30}Ag_5$, $Au_{31}Ag_3(CO)$, $Au_{32}Ag(CO)_2$, $Au_{31}Ag_3(CO)_2$, Au_{33}, $Au_{32}Ag_2$, $Au_{33}(CO)$, $Au_{31}Ag_4$, $Au_{32}Ag_2(CO)$, $Au_{33}(CO)_2$, $Au_{32}Ag_2(CO)$. [after J. De Haeck and coworkers (2011)[3]]

Figure 2-17 shows part of a typical spectrum of silver doped gold clusters reacted with CO. The full line is the baseline corrected spectrum. The grey bars are the integrals corresponding to the different stoichiometries before, and the black bars after deconvolution. In between 6400 and 6600 a.m.u. 14 species have been accounted for: $Au_{32}Ag$, $Au_{31}Ag_3$, $Au_{32}Ag(CO)$, $Au_{30}Ag_5$, $Au_{31}Ag_3(CO)$, $Au_{32}Ag(CO)_2$, $Au_{31}Ag_3(CO)_2$, Au_{33}, $Au_{32}Ag_2$, $Au_{33}(CO)$, $Au_{31}Ag_4$, $Au_{32}Ag_2(CO)$, $Au_{33}(CO)_2$, $Au_{32}Ag_2(CO)$. Although the bare Au_n and Au_nAg peaks are still quite isolated, the size of the CO doped species is hidden through overlap with neigbouring peaks. There is a significant difference between the original and deconvoluted integrals.

3 Results

This chapter closes the first part of the thesis and reports on the preliminary tests performed with the HRTTOF. The HRTTOF is combined with a binary cluster source and its performance is illustrated regarding mass range, high resolution, and mass selection. Three out of four objectives of the new instrument are realized already, with the tests on the mass range not being completed. The instrument is currently used for mass selective photofragmentation experiments, making use of the additional intermediate focal point.

3.1 Mass range

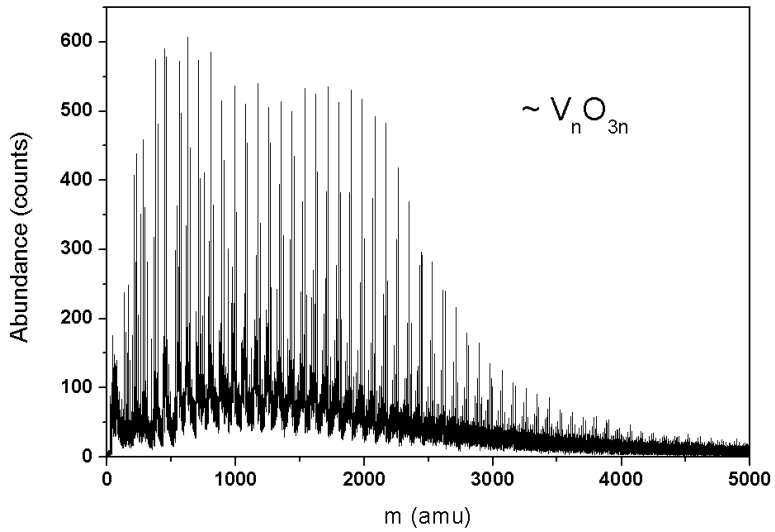

Figure 3-1: Mass abundance spectrum of positively charged vanadium oxygen clusters (V_nO_m; n=1-50, m~3n) recorded using 'curved field' extraction.

The HRTTOF uses orthogonal extraction to overcome the large velocity spread of the clusters after leaving the source. However, as explained in section 2.4.1, this limits the mass range. For this reason a novel 'curved field' extraction design was proposed and implemented. The performance of the 'curved field' extraction was tested by introducing positively charged V_nO_m clusters, which can be produced in very high abundances. For this experiment, 1% oxygen was mixed in the high purity helium backing gas. Vanadium atoms were ablated by focusing the 532 nm light of a Nd:YAG laser on a vanadium target plate. Source parameters were optimized to produce a high yield of oxygen doped vanadium clusters. The clusters travel 0.4 m before being accelerated orthogonally into the flight chamber, by an 8600 V high voltage pulse on the curved field extraction. The

clusters pass through the first and the second reflectron and reach the MCP detector after traveling over a total flight path of 5.5 m. Figure 3-1 shows a mass abundance spectrum of positively charged V_nO_m clusters. The main peaks that are visible are V_nO_m cluster with a rather fixed stoichiometry of n/m = 2.5-3.

The maximal mass range measured up to now with curved field extraction is up to m/q 4000. Most likely, this number is limited by the production of the clusters rather than to the 'curved field' extraction. Production of other types of clusters resulted in mass spectra with a smaller mass range. This number of 4000 can directly be compared with results for a single stage extraction: by removing the middle plate a linear field can be applied between the back plate and the front grid. This design was tilted to see larger clusters, which otherwise would have too big an angle to reach the detector. Though part of the mass spectrum can be investigated by scanning the angle of the extraction optic, for a given angle only a given mass range is visible. This mass window is limited to a mass range of only m/q 600. The main drawback of the 'curved field' extraction is a reduction of the efficiency. Results from simulations predict a decrease of 0 at 1 amu to 95% beyond 200 000 amu. This means that signal can be expected to be low. In practice however, the rate is often too high for the single ion count regime as discussed in section 2.5.4.

3.2 High resolution

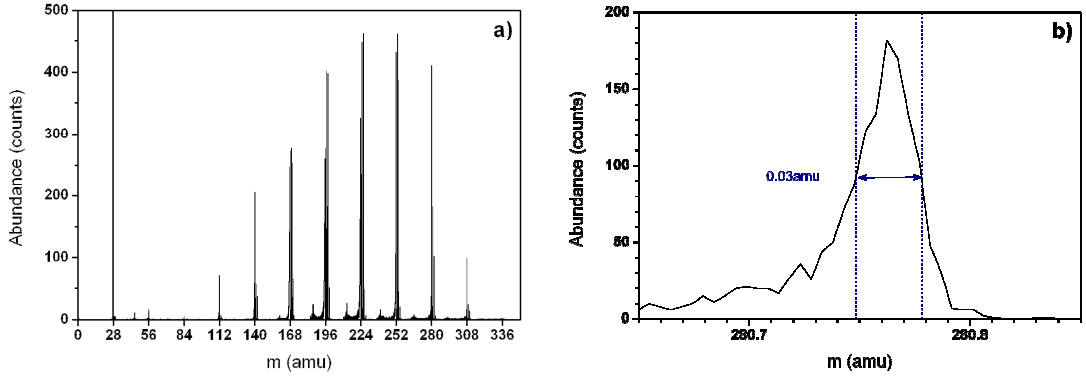

Figure 3-2: (a) Mass abundance spectrum of cationic silicon clusters measured with single stage extraction. (b) Detail of the second isotope peak of Si_{10} showing a mass resolution above 9 000.

The performance of the instrument with regards to high resolution was characterized by a short range of tests on silicon clusters. Silicon clusters are produced with good yield and reproducibility in the range from 6 to 11 atom clusters. This spectrum is collected using single stage extraction. To illustrate the mass resolution, Figure 3-2 shows an isotope peak of Si_{10} with a mass close to 281 amu. The width of the peak is 6 ns or 0.03 amu, which corresponds to a mass resolution of 9 200.

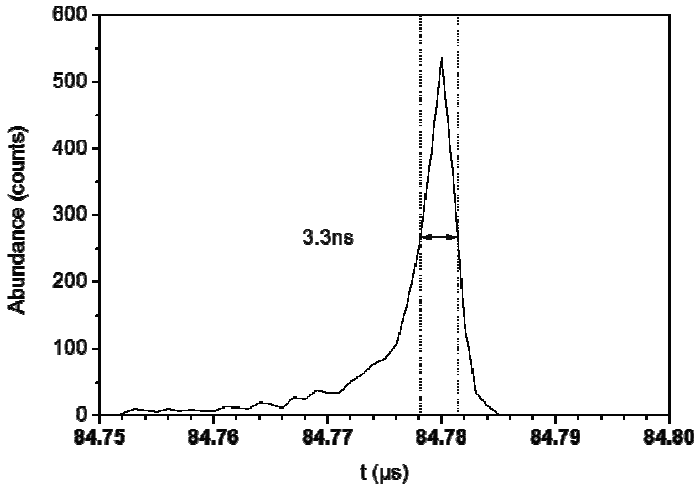

Figure 3-3: Mass abundance spectrum of cationic gold atoms measured with 'curved field' extraction, showing a mass resolution near 12 900.

A slightly higher resolution was recorded on gold atoms. Although gold clusters can be more difficult to produce compared to silicon clusters, the gold atom is always clearly present in the rising flank of the helium pulse. For this reason, gold was chosen as a first test case for the resolution. This spectrum is taken using 'curved field' extraction. Since only the gold atom is present, no meaningful mass calibration could be performed. Because the time resolution is more or less half of the mass resolution, we can estimate the mass resolution to be near 12 900. This is above the required value of 10 000. No more tests were performed to enhance the resolution, and the emphasis shifted towards mass selected photofragmentation.

3.3 Mass selection

3.3.1 Mass selection

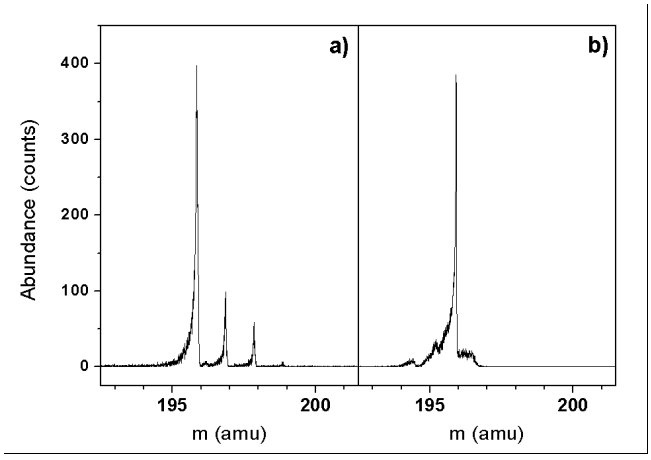

Figure 3-4: HRTTOF mass spectrum showing the isotope pattern of Si_7: (a) without mass selection, (b) with a gate time of 300 ns.

One of the requirements of the HRTTOF is the capability of performing mass selected experiments. The instrument consists of a tandem reflectron design and a mass gate in the intermediate focal point. The quality of the focal point is optimized by calculations on the required reflectron voltages. Further improvement should be reached by calibrating the instrument. As test material silicon was chosen: it has high yield and reproducibility. Another advantage of silicon is the isotope pattern. It allows testing of the mass selectivity at lower masses where the yield is much higher.

To test the mass gate, the wire type mass gate was placed in the middle of the two reflectrons of the HRTTOF. Figure 3-4 shows the mass abundance spectrum of silicon clusters in the region around Si_7, with a corresponding mass of 196 amu. The left side shows the result with the mass gate off. The right side shows the result for a gate open window of 0.3 µs centered around the first peak in the isotope pattern. The applied voltage is ±200 V. The result is similar to the result of Vlasak and coworkers, who demonstrated unit resolution for selection to m/z 167 in a tandem TOF instrument.[26] The quality of the mass selected peak will be improved by improving the focusing in the intermediate focal point and by using an aperture prior to the beam going through the mass selector.

3.3.2 Mass selected photofragmentation of cobalt clusters

The results on the mass selectivity opened up the possibility to perform mass selected photofragmentation experiments. Two windows in the center of the flight tube allow laser interaction with the cluster beam near the intermediate focal point. The first experiment performed on the HRTTOF is the mass selected photofragmentation of cobalt clusters. While in the case of metastable fragmentation laser interaction takes place before mass selection, in this configuration it takes place after the mass selection. This allows control of the amount of energy deposited into the cluster resulting in more quantitative results. One aim is to derive the binding energies of the cobalt clusters.

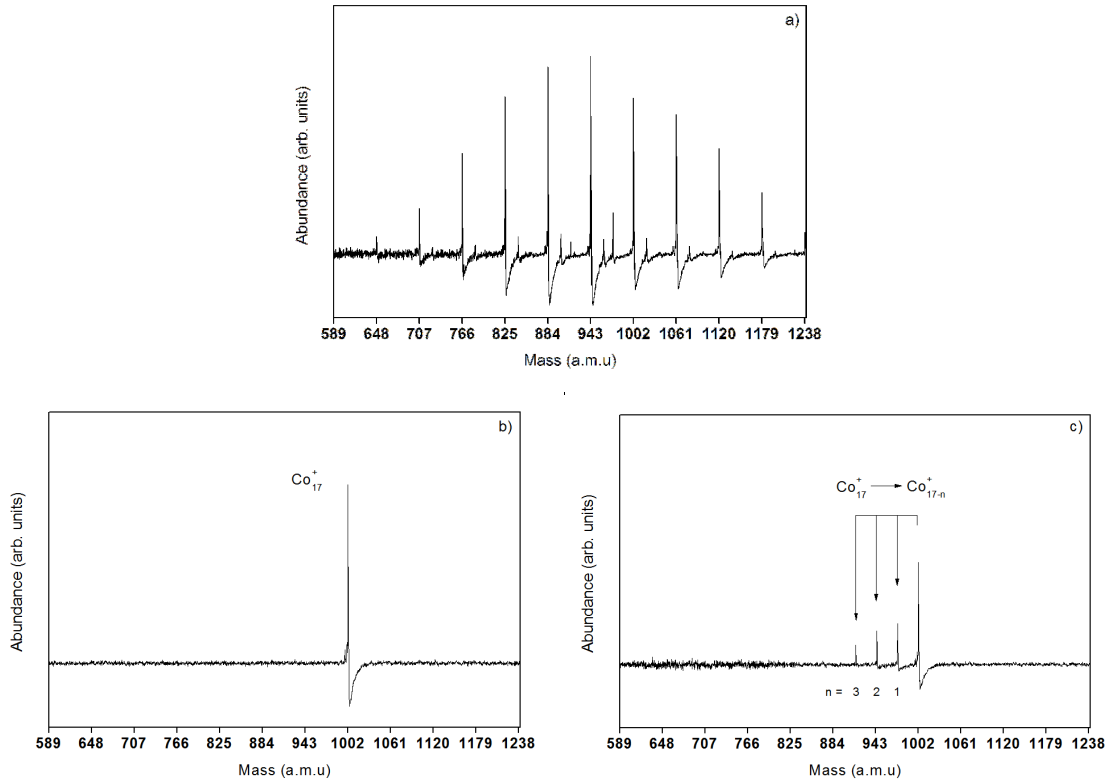

Figure 3-5: (a) Mass abundance spectrum of cationic cobalt clusters measured with single stage extraction, showing the region around 10-20 cobalt atoms, the fragmentation laser is on. (b) The same region, but with the mass gate on, selecting only Co_{17}^+ and the fragmentation laser off. (c) The same region, but with both the mass gate and the fragmentation laser on, showing Co_{17}^+ and daughter clusters that lost one up to three cobalt atoms.

Figure 3-5 (a) shows a mass abundance spectrum of cationic cobalt clusters measured with single stage extraction. This type of extraction was chosen for the enhanced yield, while the limited mass window and resolution are no real issue for this type of

experiment. The atomic mass of cobalt is around 58.9 a.m.u. and this value is chosen for the scale on the x-axis. There is a systematic peak behind the main cobalt peaks, which relates to water contaminated species. When using the mass gate, the peak corresponding to Co_{17}^+ can be selected precisely as shown in Figure 3-5 (b). When the fragmentation laser is turned on, the main peak of Co_{17}^+ decreases in intensity and additional peaks start to appear in front of this peak. The mass spectrum in Figure 3-5 (c) is taken with a 532 nm Nd:YAG laser and a laser fluence of 47.2 mJpp/cm². The additional peaks correspond to dissociation of one up to three cobalt atoms. Whether this dissociation is subsequential or the fragments also contain dimers and trimers cannot be judged from this mass spectrum. Application of equation (2.28) quantitatively confirms the identification of these three peaks as being fragments of the main peak.

3.4 Discussion and outlook

The HRTTOF was designed and implemented to offer the K.U.Leuven cluster laboratory enhanced mass resolution and mass selectivity. Three out of four objectives of the new instrument are realized already:

- An enhanced resolution (> 10 000)
- A secondary focal point for mass selected experiments
- Compatible with the K.U.Leuven binary cluster source

The requirement for a broad mass window (up to 100 000 amu) has not been proven. This is as likely related to problems with the production in the cluster source as to the new design of 'curved field' extraction: it is unclear whether the source actually produced larger clusters than measured. The above results demonstrate that a straightforward extraction design consisting of only a plate, a plate with a rectangular cut and a grid is able to extend the mass range of orthogonal extraction compared to conventional tilting of the extraction plates and using a standard set of deflection electrodes after the extraction optic. Our results also indicate that there is no loss in resolution when using this device.

A future effort will be to check whether the measured mass resolution can be increased as predicted by the simulations. This will require careful tuning of the mechanics and electronics of the system. The long detection times however constitute a major obstacle. They are due to the single ion count detection and the reduced efficiency when using curved field extraction. For this reason, the analogue detection system has been upgraded offering the possibility to work at higher detection rates. In experiments where very high mass resolution is not vital, using a linear extraction configuration might be more practical. There is also room for improvement on the mass selectivity either by calibrating the system or by improving the mechanics of the mass gate. However, there is no urgent need to perform this upgrade as the instrument is already providing interesting new experimental output, for instance on the stability of $AlPb_n$ clusters. An upcoming project will be the investigation of the magnetic properties of clusters.

Part II: Stability of (lithium doped) silicon and germanium clusters

Part II of this thesis focuses on the experimental investigation of lithium doped silicion and germanium clusters and the development of a new stability model. At the start of this thesis project the K.U.Leuven cluster laboratory had already completed a lot of pioneering work on gas phase binary clusters based on coinage metal and semiconductor elements. In this sense, this work is a continuation of the thesis work of dr. X. Wang. The focus of her work was a first comparison of lithium and a range of transition metals as dopants in silicon and germanium clusters. As part of a longstanding collaboration between our group and the K.U.Leuven Quantum Chemistry group, dr. G. Gopakumar in his thesis work had started to do structural calculations on the lithium doped germanium clusters using density functional theory (section 4.3.2).

The starting point of this work is the realization that silicon and germanium show different stability behaviour compared to most other clusters, including gold clusters. While gold clusters show dissociation by monomer or dimer evaporization, medium sized silicon and germanium clusters fragment into larger units (section 4.1.4, 4.1.5, 4.2.2). The existence of stable subunits envisages the development of new nanomaterials (section 4.4). Section 4.3 gives an overview of what is known about alkali metal doped silicon and germanium clusters. Earlier parts of chapter 4 provide a background on experimental characterization methods applied to silicon and germanium clusters (section 4.1) as well as a state-of-the-art of silicon and germanium structures for different charge states (section 4.2).

Chapter 5 describes the experimental results achieved within the framework of this thesis project. The germanium doped lithium clusters show an interesting electronic structure: the lithium atoms donate electrons into the atomic orbitals of the dopant (section 5.1.1). Small (doped) lithium clusters are hard to produce and this section is mainly relying on theoretical calcultions by dr. V.T. Ngan from the K.U.Leuven Quantum Chemistry group. Ionization efficiency measurements were performed to obtain indirect information

on structures of lithium doped silicon and germanium clusters (section 5.2). By comparing experimental photoionization efficiency curves with results from density functional theory many lowest isomers could be assigned. The theoretical calculations were done by T.M. Nguyen for silicon and T.B. Tai for germanium. While the photoioniziation efficiency measurements are complex experiments, requiring precise preparations and a team of at least two persons, photofragmentation experiments are much more straightforward. Still these experiments give access to interesting stability information (section 5.3).

Chapter 6 targets at a newly developed stability model (section 6.4). While section 6.1 and 6.2 are introductory, section 6.3 collects stability information from the previous two chapters and focuses on the density-of-state (DOS) of the most stable clusters. The structures and DOS of the different clusters were the result of a strong collaboration with the Quantum Chemistry group of Prof. M.T. Nguyen (see appendix A.4). We sincerely thank our colleagues for allowing us to use their data either in joint published articles or prior to publication.

4 Structures of silicon and germanium clusters

This chapter is the first chapter of the second part and gives a broad background of experimental and theoretical results regarding bare and metal doped silicon and germanium clusters. First there is an overview of experimental techniques and their results regarding silicon and germanium clusters. This is followed by an overview of theoretical results, highlighting the charge dependence of the structures for smaller silicon and germanium clusters and the existence of substructures for larger silicon and germanium clusters. Both features play an important role in chapter 6. This chapter closes with results on metal and coinage metal doped silicon and germanium clusters, to provide a background on the doping with lithium atoms in the next chapter.

4.1 Experimental characterization methods

4.1.1 Laser spectroscopy

There have been a number of spectroscopic investigations of small silicon and germanium clusters. Honea and coworkers performed surface plasmon-polariton enhanced Raman spectroscopy which yielded well resolved vibrational spectra for size selected Si_4, Si_6 and Si_7 clusters. [61,62] These were prepared and isolated by low-energy deposition into a solid nitrogen matrix. Structural assignments were made by comparing the measured vibrational spectra to those calculated by ab initio methods for a variety of low energy geometries. The experiment confirms that Si_4 is a planar rhombus, Si_6 is a distorted octahedron and Si_7 is a pentagonal bipyramid. These results are in agreement with absorption spectra of silicon clusters in neon, argon, and krypton matrices at 4 K which Li and coworkers measured with a vacuum Fourier-transform infrared spectrometer in the range of 50-600cm^{-1}.[63] Infrared absorption bands were assigned to Si_3, Si_4, Si_6, and Si_7 from isotopic splittings and from ab initio calculations of their vibrational frequencies and relative intensities. These assignments exclude Si_4 which is assumed to be a relatively minor species in the silicon vapor. Visible light absorption spectra from 0.94-5.58 eV are obtained for gas-phase Si_n (n = 18-41) clusters using resonant one- and two-colour photodissociation spectroscopy.[64] The spectra of all clusters were essentially identical. Many compounds containing homoatomic nine-atom clusters are characterized by single crystal X-ray diffraction. The proof that nine-atom germanium anions Ge_9^{4-} are also present in binary alloys was provided using Raman spectroscopy and X-ray diffraction methods in 1997 (Cs_4Ge_{36} and K_4Ge_{36}) and culminated in the structural characterization of the first Si_9^{4-} clusters in the binary phase $Rb_{12}Si_{17}$ one year later.[65,66,67] These compounds also contain Si_4^{4-} which has the same

tetrahedral shape as Ge_4^{4-} for germanium.[68,69] Liquid ammonia was used as a solvent to extract five- and nine-atom naked clusters of silicon in solution and allowed for the structural characterization of Si_5^{2-} and Si_9^{3-} in compounds crystallized from such solutions.[70] Crystalline materials containing Ge_5^{2-} are obtained as well.[71,72] Recently, a Ge_{10}^{2-} cluster was characterized as a fragment in $[Ge_{10}Mn(CO)_4]^{3-}$.[73] Homoatomic ligand-free Group 14 clusters with six, seven, eight, or more than ten vertices have not yet been detected in solution.

In collaboration with the group of A. Fielicke we recently measured vibrational spectra of Si_6, Si_7, and Si_{10} in the gas-phase by 'two colour' ionization.[74] This two colour ionization scheme relies on the absorption of a single or few IR photons prior to interaction with a UV photon to lift the total internal energy of the species above the ionization threshold. The direct photoionization generally prevails over the slower statistical fragmentation processes. The formed ions can be sensitively detected by means of mass spectrometry. By scanning the energy of the IR photons the ionization efficiency changes and the recorded ion intensity reflects the IR absorption spectrum of the corresponding neutral species. We applied such an IR-UV two colour ionization scheme for obtaining the vibrational spectra of neutral silicon clusters in the far-IR range between 225 and 550 cm^{-1}. These results constitute the first vibrational spectra of isolated neutral silicon clusters in the gas phase. The band observed for Si_6 is noticeably broader in comparison with those observed for the other sizes. The potential energy surface around the ground state is very flat and the structure fluctuates between the distorted octahedron, the edge-capped trigonal prism, and the face-capped trigonal prism. Si_7 is a pentagonal bipyramid and the structure of Si_{10} is identified as a fourfold capped trigonal prism in agreement with previous predictions. Other isomers of Si_{10} are at least 0.56 eV higher in energy and exhibit rather different vibrational spectra. For these three neutral silicon clusters the structures are very similar to their cationic and anionic counterparts. Lyon and coworkers present gas-phase infrared spectra for small silicon cluster cations possessing between 6 and 21 atoms.[75] Infrared multiple photon dissociation (IR-MPD) of these clusters complexed with a xenon atom is employed to obtain their vibrational spectra. These vibrational spectra give for the first time experimental data capable of distinguishing the exact internal structures of the silicon cluster cations. By comparing the experimental spectra with theoretical predictions based on density functional theory (DFT), unambiguous structural assignments for most (n = 6-11, 13-15, 18) of the Si_n^+ clusters in this size range have been made. These structural assignments provide direct experimental evidence for a cluster growth motif starting with a pentagonal bipyramid building block and changing to a trigonal prism for larger clusters.

4.1.2 Photoelectron spectroscopy

Cheshnovsky and coworkers obtained the first ultraviolet photoelectron spectra of Si_n^- and Ge_n^- (n = 3-12) clusters using a new magnetically focused time-of-flight photoelectron spectrometer.[76] An ArF excimer laser (6.4 eV) was used for photodetachment, enabling the first 3–4 eV of the valence band structure of the clusters to be probed. With few exceptions, the ultraviolet photoelectron spectroscopy (UPS) data for corresponding clusters of the two semiconductors were remarkably similar. The spectra suggest that silicon clusters with 4, 6, 7, and 10 atoms and germanium clusters with 4, 6 and 7 atoms are closed-shell species with band gaps of 1 to 1.5 eV. Müller and coworkers extended the range for silicon cluster anions up to 20 atoms.[77] Efficient cooling of species in the source allowed them to resolve multiple features in the photoelectron spectrum for all sizes studied. Spectra for an extensive set of low-energy

Si_n^- isomers found by a global search have been simulated using density functional theory and pseudopotentials. Except for n = 12 calculations for ground states agree with the measurements. This does not hold for other plausible geometries. Hence photoelectron spectroscopy (PES) data validate the tricapped trigonal prism morphologies for medium-sized silicon clusters. Hoffmann and coworkers further extended the range of photoelectron spectra for silicon anions towards sizes up to 1000 atoms.[78] The results for the smallest clusters (n = 4 to 20) are in very good agreement with UV-spectra published earlier, although some details are better resolved here, which is probably due to the low cluster temperature. Furthermore, the spectra of these small clusters are in excellent agreement with simulations. The clusters with sizes n = 20 to n = 44 exhibit rich structures as well, which have not been observed up to now.

There is a nice correspondence between these results and the ion mobility measurements by Hudgins and coworkers.[104] They have shown that between n = 27 and n = 30 the cluster structure changes from prolate to more spherical. This transition is also visible in the photoelectron spectra. From n = 20 to n = 26 (with the exception of n = 23 and n = 25) all spectra exhibit very similar profiles. Between n = 27 and n = 30 the spectra then suddenly become rather featureless, which hints at the presence of two or more isomers in the beam, which is in accordance with the observations of Hudgins and coworkers.. At n = 31 then a new profile emerges, which is fully developed at n = 33. Some remainder of this structure can be observed up to n = 40. From n = 41 again a new pattern emerges, which persists up to n = 44. In this size range the mobility measurements of Hudgins and coworkers also seem to show some structural change, although not as clear as the one around n = 29. For larger sizes all of the spectra are rather smooth and featureless. This might be due to a high density of states, but is certainly also the result of the presence of several isomers. The larger clusters with up to n = 1000 show a gradual onset at the detachment threshold. For the clusters up to n = 100 a shoulder is visible at the threshold which can be interpreted as the LUMO (lowest unoccupied molecular orbital) of the neutral cluster, which is occupied by the one additional electron. For the larger clusters this shoulder merges into the general slope of the occupied states.

Bai and coworkers combined photoelectron spectroscopy with slightly higher quality and first-principles density-functional study of Si_n^- (n = 20-45) clusters and confirm the evidence for a prolate-to-near-spherical shape transition at n~27.[79] It is shown that the tricapped-trigonal-prism (TTP) structural motif Si_9 found in most low-lying clusters Si_n^- (n = 9-19) is replaced or augmented by a series of structural motifs consisting of a bulklike “adamantane” fragment plus a magic-number cluster (Si_6, Si_7, Si_{10}) or TTP Si_9. For sizes between 28 and 45 atoms, almost all low-lying near-spherical clusters Si_n^- adopt “stuffed-cage”-like structures where the cages are homologous to carbon fullerenes in the sense that they are composed of only five- and six-membered rings. However the arrangement of the “stuffing” atoms is not yet diamondlike. Meloni and coworkers obtained photoelectron spectra of Si_n^- (n = 4-35) clusters with vacuum ultraviolet radiation at 157 nm (7.9 eV).[80] The data show spectroscopic trends consistent with the structural transformation from prolate to more spherical clusters previously observed in ion mobility experiments. In addition, they observe signal at high electron binding energy that may be analogous to the second band seen in the photoemission spectrum of bulk silicon. Photoelectron spectroscopy and ab initio calculations are also used to investigate the electronic structure of the dianion Si_5^{2-}.[81]

Burton and coworkers measured anion photoelectron spectra of Ge_n^- (n = 2-15) clusters using an incident photon energy of 4.66 eV and an improved resolution of 10 meV.[82] From these spectra the electron affinity of the corresponding neutral cluster has been

determined. In addition, the spectra of Ge_n^- (n = 2-4) clusters have been measured at photon energies of 3.49 and 2.98 eV. The assignment of the spectra of Ge_3^- and Ge_4^- is facilitated by a comparison to the similar spectra of Si_3^- and Si_4^- respectively. The spectra of the larger clusters are characterized by many broad structureless features which indicate the presence of multiple electronic transitions. Several of these were assigned based on comparison with previous *ab initio* calculations on germanium and silicon clusters. The spectra clearly indicate that Ge_4, Ge_7, and to a lesser extent, Ge_6 are closed-shell species with substantial HOMO-LUMO gaps. There is also evidence that this is the case for Ge_{11} and Ge_{14}, but not Ge_{10}.

Negishi and coworkers used photoelectron spectroscopy to study the electronic structures of germanium clusters for Ge_n^- (n = 4-32).[83] The halogen atom doping method enabled them to determine the HOMO-LUMO gap of the corresponding neutral Ge_n cluster to be 0.8-1.0 eV around n = 30. This result implies that the germanium cluster itself never emits visible emissions. The photoelectron spectra of the pure Ge_n^- cluster anions in the size range n = 2 -15 are consistent with the earlier results.

Xu and coworkers obtained vibrationally resolved anion photoelectron spectra and zero electron kinetic energy spectra for Si_n^- (n = 3-7) leading to accurate electron affinities, term energies, and vibrational frequencies for the ground and excited electronic states of the neutral clusters.[84] The assignments of excited states were aided by *ab initio* calculations and photoelectron angular distributions. The structures of anionic and neutral Ge_n ($n \leq 4$) clusters have also been elucidated using vibrationally-resolved anion photoelectron spectroscopy.[85]

4.1.3 Photoionization efficiency

Table 4-1: Ionization thresholds and vertical ionization energies for silicon and germanium clusters. In italic are the values higher than 6.42 eV (ArF laser) and in bold are the values higher than 7.89 eV (F_2 laser).

n	Ge_n Ionization treshold (eV)[a]	Si_n Ionization treshold (eV)[b]	Si_n Vertical ionization energy (eV)[c]
2	*7.58–7.76*	***>8.49***	***7.92 (0.05)***
3	***7.97–8.09***	***>8.49***	***8.12(0.05)***
4	***7.87–7.97***	***7.97–8.49***	***8.2 (0.1)***
5	***7.87–7.97***	***7.97–8.49***	***7.96 (0.07)***
6	*7.58–7.76*	***~7.90***	***7.8 (0.1)***
7	*7.58–7.76*	***~7.90***	***7.8 (0.1)***
8	*6.72–6.94*	*7.46–7.87*	
9	*7.06–7.24*	*7.46–7.87*	
10	*7.46–7.76*	***~7.90***	
11	*6.55–6.72*	*7.46–7.87*	
12	*6.94–7.06*	*7.17–7.46*	
13	*6.94–7.06*	*7.17–7.46*	
14	*7.06–7.24*	*7.17–7.46*	
15	*7.06–7.24*	*7.17–7.46*	
16	*6.72–6.94*	*6.80–6.94*	
17	-	*7.46–7.53*	
18	*6.55–6.72*	*6.80–6.94*	
19	6.4	*6.80–6.94*	
20	6.4	*7.46–7.53*	
21	6.21–6.43	*6.80–6.94*	
22	5.98–6.02	5.85-5.95	

23	5.98–6.02	5.95–6.05	
24	5.90–5.98	5.95–6.05	
25	5.90–5.98	5.90–5.95	
26	5.71–5.90	5.90–5.95	
27-28	5.71–5.85	5.80–5.90	
29	5.66–5.71	5.8	
30-31	5.63–5.71	5.70–5.80	
32-35	5.63–5.71	5.64–5.70	
36	5.63–5.71	5.60–5.64	
37-38	5.63–5.66	5.60–5.64	
39-40	5.63–5.66	5.55–5.60	
41-42	5.63–5.66	5.40–5.50	
43-45	5.60–5.63	5.40–5.50	
46-49	5.60–5.63	-	
50	5.56–5.63	-	
51-54	5.54–5.60	-	
55-57	5.54–5.56	-	
100-200	-	5.0-5.17	

[a] Yoshida and coworkers (1999)[101]; [b] Fuke and coworkers (1993)[87]; [c] Kostko and coworkers (2010)[93]

Silicon

Although other techniques like infrared spectroscopy and photoelectron spectroscopy are more powerful in the identification of cluster structures, the photoionization efficiency (PIE) curve of a cluster is a crude but straightforward fingerprint of its structure, which can guide theoretical calculations. Trevor and coworkers showed that silicon clusters up to size 7 and Si_{10} all have IEs greater than 7.87 eV, which means these clusters cannot be detected well by ionization of a F_2 excimer laser.[86] Similarly, silicon clusters up to size 21 cannot be detected by ArF excimer lasers. Tunable lasers are limited in the lower wavelength and photoionization efficiency curves for smaller silicon clusters cannot be recorded with standard equipment hampering the measurement of the smaller silicon clusters. Photoionization tresholds for Si_n ($n < 200$) were first examined and bracketed by Fuke and coworkers using laser photoionization and reflectron time-of-flight mass spectrometry.[87] Stimulated Raman scattering light of narrow bandwidth 193 nm radiation was used as the ionization light source down to 146 nm. An overview of the experimental results is given in Table 4-1. A characteristic size dependence was found for clusters smaller than 22 atoms, featuring major maxima at $n = 10$ and 20. There is also a large gap between $n = 20$ and 22. This gap was ascribed to the structural transition of neutral clusters in analogy with that found recently for small silicon cluster ions. The ionization tresholds for larger clusters with $n = 100$-200 silicon atoms were found to be 5.0-5.17 eV, which are still higher than the work function of bulk Si(111) surface.

The ionization energy (IE) of the dimer has been measured using two-photon ionization by Winstead and coworkers (7.9-8.08 eV) and Marijnissen and ter Meulen (7.9206 eV), while Boo and Armentrout estimated the dimer IE thermodynamically to be 8.04 eV.[88,89,90] In light of these experimental results, Dixon and coworkers commented on the role of excited electronic states in the photoionization of the silicon dimer.[91] The ionization potentials of Si_2 ($X\ ^3\Sigma_g^-$) to form the $X\ ^4\Sigma_g^-$ and $a^2\Pi_u$ states of Si_2^+ have been calculated at very high levels of ab initio molecular orbital theory. The calculated value of the adiabatic ionization energy (AIE) to form the $X\ ^4\Sigma_g^-$ ground state of the cation is 7.91 eV as compared to an experimental value of 7.92 eV. The predicted AIE to form Si_2

($a^2\Pi_u$) is 8.44 eV, which is close to the value found by Fuke and coworkers. Because the calculated bond distance for the ground state of Si_2, 2.255 Å, is very similar to the value predicted for the ground state of Si_2^+ ($X\ ^4\Sigma_g^-$), 2.267 Å, the vertical and adiabatic ionization potentials will be very similar.

Jaeger and coworkers estimated the ionization energy of Si_7 to be between 6.77 and 7.58 eV from photodissociation studies of metal-silicon clusters.[92] Kostko and coworkers recently reported on single photon vacuum ultraviolet photoionization of small silicon clusters (Si_n, n = 1-7) produced via laser ablation of silicon.[93] The AIEs are extracted from experimental PIE curves with the help of Franck-Condon simulations, used to interpret the shape and onset of the PIE curves.

In contrast to these relatively few experimental determinations, there have been a number of theoretical calculations of the IEs of silicon clusters at various levels of theory, and while relative trends in decreasing IE with increasing cluster size tend to agree, the absolute IEs have varied considerably.[94,95,96,97,98,114,99,100]

Germanium

Photoionization thresholds for Ge_n ($n < 57$) were examined by Fuke and Yoshida with a wide photon energy (5.0 – 8.6 eV) using laser photoionization and reflectron time-of-flight mass spectrometry.[101,102] High-output vacuum ultraviolet light generated with stimulated Raman scattering is used as the ionization light source in the energy range above 6.0 eV. The results are shown in Table 4-1. A characteristic size dependence of ionization tresholds with a maximum at n = 10 is found for clusters smaller than 22 atoms. The rather high ionization threshold of Ge_{10} in comparison with its neighbors is consistent with the results on the photodissociation study of Ge_n^+ where the fragments with lower IE carry away the charge. They also find that ionization tresholds decrease rapidly from n = 16 to 22, and then decrease at a much slower rate for larger clusters. These features in ionization tresholds are similar to those of Si_n, except for the smaller gap of Ge_n at n ~ 20. On the other hand, the ionization tresholds of medium size Sn_n (n = 15–41) clusters are found to decrease slowly without such a gap. The remarkable difference in the size dependence of the ionization tresholds for the Si_n and Ge_n clusters compared to the Sn_n clusters can be related to the existence of a structural transition in the medium-size Si_n and Ge_n clusters. In the bulk solid, both silicon and germanium have the diamond lattice structure, while tin has properties intermediate to those of germanium and lead. The ionization thresholds for germanium clusters are generally lower compared to silicon clusters, as a result germanium clusters up to size 5 with an exception for Ge_2 all have ionization thresholds greater than 7.89 eV, which means these clusters cannot be detected by ionization with a F_2 excimer laser. Similarly, germanium clusters up to size 18 cannot be detected by ArF excimer lasers. Mass spectra recorded at 193 nm with a laser fluence as low as 20 μJ/cm² still exhibit fragment ions such as Ge_{6-7}^+, Ge_{11}^+ and Ge_{14-16}^+. When the clusters are photoionized without cooling of the cluster source, this trend becomes quite prominent. In order to determine the reliable threshold ionization energy, the photofragmentation characteristic of germanium and tin clusters were examined with various laser fluences: a linear dependence on laser fluence is established to be a one-photon ionization event. It is worth noticing that the peak intensity of Ge_{10}^+ is rather high, compared with its neighbors. This trend is found to become very evident in the mass spectrum produced at higher photon energy. Since these spectra are recorded at low laser fluence to suppress multiphoton processes (about 4 μJ/cm²) and with energy higher than the ionization thresholds of Ge_n ($n > 6$), the abundance of neutral clusters may be reflected in the intensities of each cluster ion. The spectrum thus indicates that

Ge_{10} is more stable than its neighbors. Similar magic behavior has been found for Si_{10}. This is in agreement with dissociation experiments where Ge_{10} is expected to dissociate as a neutral, due to its enhanced IE.

4.1.4 Ion mobility measurements

The mobility of an ion is a measure of how rapidly it moves through a buffer gas under the influence of an electric field. The mobility of a cation or anion depends on its orientationally-averaged collision integral with the buffer gas, which in turn depends on the ion's geometry. Ions with open geometries undergo more collisions with the buffer gas and hence travel more slowly than compact ions. Thus ion mobilities provide a way to characterize an ion by its physical size. In a typical ion mobility measurement the ions pass from the source region into the drift tube through an ion gate. A helium buffer gas counter flow prevents neutral clusters from entering the drift tube. A uniform electric field carries the ions through the ion gate against the buffer gas flow. After traveling through the drift tube, ions exit through an aperture and are then focused into a quadrupole mass spectrometer. While a mobility measurement alone usually cannot uniquely identify a particular geometry (many different geometries can have the same mobility) the criteria that the calculated geometry be low in energy and have a mobility that fits the measured mobility is often sufficient to uniquely identify the ground state.[103]

High-resolution ion mobility measurements have been performed by Hudgins and coworkers for silicon cluster anions and cations in a size range from 6 to 55 atoms.[104,105,106] The smaller clusters are considered to follow a prolate growth sequence, while large clusters have a more spherical geometry.[107] The transition from prolate to more-spherical geometries is observed to start at Si_{24} for the cations. For clusters with 25 to 27 silicon atoms two isomers clearly coexist with equal abundance. From Si_{34} on, only the more spherical isomer survives. The results for the anions and the cations have the same global features. However, changing the charge often causes a shift in the isomer distribution, or causes new isomers to emerge. For example, the transition from prolate geometries to more-spherical ones is shifted to larger cluster sizes for the anions than for the cations: the equal coexistence of the different types of isomers occurs for anions with 28 to 29 silicon atoms, and the prolate isomer survives up to much larger sizes. Apparently, the two extra electrons in the anions stabilize the prolate isomers relative to the more-spherical ones. The mobilities of the anions are systematically smaller than those of the cations, presumably because of differences in the exterior electron densities.

Jackson and coworkers compared calculations for low-energy Si_n^+ (n = 20-26) isomers with the measurements of Hudgins and coworkers.[140,104] The preferred shape shifts as the clusters grow: compact Si_n^+ structures lie above the prolate for n = 23, closely compete with them for n = 24 and 25, and overtake them for n = 26. The transition in neutrals occurs a bit later: compact isomers become degenerate with prolate for Si_{26} and lower for Si_{27}. The results match the experiment perfectly, also taking into account the less abundant isomers. However, this comparison merely distinguishes between compact or elongated families and gives no clue on the actual shape or subunits present.

Bulk germanium and silicon pack in the same diamond lattice and the geometries of smallest ($n \leq 10$) Ge_n and Si_n clusters appear to be identical by both calculation and experiment. So it was often assumed that the geometries of silicon and germanium clusters would be identical except for the 4% difference in the bond lengths. However, Hunter and coworkers also examined the mobilities of Ge_n^+ (n = 7–54) and Ge_n^{2+} (n = 44–86) clusters and revealed that the structural transition to more spherical geometries

begins at n ~ 65, almost three times the size where this occurs for Si_n^+ species.[108] They have observed an elongated growth for the Ge_n^+ cluster ions with n = 10–35 and a gradual deviation from this growth sequence for the clusters with more than 35 atoms. From comparison with the results on the dissociation energies, they have proposed the structures of the Ge_n clusters with up to ~70 atoms as weakly bound assemblies of small stable fragments such as Ge_7 and Ge_{10}. The structural transition at around 70 atoms has been ascribed to a reconstruction to a more compact bulklike structure. The size dependent features in mobilities of Ge_n^+ and Si_n^+ start differing at n ~ 15. So in the intermediate size regime the geometries of silicon and germanium clusters are significantly different and perhaps the first question to answer is where and how the growth patterns of silicon and germanium clusters diverge.

4.1.5 Mass selected dissociation experiments

Injected ion drift tube techniques have been used by Hunter and coworkers to probe the geometries of germanium cluster cations.[108] At high injection energies the cluster ions can be heated to the point where they fragment as they enter the drift tube. Estimates of the dissociation energies can be obtained from detailed analysis of the injection energy thresholds for dissociation using a modified impulsive collision model to estimate the degree of collisional excitation that occurs as the clusters enter the drift tube and a statistical model to describe the subsequent fragmentation of the heated clusters. The cohesive energy of bulk germanium is 3.85 eV/atom, and the dissociation energies of clusters with up to 10 atoms are comparable with this value. However, for clusters with more than 11 atoms the dissociation energies drop precipitously and remain at ~1.2 eV. This behavior is totally different from the behavior of large silicon clusters where the dissociation energies smoothly approach the bulk cohesive energy. It is reasonable to consider the larger germanium clusters as loosely bound assemblies of small strongly bound fragments like Ge_7 and Ge_{10}. It appears that the structural transition at ~70 atoms may reflect a change to a more bulk like bonding arrangement.

It is known for long time that medium-sized Si_n and Ge_n clusters dissociate into small fragments rather than monomers and dimers upon photodissociation.[82,109] Mass selected laser photodissociation of silicon and germanium cations prepared by laser vaporization and supersonic beam expansion has been investigated using tandem time-of-flight mass spectrometry by Zhang and coworkers.[110,111] Silicon clusters up to size 80 and germanium clusters up to size 40 were studied. The positive cluster ions were probed with the second (532 nm), third (355 nm), and fourth (266 nm) harmonics of a Q-switched Nd:YAG laser and with the KrF (249 nm) and ArF (193 nm) excimer laser lines. As a general observation, the nature of the fragmentation patterns does not depend qualitatively upon the fragmentation laser used, although there are significant dependencies upon fragmentation laser fluence. For both silicon and germanium, the apparent positive ion fissioning process can better be explained by the loss of neutral fragments. The smaller Si_n^+ clusters preferentially lose Si_{10} and to a lesser extend Si_7. For the larger Si_n^+ clusters (n > 30) a subsidiary channel of monomer evaporation appears. The Ge_n^+ clusters lose Ge_7 fragments at smaller sizes and Ge_{10} at larger sizes, at least up to n = 40.

Qin and coworkers investigated the stabilities and fragmentation energies of Si_n clusters (n = 2–33).[112] The relative stability of the clusters can be estimated through the second order difference in energy, Δ^2E. Local maximum peaks for Δ^2E are found at n = 4, 7, 10, 12, and 14, indicating that the clusters with these values of n are more stable than their neighboring clusters. The medium sized silicon clusters decompose preferably into Si_7

and Si_{10}: their fragmentation energies are smaller compared to other channels, showing that Si_7 and Si_{10} would appear frequently in fragmentation products. It is found that when n = 11 the fragmentation energy curve has a sudden drop, and when n reaches 21 the fragmentation energy rises again. This phenomenon implies that Si_n clusters with n = 11–20 are readily dissociated, and this is in good agreement with the experimental results.

Zhao and coworkers calculated the second order difference in energy, Δ^2E for Ge_n clusters (n = 3–32).[112] The calculated values of Δ^2E show maxima at n = 4, 7, 10, 12, and 14. Ge_7 and Ge_{10} correspond to prominent peaks. Ge_{20}, Ge_{23}, Ge_{26} and Ge_{29} also exhibit special stability because each of these clusters contains two stable Ge_{10} subunits. These results also suggest that Ge_{10} is a very favourable building block for the growth of large germanium clusters. The cohesive energy of bulk germanium is 3.85 eV per atom, and the fragmentation energies of clusters with up to 10 atoms are comparable to the bulk cohesive energy. These small-sized clusters with large fragmentation energies are not easy to dissociate. For clusters with more than 11 atoms, the fragmentation energies drop sharply. In the fragmentation products, Ge_6, Ge_7 and Ge_{10} are obviously more abundant, this is in agreement with the experimental results.

4.2 Sizes and structures

There are numerous theoretical studies investigating the structure of silicon and germanium clusters by different groups and only the most relevant results will be discussed below. Details of the calculations can be found in the references. Zdetsis did an extensive search on structures for small Si_n and Si_n^{2-} (n = 5-13) clusters and $Si_n^{+/-}$ (n=6,10) clusters.[113,114] Xu and coworkers did an extensive search on structures for small Ge_n and Ge_n^- (n=1-6).[115] King and coworkers did a limited search on structures for small Ge_n^x (n = 5-13; x = -6,-4,-2,0,+2,+4,+6) clusters.[116,117,118,119,120,121,122,123,124,125] Liang and Li did an extensive search on medium-sized clusters Ge_n (n = 21-25) clusters and suggested that low-lying prolate clusters could be built upon stacked tri-caped trigonal prism (TTP) motifs.[126] Zeng and coworkers did a limited search on structures for medium sized Ge_n (n = 12-29) and Si_n (n = 10-26, 39, 40, 50, 60, 70, 80) clusters.[127,128,129,130] They suggested that most low-lying medium sized clusters consist of the six/nine and six/ten motifs. J.J. Zhao and coworkers did a limited search on structures for medium Ge_n (n = 2-25; 30-39) and Si_n (n = 30-50) clusters.[131,132,133,134] Oña and coworkers did a limited search on structures for Si_n (n = 18-60) clusters.[135] The most recent work is from Ho and coworkers who did a limited search on structures for medium Ge_n (n = 2-44) and Si_n (n = 2-33) clusters.[136,137,138,139,112] Jackson and coworkers did a limited search on structures for charged $Si_n^{(+)}$ (n = 20-27) clusters.[140] Zhou and coworkers did a limited search on structures for charged $Si_n^{+/-}$ (n = 31-50) clusters.[141] Below is a short overview of the most stable structures. An overview of the geometries of deltahedral structures and bare silicon and germanium clusters can be found in Appendix A.4.

4.2.1 Charge dependence of small silicon and germanium clusters

The 5 vertex trigonal bipyramid

The global minimum of the Ge_5^{2-} and the Si_5^{2-} dianion is a trigonal bipyramid of D_{3h} symmetry, analogous to the structure of Sn_5^{2-}, Pb_5^{2-} and $B_6H_6^{2-}$ and can be considered a *closo*-cluster.[81,113,116] The equatorial (eq) and axial (ax) bond lengths of this dianion are 2.535 and 2.350 Å for Si_5^{2-} found experimentally in $(Rb\text{-}crypt)_2Si_5{\bullet}4NH_3$. The computed equatorial (eq) and axial (ax) bond lengths are 2.818 and 2.577 Å for Ge_5^{2-}, this is 0.1 Å

longer than those found by X-ray diffraction of (2,2,2-crypt-K)$_2$Ge$_5$•THF.[71] However, the computed eq/ax length ratio of 1.09 is within 0.01 of the 1.08 ratio also found for Si_5^{2-}, Ge_5^{2-}, Sn_5^{2-} and Pb_5^{2-}.[142] The global minimum of the Ge_5^- and Si_5^- anion also yields a trigonal bipyramid of D_{3h} symmetry.[81,115] The equatorial (eq) and axial (ax) bond lengths of the anion are 2.947 and 2.486 Å for Ge_5^- and 2.751 and 2.346 Å for Si_5^-.

The global minimum of the neutral Si_5 and Ge_5 cluster is found to be an oblate trigonal bipyramid of D_{3h} symmetry, which is compressed along the threefold axis.[81,113,143,116] The equatorial (eq) and axial (ax) bond lengths of the neutral are 3.073-3.118 Å and 2.316-2.328 Å for Si_5 and 3.351 and 2.491 Å for Ge_5. Going from the neutral to the dianion the oblate trigonal structure gets stretched among its axis, as can be seen in the change in the eq/ax length ratio (Si: 1.33 → 1.17 → 1.08; Ge: 1.35 → 1.19 → 1.09). The reason can immediately be seen from the DOS. The MOs for the neutral trigonal bipyramidal (D_{3h}) structure can be assigned to $1S^21P^61D^{10}2S^2$. The next orbital (LUMO for the neutral and HOMO for the dianion) has the appearance of an F_{z^3} orbital, which has a node along the C_3 axis between the two axial vertices. When the additional electrons occupy this orbital, the structure becomes more strongly σ-antibonding and the axial vertices will move further apart.

The 6 vertex octahedron

The global minimum of the Si_6^{2-} and Ge_6^{2-} dianion is the O_h octahedron, fully analogous to the $B_6H_6^{2-}$ borane structure, in agreement with Lipscomb's and Wade's rules.[114] The high stability of the octahedral Si_6^{2-} structure is also reflected in the fully closed highly degenerate valence energy levels. The computed edge lengths in octahedral Ge_6^{2-} are 2.687 Å as compared with 2.541 Å found experimentally by X-ray diffraction for the complex $[Ge_6\{Cr(CO)_5\}_6]^{2-}$.[144,116] The global minimum of the Si_6^- and Ge_6^- anion is a D_{4h} structure.[114,115] The total energy of the Si_6^- anion is almost 2 eV lower compared to the neutral cluster, consistent with the high electron affinity of silicon. Remarkably, this structure is also lower in energy than the dianion. The equatorial (eq) and axial (ax) bond lengths are 2.385 and 2.760 Å for Si_6^- and 2.793 and 2.613 Å for Ge_6^-.

The three competing structures of neutral Si_6 are of D_{4h}, C_s and C_{2v} symmetry.[63,74,114] Each of these structures has been considered at different times as the real equilibrium geometry of Si_6, as various methods give fluctuating energy differences of the order of 0.005 eV. The experimental IR spectrum of Si_6 is dominated by a single high intensity band around 460 cm^{-1}.[63] The calculated IR spectra for all structures are consistent with this result, as the spectra for the three structures are practically indistinguishable. In reality all three low energy structures can be considered as different instances of the same fluxional structure. The band in the IR spectrum is noticeably broader in comparison with those observed for other sizes, which might confirm the fluctual behaviour.[74] Removal of two skeletal electrons from Ge_6^{2-} leads to the neutral species Ge_6, which has a C_{2v} structure, which can be interpreted as a trigonal bipyramid with the sixth vertex capping one of the equatorial edges.[116,115] This structure also originates from a distortion of the D_{4h} structure higher in energy by only 0.02 eV. The D_{4h} equatorial (eq) and axial (ax) bond lengths are 2.946 and 2.560 Å for Ge_6. Going from the neutral to the dianion the oblate germanium octahedron gets quenched among its axis, as can be seen in the change in the eq/ax length ratio (Ge: 1 → 1.07 → 1.15).

The structure of Si_6^+ is an edge-capped trigonal bipyramid (which can also be seen as a distorted octahedron) with C_{2v} symmetry.[75,114] The observed IR spectrum is rather straightforward with two features at 411 and 441 cm^{-1}.[75] The computed C_{2v} IR spectrum

fits these experimental peaks well. The energy difference between neutral and cation is 7.6 eV, depicting the cation as relatively unstable.

The 7 vertex pentagonal bipyramid

The ground state of the Ge_7^{2-} and the Si_7^{2-} dianion is a D_{5h} pentagonal bipyramid and can be considered a *closo*-cluster.[113,116] The equatorial (eq) and axial (ax) bond lengths of this dianion are 2.402 and 2.634 Å for Si_7^{2-} and 2.578 and 2.829 Å for Ge_7^{2-}.

The ground state of the neutral Ge_7 and the Si_7 cluster is a D_{5h} pentagonal bipyramid and can be considered a *closo*-cluster.[61,63,74,113,116] The equatorial (eq) and axial (ax) bond lengths of the neutral are 2.509 and 2.491 Å for Si_7 and 2.689 Å for Ge_7. The structure of Si_7 has been confirmed by IR spectroscopy.[74] This structure is almost a perfect deltahedron with an eq/ax ratio of 1.00 for germanium and 1.01 for silicon. From photoelectron spectroscopy a HOMO-LUMO gap can be assigned of ~1.6 eV, which is the highest value among neutral germanium clusters. The ground state of the Si_7^+ cation is a pentagonal bypyramid structure. This structure matches the observed IR spectrum for Si_7^+, which contains only two features at 385 and 408 cm^{-1}.[75]

Going from the neutral to the dianion, the oblate pentagonal structure gets stretched among its axis, as can be seen in the change in the eq/ax length ratio (Si: 1.01 → 0.91; Ge: 1.00 → 0.91). The reason is similar for the case of the trigonal bipyramid and can immediately be explained by the density of states. The MOs for the neutral trigonal bipyramidal (D_{3h}) structure can be assigned to $1S^2 1P^6 1D^{10} 2S^2 1F^8$. The next orbital (LUMO for the neutral and HOMO for the dianion), is the F_{z^3} orbital of similar symmetry as the F_{z^3} HOMO in the trigonal bipyramid. When the axial vertices of Ge_7^{2-} are compressed to within bonding distance in going from the ordinary pentagonal bipyramid of Ge_7^{2-} to the oblate pentagonal bipyramid of Ge_7, this F_{z^3} orbital becomes more strongly σ-antibonding thereby accounting for the two less skeletal electrons in an oblate pentagonal bipyramidal structure. The bonding MO patterns in the five and seven-vertex bipyramidal clusters are thus completely analogous except for four more F bonding orbitals in the seven-vertex clusters corresponding to the two "extra" vertices and the eight additional total electrons.

The 8 vertex tetracapped tetrahedron

The global minimum of the Si_8^{2-} dianion is a D_{2d} bisdisphenoid, analogue to the structure of $B_8H_8^{2-}$, and can be considered a *closo*-cluster.[113] The bisdisphenoid can best be conceived as the deltahedral equivalent of a square antiprism. The square antiprism is an *arachno*-structure, which requires a total charge of 4+2 electrons following Wades's rules. The D_{4d} square antiprism is indeed found for Ge_8^{6-} as the global minimum. The ground state of the Ge_8^{2-} dianion is a tetracapped tetrahedron, which lays 0.17 eV below the bisdisphenoid.[119] This deltahedron is no longer convex and much less "spherical" than the bisdisphenoid since four of the vertices have degree 3 and the other four vertices have degree 6. However, the molecular orbital (MO) pattern still exhibits a spherical harmonic pattern ($1S^2/1P^6/1D^6/2S^2/1D^4/1F^2 1F^6 1F^6$) with the last triply degenerate set as the HOMO. The LUMO is a triply degenerate set of the first G orbitals with a hexagonal prismatic lobal pattern. The germanium dianion has the lowest energy among the different charge states.

The structure of the lowest energy neutral Si_8 cluster was found to be of C_{2v} symmetry.[113] The D_{2d} structure of the dianion is dynamically unstable for Si_8. The same is true for the Si_8^- anion. Distortion along the displacement patterns of both neutral and anionic cluster leads to two new structures of C_{2v} and C_2 symmetries. The C_{2v} is the lowest energy

structure, whereas the C_2 structure is higher in energy by only 0.15 eV. The four lowest lying computed structures for Ge_8 (within 0.23 eV), are all of low symmetry (C_s or C_2).[119] The ground state is a face capped pentagonal bipyramid. An edge-capped pentagonal bipyramid structure is computed to be the lowest lying isomer for the silicon cation (computed to be over 0.65 eV lower than any other isomer), and the predicted IR spectrum matches the experiment well, especially as this computed isomer has an intense absorption at 264 cm^{-1}.[75] The global minimum for the dication Ge_8^{2+} is a low symmetry C_s capped pentagonal bipyramid. The next structure at +4.7 kcal mol^{-1} above the global minimum can be described as a trigonal bipyramid with bridges along each of the three equatorial-equatorial bridges and thus has D_{3h} symmetry. Structures with 8 vertices show a transformation from pentagonal at lower charge to square motifs at higher charge.

The 9 vertex tricapped trigonal prism

There is a large amount of experimental information on Ge_9^{4-} structures with various counterions.[145] Both the C_{4v} capped square antiprism and the D_{3h} tricapped trigonal prism are found. The capped square antiprism with a single nontriangular face is predicted by Wade's rules for a *nido* compound. Computations for the Ge_9^{4-} cluster indicate that the capped square antiprismatic and tricapped trigonal prismatic structures have very similar energies. The minimum energy structure for Ge_9^{4-} is actually a tricapped trigonal prism similar to the experimentally found structure for the isoelectronic Bi_9^{5+}.[117] But the capped square antiprism is only 0.01 eV higher in energy with only a single very small imaginary frequency. This is in accord with the fluxionality of the closely related Sn_9^{4-} and Pb_9^{4-} ions observed experimentally by metal NMR.[146,147] The structure of Si_9^{3-} can be viewed as a tricapped trigonal prism with variously elongated prismatic edges. The structure found experimentally in $(K\text{-crypt})_3Si_9{\bullet}8NH_3$ with one elongated edge also resembles a capped square antiprism. These clusters carry an odd number of cluster-bonding electrons, 21, and are paramagnetic according to EPR measurements. The electron-rich "free radical" Ge_9^{3-} cluster is also known experimentally as a tricapped trigonal prism.[148] The same optimized tricapped trigonal prismatic structure with a rigorous C_1 rather than the idealized D_{3h} symmetry is computed for the gas phase cluster.[117] The global minimum for Ge_9^{2-} is the D_{3h} tricapped trigonal prism, analogue to $B_9H_9^{2-}$ and which is a *closo*-structure.[117] The global minimum for Si_9^{2-} is a C_s structure obtained through a Jahn-Teller distortion from the D_{3h} tricapped trigonal prism.[113]

The global minimum for the hypoelectronic Ge_9 is a bicapped pentagonal bipyramid.[117] However, a second structure for Ge_9 only 0.20 eV above this global minimum is the C_{2v} flattened tricapped trigonal prism structure found experimentally for the isoelectronic Tl_9^{9-}. The global minimum for Si_9 is the same C_s structure as for the dianion. The global minimum of the Si_9^+ cluster is thought to have a bicapped pentagonal bipyramid structure. It yields an infrared spectrum very similar to the experimental result.[75]

The tricapped trigonal prism and capped square antiprism are closely related by a single diamond-square process involving rupture of an edge connecting two degree 5 vertices of the tricapped trigonal prism. It would not be very surprising that they are readily interconverted in fluxional processes. The germanium dianion has the most stable structure compared to the other charge states: $Ge_9^{2-} < Ge_9 < Ge_9^{3-} < Ge_9^{4-}$. The shape of tricapped trigonal prisms can be described by the ratio of the vertical "height" of the prism (v) to the horizontal basal edge length (h). A v/h ratio close to 1 is found for Ge_9^{2-} which is also energetically the most stable structure. The v/h ratio of Ge_9^{3-} is slightly higher (1.06), followed by Ge_9^{4-} with a ratio of 1.15. In this case the capped square antiprism becomes competitive to the tricapped trigonal prism. The 10 lowest lying

bonding MOs in both the tricapped trigonal prismatic and capped square antiprismatic clusters correspond to $1S^2 1P^6 1D^{10} 2S^2$. These 10 bonding MOs may be considered to correspond approximately to the multicenter core bond and the external lone pairs.[117] The remaining bonding MOs for both Ge_9^{2-} and Ge_9^{4-} correspond to seven 1F orbitals and two or three 2P orbitals. These orbitals arise mainly from surface bonding.[117]

The 10 vertex bicapped square antiprism

The global minimum for Si_{10}^{2-} and Ge_{10}^{2-} is a D_{4d} bicapped square antiprism, completely analogous to the corresponding isoelectronic borane $B_{10}H_{10}^{2-}$.[114] Dissociation experiments[110] and ab initio calculations[149] suggest that Si_{10}^-, Ge_{10}^-, and Sn_{10}^- are expected to have similar stable structures and are expected to exhibit similar photoelectron spectral feature such as a large energy separation between the first and second peaks as is observed for Si_7^-. For Si_{10}^-, the large HOMO–LUMO gap is observed in the photoelectron spectrum as is expected, however, Ge_{10}^-, and Sn_{10}^- exhibit no peak structure near the threshold.[76,83,84] The most stable Si_{10}^- cluster has been found to have the geometry of a tetracapped trigonal prism, while the bicapped antiprism structure, which reproduces the observed photoelectron spectrum, has been found to be the lowest energy isomer for Ge_{10}^-. In analogy to the O_h structure of Si_6, the "generating" structure of Si_{10}^- is the D_{4d} bicapped square antiprism.[114] However, this D_{4d} structure is dynamically unstable like the D_{4h} structure of neutral Si_6, leading after proper distortion to two nearly isoenergetic states of C_{2v} and D_2 symmetries, separated by a very small and narrow energy barrier. As a result the D_{4d} structure of the anion is a transition state and the system is highly fluxional. The anion is the most stable charge state and is about 10 eV higher in energy compared to the cation.

The global minimum of the neutral Si_{10} and Ge_{10} cluster is a C_{3v} tetracapped trigonal prism.[114, 121] The structure of the neutral Si_{10} cluster has been confirmed by IR spectroscopy.[74] The silicon photoelectron spectrum indicates that Si_{10} has a low electron affinity and a large electronic gap, indicating that Si_{10} is a stable, closed-shell species.[76] However, there is no evidence for a comparable gap in the case of germanium. This could be due to differing geometries and/or electronic configurations in either the neutral or anion cluster. Li and coworkers found a gap of 1.3 eV between the C_{3v} tetracapped trigonal prism and a lower lying T_d tetracapped octahedron, while for silicon they confirmed the lowest energy structure.[150] Comparison with the experimental IR spectrum identifies a tetracapped trigonal prism as the geometry for the cation.[75]

The mass abundance of silicon and germanium clusters in the experimental mass spectrum drops gradually and significantly after size 10. This transition is accompanied by the appearance of a multitude of low symmetry structures as low lying isomers in DFT studies. These structures often build upon 9 and 10 vertex structures by capping trigonal faces. It is found that the Si_{11}^{2-} dianion is unambiguously of a lower C_s symmetry.[113] The global minimum within the Ge_{11}^{2-} set is a bicapped TTP structure distorted from D_{3h} to C_{2v} symmetry.[120] However, other low lying isomers are present. The neutral Si_{11} cluster of C_s symmetry is only 0.015 eV lower than a C_{2v} structure.[113] There are many isomers for Ge_{11}, which all have low symmetry.[120] Comparing the observed Si_{11}^+ IR spectrum with those predicted for different isomers assigns the C_s symmetry structure previously predicted.[75] It can be described as the Si_{10}^+ ground state capped by an additional atom. The global minimum for the Si_{13}^{2-} dianion is a C_s structure which is 0.31 eV lower in energy compared to the C_{2v} structure corresponding to $B_{13}H_{13}^{2-}$. The C_{2v} structure corresponding to $B_{13}H_{13}^{2-}$ can be conceived as a capped square antiprism sharing its square face with another square antiprism. It is lower in

energy than more spherical structures. The global minimum for the neutral Si_{13} cluster is the same C_s structure as the dianion. However, in this case the closely related C_{2v} structure corresponding to $B_{13}H_{13}^{2-}$ is only 0.015 eV higher in energy and probably shows fluctual behaviour. For the Si_{13}^{+} cluster, a starshaped structure best described as four atoms capping deltahedral faces of the Si_9^{2-} ground state has a computed infrared spectrum in agreement with that observed in the IR experiment.[75]

The "missing" 12 vertex icosahedron

Due to the prevalence of deltahedral structures amongs silicon and germanium clusters, it is logic to predict an icosahedral structure for the 12 vertex system. Surprisingly, no icosahedral shape has been found for any low lying isomer of silicon or germanium clusters, even among various charge states. The ground state structures of the Ge_{12}^{2-} and the Si_{12}^{2-} dianion have C_s symmety and are lower in energy than the I_h icosahedral structure, which is only a local minimum.[113,122] The 12-vertex bare germanium cluster is different from $B_{12}H_{12}^{2-}$ and related boranes since they have external lone pairs rather than external hydrogen atoms. Such external lone pairs can become involved in the skeletal bonding, particularly in concavities or even at high degree vertices of relatively low curvature. Furthermore, germanium, like its lighter congener carbon, often prefers vertex degrees of four rather than five. The lower energy of the C_s structure could also be attributed to its low symmetry which facilitates an uneven distribution of electronic charge, thus allowing extra electrostatic interactions between oppositely charged regions.

The neutral Si_{12} cluster shares the same C_{2v} symmetry with the corresponding $B_{12}H_{12}$ borane.[113] The lowest energy structure for Ge_{12} is closely related to the lowest energy structure for Ge_{12}^{2-} except that it has become a bicapped *nido* structure.[122] Si_{12}^{+} has previously been predicted to have a C_s structure containing a distorted tricapped trigonal prism building block. However, for the Si_{12}^{+} cluster no satisfactory agreement between theory and IR experiment has been obtained so far for an extended number of computed isomers.[75]

Recently, endohedrally doped $Ge_{12}Li^{(-)}$ clusters with an icosahedral shape were shown to be lowest energy structures.[151] The high thermodynamic stability of the clusters considered is the result of a combination of their closed crystal field splitting shell, aromatic character and electrostatic attraction.

4.2.2 Elongated structures

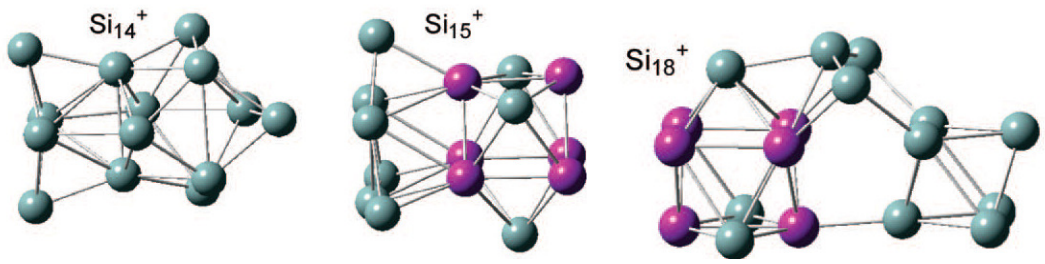

Figure 4-1: Structures for medium sized Si_n^{+} clusters experimentally confirmed by IR spectroscopy. These three structures clearly indicate the transgression towards stacked, elongated structures. [from Lyon and coworkers (2009)[75]]

Despite the many advances in experimental characterization of clusters over the two past decades, detailed morphology for most medium-sized clusters cannot be determined solely from experiments. Hence, determination of cluster structures has mainly relied on DFT and *ab initio* quantum-mechanical calculations. It is well known that as the size of

clusters increases the number of local minima increases rapidly and so does the computational time required for the unbiased global search, particularly when the global search is combined with DFT or *ab initio* calculations. While the structures of small silicon and germanium clusters (n < 12) are reasonably well established by now, the precise structure of the larger sizes cannot be trusted with the same confidence, with each computational study revealing new lowest isomers. The problem is even better illustrated by the work of Lyon and coworkers who recorded vibrational spectra of Si_n^+ in a size range between 6 and 21 atoms. In the size range above $n = 11$, only 3 structures could be identified, while the quality of the experimental spectra is still sufficient. Figure 4-1 shows the structures confirmed by the experiment. A good fit with the IR experiment is obtained for the Si_{14}^+ structure which is also found in ion mobility measurements and which is only 0.07 eV higher in energy than the computed global minimum.[75] It is an elongated structure, which has a complex shape, starting a transition to elongated clusters which are composed of different subunits. The existence of these subunits is experimentally confirmed with the IR spectra of Si_{15}^+ and Si_{18}^+. In both cases the capped square antiprism acts as a subunit, while in Si_{18}^+ even a second octahedral subunit can be conceived. The presence of stable subunits is also apparent from dissociation experiments as discussed in section 4.1.5.

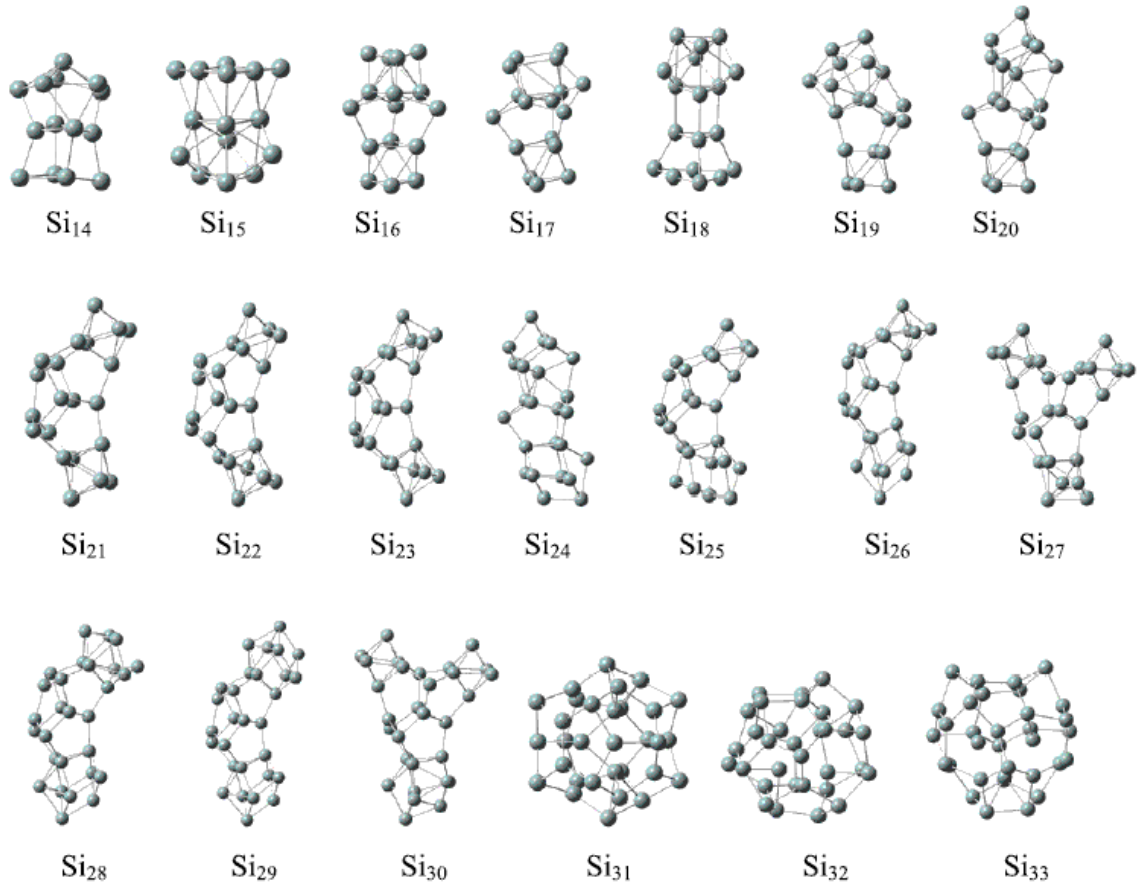

Figure 4-2: Overview of typical medium sized silicon structures, showing the transition from elongated towards stacked (first row) and from stacked towards spherical (third row) structures. [from Qin and coworkers (2009) **[139]**]

Qin and coworkers studied the fragmentation behavior of the lowest-energy structures of Si_n clusters (n = 14-33) by DFT methods.[139] Figure 4-2 shows the lowest-energy isomers: all of the structures were confirmed to be local energy minima by frequency analysis. For Si_n (n = 8-30), the geometries favor prolate structures, and the structures for n > 19

consist of two or three stable subunits. These stable subunits are connected by Si_6 or Si_9 units, both of which are diamond lattice segments. In this work, when n reaches 31, the structures of Si_n transform into cages. More precisely, in the size range around the transition point, the stabilities of prolate and cage structures compete with each other, and their binding energies are very similar.

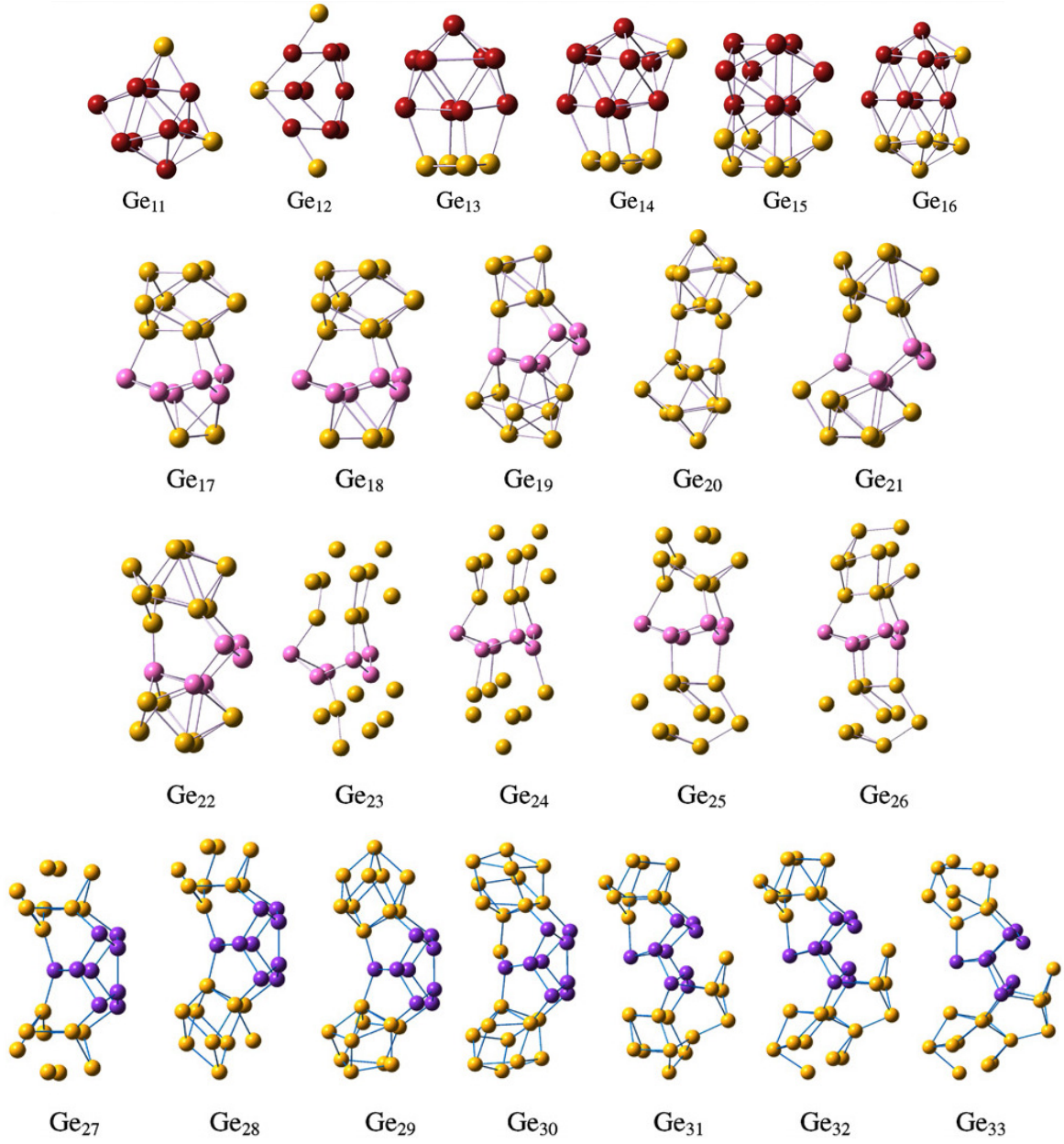

Figure 4-3: Overview of typical medium sized germanium structures, showing the transition from elongated towards stacked structures. The transition towards spherical clusters takes place at much higher sizes around 65. [From Zhao and coworkers (2008)[137]]

Ion mobility measurements by Hunter and coworkers have revealed that the medium-sized cations Ge_n are generally prolate in shape and the structural transition from the prolate to spherical-like shape appears at n ~65 were different isomers coexist.[108] Although small and medium-sized silicon and germanium have similar structures this transition takes place at an earlier size range of 24–30 for silicon clusters. The most relevant experimental information on anionic systems, up to size 40, comes from laser photofragmentation studies by Zhang and coworkers.[110,111] These experiments clearly shows that semiconductor clusters dissociate larger fragments with a preference for 6, 9 or 10 atoms. This is in sharp contrast to metal clusters that dissociate only monomers and

dimers. Zhao and coworkers studied the fragmentation behaviour of the lowest-energy structures of Ge_2–Ge_{33} using all-electron DFT methods.[137] They predict that the fragmentation products of Ge_6, Ge_7, and Ge_{10} clusters are abundant and appear frequently in fragmentation processes, which is in line with the experimental observations. The lowest-energy structures of germanium clusters (n = 11–33) are presented in Figure 4-3. It can be seen that the TTP motif is prevailing in almost all of these structures. For Ge_{17}–Ge_{26} they contain a Ge_6 link unit, except for Ge_{20}. All Ge_n clusters in the size range 27–29 contain a Ge_9 link unit, which acts as a linkage connecting to two small clusters. The lowest-energy structures of Ge_{19}–Ge_{29} are consistent with the calculated results of Yoo and coworkers, though the latter discuss other competitive structures based on the Ge_9 link unit and octagonal subunits. The lowest-energy geometries of Ge_{30}–Ge_{33} keep a similar growth pattern with a Ge_9 linkage connecting with three small clusters including a Ge_4 cluster. The shape of the clusters is clearly prolate.

4.3 Metal doped silicon and germanium clusters

Section 4.2 provided some important clues towards the understanding of bare silicon and germanium clusters. Most remarkable is that larger clusters consist of smaller units that can be used as stable building blocks. These units are not always identical to the counterpart neutral clusters that have the same number of atoms. And as the structure and stability of these smaller clusters depends on the charge state, it is interesting to look beyond neutral clusters and look for stable clusters both in function of size and charge state. It is hard to probe charge dependence directly. However, chapter 5 will describe that by doping silicon and germanium clusters with lithium, information is retrieved on the bare negatively charged clusters. Because of that, this section already provides a background on alkali metal doped silicon and germanium clusters. Coinage metals sometimes behave like alkali metals in cluster compounds and this subject is touched shortly as well. The behaviour of transition metal dopants is completely different and is discussed extensively in the thesis work of Vu Thi Ngan[152] and Pieterjan Claes[153].

4.3.1 Sodium doped silicon clusters

Zubarev and coworkers combined photoelectron spectroscopy and ab initio calculations to investigate the electronic structure and chemical bonding of Si_5^- and Si_5^{2-} in $NaSi_5^-$.[81] Photoelectron spectra of Si_5^- and $NaSi_5^-$ are obtained at several photon energies and are compared with theoretical calculations at different levels of theory.[154,155] Excellent agreement is observed between experiment and theory, confirming the obtained ground-state structures for Si_5^- and Si_5^{2-}, which are both found to be a trigonal bipyramid with D_{3h} symmetry at several levels of theory. Na^+ is coordinated to the face of Si_5^{2-}.

Sodium doped silicon clusters (Si_nNa_m; n = 1-14, m = 1-5) produced by two types of laser vaporization were studied by Kishi and coworkers[156] The adsorption of sodium atoms on the Si_n clusters leads the substantial lowering of the ionization energy of Si_nNa_m clusters. This feature is consistent with that of the sodium adsorption on the Si(100) surface for which the work function is effectively decreased. The reactivity toward NO molecules was measured with a fast flow reactor, and the anticorrelation between the IEs and the reactivity was clearly observed: species having low IE exhibit high reactivity and *vice versa*. Moreover, a clear parallelism between the IEs of Si_nNa and the electron affinities (EA) of Si_n is found. There are three local minima at n = 4, 7 and 10. This is consistent with the fact that the structure of Si_nNa clusters keeps the frame of the corresponding Si_n cluster unchanged and that the electronic structure of Si_nNa is similar to that of the

corresponding negative ion Si_n^- and the parentage of the SOMO of Si_nNa is the LUMO of the corresponding Si_n.

In addition to the experimental studies, the geometries, adsorption energies, and vertical ionization energies of Si_nNa (n = 1–7) were investigated with *ab initio* MO calculations including electron correlation. The most stable isomers of the Si_nNa clusters (n = 2–7) have the bridge-site-type structures, in which a 3*s* electron of a sodium atom effectively works as an excess electron and is localized on the silicon framework. Furthermore, for the bridgesite-type isomers, the π bonding between the silicon atom and the sodium atom is induced by the backdonation to the $3p_\pi$ level of sodium. Because the LUMOs of Si_n (n = 4–7) are principally antibonding, the larger the effect of the backdonation is, the more stable the Si_nNa (n = 4–7) are. Indeed, the net charge on the sodium atom of the most stable isomers for Si_n (n = 4–7) is smaller than the others. The electronic structure and the Si_n framework of Si_nNa are similar to that of the corresponding negative ion Si_n^-. The calculated IEs of Si_nNa (n = 1–7) are in good agreement with the experimental ones.

Electronic properties of $Si_nNa_m^-$ (n = 1-14, m = 1-5) cluster anions were further investigated by photoelectron spectroscopy using a magnetic-bottle type electron spectrometer.[157] The electron affinities of $Si_nNa_m^-$ were determined from the threshold energies in the photoelectron spectra of $Si_nNa_m^-$. Besides, the geometries and energies of Si_nNa^- (n = 1–7) were investigated with *ab initio* MO calculations. By the adsorption of a sodium atom on Si_n, the EA decreases for n = 4–6, but increases for n > 7. The calculations for Si_nNa^- show that the Si_n framework for n = 4–6 accepts at least two excess electrons. For Si_7Na^-, however, the charge transfer from the sodium atom scarcely occurs to avoid distorting the close-packed Si_7 framework. For some of Si_nNa_m, the IEs and EAs decrease monotonically for each sodium adsorption, indicating the independent adsorption of sodium atoms on the Si_n framework, which corresponds to a multiply charged anion Si_n^{m-}. On the other hand, there is a series of Si_nNa_m (n = 6, 7, 10) in which the IEs and EAs show an even–odd alternation against the number of sodium atoms: the sodium atoms are said to be adsorbed as a Na_m cluster.

4.3.2 Lithium doped germanium clusters

Mass abundance spectrum

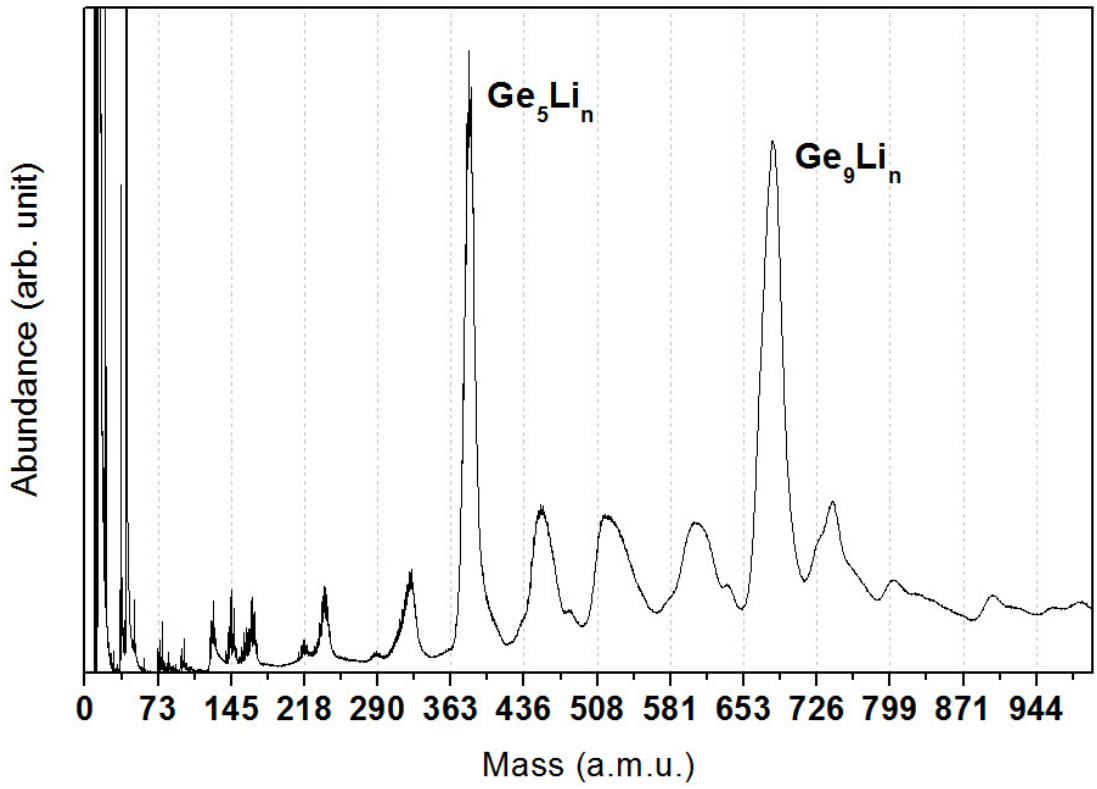

Figure 4-4: RTOF mass abundance spectrum of Ge_nLi_m clusters photoionized by an ArF laser (6.42 eV). The vertical lines match the position of pure Ge clusters. [from G. Gopakumar and coworkers (2009)[4]]

Figure 4-4 shows a RTOF mass abundance spectrum of photoionized lithium doped germanium clusters.[4] The vertical lines match the position of pure germanium clusters. Only very small traces of pure germanium clusters are present and the spectrum is dominated by broad shapes, consisting of multiple peaks which reflect the coexistence of Ge_n clusters doped with different amounts of lithium. For each value of n there is an optimal stoichiometry between germanium and lithium atoms. Due to the isotopic nature of germanium and lithium, the contributing peaks cannot readily be resolved with our current instrumentation except for the smallest sizes. To determine the precise stoichiometry for the most abundant clusters, each conglomerate of peaks was fitted with the isotope pattern for the corresponding bare germanium cluster.

For the smallest Ge_nLi_m clusters a low abundance of doped clusters is found and bare germanium peaks are still present. For the lithium doped germanium monomer, one up to three lithium atoms are found, but all species are heavily oxidized. $GeLi_3O_2$ turns out to be the most abundant, with no apparent unoxidized $GeLi_3$ in the mass spectrum, closely followed by GeLi(O). Smaller peaks are found for $GeLi_2(O)$. For the dimer and trimer, Ge_2Li_m and Ge_3Li_m show comparable behavior with small amount of lithium doping and a maximum for $m = 3$. In both cases, traces of oxidized species are insignificantly low. For Ge_4Li_m the maximal amount of doping has shifted to $m = 5$, with a smaller contribution for $m = 4$ also present. The next series of sizes from $n = 5$ up to 10 shows high abundances of doped germanium clusters. Most distinct are the sizes $n = 5$ and $n = 9$. Ge_5Li_m has a sharp peak at $m = 3$ and a small tail. Although this peak is very high, the bare Ge_5 peak is almost absent, both in the doped and bare germanium mass spectra. For

Ge_6Li_m there is a strong peak with a long tail at m = 2, while for Ge_7Li_m this shape starts at m = 1. It is unlikely but not excluded that part of the tail is due to oxidized species. Ge_5Li_3, Ge_6Li_2 and Ge_7Li_1 each have 8 atoms. The situation for Ge_8Li_m is less straightforward: though there is a maximum for m = 3, a broad number of lithium atoms leads to competing structures. While for bare germanium clusters, Ge_{10} is more abundant than Ge_9, upon doping this order is reversed. Ge_9Li_m is centered on Ge_9Li_4, but Ge_9Li_3 and Ge_9Li_5 are clearly present, as the peak is significantly broader than the bare Ge_9 peak. Ge_9Li_5 is most abundant, closely followed by Ge_9Li_4. $Ge_{10}Li_m$ has a maximum for m = 2, but noticeably also has a significant contribution from the bare germanium peak. Ge_{11} and Ge_{12} do not gain much upon doping and remain small as in the bare mass spectrum.

DFT calculations of Ge_nLi_m (n = 2-7; m = 1-3)

The most abundant species for Ge_nLi_m with n = 2 and 3 are Ge_2Li_3 and Ge_3Li_3. These clusters were subjected to extensive theoretical studies using the robust *ab initio* methodologies and the popular density functional approach.[158,159] Structurally Ge_2Li_3 falls under C_{2v} symmetry, while a C_s symmetry has been located as the global minimum for Ge_3Li_3.

The global minimum for Ge_4 is a rhombic structure that falls under the D_{2h} symmetry, in agreement with earlier studies.[115] Addition of an electron leads to the formation of the anion for which a rhombic lowest-lying structure has been located similar to the neutral molecule. Geometrically this structure is very much similar to the neutral counter part. During the progressive doping the Ge_4 unit undergoes a geometrical change from planar rhombic to a butterfly-like structure. The global minimum for the bare neutral Ge_5 is a D_{3h} symmetric structure in agreement with previous work. Doping of the Ge_5 unit with lithium atoms shows the same trend as in the case of the tetramer where the latter normally acts as a bridging entity. In the case of the neutral system, progressive lithiation occurs at successive positions leading to the C_{2v} symmetric tri-lithiated Ge_5. The three lithium atoms in Ge_5Li_3 mainly act as bridging units. Structurally, the cationic structures take different geometries as compared to the neutral counterpart.

There were no experimental geometries available for Ge_{6-8} and its anions, but our result is consistent with the ones reported previously.[116,115] Upon doping with lithium atoms the geometries and electronic structure of bare germanium clusters changes considerably. For Ge_6Li a C_{2v} symmetryic structure is found which is geometrically similar to the lowest-lying electronic state of Ge_7. The geometry of the cation is considerably different from that of the neutral counterpart. Progressive lithiation results in Ge_6Li_2 with a C_s symmetric structure. The structure can be better modeled as two lithium atoms distributed symmetrically around the Ge_6 unit. The geometry of the lowest-lying electronic state of the cation is very much similar to that of the neutral counterpart. For Ge_7Li a C_{2v} symmetric structure has been located as the global minimum. This structure can be better modeled as the Ge_7 unit with the lithium atom acting as a bridging entity. The geometry of the cation is similar to that of the neutral counterpart. Similar to the case of Ge_6Li_2 the progressive addition of the lithium atom to Ge_7Li prefers a symmetrical position around the Ge_7 unit. The geometry of the low-lying isomer of the cation is similar to that of the neutral counterpart. For Ge_8Li a C_s symmetric structure has been derived. The geometry of the cation shows considerable difference compared to the neutral cluster.

4.3.3 Coinage metal doped silicon and germanium clusters

In our group the abundance of neutral and cationic copper doped silicon and germanium clusters was previously investigated using a mass abundance reflectron time-of-flight mass spectrometer.[160,161] The spectrum for Si_nCu^+ clusters after 7.89 eV laser fragmentation (0.6 mJ/cm^2) shows a clearly different pattern compared to chromium and manganese dopants featuring mainly Si_6Cu^+, $Si_{7\text{-}9}Cu^+$, and $Si_{10}Cu^+$ as abundant sizes, while there is no sign for an enhanced abundance of doped Si_nCu^+ species in the size range n = 14–16. A laser fluence dependence measurement shows a strong increase for $Si_{10}Cu$, suggesting it to be a favorable fragment. The results for $Ge_nCu^{(+)}$ species are similar with enhanced abundances for $Ge_7Cu^{(+)}$and $Ge_{10}Cu^{(+)}$ (6.42 eV, 0.06-1 mJ/cm^2). Si_nCu clusters (n = 4, 6, 8, 10, 12) are very thoroughly studied computationally. An extensive isomer search for $Si_{10}Cu$ claims that the high abundance observed in the mass spectra should not be ascribed to the geometric stability of a specific (highly symmetric) dopant-encapsulated structure, but rather to the existence of a multitude of near-degenerate isomers. Important to note is that endohedrally doped structures for $Si_{10}Cu$ are unfavourable. Beck[162] previously found similar results: the most prominent peak for neutral clusters ionized with 7.89 and 6.42 eV photons is $Si_{10}Cu$, with other peaks in the size range $Si_{6\text{-}10}Cu$. Surprisingly, he noticed a decrease in abundance for Si_8Cu and $Si_{11}Cu$ going from 6.42 to 7.89 eV photons. He explains this by the relatively low electron affinity of the Si_8^+ and Si_{11}^+ cations compared to their neighbours, which in their case is lower than the IE of copper (7.7 eV). He suggest that a charge transfer from copper to the cluster cation is a stabilizing effect which cannot occur for energetic reasons, in the 8 and 11 silicon atom clusters. A combined far-infrared spectroscopic and computational study of the growth mechanisms of small Si_nV^+ and Si_nCu^+ clusters with n < 12 shows that vanadium and copper follow two different paths: while vanadium prefers substitution of a silicon atom in a highly coordinated position of the cationic bare silicon clusters, copper favors adsorption to the neutral or cationic bare clusters in a lower coordination site.[163]

The structure, stability and electronic property of the Ge_nAu (n = 2–13) clusters were systematically investigated with DFT.[164] Upon examining the lowest energy structures, it is found that the growth behaviors for the small-sized Ge_nAu (n = 2–9) clusters and relatively large-sized Ge_nAu (n = 10–13) clusters are different. As the number of germanium atoms increases, the gold atom would gradually move from convex to surface and to interior sites. For the most stable structures of Ge_nAu (n = 10–13) clusters, the gold atom would be completely surrounded by the germanium atoms to form gold-encapsulated Ge_n cages. Natural population analysis shows that the charges always transfer from the gold atom to the Ge_n framework except for the Ge_2Au cluster. This indicates that the gold atom acts as electron donor while the 5d orbitals of the gold atom are not significantly involved in chemical bonding. Abundance mass spectra on gold doped germanium cations show a similar trend as for copper with enhanced abundances for singly and doubly doped $Ge_{7\text{-}10}$ cations. Using DFT calculations the lowest-energy structures of $AuSi_n$ (n = 1–16) clusters are obtained as well.[165] In the lowest-energy configurations, the gold atom prefers to occupy a surface site for smaller clusters with n < 11. Starting from n = 11, the gold atom begins to occupy the interior site and for n = 12 the gold atom completely falls into the interior site forming an $Au@Si_{12}$ cage. In this case the charge transfer takes place from the cluster towards the gold atom. Doping with gold atoms is clearly different from doping with alkali metal atoms.

4.4 Nanomaterials

4.4.1 Nanorods

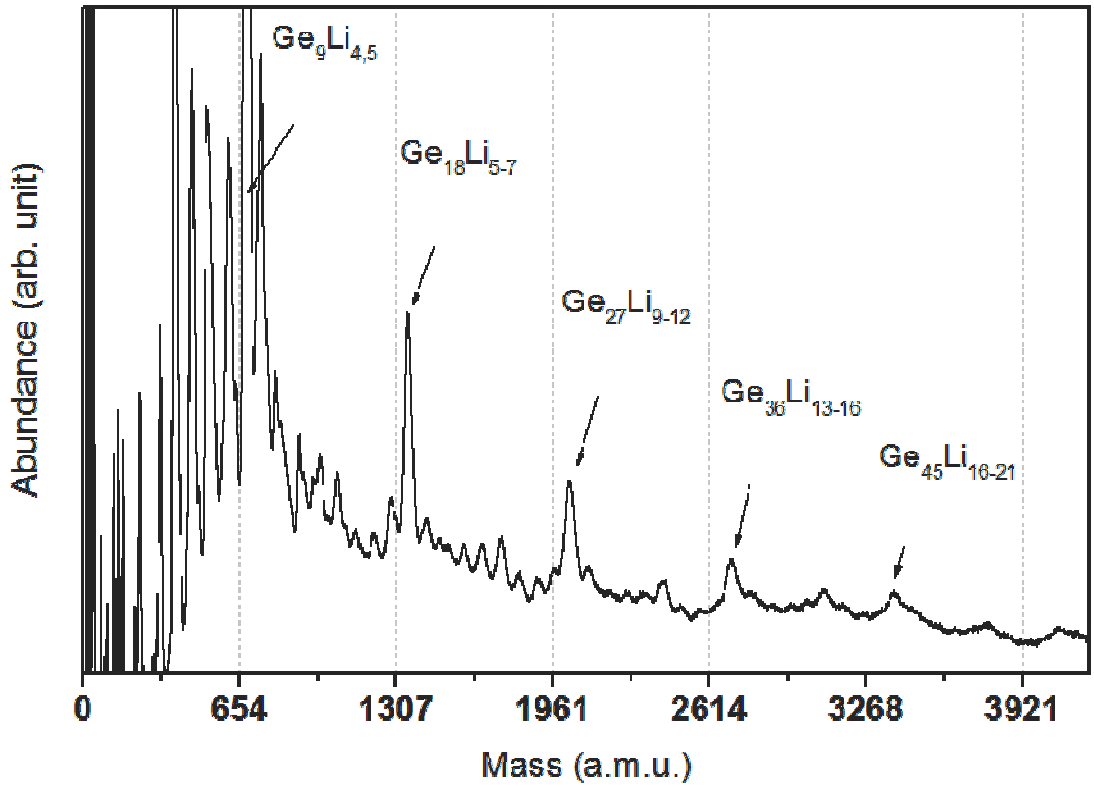

Figure 4-5: RTOF mass abundance spectrum of Ge_nLi_m clusters photoionized by ArF laser light (6.4 eV, 250 μJ/cm^2). The vertical lines match the position of pure Ge_{9p} clusters. [from G. Gopakumar and coworkers (2009)[4]]

Figure 4-5 shows a mass spectrum of $Ge_nLi_m^{(+)}$ clusters.[4] The dotted vertical lines are plotted at the positions that match the abundances of Ge_{9n} clusters. The first peak in this pattern is Ge_9Li_m. The position of the other enhanced peaks can be estimated from the mass spectra as corresponding to $Ge_{18}Li_{5\text{-}7}$, $Ge_{27}Li_{9\text{-}12}$, $Ge_{36}Li_{13\text{-}16}$ and $Ge_{45}Li_{16\text{-}21}$. The absence of clear reference peaks makes precise determination of the stoichiometry of the larger clusters impossible with our instruments current mass resolution, hence the number of lithium atoms is given by a range instead of a precise number.

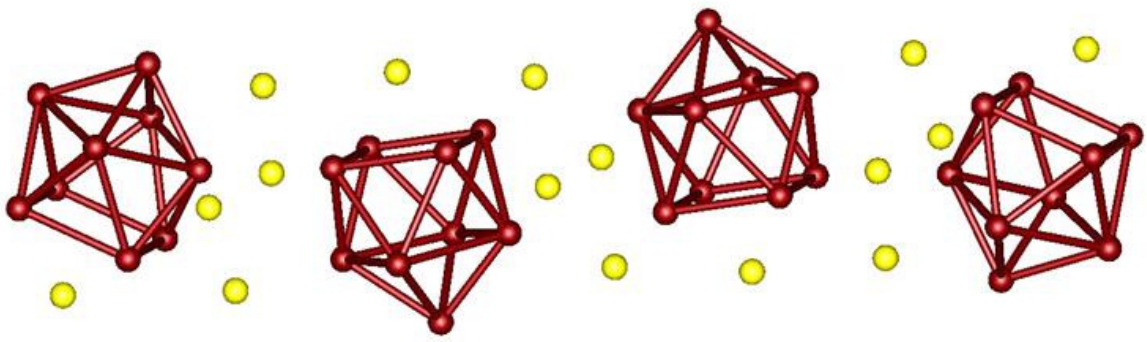

Figure 4-6: Optimized molecular geometry for $Ge_{36}Li_{16}$ at B3LYP/SV(P) level within the proposed theoretical model. Maroon colour balls are germanium atoms and yellow balls are lithium atoms.

We propose a theoretical model towards a structural understanding of the appearance of $[Ge_9]^{x-}$ oligomers in the gas phase. Structural details of a Ge_9 dimer, trimer, and tetramer have been characterized by the Sevov group as a combination of Ge_9 units arranged in a linear fashion.[173] Of the various combinations considered, our computations suggest the combination of *nido*-Ge_9 units with several numbers of surrounding lithium atoms as the lowest energy ones. The first member of this series is $Ge_{18}Li_6$ which contains two *nido*-Ge_9 units surrounded by six lithium atoms. A lithium atom acts as a capping entity at the base of each *nido*-Ge_9 unit. The remaining four lithium atoms are distributed around the Ge-Ge bond connecting the two *nido*-units. $Ge_{18}Li_6$ possesses a large HOMO-LUMO of 2.68 and 2.96 eV at B3LYP/ECP and B3LYP/SV(P), respectively. Progressive addition of a Ge_9 unit and a number of lithium atoms results in a symmetrical growth pattern of the $Ge_{18}Li_6$ cluster to its next higher member $Ge_{27}Li_{11}$. Structurally it falls under C_{2v} symmetry with three Ge_9 *nido*-units connected to each other in a linear fashion with lithium atoms around it. This structure is characterized as an energy minimum with all real vibrational frequencies at the B3LYP/ECP level. A simililar building pattern leads to the formation of a chain like $Ge_{36}Li_{16}$ which includes four *nido*-Ge_9 units and is surrounded by a number of lithium atoms. This structure falls under C_s symmetry and the lithium atoms are distributed in a symmetrical way.

Among various polyhedra from group IV elements, nine atom clusters receive considerable attention as for them the cluster coupling phenomena shows a controlled growth.[145,166,167,168] The $[Ge_9]^{4-}$ building block can be prepared chemically in the form of its K_4Ge_9 precursor.[169] It is known that $[Ge_9]^{4-}$ Zintl clusters in ethylenediamine self-oxidize to form oligomers and linear polymer chains.[170,171,172] Dimers, trimers, tetramers and even infinite chains of Ge_9^{x-} were synthesized in solution by the Sevov group.[170,171,173,174] Red crystals were obtained, from which X-ray diffraction revealed the alternated 'up' and 'down' stacking of tricapped trigonal prism Ge_9 units. The reduction of the overall charge is not completely understood. Band structure calculations suggest delocalized bonding with a charge requirement of 2– per Ge_9 unit for all polymeric doubly linked chains.[175]

Recently, group IV Zintl compounds were used as building units for mesoporous semiconductors.[176,177,178,179,180] G. Armatas and M.G. Kanatzidis reported on the surfactant-directed assembly of mesoporous metal/germanium-based semiconducting materials from coupling of anionic $(Ge_9)^{4-}$ clusters with various linking metal (Sb, In, Sn, Pb, and Cd) ions. The resulting materials feature a metal/Ge_9 framework perforated by regular arrays of mesoporous channels. The mesoporous structures exhibit energy gaps in the range of 1.48-1.70 eV as well as strong photoluminescence at room temperature with emission energies varying from 740 to 845 nm. The emission depends on pore wall thickness and framework composition. This suggests possible application in visible light photocatalysis and solar energy conversion. The photoemission spectra can be sensitive to organic molecules small enough to enter the pores and engage in electron-acceptor interactions with the semiconductor framework. These results point to the intriguing new direction where materials based on Ge_9 clusters can be anticipated using metal coordinative chemistry. Coordinative and oxidative coupling reactions of $(Ge_9)^{4-}$ with various transition-metal ions have produced interesting species, including $[Ge_9Zn(C_6H_5)]^{3-}$, $[Au_3Ge_{45}]^{9-}$, and the polymeric chain $\{[Hg(Ge_9)]^{2-}\}$.[181,182,183,184,185]

4.4.2 Organic ligands

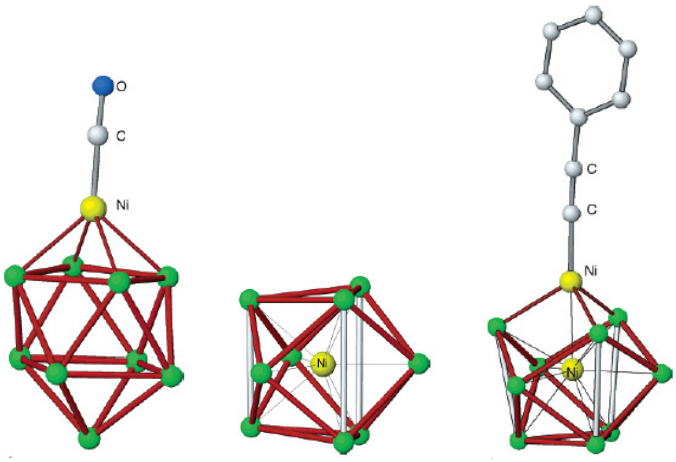

Figure 4-7: Examples of nickel ligand-capped Ge_9 clusters: $[Ge_9Ni\text{-}CO]^{3-}$, $[Ni@(Ge_9Ni\text{-}CCPh)]^{3-}$, and $[Ni@Ge_9]^{3-}$ [from J.M. Goicoechea and coworkers (2006)[70]]

The reactivity of Ge_9 is not limited to the formation of polymers. Ge_9^{4-} can for instance be functionalized by a variety of groups such as $-SbPh_2$, $-SbPh_2$, $-BiPh_2$, $-GeMe_3$, $-GePh_3$, $-SnMe_3$, $-SnPh_3$, $-Si(SiMe_3)_3$ etc.[186,167] Reactions in solution of K_4Ge_9 with $Ni(COD)_2$ (COD=cyclooctadiene) and $Ni(PPh_3)_2$ resulted in Ni-ligand capped Ge_9 clusters, some with and some without the presence of an interstitial nickel atom.[187] The presence of an interstitial atom will alter the electronic structure of the cluster, making it possible to modulate the optical response. The doping with single dopants can be extended: a linear dimer is found to be present in $[Ni_3@(Ge_9)_2]^{4-}$, by enlarging the system to two vertex-fused Ge_9 clusters. This realization can be conceived as the onset of a magnetic nanorod. Figure 4-7 shows a series of nickel ligand-capped Ge_9 clusters, some with and some without an interstitial nickel atom, were chemically synthesized and characterized in solution by electrospray mass spectrometry, IR spectroscopy, and ^{13}C NMR.[181] All species were structurally characterized in crystalline compounds. The empty cluster $[Ge_9Ni\text{-}CO]^{3-}$ is a bicapped square antiprism where one of the capping vertexes is the nickel atom. The Ge-Ge distances fall in the range 2.52-2.82 Å with the shortest ones occurring around 4-bonded atoms while the longest ones correspond to distances between 5-bonded atoms. The endohedral clusters are tricapped trigonal prisms where an additional 10th vertex of monoligated nickel caps a triangular base of the trigonal prism. All atoms of the cluster are equidistant from the central nickel atom, i.e., the cluster is very close to spherical. More information on functionalized Zintl ions can be found in a recent review paper.[188]

5 Experimental investigation of lithium doped silicon and germanium clusters

This chapter gives an overview of experiments conducted in the framework of the investigation of lithium doped silicon and germanium clusters. It starts with the germanium doped lithium clusters, which show subsequent filling of atomic germanium orbitals by electrons donated by the highly ionic lithium atoms. Mass abundance spectra of neutral lithium doped silicon and germanium clusters are further investigated by photoionization efficiency measurements. The last section investigates the fragmentation mass abundance spectra of bare and lithium doped silicon and germanium cations giving direct information on stability features.

5.1 Ge_1Li_m and Si_1Li_m: filling of atomic orbitals

5.1.1 Lithium doped germanium monomer

Introduction

Since the experimental detection of the stable oxides and carbides of the type Li_3O[189,190] and Li_6C,[191] lithium clusters mixed with other elements have attracted considerable interest. Although clusters doped by boron Li_nB,[192] oxygen Li_nO,[193] aluminum Li_nAl,[194] carbon Li_nC[195] and tin Li_nSn[196,197] have theoretically been investigated, relevant experimental information is rather scarce. Our lab has earlier produced the lithium monoxides Li_nO (n = 2-70)[198] and lithium monocarbides Li_nC ($n \leq 70$)[199] and subsequently measured their ionization energies. As a first step in the study of the binary clusters Li_nGe_m, we report the experimental observations of Li_nGe^+ with n = 1-7, along with the results of a detailed theoretical investigation on their equilibrium geometries, electronic structures stabilities and bonding properties.[200] The DFT calculations were performed by Vu Thi Ngan and coworkers from the K.U.Leuven Chemistry Department. Some aspects of the electronic distribution of the small neutral clusters Li_nGe (n = 1–4) have been examined earlier in a similar collaboration.[158]

Experimental results

Lithium doped germanium clusters are experimentally produced using a dual-target dual-laser vaporization source. Two rectangular targets of germanium and lithium are placed beside each other and moved in a closed-loop pattern under computer control. The targets are exposed to the focused 532 nm laser light of two pulsed Nd:YAG lasers.

Synchronous with the ablation of the target surfaces, helium gas is injected into the source by a pulsed gas valve, typically with a pressure of 5-6 bar. Cluster formation is initiated by collisions between atoms and clusters of the vaporized material and inert-gas atoms. The source is cooled to -40 °C by liquid nitrogen. The mixture of atoms, clusters and inert gas undergoes a supersonic expansion into a vacuum chamber through a nozzle. The nozzle has a conical shape with an opening angle of 10 °, and a throat diameter of 1.5 mm. The isentropic expansion reduces the temperature of the cluster beam and ends the cluster-growth process because of the rapidly decreasing density. The clusters are detected by a reflectron time-of-flight (RTOF) mass spectrometer (M/ΔM≈800). In the extraction region clusters interact with focused high energy laser light (6.4 eV, ArF excimer laser) and absorb multiple photons, resulting in a considerable increase in excess energy. This leads to a significant probability of localizing enough internal energy to overcome the dissociation energy of a fragment or atom. As long as the free energy of the formed daughter fragments exceeds the binding energy of a constituent atom, this evaporation chain continues. Finally the evaporation chain terminates at cluster configurations that are more stable than other cluster sizes at the same temperature. This results in the observation of stability patterns in the experimental mass spectrum.

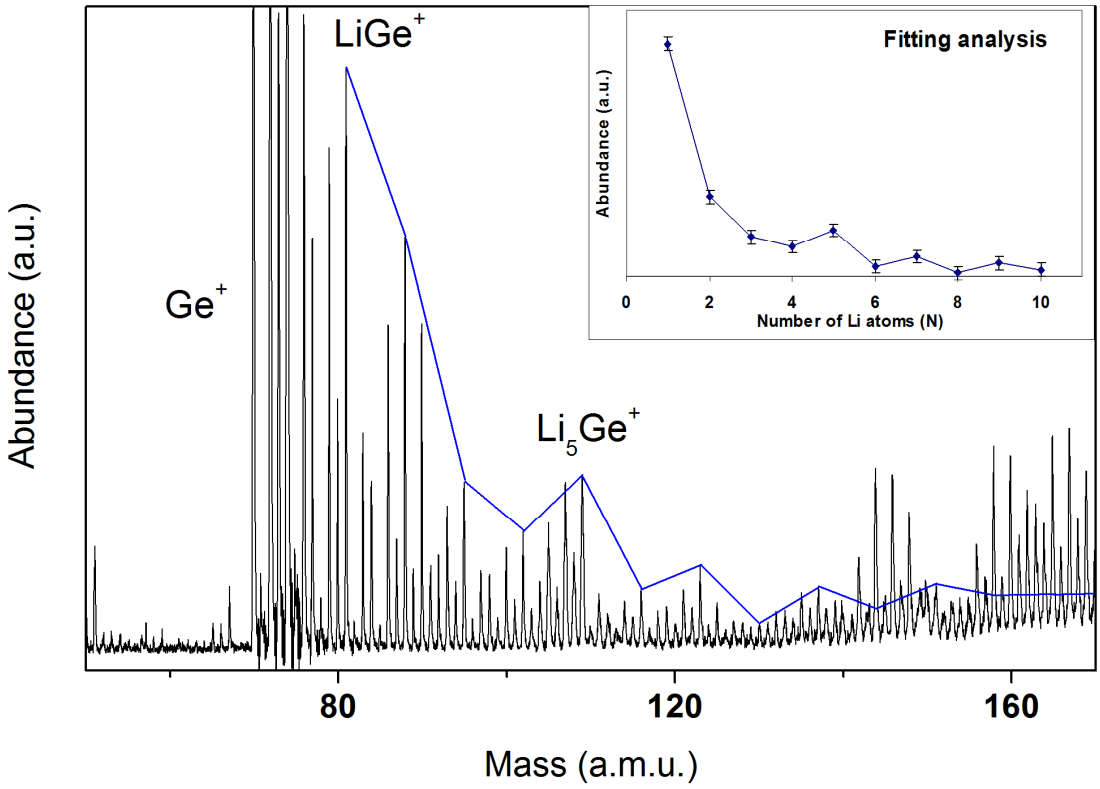

Figure 5-1: RTOF mass abundance spectrum of Li_nGe^+ clusters, photodissociated by focused high fluence laser light from an ArF laser (6.4 eV). (inset) Abundances of Li_nGe^+ clusters obtained by fitting the mass spectrum with isotope distributions for germanium and oxygen doped lithium clusters. [from V.T. Ngan and coworkers (2009)[200]]

Figure 5-1 shows a photodissociation mass spectrum of positively charged germanium doped lithium clusters. The highest peaks corresponding to Li_nGe^+ are connected by a solid line. The main features are the abundance enhancement of Li_5Ge^+ and an odd-even staggering starting at Li_4Ge^+. Using simple electron counting rules Li_5Ge^+ is conceived to have 8 delocalized electrons, including three electrons from the Ge^+ ion and one electron from each lithium atom. This number corresponds with a magic number for the spherical shell model for metal clusters. The experimentally observed odd-even effect can be

attributed to a stability enhancement for an even number of delocalized electrons, and is related to a deformation driven degeneracy lifting of the electronic energy levels, with singly occupied electron levels having higher energy.[201]

A more detailed analysis of the abundances of the different cluster sizes has been performed by using a fitting procedure incorporating calculated isotope distributions for germanium and oxygen doped lithium clusters in the given size range. Formation of oxide aggregates is hard to avoid for lithium clusters and has been investigated and discussed elsewhere.[159,202] After dissociation the main oxygen-containing species left in the mass spectrum are GeO^+ and Li_8GeO^+. Both lithium and germanium have multiple stable isotopes, which need to be accounted for in order to deduce the abundances observed in the mass spectrum correctly. The error on the mass calibration is below 0.1 a.m.u. in this size range, rendering identification of all peaks unambiguous. The obtained abundances of Li_nGe clusters for sizes for n = 1-10 are shown in the insert of Figure 5-1 and confirm the two observations discussed above.

DFT results

During the search for structures, geometries of all possible forms were fully optimized making use of the density functional theory with the popular hybrid B3LYP functional,[203,204] in conjunction with the all electron augmented correlation consistent basis set aug-cc-pVnZ[205,206] (with n = D, T and Q, depending on the size of the species). For each spin manifold, geometry optimization was carried out with and without imposing symmetry constraint on the different initial configurations. Harmonic vibrational frequencies were subsequently calculated to characterize the located stationary points as equilibrium structures having all real vibrational frequencies. Figure 5-2 shows geometrical structures of the ground states of $Li_nGe^{0,+}$ (n = 1-7) clusters.

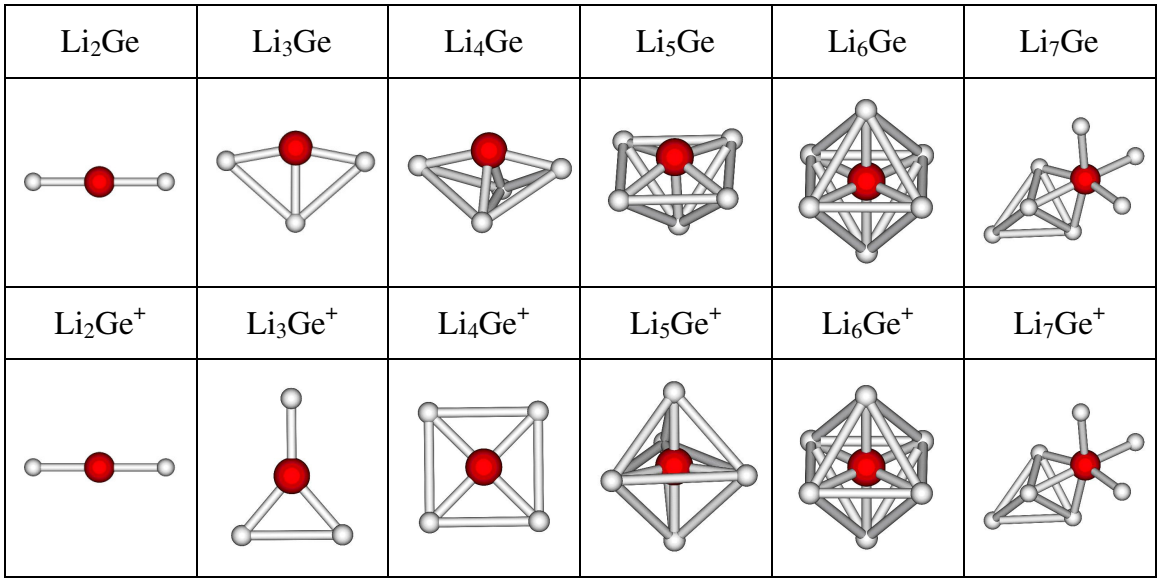

Figure 5-2: Geometrical structures of the ground state of $Li_nGe^{0,+}$. [from V.T. Ngan and coworkers (2009)[200]]

LiGe and $LiGe^+$

The ground state of LiGe is a high spin state with a bond length of 2.402 Å. There is an apparent electron transfer (0.78 e) from the 2s(Li) to the $4p_z$(Ge) orbital, which characterizes an ionic Li-Ge bond. Thus the 4p shell of germanium is half filled by receiving one electron from 2s(Li). This is confirmed by its natural electron configuration ([core]$4s^{1.97}4p^{2.79}4d^{0.02}$) and it partly accounts for stability in accordance

with Hund's rule. Similarly, the cation $LiGe^+$ adopts the high spin lowest-lying state. The natural electron configurations of lithium ($[core]2s^{0.09}2p^{0.03}$) and germanium ($[core]4s^{1.98}4p^{1.88}4d^{0.01}$) suggest that the $LiGe^+$ can best be regarded as a complex between a germanium atom and a lithium cation with a long bond length of 2.824 Å. The ionization energy to remove one electron from the quartet LiGe to form the triplet $LiGe^+$ is 6.35 eV, which turns out to be the highest value in the series of the considered germanium doped lithium clusters.

Li_2Ge and Li_2Ge^+

A linear triplet structure is the electronic ground state for Li_2Ge. A question of interest is why the linear structure is more stable than the bent one while the isovalent species GeH_2 is well-known having a bent structure. The bond primarily arises from the overlaps between $4p_z$(Ge) and 2s(Li) MOs. The extent of orbital overlap is larger at the linear geometry than the bent one. Hence, in the linear shape electrons are more easily transferred from lithium to germanium. As a result, the positive charge on lithium of the linear Li_2Ge (0.77 e) is larger than that of the bent Li_2Ge (0.50 e). For the Li_2Ge^+ cation, a bent quadruplet and a linear doublet form are competitive ground states, with the linear doublet state being the lowest-lying. This results from a competition between the electronic (not linear) and the geometric structure (linear).

Li_3Ge and Li_3Ge^+

The D_{3h} equivalent triangle structure, which is the corresponding ground state of Li_3C, has been characterized as a second-order saddle point on the doublet potential energy surface (PES) of Li_3Ge which leads to the T-shaped ground state. The D_{3h} structure turns out to be a local minimum on the singlet potential energy surface of the cation while the triplet isosceles triangle structure is the global minimum just a little more stable (0.04 eV) than the D_{3h} structure.

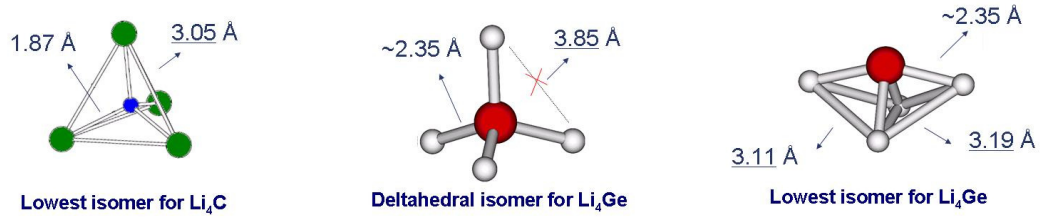

Figure 5-3: Comparison of structures for Li_4C and Li_4Ge illustrating differences in bond lengths. [after P. Lievens and coworkers (1999)[199]; from V.T. Ngan and coworkers (2009)[200]]

Li_4Ge and Li_4Ge^+

Reed and coworkers[30] found that unlike the established tetrahedral structure of Li_4C, the isovalent Li_4X (X = Si, Ge, Sn) prefer a C_{2v} geometry analogous to that of SF_4. The global minimum of Li_4Ge is here confirmed to be a C_{2v} open structure. All starting geometries invariably lead to the C_{2v} rhombus minimum on the singlet PES of Li_4Ge. This means that this isomer is very stable. The Li_4Ge^+ cation has a lowest-lying state characterized by a D_{4h} square planar structure. Interestingly, Li_4Ge does not adopt the tetrahedral structure like Li_4C. The Ge-Li bond lengths in the two geometries stay almost the same (~2.3 – 2.4 Å), but the Li-Li distances make the difference (3.850 Å in T_d, Li_{eq}-Li_{eq} = 3.198 Å in C_{2v}). It is possible that due to the relatively smaller radius of carbon, Li_4C adopts the T_d structure as the lowest-energy isomer. In this structure, the shorter Li-Li distances of 3.046 Å make the overlaps between orbitals of different lithium atoms stronger than those in the T_d structure of Li_4Ge.

Li_5Ge and Li_5Ge^+

The most stable structure of Li_5Ge is obtained by subsequent addition of one lithium atom to the Li_4Ge rhombus. This results in a C_{4v} square pyramid form. Upon removal of one electron from Li_5Ge, a D_{3h} cage structure is located as the lowest-lying state of Li_5Ge^+. However, the square pyramid is calculated to be only 0.004 eV less stable than the D_{3h} structure. This cation appears as the most pronounced peak in the photodissociation mass spectrum.

Figure 5-4: Comparison of structures for Li_6C and Li_6Ge illustrating differences in bond lengths. [after P. Lievens and coworkers (1999)[199]; from V.T. Ngan and coworkers (2009)[200]]

Li_6Ge and Li_6Ge^+

Li_6Ge was studied theoretically in the set of MX_6 (M = C-Pb, X = Li-K) compounds.[207,208] The octahedral structure of Li_6Ge, as other clusters in the set, was found as a stable minimum. Li_6Ge is confirmed here to possess an O_h structure in which the germanium atom is surrounded by six lithium atoms. It is actually at this size that germanium becomes encapsulated in the lithium cage while it occurs for the carbon atom already at Li_4C. Removal of one electron from of the Li_6Ge octahedron results in a similar structure for the cation ground state. Although Li_6C and Li_6Ge are isoelectronic, the second is less stable. Because the atomic radius of carbon is smaller than that of germanium, the Li-Li distances in Li_6C are significantly shorter than those in Li_6Ge. Consequently, the in-phase overlaps of 2s(Li) in the HOMO of Li_6C are larger, lowering the energy of the HOMO. As a comparison, the octahedral isomer of Li_6 has average bond lengths of 2.81 Å, while twice its atomic radius amounts to ~2.9 Å. This proves that the lithium atoms in the Li_6C cluster are indeed within bonding distance.

Li_7Ge and Li_7Ge^+

The C_{2v} pentagonal bipyramid, which is a distortion form D_{5h}, is not a local minimum as in the case for Li_7C. On the doublet PES of Li_7Ge, the lowest-energy form is the C_{3v} structure shown in Figure 5-2: the germanium atom seems to have only six coordinates due to the long distance between the capping lithium atom and the germanium atom (4.612 Å). The lowest-lying state of Li_7Ge^+ is the C_{3v} state having a coordination number of seven, because the bond length of 2.585 Å between the capping lithium atom and the central germanium atom is similar to other bond lengths in this structure. Thus both neutral and cationic forms of Li_7Ge have a similar ground structure, even though the cation is more spherical than the neutral. The Li-Ge bond in Li_nGe clusters is dominated by its ionic character. Due to the small covalent character, germanium can make bond with up to seven lithium atoms. The lithium atoms do not directly bond to one another, but through germanium or pseudo atoms.

Discussion

The geometrical structures for the germanium doped lithium clusters are built up based on the subsequent addition of lithium atoms to a central germanium atom up to Li_6Ge, the seventh lithium atom starts capping to the face of the octahedral Li_6Ge core. While $Li_3Ge^{0,+}$ and Li_4Ge^+ prefer planar geometry, the clusters from Li_4Ge to Li_7Ge and the corresponding cations exhibit non-planar shape. The investigated clusters clearly

illustrate the transition from atomic to cluster orbitals with the electronic structure dominated by the germanium atom. Because of the ionic nature of the Li-Ge bonds and the absence of Li-Li bonds, the germanium atomic orbitals are subsequently filled going from $LiGe^+$ to Li_5Ge^+: from $4s^24p^2$ to $4s^24p^6$. This corresponds to the filling of cluster orbitals going from $1S^21P^2$ to a filled $1S^21P^6$ configuration. Here the molecular orbitals of the cluster and the atomic orbitals of germanium basically coincide. This implies that Li_4Ge and Li_5Ge^+ have closed shells. For the next shell closure the lithium atoms start to play a more active role: forced by the configuration of the germanium 4p orbitals they form an octahedral structure, but the lithium s-orbitals now form a 2S molecular orbital, in essence the next shell closure. This leads to an electronically and configurationally very stable Li_6Ge structure, reminiscent of Li_6C.

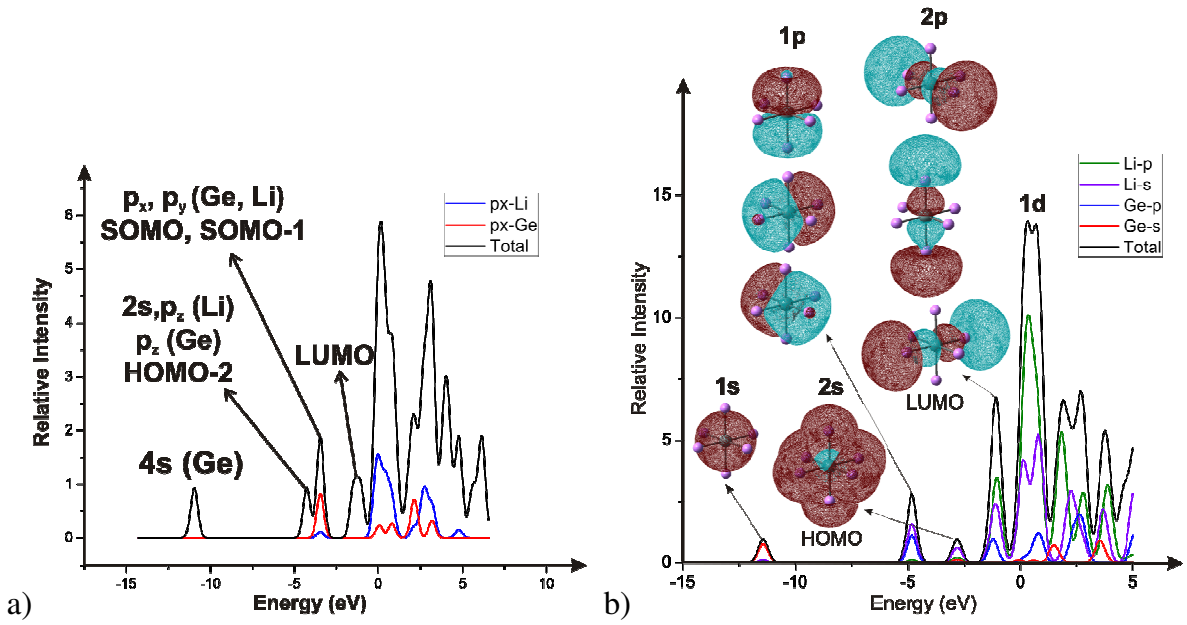

Figure 5-5: Density of states of (a) the linear triplet state Li_2Ge, and (b) and the singlet state of the octahedron Li_6Ge. [from V.T. Ngan and coworkers (2009)[200]]

The density of states (DOS) of this cluster, as displayed in Figure 5-5 b, confirms that the first 1S orbital is mainly composed by 4s(Ge) orbital. The three degenerate 1P orbitals have high contributions of 4p(Ge) and 2s(Li) orbitals. The second 2S, a highly delocalized MO, is composed mainly of 2s(Li). The frontier MOs of Li_6Ge describe indeed a closed shell configuration: $1S^21P^62S^22P^01D^0$. In this case, the energy level of 2P shell is pulled down even lower than the 1D shell. This may be because of the large negative charge on the germanium atom (-3.65 e). Applying the shell model with modified series 1S/1P/2S/2P/1D for $Li_nGe^{0,+}$ (n = 1-7) we can interpret the stability of those clusters. Their number of valence electrons range from 4 to 11 in which two magic numbers of 8 and 10 can be found. The clusters with the magic number of electrons are Li_4Ge, Li_5Ge^+ (8 electrons), Li_6Ge, Li_7Ge^+ (10 electrons). In this context, they should be more stable than the others. Actually, Li_4Ge and Li_6Ge show higher stability from the fragmentation energy plot and large HOMO-LUMO gaps.[200] The Li_5Ge^+ and Li_7Ge^+ express the maxima in HOMO-LUMO gaps as well. It is interesting that these four clusters prefer spherical geometries. For example, the Li_5Ge^+ prefers a trigonal bipyramid D_{3h} structure to the square pyramid C_{4v} of Li_5Ge. The Li_7Ge^+, a mono-capped octahedron, becomes much less prolate than the corresponding neutral by shortening the bond length between the capping lithium atom and germanium (2.585 Å of cation vs. 4.612 Å of neutral).

5.1.2 Lithium doped silicon monomer

Li_4Si	Li_5Si	Li_6Si	Li_7Si	Li_8Si	
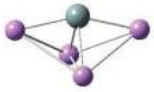	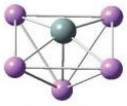	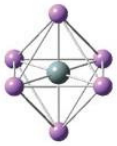	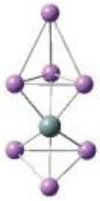		
Li_2C	Li_3C	Li_4C	Li_5C	Li_6C	Li_7C
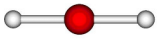	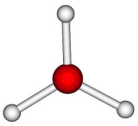	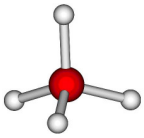	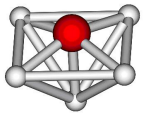	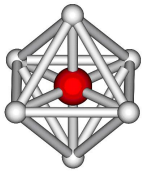	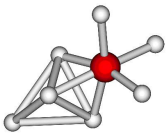
Li_2C^+	Li_3C^+	Li_4C^+	Li_5C^+	Li_6C^+	Li_7C^+
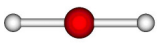	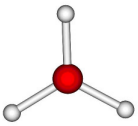	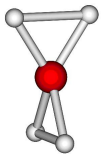	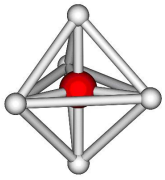	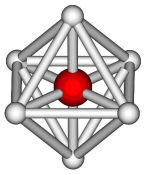	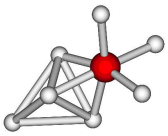

Figure 5-6: Geometrical structures of the ground state of Li_nSi. [from N. He and coworkers (2008)[209]] Geometrical structures of the ground state of $Li_nC^{0,+}$. [after P. Lievens and coworkers (1999)[199]]

Results from our work for lithum doped germanium clusters can be compared with theoretical work from Ning He and coworkers who systematically studied $SiLi_n$ clusters (n = 4–16) with different symmetries in various isomeric forms.[209] The optimized geometries of $SiLi_n$ (n = 4-8) are displayed in Figure 5-6. For comparison, also structures for CLi_n are shown. All isomers were reoptimized at the higher B3LYP/6-31111G(2d) level. Three affiliated structures with C_{2v}, C_{4v}, and O_h symmetry are energy minima for $SiLi_4$, $SiLi_5$, and $SiLi_6$, respectively, which is consistent with previous studies on the geometries of $SiLi_4$ and $SiLi_6$.[207,210] Moreover, these structures are identical to the germanium case. All lithium atoms in small clusters $SiLi_n$ (n = 4-6) favor direct coordination to the center silicon atom. For $SiLi_7$, a six-coordinated structure similar to our $GeLi_7$ structure is lower in energy than a structure in which all seven lithium atoms directly bond to the core silicon atom. Similarly, the global minimum of $SiLi_8$ is $(SiLi_6)Li_2$, with a hexa-coordinated silicon and two faces of the octahedron capped by lithium atoms. When the cluster size increases further, extra lithium atoms are attached to a core of $SiLi_7$, $SiLi_8$, or $SiLi_9$ subunits. As a result, the role of the silicon atom becomes less important and the clusters develop metallic characteristics and become similar to the bare lithium clusters. These results indicate that insertion of a single silicon atom has a dramatic effect on the structures of small lithium clusters. Also in the case of silicon, the silicon atomic orbitals dominate the structure and stability of the cluster, and the lithium atoms serve as electron donors. A more detailed study was performed by calculating the cohesive energies, the vertical ionization energies and the vertical electron affinities. They all indirectly highlight the special stability of $SiLi_6$. This conclusion is further

supported by calculations of the (average) binding energy and the HOMO-LUMO gap as a function of the number of lithium atoms. This result is consistent with the previous studies that clusters with 8 or 10 valence electrons would be most stable.[211]

Comparison

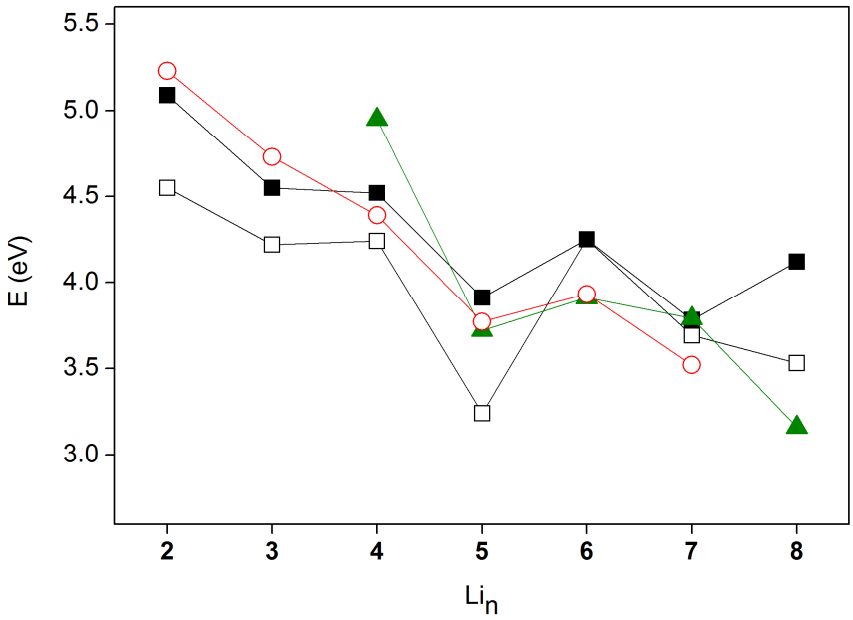

Figure 5-7: Comparison between IEs of carbon (□: experimental ionization threshold, ■: calculated VIE)[199], silicon (▲: calculated VIE)[209] and germanium (○: calculated AIE)[200] doped lithium clusters.

Figure 5-7 gives a comparison between the ionization energies of carbon, silicon and germanium doped lithium clusters. For CLi_n clusters, CLi_5 and CLi_7 show a drop in VIE, indicative of the high thermodynamic stability of CLi_6.[195] Clearly, $GeLi_m$, $SiLi_m$ show similar trends of IE for $n < 9$ but the strong features fade out a bit. For these systems, the 8 valence electron system becomes competetive or even more stable than the 10 valence electron system. This difference can directly be related to the atomic sizes and electronic structure of the different elements. The lowest-energy valence MO (1S) is derived from the in phase overlap of s type atomic orbitals. The three higher MOs (1P) are each composed of p type atomic orbitals (from carbon, silicon or germanium) in combination with 2s(Li). Filling these four MOs, fills an 8-electron shell, stabilizing systems such as Li_4Ge and Li_5Ge^+. This is confirmed by the largest HOMO-LUMO gaps of 8-electron species Li_4Ge and Li_5Ge^+. Moreover, the abundance of Li_5Ge^+ stands out in the experimental mass spectrum. The fifth MO (2S) however is obtained by the out-of-phase combination of s type atomic orbitals of the central dopant and in phase overlap of 2s(Li): the larger the overlap of the 2s(Li), the lower the MO energy. As the size of the central atom increases, going from carbon, over silicon to germanium, the *S*-Li (*S* = C, Si, Ge) and accordingly the Li-Li distance increase. For instance, the atomic radius of germanium is much larger than that of carbon (1.25 vs 0.7 Å) and the distance between lithium atoms in Li_nGe is significantly longer than that in Li_nC. Consequently, the in-phase overlaps in the fifth MO of Li_nGe are less than that of Li_nC, and then the energy gap between the fourth and fifth MOs of Li_nGe is larger than that of Li_nC. A computational study of twenty-four M_6X clusters shows a clear correlation between bond lengths and binding energies.[207] For the 8 electron system, the HOMO involves the overlap between lithium orbitals and the p orbitals of the central atom, rather than directly between lithium orbitals. This overlap is disfavoured in the case of carbon because of the large energetic difference between the orbitals.

Conclusion

Already in the case of the silicon and germanium doped lithium clusters a number of observations can be drawn which play an important role in understanding the lithium doping of silicon and germanium clusters:

- Lithium behaves as a strong electron donor.
- The electrons from the lithium atoms start filling the atomic orbitals of silicon and germanium atoms.
- Closing electronic shells of silicon and germanium atoms by doping with lithium results in enhanced stability.
- The stability is improved if a spherical shell closing coincides with a spherical symmetric geometry.
- Differences between carbon and germanium (silicon) can be explained by differences in atom size and bond lengths. In section 6.4 these differences will be discussed further considering the relative position of the energy levels of the participating orbitals.

5.2 Ionization energies

5.2.1 Experimental method and data evaluation

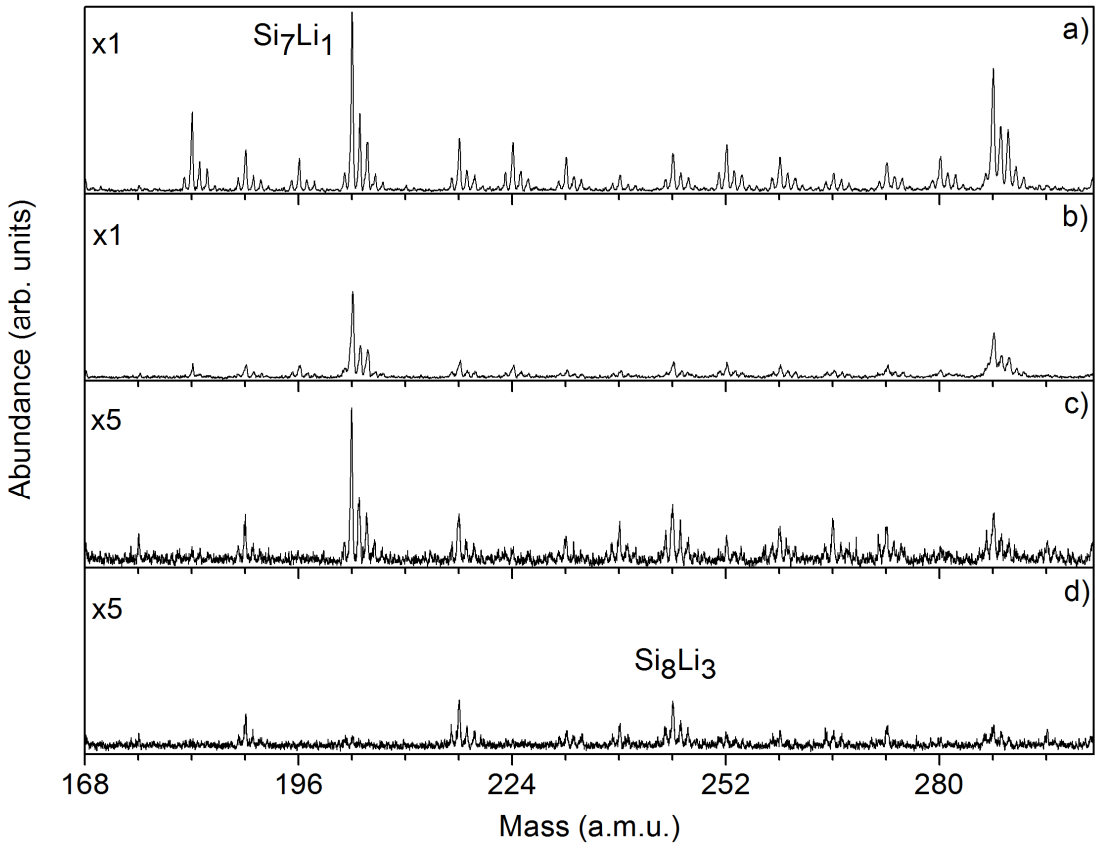

Figure 5-8: Mass abundance spectra of neutral Si_nLi_m clusters produced at 140 K and ionized using variable laser light: (a) 6.42 eV laser light at 183 µJ/cm² (b) 6.12 eV laser light at 192 µJ/cm² (c) 5.84 eV laser light at 245 µJ/cm² (d) 5.44 eV laser light at 213 µJ/cm² The vertical scale of spectra (c) and (d) is five times enlarged compared to the vertical scale of spectra (a) and (b).

Binary Si_nLi_m and Ge_nLi_m clusters were produced in a pulsed (10 Hz) dual-target dual-laser vaporization source.[9] Rectangular silicon (germanium) and lithium targets are ablated by two independent pulsed Nd:YAG lasers (532 nm) with typical energy densities of 8 and 0.2–1.0 mJ/cm² for the silicon (germanium) and lithium targets, respectively. Following vaporization, the silicon and lithium atoms mingle with high purity helium gas, which is introduced in the formation chamber through a pulsed valve and starts the cluster formation process. The cluster source is cooled by a regulated flow of liquid nitrogen to a temperature of 140 K. Neutral clusters are skimmed and ionized inside the extraction region of a reflectron time-of-flight mass spectrometer. Ionic species produced directly in the source are repelled by an electrostatic field. By variation of the ablation lasers energies and the ion extraction timing, clusters with various amounts of lithium doping could be sampled.

The ionization energies are determined with threshold photoionization spectroscopy, using a procedure that was applied in our group before.[198,212] Mass spectra are recorded at different photon energies in the 4.68-5.72 and 5.84-6.24 eV range with a 0.04 eV step size using a dye laser (Sirah CSTR-LG-24). This is illustrated in Figure 5-8 showing the result for the following photon energies: (a) 6.42 eV, (b) 5.84 eV, (c) 5.84 eV, and (d) 5.44 eV. The abundance of all peaks decreases with decreasing photon energy, but not at the same rate for all species: while peaks corresponding to singly doped species are most abundant, species with three lithium atoms remain detectable even at lower photon energies. The vertical scale of spectra (c) and (d) is enlarged five times compared to (a) and (b) for clarity.

In order to limit the influence of source production fluctuation, reference spectra are taken with 6.42 eV photons from an excimer laser (Lambda Physik Compex 102). An analog controller switched alternatively between the tunable dye laser and the reference laser and drove the recorded signal in two different channels of the oscilloscope. Laser energies are kept below 250 µJ/cm² to avoid multi-photon effects. A drawback of this low energy is the low cluster signal. To enhance the signal to noise ratio measurements at each photon energy were repeated multiple times, with each measurement being an acquisition of 3000 cluster production cycles. The diameter of the tunable and reference laser beam was equal and care was taken to have a good overlap between both beams so that they irradiated the same area of the cluster beam.

Photoionization efficiency (PIE) curves are obtained by first integrating the peaks in the mass spectrum. The integrated intensities are converted into ionization efficiencies by division with the amount of produced clusters and the amount of incident photons, using the reference spectra and the measured laser powers, respectively. Plotting the ionization efficiency as function of the photon energy yields the PIE curves. Different empirical methods have been proposed to derive the vertical ionization energy (VIE) and the adiabatic ionization energy (AIE) from the PIE curves.[212,213,214,215] The VIE is the energy difference between the ground state of the neutral and the cation in the neutral cluster's geometry. The AIE corresponds to the energy difference of the neutral and cationic cluster, both in their relaxed ground states. The difference between the AIE and the VIE can be large, especially for small clusters when the geometric relaxation can be considerable.

We apply the displaced harmonic oscillator model to derive the VIE.[216] Assuming that photoionization is a step function transition from a specific initial electronic state to a specific final electronic state, PIE curves can be represented by a sum of error functions, one for each electronic transition:

$$I(E) = \sum_i A_i \left[1 + erf\left(\sqrt{4\ln 4}\, \frac{(E-\mu_i)}{FWHM_i} \right) \right] \tag{5.1}$$

With the error function:

$$erf(x) = \frac{2}{\sqrt{\pi}} \int_0^x e^{-u^2} du \tag{5.2}$$

The parameter A_i measures the intensity of the transitions, $FWHM_i$ is the width of the error function which results from vibrational broadening and μ_i is the inflection point of the error function representing the energy difference of the two electronic states. The VIE corresponds to the value of μ_1 and is obtained by fitting the PIE curves to this function. The lack of precise information on the cluster temperatures, Franck–Condon factors, and vibrational frequencies of neutral and ionic clusters leads to a physical uncertainty of at least 0.1 eV. The statistical uncertainties of the fitting procedure are of the order of 0.05 eV.

The measurable property most closely related to the AIE is the ionization threshold.[215] However, the measured ionization threshold can differ from the AIE if the Franck–Condon factor for the transition between the neutral and cationic ground state is zero, in which case the ionization threshold is an upper value for the AIE. This is particularly the case if the neutral and cationic ground state geometries differ substantially. On the other hand, thermal occupation of excited states in the neutral clusters can allow ionization at photon energies below the AIE, in which case the measured ionization threshold is lower than the AIE. The last effect typically is small for cold clusters (~0.01 eV). The ionization threshold is derived from the above defined fitting function for the PIE curve:

$$aIP_i = \mu_i - \frac{2}{3} FWHM_i = \frac{4\sqrt{2\ln 2}}{3} \sigma_i \tag{5.3}$$

The constant of 2/3 corresponds to 1.3% of the total height of the step function and represents the onset. The statistical uncertainty in the determination of the first linear increase of the PIE curves strongly depends on the quality of the fit.

5.2.2 Ionization energies of lithium doped silicon clusters

Mass abundance spectrometry

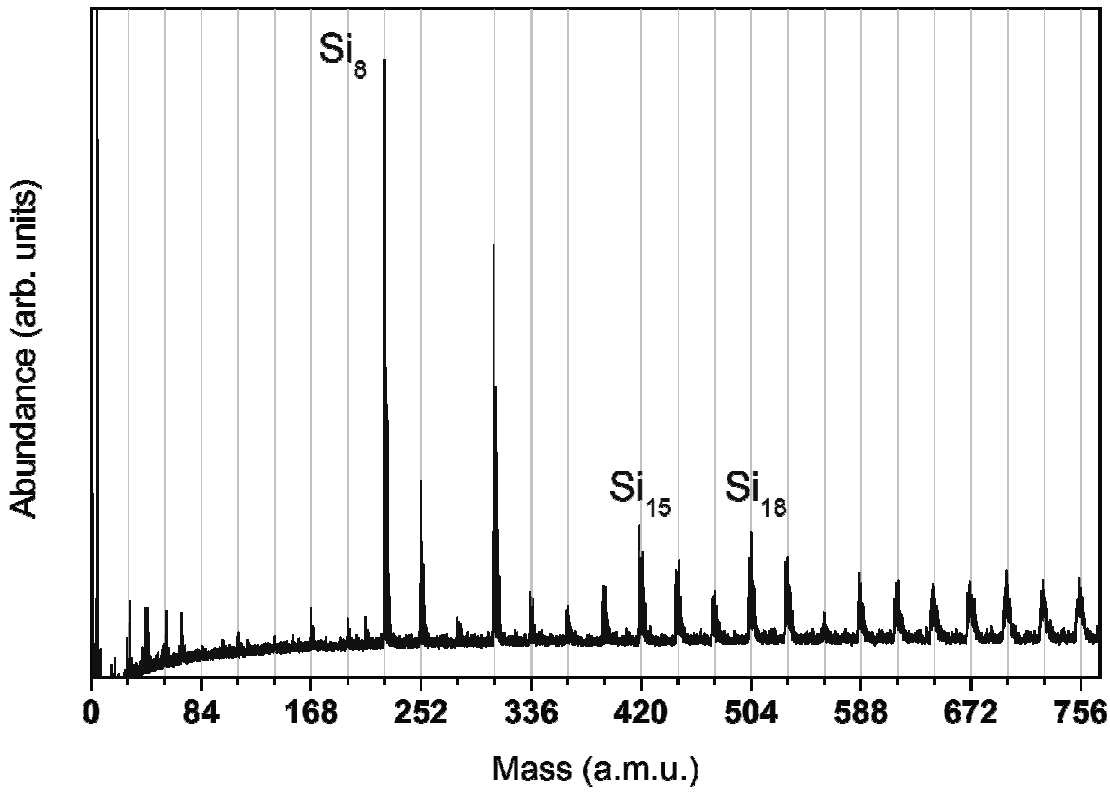

Figure 5-9: Mass abundance spectrum of bare Si_n clusters after laser photoionization with 7.89 eV photons from an F_2 excimer laser with an energy density of 230 μJ/cm². The clusters are produced in a source at room temperature.

Figure 5-9 shows a mass spectrum of neutral Si_n clusters after laser ionization with 7.89 eV photons. The two peaks corresponding to clusters of size 8 and 11 clearly stand out. However, the abundance of all clusters with less than 12 atoms is not or not correctly represented in this mass spectrum due to a high VIE. Before the spectrum starts to level off, there appear local maxima at size 15 and 18, similar to the bare germanium spectrum.

Typical mass abundance spectra of neutral Si_nLi_m obtained by postionization using 6.42 eV and 7.89 eV photon energies are shown in Figure 5-10. The laser energy density is kept low enough to ensure that no significant amount of photon induced fragmentation takes place. Mass interference between the main isotopes of Li_4 (28.06 amu) and Si (27.98 amu) hampers the mass spectrum analysis. We avoided overlapping peaks as much as possible by controlling the amount of lithium doping. Moreover, the ionization energy of small lithium-poor silicon clusters is significantly higher than that of small lithium-rich clusters, so they are only present in mass spectra taken with 7.89 eV postionization (Figure 5-10 (b)). For larger sizes, however, the ionization energies of the lithium-poor clusters are within the experimental 4.68 – 6.24 eV range and the overlap between Si_nLi_{m+4} and $Si_{n+1}Li_m$ clusters in the mass spectra occurs. Despite the different isotope patterns of Si_nLi_{m+4} and $Si_{n+1}Li_m$, which allow for identification and weighing of the different stoichiometries, the induced uncertainty limits the ionization energy analysis to Si_nLi_m sizes with $n \leq 11$.

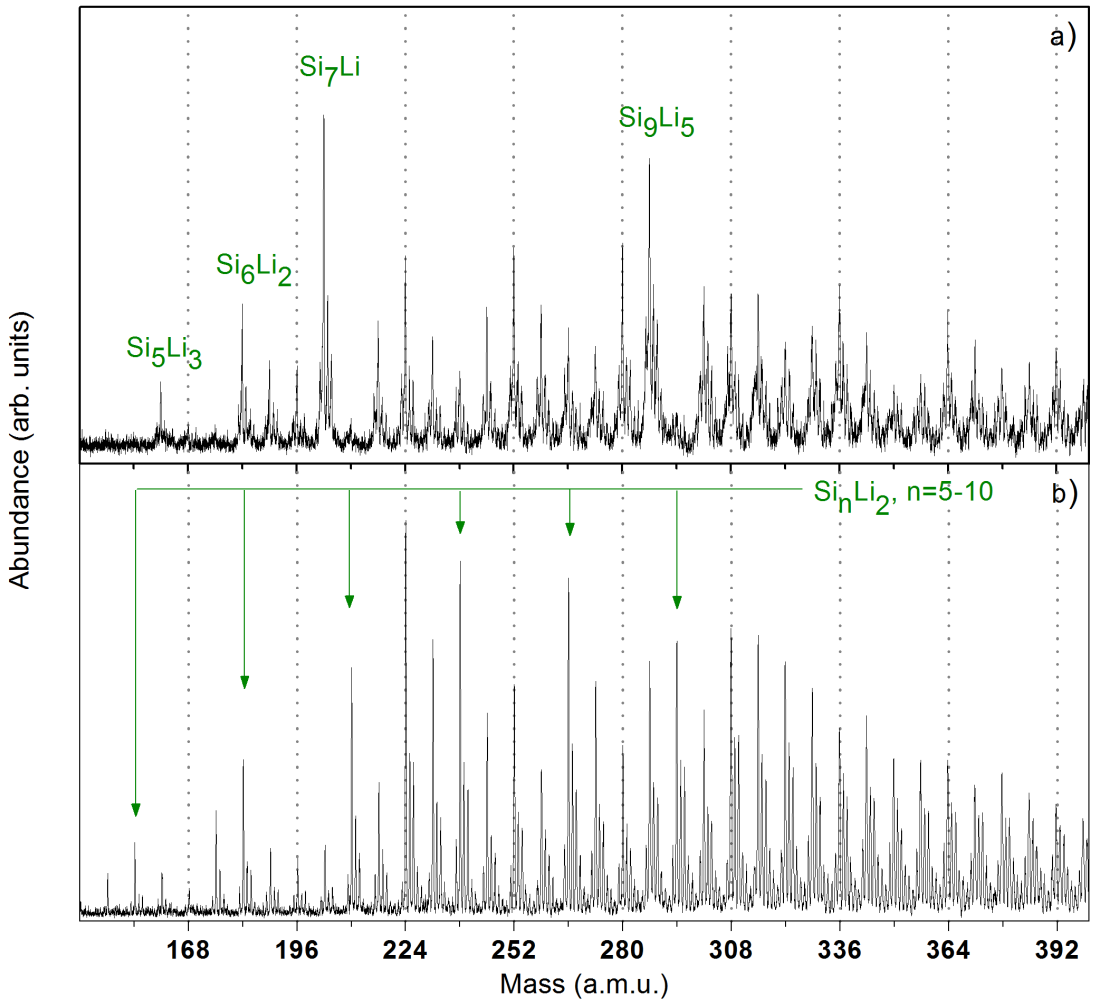

Figure 5-10: (a) Mass abundance spectrum of neutral Si_nLi_m clusters produced at 105 K and ionized using 6.42 eV laser light (energy density: 160 µJ/cm²). b) Mass abundance spectrum of Si_nLi_m clusters produced at 90 K and ionized using 7.89 eV laser light (energy density: 230 µJ/cm²). The arrows mark Si_nLi_2 clusters.

Certain sizes are more prevalent than others in the mass abundance spectra. In Figure 5-10 (a) enhanced peaks appear for Si_5Li_3, Si_6Li_2, Si_7Li_1, Si_9Li_5, and Si_nLi_4. One can, however, not directly relate the enhanced abundances to enhanced stabilities because the ionization energy of many Si_nLi_m species, and in particular of bare Si_n clusters, is higher than 6.42 eV and their corresponding peaks are therefore absent. This is clear when comparing with the high abundances for Si_nLi_2 clusters in the mass spectrum taken at a photon energy of 7.89 eV. Also no Si_n clusters with n = 1–7 and 10 are observed, because their ionization energy is above 7.89 eV.

Photoionization efficiency curves

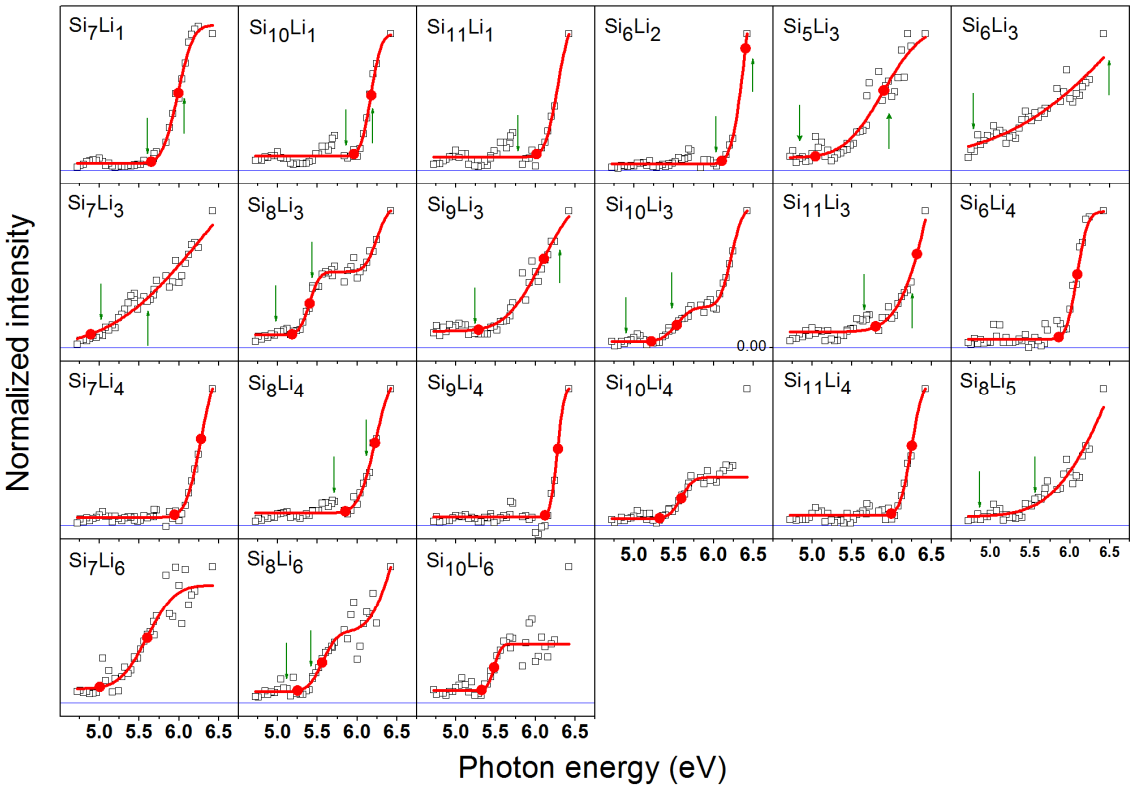

Figure 5-11: PIE curves of the Si_nLi_m clusters ($n \leq 11$, $m \leq 6$), which have an AIE below 6.25 eV. The open squares represent the experimental data, while the solid (red) lines represent smeared out step functions fitted to the data. The (red) circles square represent the experimental VIE and the ionization treshold. The calculated VIE and AIE are indicated by (green) arrows.

Figure 5-11 shows photoionization efficiency (PIE) curves of the Si_nLi_m clusters. The open squares represent the experimental data, while the solid (red) lines are the smeared out step functions fitted to the data. The scatter at the baseline is mainly due to the low signal to noise ratio. The experimental VIE and the ionization threshold are both indicated in the figures with a (red) dot. Without saturation in the PIE curve the fitting is liable to large deviations and in certain cases ($Si_{11}Li_1$, Si_6Li_3, Si_7Li_3, Si_8Li_5) there is no value assigned to the VIE. As observed in earlier IE measurements a single photoionization curve cannot always be described by a single step function, and multiple steps or slopes might be present. This is clearly the case for Si_8Li_3 and $Si_{10}Li_3$. Quantum chemical computations are carried out with the Gaussian 03 suite of programs.[217] Geometry optimizations are performed for all studied clusters, both in the neutral and the cationic charge state, using the pure B3LYP hybrid functional[218] in conjunction with the 6-311+G(d,p) basis sets. Vibrational frequency analyses characterized all optimized structures as minima and gave zero point vibrational energies. An overview of the lowest isomers can be found in appendix A.4. The positions of the calculated VIEs and AIEs are indicated by (green) arrows in Figure 5-11. The AIEs shown are calculated for a transition from the neutral ground state to the cation ground state, which is always lower than from the neutral ground state to the local minimum on the cation PES corresponding to the geometry of the neutral ground state (after relaxation). A quantitative overview of the experimental and calculated values is given in Table 5-1. The error for the experimental data is the standard error on the fitted data.

Table 5-1: Overview of the experimental and calculated values for the VIE, the calculated values for the AIE and the ionization thresholds of the Si_nLi_m clusters. The standard error from the fitting procedure is given between brackets.

Cluster	Ionization threshold (eV)	AIE-Th. (eV)	VIE-Exp. (eV)	VIE-Th. (eV)
Si_7Li_1	5.65 (0.04)	5.60	5.98 (0.01)	6.06
$Si_{10}Li_1$	5.95 (0.05)	5.85	6.17 (0.01)	6.19
$Si_{11}Li_1$	6.01 (0.16)	5. 77	> 6.2	6.89
Si_6Li_2	6.10 (0.26)	6. 03	6.40 (0.15)	6.47
Si_5Li_3	5.04 (0.35)	4.82	5.89 (0.09)	5.96
Si_6Li_3	4.40 (1.07)	4.80	> 5.7	6.49
Si_7Li_3	4.88 (0.23)	5.03	> 5.7	5.61
Si_8Li_3	5.18 (0.06)	4.97	5.40 (0.01)	5.44
Si_9Li_3	5.28 (0.26)	5.24	6.09 (0.08)	6.31
$Si_{10}Li_3$	5.21 (0.11)	4.85	5.54 (0.02)	5.48
$Si_{11}Li_3$	5.97 (0.19)	5.65	6.32 (0.07)	6.25
Si_5Li_4	4.63 (0.73)	-	5.35 (0.13)	-
Si_6Li_4	5.85 (0.05)	-	6.09 (0.01)	-
Si_7Li_4	5.94 (0.07)	-	6.28 (0.02)	-
Si_8Li_4	5.85 (0.11)	5.71	6.23 (0.03)	6.11
Si_9Li_4	6.12 (0.09)	-	6.28 (0.02)	-
$Si_{10}Li_4$	5.32 (0.08)	-	5.59 (0.02)	-
$Si_{11}Li_4$	5.99 (0.08)	-	6.25 (0.02)	-
Si_8Li_5	5.27 (1.31)	4.85	> 6.0	5.57
Si_7Li_6	5.00 (0.22)	-	5.60 (0.04)	-
Si_8Li_6	5.25 (0.21)	5.11	5.56 (0.05)	5.42
$Si_{10}Li_6$	5.32 (0.11)	-	5.48 (0.02)	-

For the singly doped silicon clusters, only three species (Si_7Li, $Si_{10}Li$ and $Si_{11}Li$) have a VIE low enough to be measured in our 4.68 to 6.42 eV energy window. In all three cases there are features in front of the ionization threshold: they are part of the PIE curves of $Si_{n-1}Li_5$ species which were present in the cluster beam even with low lithium concentration in the source. Both Si_7Li and $Si_{10}Li$ have the same geometric and electronic core as their cationic as well as their undoped counterparts. The additional lithium atom forms a strong ionic bond. Analysis of the density of states (DOS) shows that the additional electron due to the lithium dopant is located in a high energetic SOMO. This suggests that the neutral structure of Si_7 and Si_{10} is already electronically stable, giving rise to the very low VIE for the lithium doped species. A similar argument was proposed by Kishi and coworkers to explain the relatively low IE of Si_7Na and $Si_{10}Na$.[156] $Si_{11}Li$ presents a different case. The calculated value of 6.89 eV lies outside the measurement energy window and without saturation it is hard to pin down a trustable value for the experimental VIE. A more symmetric low lying isomer exists that has a VIE of only 6.47 eV.

For the doubly doped silicon clusters, only Si_6Li_2 has a VIE low enough to be recorded in this experiment. In this case the doubly doped system is geometrically and electronically almost identical to the singly doped system. Si_6Li_2 is geometrically similar to Si_7Li, which would suggest that Si_6Li is the more stable structure. This is certainly not apparent from the mass abundance spectrum. Remarkable is that Si_6^{1-} has been predicted to be

more stable than both Si_6^{2-} and Si_6, although in this case the structure is octahedral and not pentagonal and direct comparison is not possible.[114]

All triply doped species, except Si_8Li_3, have shallow PIE curves. Through vibrational excitations the neutral cluster can attain a geometry which corresponds to a cationic structure which is lower in energy on the cation PES than the structure of the neutral. In this case ionization can take place at a lower energy compared to the VIE which results in the broadening of the step function. The larger the change in geometry between the neutral and cation ground state, the larger this broadening might become. Indeed, from appendix A.4 it is clear that significant change in geometry occurs for all triply doped species. Si_8Li_3 and also $Si_{11}Li_3$ have a steeper PIE curve than the other triply doped species and show a clear step in the PIE curve. This will be discussed in section 5.2.4. Though structures with more than 3 lithium atoms were not investigated theoretically, some general comments can be made based on the PIE curves. All Si_nLi_4 (n = 6-11) species have relatively high VIE and show a sharp step function, which both suggest a more stable structure than the Si_nLi_3 species. Si_8Li_5 shows a more smeared out step function, reminiscent of the triply doped species, while the PIE curves for six lithium atoms again show sharper features like the other even doped species.

There is no good agreement between the experimental and calculated values for VIE and AIE for Si_7Li_3 and Si_8Li_5 and we can only conclude that the currently lowest isomers probably are not the ground state. In all other cases there is reasonable agreement between the experimental values and the DFT calculations and the isomers presented in Appendix A.4 form a strong set of candidates for the true ground state lithium doped silicon isomers.

5.2.3 Ionization energies of lithium doped germanium clusters

Mass abundance spectrometry

Figure 5-12 shows a mass spectrum of neutral Ge_n clusters after laser ionization with 7.89 eV photons. The peaks corresponding to clusters of size 6 to 11 clearly stand out. The relatively low abundance of Ge_7 is due to its high VIE. This also explains the absence of smaller species. Sizes 12 and 13 have low abundances pointing towards a low stability of the icosahedron. Before the spectrum starts to level off, there appear local maxima at size 15 and 18. These clusters might very well contain the stable Ge_9^{x-} building block. The photoionization spectrum from Yoshida and coworkers, which is taken under similar conditions, shows very similar features.[101]

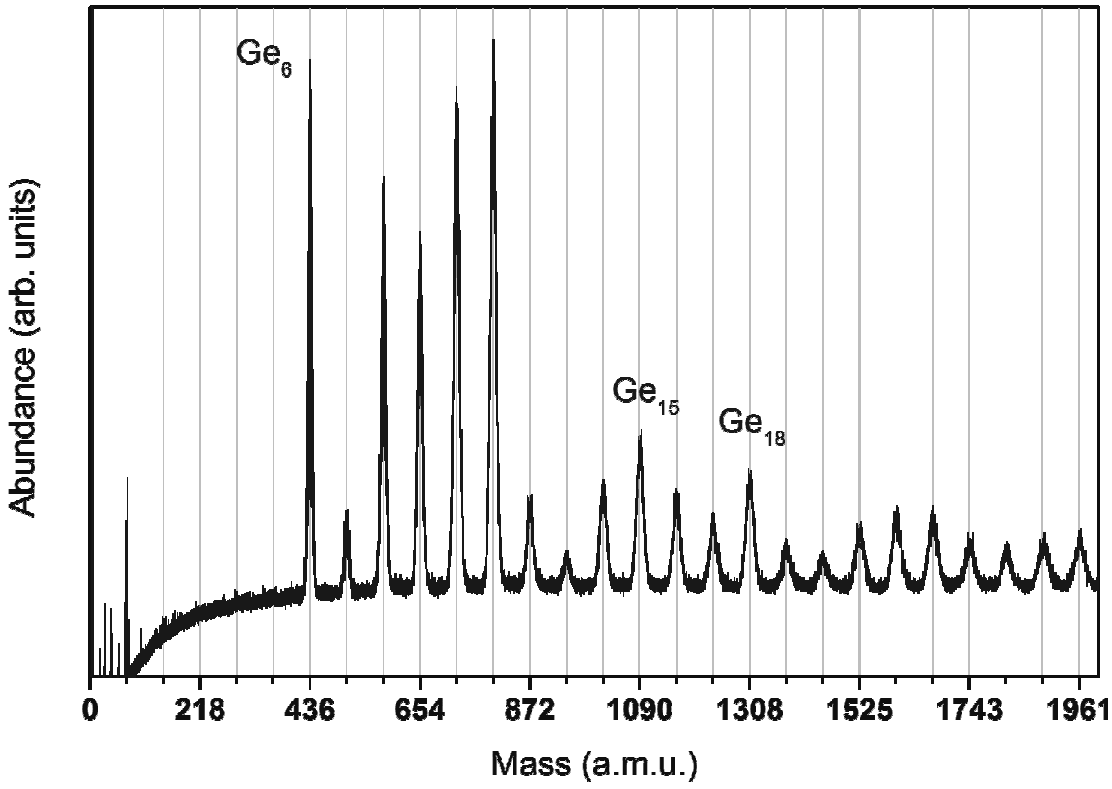

Figure 5-12: Mass abundance spectrum of bare Ge_n clusters after laser photoionization with 7.89 eV photons from an F_2 excimer laser with an energy density of only 100 µJ/cm². The clusters are produced in a source at a temperature of 90 K.

Figure 5-13 gives an example of photoionization spectra of neutral Ge_nLi_m (n = 5-12) clusters after laser ionization. The upper spectrum is taken with 6.42eV photons from an ArF laser, at an energy density of about 200 µJ/cm². The spectra are dominated by broad shapes, consisting of multiple peaks which reflect the coexistence of Ge_n clusters doped with different amounts m of lithium atoms. The bars indicate the relative intensities of the different stoichiometries (n,m) derived after deconvolution. The preferred amount of lithium dopants seems to be strongly size dependant. Species like Ge_6Li_2, Ge_7Li_1 and $Ge_{10}Li_1$ seem to be more abundant than others. These maxima however do not necessary reflect the actual abundances of the Ge_nLi_m clusters produced in the source, because ionization efficiencies can vary among different stoichiometries. It is known that bare Ge_n clusters with n<18 cannot efficiently be ionized by 6.42 eV photons. We can expect the same thing to happen to certain lithium doped species in this size range as well. This is indeed confirmed by the Ge_nLi_m mass spectrum taken at a photon energy of 7.89 eV (Figure 5-13 b): bare as well as singly and doubly doped species gain in intensity and new maxima appear in the spectrum: all doubly doped species are now relatively high in intensity. At this energy the ionization efficiency of certain species is still reduced. Judged on the results of Yoshida and coworkers the abundance of bare Ge_7 is strongly underestimated and could well be double the abundance of bare Ge_6. These mass spectra underline the importance of photoionization efficiencies in the analysis of silicon and germanium mass spectra and allow for bracketing of the ionization energies outside the range of our measured PIE curves.

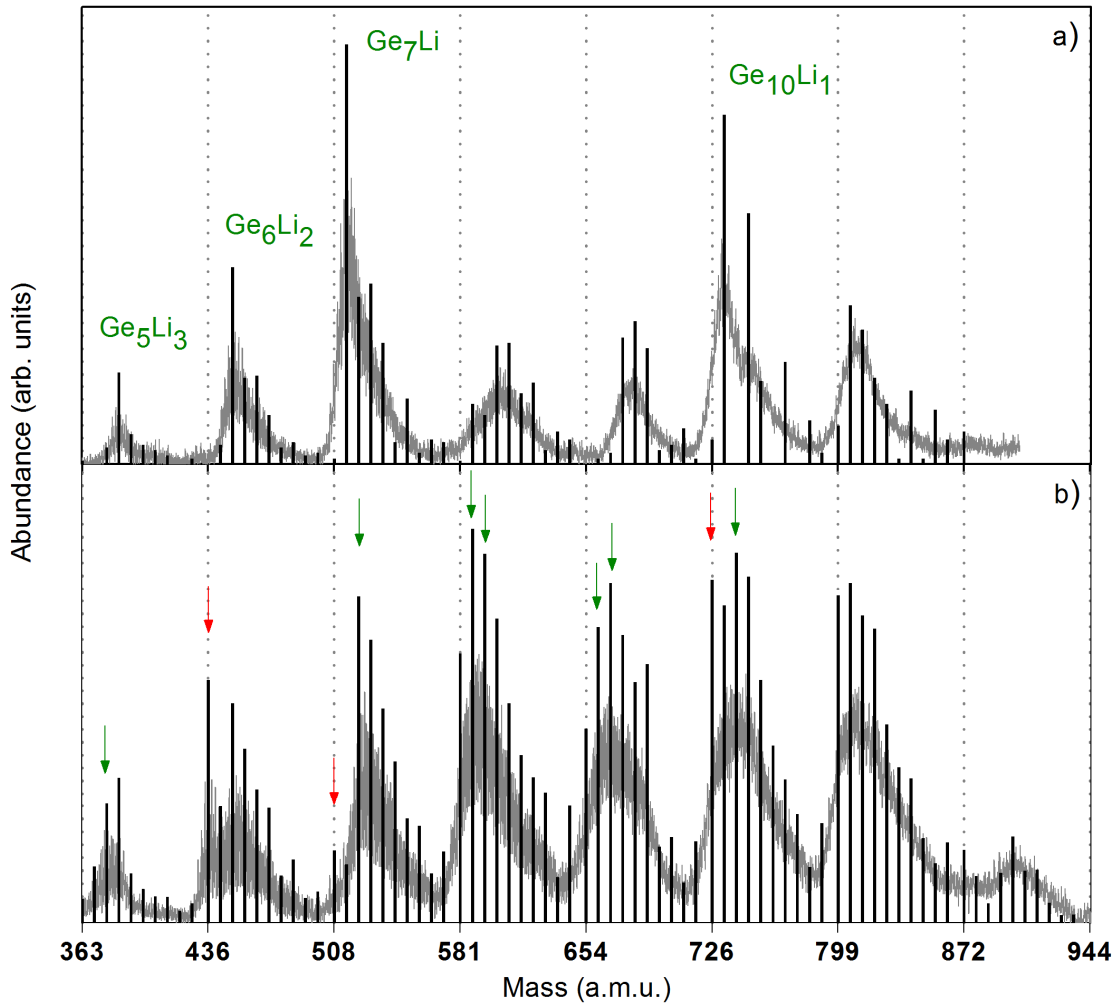

Figure 5-13: (a) Typical photoionization spectra of neutral Ge_nLi_m clusters after laser ionization with 6.42 eV photons from an ArF excimer laser with an energy density of ~200 µJ/cm². The clusters are produced in a source at room temperature. The blue spectrum is taken with a higher lithium content compared to the red spectrum. (b) Typical photoionization spectrum of neutral Ge_nLi_m clusters after laser ionization with 7.89 eV photons from an F_2 excimer laser and an energy density of 230 µJ/cm². The clusters are produced in a source at a temperature of 85 K. The (green) bars in the background indicate the relative intensities of the different stoichiometries (*n,m*) after deconvolution.

Remarkable is the disappearance of the highly abundant Ge_7Li_1 from ionization with 6.24 eV photons to 7.89 eV photons. A possible explanation is that the incident photon ionizes an electron from a lower lying energy level. A 7.89 eV photon is able to excite an electron from the SOMO-1. If this orbital has a strong bonding character, the lithium cation will no longer make a chemical bond with the cluster. It is also possible that after ionization, the electron in the SOMO will fall back to the now empty SOMO-1. Due to the large gap between these orbitals and the very small dissociation energy of the lithium atom, the lithium bond might break. In both cases, the result is a neutral Ge_7 cluster, which is not detected anymore. This effect might also be present for $Ge_{10}Li_1$.

Photoionization efficiency curves

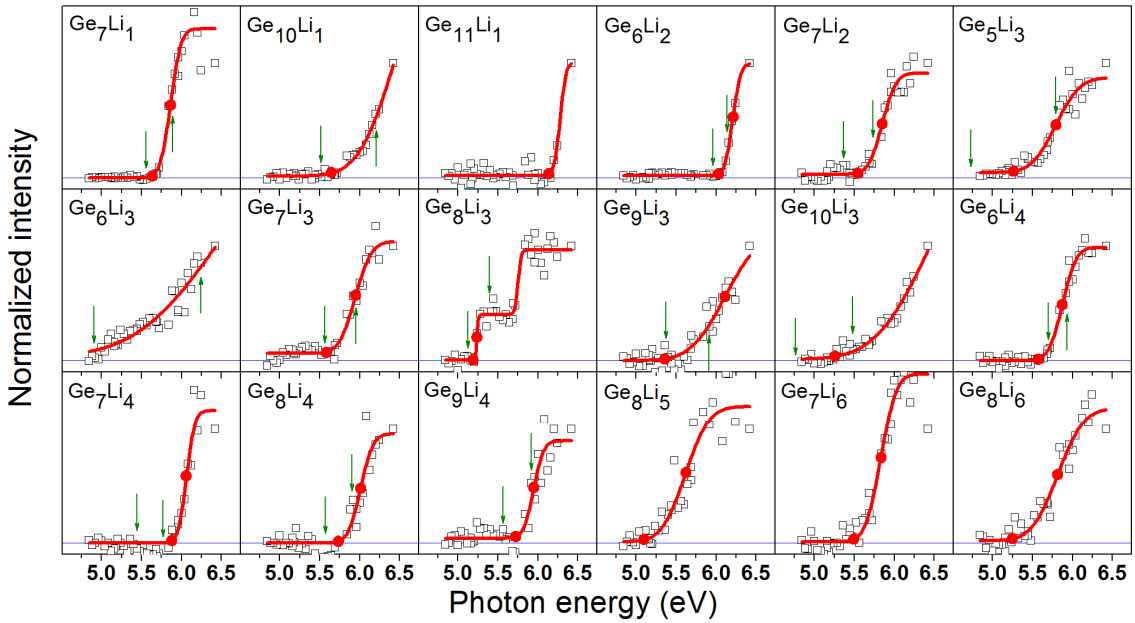

Figure 5-14: PIE curves of the Ge_nLi_m clusters ($n \leq 11$, $m \leq 6$), whit an AIE below 6.25 eV. The open squares represent the experimental data, while the solid (red) lines represent smeared out step functions fitted to the data. The experimental VIE and the ionization threshold are both indicated by a (red) dot. The positions of the calculated VIE and AIE are indicated by (green) arrows.

Figure 5-14 shows photoionization efficiency (PIE) curves of the Ge_nLi_m clusters. The open squares represent the experimental data, while the solid (red) lines are the smeared out step functions fitted to the data. The scatter at the baseline is mainly due to the low signal to noise ratio. A steep slope of the PIE curve indicates that the geometry of the neutral and the cationic cluster is similar and thus little geometric relaxation takes place following ionization. The experimental VIE and the ionization threshold are both indicated in the figures with a (red) dot. The ionization threshold is an upper value for the calculated value of the AIE. The positions of the calculated VIEs and AIEs are indicated by (green) arrows. The AIEs shown are from the neutral to the relaxed corresponding cation. Without saturation in the PIE curve the fitting is liable to large deviations and in certain cases (Ge_6Li_3, Ge_8Li_5) there is no value assigned to the VIE. As observed in earlier IE measurements a single photoionization curve cannot always be described by a single step function, and multiple steps or slopes might be present. This is clearly the case for Ge_8Li_3.

Quantum chemical computations are carried out using the Gaussian 03[219] and Molpro 06[220] suites of programs. Geometries and harmonic vibrational frequencies of the lower-lying isomers are determined with the hybrid B3LYP functional, which involves the Becke three-parameter exchange[221] and the Lee–Yang–Parr correlation[204] functional. The search for all possible low-lying isomers of Ge_nLi_m (n = 5–10; m = 1–4) is performed using a stochastic search algorithm which is recently developed.[222] An overview of the lowest isomers can be found in appendix A.4. The error for the experimental data is the standard error on the fitted data. If significant traces of species are found in the mass abundance spectra taken with 6.42 eV ionization photons, but no VIE could be derived, this is indicated by < 6.42 eV for the ionization threshold.

Table 5-2: Overview of the experimental VIEs and AIEs obtained from fitting the photoionization efficiency curves with a smeared out step function and calculated VIEs and AIEs, obtained at B3LYP/6-311+G(d) level of theory for Ge_nLi_m clusters. A star (*) indicates agreement with an isomer above the calculated ground state.

Cluster	Ionization threshold (eV)	AIE-Th. (eV)	VIE-Exp. (eV)	VIE-Th. (eV)
Ge_7Li_1	5.63 (0.08)	5.57	5.86 (0.02)	5.89
$Ge_{10}Li_1$	5.65 (0.24)	5.52	> 6.05	6.20
$Ge_{11}Li_1$	6.14 (0.12)		6.28 (0.03)	
Ge_6Li_2	6.03 (0.02)	5.96	6.21 (0.00)	6.14
Ge_7Li_2	5.54 (0.08)	5.36*	5.85 (0.02)	5.74*
Ge_5Li_3	5.26 (0.14)	4.74	5.79 (0.03)	5.80
Ge_6Li_3	< 5.5	4.77x		6.24
Ge_7Li_3	5.59 (0.08)	5.56*	5.94 (0.02)	5.94*
Ge_8Li_3	5.20 (0.21)	5.12	5.24 (0.02)	5.40
Ge_9Li_3	5.36 (0.36)	5.37	6.11 (0.12)	5.92
$Ge_{10}Li_3$	5.25 (0.61)	4.85	> 5.5	5.45
Ge_5Li_4	4.98 (0.14)	5.00	5.12 (0.03)	5.19
Ge_6Li_4	5.57 (0.05)	5.71	5.87 (0.01)	5.93
Ge_7Li_4	5.88 (0.06)	5.45	6.06 (0.01)	5.77
Ge_8Li_4	5.73 (0.12)	5.58	6.01 (0.03)	5.90
Ge_9Li_4	5.72 (0.11)	5.55*	5.95 (0.02)	5.87*
$Ge_{10}Li_4$	< 6.42	5.01		5.39
Ge_8Li_5	5.10 (0.38)		5.62 (0.07)	
Ge_7Li_6	5.49 (0.12)		5.83 (0.03)	
Ge_8Li_6	5.24 (0.15)		5.82 (0.03)	

For the singly doped silicon clusters, only three species (Ge_7Li, $Ge_{10}Li$, and $Ge_{11}Li$) have a VIE low enough to be measured in our 4.68 to 6.42 eV energy window. From Figure 5-13 it is clear that Ge_8Li and $Ge_{11}Li$ have an AIE lower than 6.42 eV while all others are below 7.89 eV. While the neutral and cation ground state are the same for Ge_7Li, there is a small change in the position of the lithium atom in the case of $Ge_{10}Li$. This explains the steeper step function for Ge_7Li compared to $Ge_{10}Li$. Both Ge_7Li and $Ge_{10}Li$ have the same geometric but also the same electronic core as their undoped counterparts. Analysis of the density of states (DOS) shows that the additional electron due to the lithium dopant is located in a high energetic SOMO. This suggests that the neutral structure of Ge_7 and Ge_{10} is already electronically stable, giving rise to the very low VIE for these lithium doped species.

Of the doubly doped silicon clusters, only for Ge_6Li_2 and Ge_7Li_2 the VIE could be derived. From Figure 5-13 it is clear that Ge_8Li_2 and $Ge_{11}Li_2$ have an AIE lower than 6.42 eV while all others are below 7.89 eV. Ge_6Li_2 is geometrically similar to Ge_7Li and also shows a steep slope in the PIE cure. However, the electronic structure is completely different, as Ge_6Li_2 is a closed shell structure. For Ge_7Li_2 the lowest isomer has an AIE of 6.19 eV and a VIE of 6.50 eV. This doesn't explain the shape of the experimental PIE curve. The lithiated pentagonal bipyramid only 0.05 eV higher than the ground state, however, matches the experimental result much better.

With the exception of Ge_7Li_3 and Ge_8Li_3 all triply doped species show a shallow step function suggesting a considerable change in geometry between the neutral and cationic ground state. For Ge_5Li_3 this can be confirmed from the structures in appendix A.4. For

Ge_6Li_3 the match doesn't look good, because the AIE is clearly higher than the ionization threshold. However, the neutral structure is not the ground state on the cation PES and a vibrationally excited state of the neutral might very well reach a cationic structure which is lower in energy. This would result in a longer tail in the PIE curve, going as low as 4.90 eV taking into account the current cation ground state. For Ge_7Li_3 there is a good agreement with the second lowest isomer (0.05 eV), while the odd looking ground state is excluded as both its VIE and AIE are below 5.5 eV. The PIE curve of Ge_8Li_3 clearly shows two steps. The same strong feature was observed for Si_8Li_3 and will be discussed in section 5.2.4. Ge_8Li_3 has a steeper PIE curve than the other triply doped species. There is no match between experiment and calculations for $Ge_{10}Li_3$ and the isomer that was found by DFT calculation, is probably not the global minimum, unless a small step is involved as in the case of $Si_{10}Li_3$.

All Ge_nLi_4 (n = 5-9) species have relatively high VIE and show a sharp step function. The ground state structures of Ge_5Li_4 and Ge_6Li_4 are well confirmed by the experiment and both have indeed similar structures for the neutral and the cationic ground state. This is not the case for Ge_7Li_4, and the ground state has probably not been found here. For Ge_8Li_4 again there is better agreement, while the agreement for Ge_9Li_4 is very good with the second lowest isomer (0.03 eV), but the calculated ground state cannot be excluded either. Both isomers have the same symmetric capped square antiprism germanium core.

In all cases, except for $Si_{10}Li_3$ and $Ge_7Li_{2\text{-}4}$ there is reasonable agreement between the experimental values and the results for the calculated ground states presented in Appendix A.4.

5.2.4 Discussion

Post-threshold features

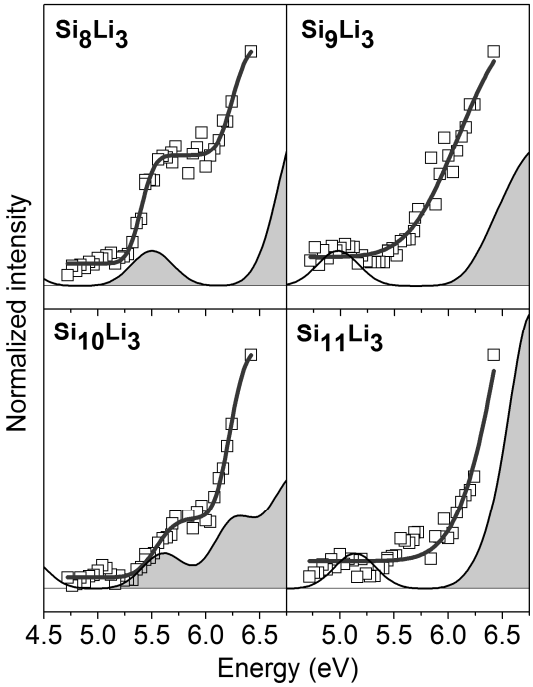

Figure 5-15: Photoionization efficiency (PIE) curves and density of states (DOS) for selected Si_nLi_3 clusters. The open squares correspond to the averaged experimental data. The solid lines represent smeared out step functions fitted to the data. The solid lines represent the computed DOS, the filled DOS is shaded. The energy axis of the DOS is reversed to match the PIE curve.

Several PIE curves show post threshold features as was observed before for carbon doped lithium clusters and small silicon clusters.[223,93] These features are more distinct at lower temperature, suggesting that they are related to electronic properties. Kostko and coworkers suggested before that these features resemble the structure that might result from the production of higher lying electronic states of the cations.[93] These steps might also be directly related to the electronic states of the neutral cluster. Figure 5-15 shows the total DOS around the singly (highest) occupied molecular orbital (SOMO) in the case of Si_nLi_3 (n = 8-11). The energy scale is reversed to match the PIE curve, which means that the orbitals at the left side of the SOMO are the unoccupied orbitals in this graph. For each of the four systems it is clear that the SOMO matches the first step in the PIE curve, while the next orbital matches the position of a higher step. For Si_8Li_3, the distance between the SOMO and the next filled orbital is relatively large, and the same is true for the distance between the steps. For Si_9Li_3 and $Si_{11}Li_3$ the distance between the SOMO and the next filled orbital is rather small, and one single step appears in the PIE curve. $Si_{10}Li_3$ shows an intermediate situation.

When a photon interacts with a cluster, depending on its energy it can ionize or excite electrons from a range of different energy levels. The excess energy can be carried away by the electron as kinetic energy or being dissipated into vibrational energy inside the cluster. In photoelectron spectroscopy photons with a fixed energy are used to ionize electrons from a cluster. While many electrons take away the excess energy in the form of kinetic energy, there is a large background of electrons at very low energy: photons will ionize clusters with increased oscillator strength for photon energies that match electronic levels. A similar feature we spot here: upon changing the photon energy in our experiment, photons preferentially ionize different energy levels of the DOS whenever their energy matches a given electronic level.

Size dependence

Figure 5-16 gives an overview of the AIEs and VIEs of Si_nLi_m clusters (n = 5-11, m = 0-4) against the number of silicon atoms in the cluster. The calculated IE is shown with empty symbols, while the experimental values are shown in full symbols. As mentioned before, there is good agreement between experimental values and theoretical values. There is also a strong similarity between the ionization efficiency of silicon and germanium clusters. The lithium doping effectively decreases the VIE of the bare silicon clusters, though the amount of decrease of the VIE with increasing lithium content shows different patterns at different sizes. A similar result was obtained in the case of sodium doped silicon clusters Si_nNa_m (n = 1-14, m = 1-5) by Kishi and coworkers[156] Lithium, just like sodium, acts like a strong electron donor. Subsequent addition of lithium atoms equals the addition of excess electrons to both the electronic and geometric framework of the bare silicon clusters and gives information on the character of their electron-accepting orbitals. Values of the IE of systems with an even number of electrons often exceed or equal the value of the IE of systems with one lithium dopant less.

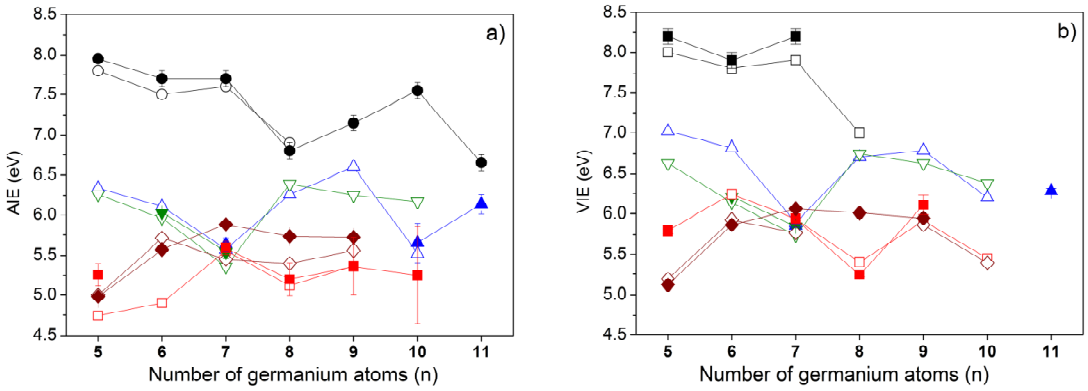

Figure 5-16: (a) Overview of the ionization treshold (full symbols) and the calculated AIE (empty symbols) for: Ge_n (●), Ge_nLi_1 (▲),Ge_nLi_2 (▼),Ge_nLi_3 (■),Ge_nLi_4 (◆). (b) Overview of the experimental VIE (full symbols) and the calculated VIE (empty symbols) for: Ge_n (●), Ge_nLi_1 (▲),Ge_nLi_2 (▼),Ge_nLi_3 (■),Ge_nLi_4 (◆). Data on bare Ge_n clusters is taken from Fuke and coworkers (1999).[101,102]

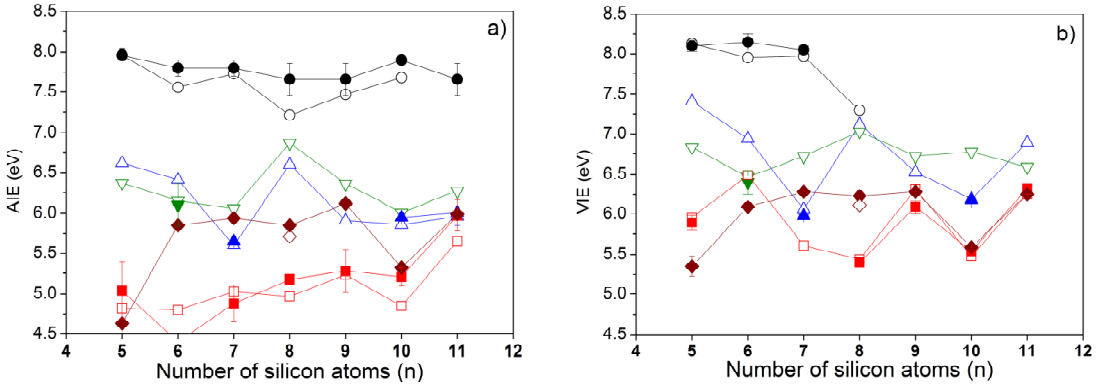

Figure 5-17: (a) Overview of the ionization treshold (full symbols) and the calculated AIE (empty symbols) for: Si_n (●), Si_nLi_1 (▲),Si_nLi_2 (▼),Si_nLi_3 (■),Si_nLi_4 (◆). (b) Overview of the experimental VIE (full symbols) and the calculated VIE (empty symbols) for: Si_n (●), Si_nLi_1 (▲),Si_nLi_2 (▼),Si_nLi_3 (■),Si_nLi_4 (◆). Data on bare Si_n clusters is taken from Fuke and coworkers (1993), Kostko and coworkers (2010) and Zhao and coworkers (1995).[87,93,95]

5.3 Photofragmentation of lithium doped silicon and germanium clusters

When clusters interact with low fluence laser light, a fraction of them will be ionized when the adiabatic ionization energy is lower than the photon energy. At higher laser power dissociation can take place: clusters are heated by multiphoton absorption and cooling occurs through fast sequential evaporation of atoms and larger fragments. Only the fragments that are positively charged will be detected in the time-of-flight mass spectrometer. In general the electron affinity of a cluster drops towards larger sizes and only the largest fragment will remain as a cation. Although the fragments that dissociate might show an enhanced stability, for example Si_7 (Ge_7) and Si_{10} (Ge_{10}), they cannot be detected in our mass spectrum. Unfortunately, the lithium cation has a low electron affinity and upon dissociation the remaining cluster will be left in a neutral state. Only systems with a binding energy high enough to resist lithium dissociation are detected in our mass spectrum. They can still be fragments though from a larger cluster that lost germanium monomers or smaller fragments. Anyhow, the maxima that appear in the mass abundance correspond to cationic species with an enhanced stability. While ionization of clusters gives information on neutral clusters, photofragmentation rather gives information on cations.

5.3.1 Photofragmentation of lithium doped germanium clusters

Bare germanium clusters

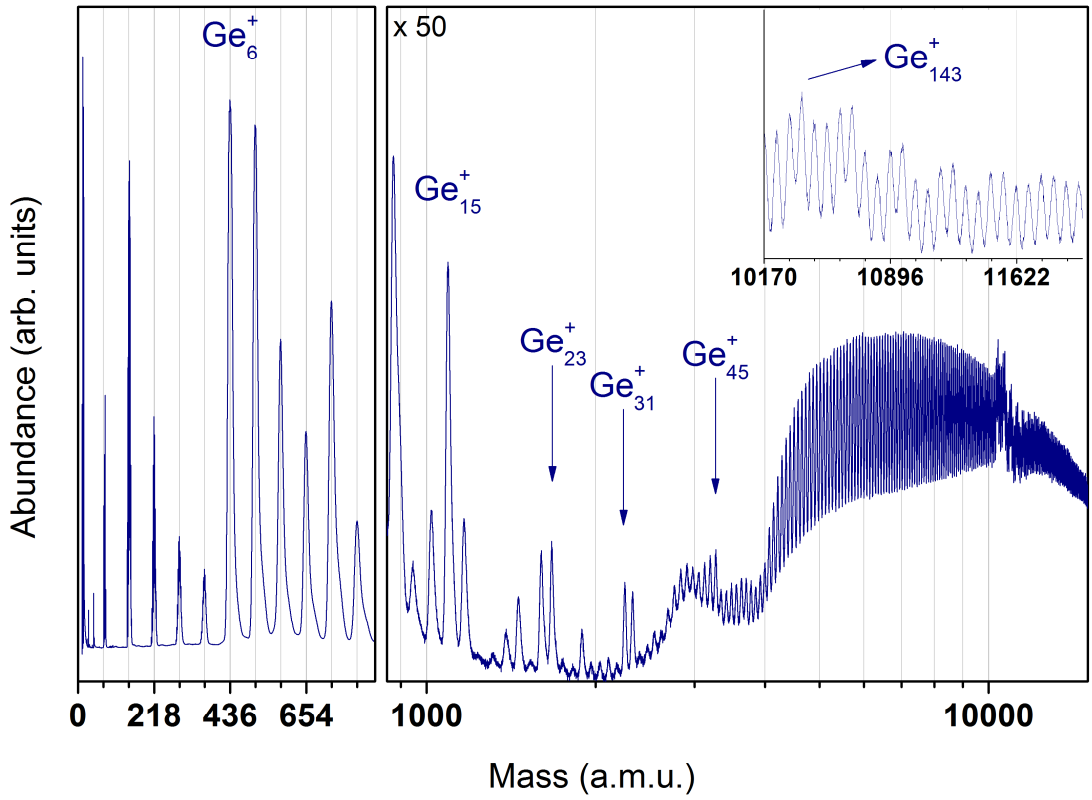

Figure 5-18: Mass abundance spectrum of Ge_n^+ cations after modest laser fragmentation with 6.42 eV photons from an ArF excimer laser and an energy density of 1500 µJ/cm². The clusters are produced in a source at room temperature. From Ge_{12}^+ on the horizontal axis is in logscale and the vertical axis is amplified 50 times. Inset: The region after Ge_{140}^+ shows a sudden size dependant variation.

Figure 5-18 shows a typical mass abundance spectrum of bare Ge_n^+ cations after modest laser fragmentation with 6.42 eV photons from an ArF excimer laser and an energy density of 1500 µJ/cm². The clusters are produced in a source at room temperature. The species up to size 21 all have high VIEs and the peaks in the spectrum can therefore be attributed to fragments. Local maxima in abundance appear for sizes 2, 6, 10, 15, 18, 23, 26, 31, and 45. Some global features appear as well: the spectrum gradually lowers in abundance beyond size 6-7, picks up again around size 31 and again after size 53. This last feature is very strong and size independent and might be related to the oblate to spherical tranisition of the germanium clusters. Surprisingly, at Ge_{142}^+ a new feature appears: it can best be described as a series of consecutive pairs of higher and lower abundance.

Lithium doped germanium clusters

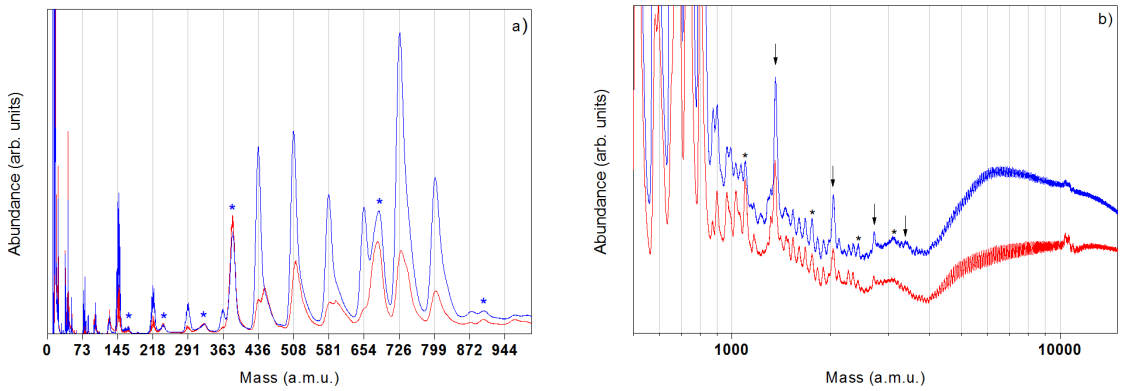

Figure 5-19: Mass abundance spectra of $Ge_nLi_m^+$ cations after modest laser fragmentation with 6.42 eV photons from an ArF excimer laser. The clusters are produced in a source at room temperature. The red spectrum is recorded with an energy density of ~1000 µJ/cm², while the blue spectrum is recorded with a higher energy density of ~2700 µJ/cm². (a) Lower mass side of the mass spectrum. Stars (*) indicate lithium doped species that survive at the higher energy density. (b) Higher mass side of the mass spectrum (in log scale). The series $Ge_{9x}Li_m^+$ is indicated by an arrow and the series $Ge_{9x+6}Li_m^+$ is indicated by a star (*).

Figure 5-19 shows a typical mass abundance spectrum of $Ge_nLi_m^+$ cations after laser fragmentation with 6.42 eV photons from an ArF excimer laser. The clusters are produced in a source at room temperature. The red spectrum is recorded with an energy density of ~1000 µJ/cm², while the blue spectrum is recorded with a higher energy density of ~2700 µJ/cm². For the smallest sizes stable stoichiometries appear for $Ge_2Li_3^+$, $Ge_3Li_3^+$, $Ge_4Li_5^+$: for all these sizes an increase of the bare germanium cluster is apparent, but not at the cost of the doped peak. This might suggest that these species are stable cations, but do not appear as fragments. For the medium size species, maxima appear which are reminiscent of the neutral case for lower fluences, but at ~2700 µJ/cm² most of the doped species have almost disappeared and the bare clusters become far more prominent. Two striking exceptions are $Ge_5Li_3^+$ and $Ge_9Li_5^+$, reflecting an enhanced stability for these stoichiometries. Going to larger sizes we see more doped species surviving at higher laser fluence. Clear examples are $Ge_{12}Li_4^+$, $Ge_{13}Li_{3/7}^+$, $Ge_{14}Li_7^+$, Two series emerge among the larger clusters: $Ge_{9x}Li_m^+$ and to a lesser extend $Ge_{9x+6}Li_m^+$. Similar features for neutral clusters were previously investigated by mass spectrometry and DFT calculations.[4] A new pattern arises around 4000 a.m.u. (56 germanium atoms) with a sudden increase in abundance and the absence of any size dependence. Some surprising features appear around 10000 a.m.u. where Ge_n^+ (n=142, 143, 146, 147 …) stick out. This is identical to the bare germanium spectrum.

To make sure the features discussed above are not due to ionization energies, we also collected a mass spectrum with 7.89 eV photons. Figure 5-20 shows a typical mass abundance spectrum of $Ge_nLi_m^+$ cations after modest laser fragmentation with 7.89 eV photons from an F_2 excimer laser and an energy density of 1670 µJ/cm². The clusters are produced in a source at a temperature of 85 K. The lithium amount in this spectrum is lower compared to the two spectra above allowing deconvolution of the spectra. The result is shown in Figure 5-20 (a): the bars indicate the relative intensities of the individual stoichiometries (*n,m*). The conclusions remain the same as for the ArF excimer laser above: for the smallest sizes the same stoichiometries $Ge_2Li_3^+$, $Ge_3Li_3^+$, and $Ge_4Li_5^+$ appear. Also in this case two peaks clearly identified as $Ge_5Li_3^+$ and $Ge_9Li_5^+$ stick out. For the other medium size species, maxima are not very distinct and slightly depend on the lithium amount and laser fluence as well as on the ionization energies. The

two series, apparent in Figure 5-19 and best described as $Ge_{9x}Li_m^+$ and $Ge_{9x+6}Li_m^+$ are also present in this spectrum, but less pronounced due to the lower lithium amount. Larger sized clusters where not recorded in this spectrum.

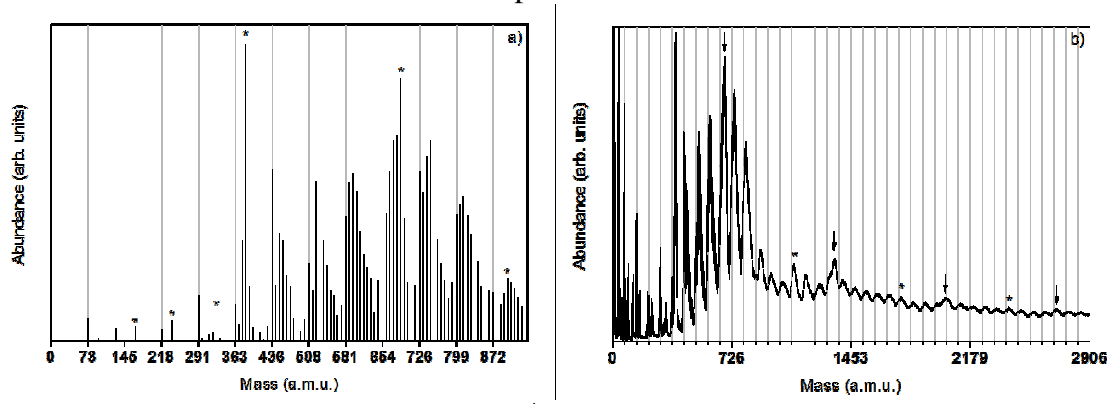

Figure 5-20: Mass abundance spectrum of $Ge_nLi_m^+$ cations after modest laser fragmentation with 7.89 eV photons from an F_2 excimer laser and an energy density of 1670 µJ/cm². The clusters are produced in a source at a temperature of 85 K. (a) Lower mass side of the mass spectum. The bars indicate the relative intensities of the different stoichiometries (*n,m*) after deconvolution. Stars (*) indicate the same sizes as in Figure 5-19 (a). (b) Higher mass side of the mass spectrum. The series $Ge_{9x}Li_m^+$ is indicated by an arrow and the series $Ge_{9x+6}Li_m^+$ is indicated by a star (*).

5.3.2 Photofragmentation of silicon clusters

Bare silicon clusters

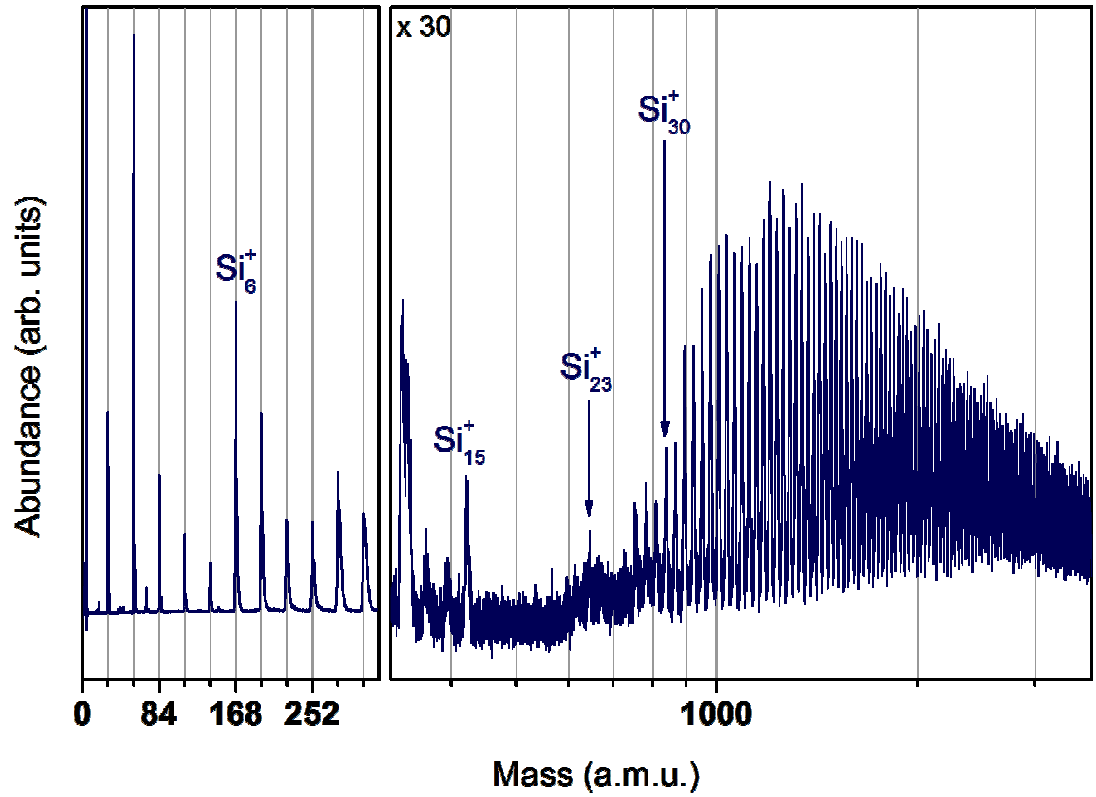

Figure 5-21: Mass abundance spectrum of bare Si_n^+ cations after modest laser fragmentation with 6.42 eV photons from an ArF excimer laser and an energy density of 8100 µJ/cm². The clusters are produced in a source at room temperature. From Ge_{12}^+ on the horizontal axis is in logscale and the vertical axis is amplified 30 times.

Figure 5-21 shows a typical mass abundance spectrum of bare Si_n^+ cations after substantial laser fragmentation with 6.42 eV photons from an ArF excimer laser and an energy density of 8100 µJ/cm². The clusters are produced in a source at room temperature. The species up to size 21 all have high VIEs and the peaks in the spectrum can therefore be attributed to fragments. Local maxima in abundance appear for sizes 2, 6, 10, 15, and 23. This result is similar to the germanium case. Also in the case of silicon a similar global feature appears: the spectrum gradually lowers in abundance beyond size 6 but picks up again around size 27. As for germanium, this number matches the predictions for the oblate to spherical transitions in silicon clusters.

Photofragmentation of lithium doped silicon clusters

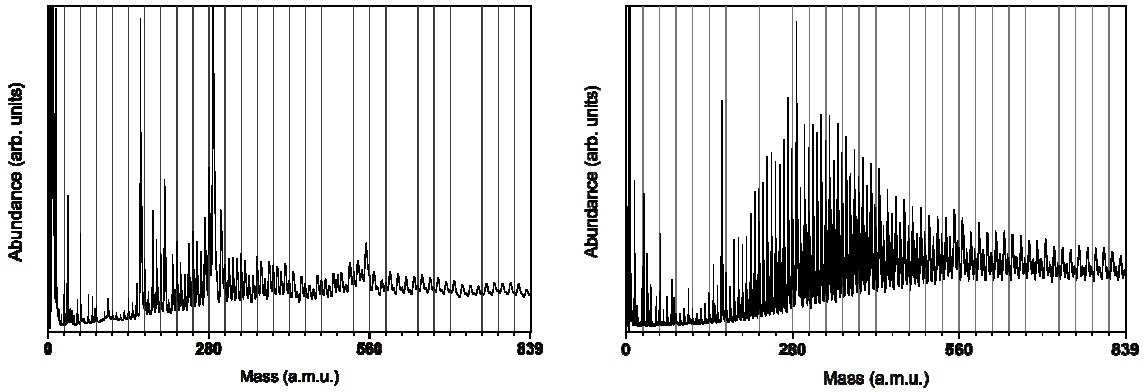

Figure 5-22: (a) Mass abundance spectrum of $Si_nLi_m^+$ cations after modest laser fragmentation with 6.42 eV photons from an ArF excimer laser and an energy density of ~1500 µJ/cm². The clusters are produced in a source at room temperature. (b) Mass abundance spectrum of $Si_nLi_m^+$ cations after modest laser fragmentation with 7.9 eV photons from an F_2 excimer laser and an energy density of 1670 µJ/cm². The clusters are produced in a source at a temperature of 85 K.

Figure 5-22 (a) shows a typical mass abundance spectrum of $Si_nLi_m^+$ cations after laser fragmentation with 6.42 eV photons from an ArF excimer laser. The clusters are produced at room temperature. The spectrum is recorded with an energy density of ~1500 µJ/cm². Figure 5-22 (b) shows a typical mass abundance spectrum of $Si_nLi_m^+$ cations after laser fragmentation with 7.89 eV photons from an F_2 excimer laser. The clusters are produced in a source near liquid nitrogen temperature. The spectrum is recorded with an energy density of 1670 µJ/cm² and higher lithium concentration than the other one. For both spectra, two large peaks dominate the spectrum: they correspond to $Si_5Li_3^+$, $Si_9Li_5^+$. Although having the same mass, the peak of $Si_9Li_5^+$ can very well be distinguished from $Si_{10}Li_1^+$ due to the difference in isotope pattern. Overall, the results are very similar to the germanium case: for the smallest sizes the same stoichiometries appear as for germanium: $Si_2Li_3^+$, $Si_3Li_3^+$ and $Si_4Li_5^+$. The two series at higher sizes corresponding to $Si_{9x}Li_m^+$ and $Si_{9x+6}Li_m^+$ are restricted to the first one or two members. The silicon spectra reveal a profound odd-even staggering, most clearly at higher sizes, with odd numbers of lithium dopants more abundant than even numbers of lithium dopants. Even numbers of lithium atoms do not survive as cations and are preferentially dissociated. Overall, the results are very similar to the germanium case.

6 A shell model for silicon and germanium clusters

This chapter is the final chapter of part II and provides deeper insight in the stability patterns for bare and doped silicon and germanium clusters. It starts with a short overview of existing models that help understand stability features. After identifying the most stable systems based on experimental evidence and theoretical predictions, we investigate their density of states more closely. This is concluded in a proposed model explaining the structure and charge state of these systems.

The stability of a cluster is a close interplay between its geometric and electronic structure. This makes sense, because the total energy of a system is determined by the energy levels of the electrons in a given potential determined by the ionic cores of the atoms. The geometric structure can be described by the coordinates of all atoms, while the electronic structure can be represented by molecular orbitals and the density of states (DOS). The DOS shows clear shell features, this means a bunching of energy levels, and systems that fill an electronic shell will be more stable than others. This is closely related to the octet rule for molecules, where atoms tend to completely fill their outer shell with electron pairs from chemical bonds or with lone pairs to attain the same electronic configuration as their reference noble gas element. The stability model for clusters depends on the number and type of delocalized electrons. For noble gas clusters, the electronic interaction between the different atoms is very limited and the stability of the clusters is determined by close packing and filling of atomic shells. On the other hand, there is strong delocalization of valence electrons in the case of simple metal clusters, especially alkali metals but also coinage metals and some di- and trivalent elements. Here the geometric structure seems to play a minor role and stability features can mainly be explained on the basis of an electron gas in a (near) spherical potential and its rigid set of shell closings.

For silicon and germanium clusters, containing both s and p type electrons, the stability features are not well understood. While the stability of certain species can be understood on the basis of electronic shell closings there is also the appearance of stable geometric motifs. We will show that the energy splitting between the s and the p type electrons is vital in understanding the stability of silicon and germanium clusters. Using concepts of molecular orbital theory and crystal field splitting we will show that the number of valence s electrons determines the ionic symmetry and the optimal charge state to fill the according closed electronic shells.

6.1 Shell models for metal clusters

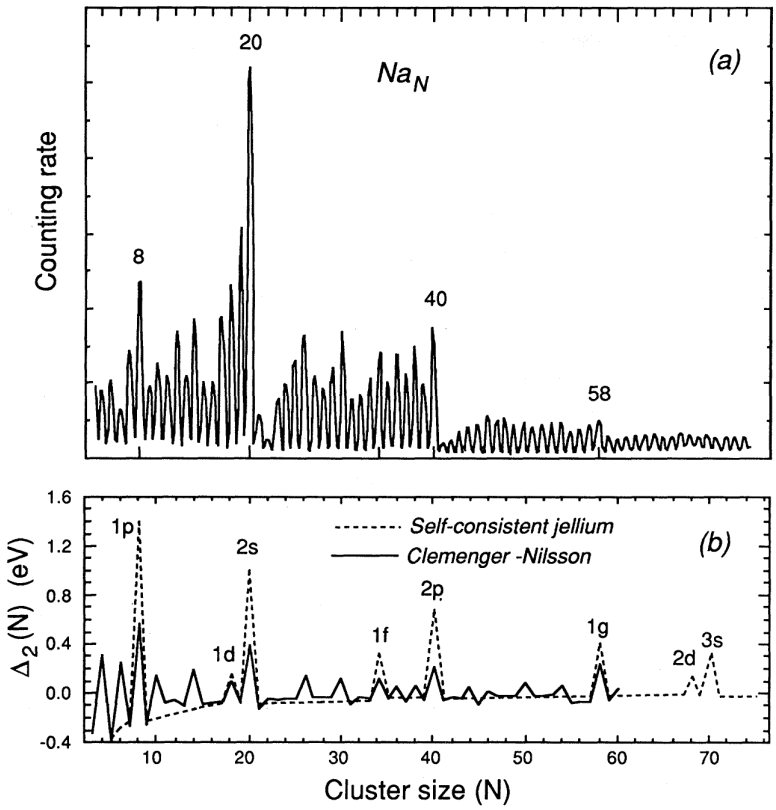

Figure 6-1: Sodium cluster abundance spectrum: (a) experimental (b) dashed line, using Woods-Saxon potential; solid line, using the ellipsoidal shell model. [(a) from W.D. Knight and coworkers (1984)[225]; (b) from W. de Heer (1993)[224]]

Electronic shell structure is clearly observed in many simple and coinage-metal cluster systems. The famous mass abundance spectrum in Figure 6-1 (a) suggests that to lowest order the valence electrons in sodium are confined in a spherically symmetric potential.[224,225] Such a potential automatically gives rise to spherical shell structure because of its symmetry, where the valence electrons successively fill the degenerate levels. As for atoms, the electronic system of the cluster with exactly the right number of electrons to complete a shell is very stable. When one more atom is added to the cluster, its valence electron will occupy a state with considerably higher energy, and hence the stability of the cluster is reduced. The reduced stability is reflected in a reduced abundance, explaining the large abundance drops after each shell-closing number in Figure 6-1 (a). Both the jellium model and the phenomenological shell model results in the same progression of electronic levels and closed shells $1S^2/1P^6/1D^{10}/2S^2/1F^{14}/2P^6/1G^{18}/2D^{10}/3S^2/\ldots$ corresponding to the so-called magic numbers 2, 8, 18, 20, 34, 40, 58 …

Approximating small clusters with spheres can only be justified for closed shell structures. From the Jahn-Teller theorem it follows that open-shell clusters must distort. As demonstrated by Clemenger the fine structure in Figure 6-1 (b) is a manifestation of these distortions.[226] Clemenger introduced a deformable potential well that is particularly well suited to account for this effect. In fact he simply adapted the well-known Nilsson model extensively used to estimate the shapes of atomic nuclei.[227] As in the spherical shell model, the ellipsoidal Clemenger-Nilsson model predicts enhanced stabilities for closed-shell clusters. However, in addition, the spheroidal distortions cause subshell

closings which are also seen in the spectra. The electronic shell structure of sodium cluster, both in cationic and anionic states has been directly observed by photoelectron spectroscopy (PES).[228,229] Shell closings and openings of additional shells can be clearly seen up to cluster sizes containing 200 atoms: the overall agreement with the shell model is excellent.

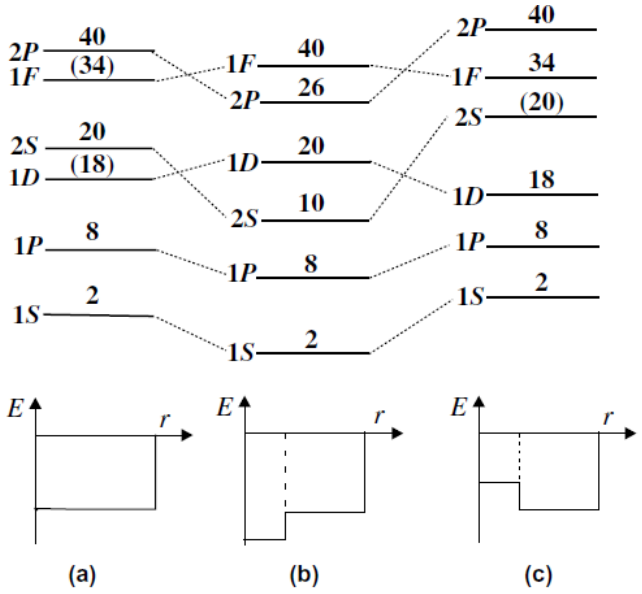

Figure 6-2: Schematic representation of the single particle energy levels in the standard jellium model (a) and in the two-step jellium model with a depression (b) and an increase (c) in the central part of the background potential. Note the lowering of the 2S and the 2P levels in (b) causing the magic numbers 10 and 26, and the lifting of the 2S level in (c) enhancing the magic number 18. [from E. Janssens and coworkers (2004)[230]]

A two-step spherical jellium model was introduced to deal with doped simple and coinage metal clusters.[230] Host and impurity atoms are characterized by a different but uniform positively charged background. Two situations can be distinguished. If the central heteroatom is more electronegative than the host atoms, the effective potential is more attractive at the center of the cluster. Orbitals that have (most of) their density in the center (i.e., S, and to a lesser extent P levels) will energetically be favored, while orbitals that have several nodal planes crossing the origin (D and F levels) remain relatively unaffected. The level sequence becomes $1S^2/1P^6/2S^2/1D^{10}/2P^6/1F^{14}$... with corresponding magic numbers 2, 8, 10, 20, 26, 40... as is shown in Figure 6-2 (b). If the central heteroatom is less electronegative than the host atoms, it causes a hump in the center of the potential. This leads to an upward shift of the NS levels relative to the levels with non-zero angular momentum. Regardless of the exact shape of the potential this again will cause level shifts, e.g., enlarge the gap between the 1D and 2S levels, and decrease the spacing between the 2S and 1F levels. The magic number 20 disappears in favor of the magic number 18, resulting in a $1S^2/1P^6/1D^{10}/2S^21F^{14}/2P^6$... level sequence with magic numbers 2, 8, 18, 34, 40... as is shown in Figure 6-2 (c).

6.2 Chemical stability rules

The polyhedral skeletal electron pair theory provides simple electron counting rules used to predict the structure of electron deficient clusters. They were originally formulated by K. Wade and further developed by Mingos and others, and are sometimes known as Wade's Rules or Wade / Mingos rules.[231] The rules were originally developed to aid the prediction of the structures of borane and carborane cluster compounds and are based on

a molecular orbital treatment of the bonding. The rules only apply to clusters that have deltahedral geometry, as the boranes and carboranes. This method, if applicable to silicon and germanium clusters, has a low predictive value and a more elaborate approach is needed.

In chemistry, molecular orbital (MO) theory is a method for determining molecular structure in which electrons are not assigned to individual bonds between atoms, but are treated as moving under the influence of the nuclei in the whole molecule.[232] MO theory provides a global, delocalized perspective on chemical bonding. In MO theory, any electron in a molecule may be found anywhere in the molecule, since quantum conditions allow electrons to travel under the influence of an arbitrarily large number of nuclei, so long as permitted by certain quantum rules. Although in MO theory some molecular orbitals may hold electrons which are more localized between specific pairs of molecular atoms, other orbitals may hold electrons which are spread more uniformly over the molecule. Thus, overall, bonding (and electrons) are far more delocalized (spread out) in MO theory, than is implied in valence bond (VB) theory. This makes MO theory more useful for the description of extended systems like clusters.

In this theory, each molecule has a set of molecular orbitals, in which it is assumed that the molecular orbital wave function ψ_f may be written as a simple weighted sum of the n constituent atomic orbitals χ_i, according to the following equation:[233]

$$\psi_j = \sum_{i=1}^{n} c_{ij}\chi_i \tag{6.1}$$

The c_{ij} coefficients may be determined numerically by substitution of this equation into the Schrödinger equation and application of the variational principle. This method is called the linear combination of atomic orbitals (LCAO) approximation and is used in computational chemistry. Molecular orbitals are further divided according to the types of atomic orbitals combining to form a bond. In the case of clusters, the cluster orbitals (S, P, D, F …) are similar in shape to atomic orbitals (s, p, d, f …).

Chemical substances will form a bond if their orbitals become lower in energy when they interact with each other. Different chemical bonds are distinguished that differ by electron cloud shape and by energy levels. Molecular orbitals are often divided into bonding orbitals, anti-bonding orbitals, and non-bonding orbitals. A molecular orbital is merely a Schrödinger orbital which includes several, but often only two nuclei. If this orbital is of type in which the electron(s) in the orbital have a higher probability of being between nuclei than elsewhere, the orbital will be a bonding orbital, and will tend to hold the nuclei together. If the electrons tend to be present in a molecular orbital in which they spend more time elsewhere than between the nuclei, the orbital will function as an anti-bonding orbital and will actually weaken the bond. Electrons in non-bonding orbitals tend to be in deep orbitals (nearly atomic orbitals) associated almost entirely with one nucleus or the other, and thus they spend equal time between nuclei or not. These electrons neither contribute nor detract from bond strength.

Although the energies (DOS) and shapes of molecular orbitals can be derived by solving the Schrödinger equation, it is possible to a certain extent to derive these qualitatively in a more intuitive way starting from the bonding of atomic orbitals. The interaction to form a molecular or cluster orbital from two (or more) atomic orbitals is illustrated in the molecular orbital diagram of Figure 6-3. A molecular orbital diagram, or MO diagram for short, is a qualitative descriptive tool explaining chemical bonding in molecules in

terms of molecular orbital theory in general and the Linear combination of atomic orbitals molecular orbital method (LCAO method) in particular.[234,235,236] A fundamental principle of these theories is that as atoms bond to form molecules, a certain number of atomic orbitals combine to form the same number of molecular orbitals, although involved electrons may be redistributed among the orbitals. It explains why some molecules exist and not others, how strong bonds are, and what electronic transitions can take place. Molecular orbital diagrams are diagrams of MO energy levels, shown as short horizontal lines in the center, flanked on the sides by constituent AO energy levels for comparison, with the energy levels ranging from low energy at the bottom to high energy at the top. Lines, often dashed diagonal lines, connect MO levels with their constituent AO levels. Often even for simple molecules, AO and MO levels of inner orbitals and their electrons may be omitted from a diagram for simplicity.

In MO theory molecular orbitals form by overlap of atomic orbitals. The atomic orbital energy correlates with electronegativity as a more electronegative atom holds an electron more tightly thus lowering its energy. The two atomic orbitals can overlap in two ways depending on their phase relationship. The phase of an orbital is a direct consequence of the wave-like properties of electrons. The sign of the phase itself does not have physical meaning except when mixing orbitals to form molecular orbitals. Then two same-sign orbitals have a constructive overlap forming a molecular orbital with the bulk of electron density located between the two nuclei. This MO is called the bonding orbital and its energy is lower than that of the original atomic orbitals.

Atomic orbitals can also interact with each other out-of-phase which leads to destructive cancellation and no electron density between the two nuclei at the so-called nodal plane depicted as a perpendicular dashed line. In this anti-bonding MO with energy much higher than the original AO's, any electrons present are located in lobes pointing away from the central internuclear axis.

The next step in constructing an MO diagram is filling the newly formed molecular orbitals with electrons. The Aufbau principle states that orbitals are filled starting with the lowest energy. The Pauli exclusion principle states that the maximum number of electrons occupying an orbital is two having opposite spins. Hund's rule states that when there are several MO's with equal energy, the electrons fill into the MO's one at a time before filling two electrons into any. The filled MO highest in energy is called the Highest Occupied Molecular Orbital or HOMO and the empty MO just above it is then the Lowest Unoccupied Molecular Orbital or LUMO. The electrons in the bonding MO's are called bonding electrons and any electrons in the antibonding orbital would be called antibonding electrons. The reduction in energy of these electrons is the driving force for chemical bond formation.

The relative order in MO energies and occupancy correspond with electronic transitions found in photoelectron spectroscopy (PES). In this way it is possible to experimentally verify MO theory. In general sharp PES transitions indicate nonbonding electrons and broad bands are indicative of bonding and antibonding delocalized electrons. Bands can resolve into fine structure with spacings corresponding to vibrational modes of the molecular cation (Franck–Condon principle).

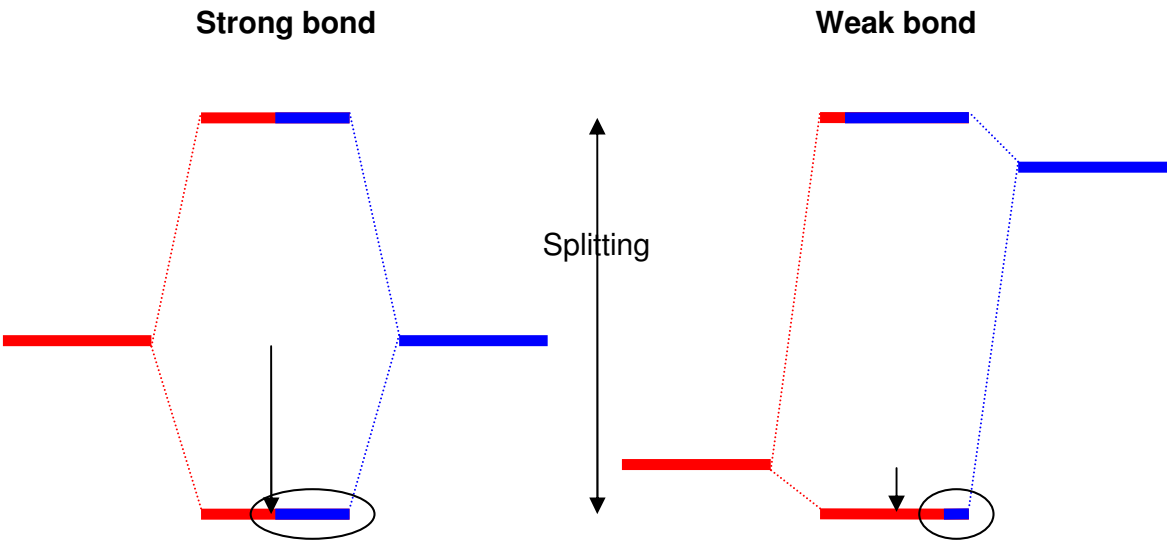

Figure 6-3: Fundamentals of bonding using molecular orbital diagrams.

The energy difference (splitting) between the bonding and antibonding molecular orbitals is smaller if the spatial overlap between the contributing atomic orbitals is large. This is why the splitting depends on the symmetry ($\sigma > \pi$) and the type (p > s) of the atomic orbitals and on the distance between the atoms. The character of each molecular orbital depends on the relative energy distance of the atomic orbitals. If a molecular orbital is closer in energy to one atomic orbital than the other it will have a larger contribution of this atomic orbital. If two atomic orbitals have the same energy, the molecular orbitals will have equal contribution of both. If the energy distance between the two atomic orbitals is equal or exceeds the energy splitting the molecular orbitals maintain their local atomic character.

6.3 Stability of lithium doped semiconductor species

6.3.1 Growth mechanism

In order to estimate the charge on the lithium atoms, natural population analysis (NPA) is performed. Our results revealed that the net atomic charges of lithium atoms of Ge_nLi_m vary in the range of 0.83 - 0.93 e. Consequently, the ionic character is firmly established in the chemical bonding of the lithium-doped germanium clusters. The neutrals S_nLi_m and cations $S_nLi_m^+$ can thus be considered as $S_n^{m\delta-}$-mLi$^{\delta+}$ and $S_n^{(m\delta-+1)}$-mLi$^{\delta+}$, complexes respectively. Similar behavior was previously found for Si_nNa_m clusters. This implies a strong similarity between the cation $S_nLi_{m+1}^+$ and the isoelectronic neutral S_nLi_m.

Appendix A.4 gives an overview of global minimum structures for $Si_nLi_m^{(+)}$ (n = 5-11, m = 0-3 and $Ge_nLi_m^{(+)}$ (n = 5-10, m = 0-4). The ground state of the cation $S_nLi_{m+1}^+$ has often the same geometric shape as the ground state of the corresponding neutral S_nLi_m. For germanium the exceptions are: $Ge_7Li_{3\text{-}4}^+$ and $Ge_8Li_{1\text{-}4}^+$. For silicon the exceptions are $Si_8Li_4^+$ and $Si_{11}Li_2^+$. Moreover, it is apparent that for almost all sizes silicon and germanium clusters have the same framework. We will therefore use the abbreviation S to refer to both silicon and germanium. The exceptions are $S_7Li_3^+$, $S_8Li_{1\text{-}4}^+$ and S_9Li_1, $S_9Li_2^{(+)}$ and $S_9Li_3^+$. In the case of size 7 and 8 this involves low lying isomers, while in the case of size 9 it involves distinct different growth patterns where silicon prefers a pentagonal face and germanium a more symmetric square face.

Appendix A.5 gives an overview of the density of states (DOS) of the global minimum structures for $Si_nLi_m^{(+)}$ (n = 5-11, m = 0-3) cations and neutral clusters. The isoelectronic species are plotted on top of each other. Each DOS has been shifted to start with the first delocalized orbital 1S at the same position, to compare the evolution of the relative position of the different cluster orbitals. The gap at the right side of the depicted figure is the HOMO-LUMO gap, which is quite distinct in most cases. Only a small part of the unfilled orbitals is shown (at the right edge), but above the LUMO the DOS continues basically as an uninterrupted band. It is immediately clear that isoelectronic species have almost identical DOS, confirming that lithium can serve as an electron donor. The exceptions coincide with differences in geometric structure.

This simple building scheme has high predictive value in calculating cationic clusters based on knowledge of the shape of the neutral species. But can we bring this one step further: do the lithium doped clusters S_nLi_m represent bare cluster S_n^{-m} anions? We will compare our results of lithium doped germanium clusters with the bare anions discussed in section 4.2.1. The global minima of Ge_5^{2-}, Ge_5^- anions have the same structure as the core of their corresponding lithium doped structures. Similar, the global minimum of the Ge_7^{2-} dianion is a pentagonal bipyramid of D_{5h} symmetry, like the structure of the neutral ground state, but stretched along its axis with increasing negative charge. There is disagreement for size six: while S_6^{x-} (x = 0-2) is build around an octahedral motif, the lithium doped species S_6Li_1 and S_6Li_2 adopt the pentagonal shape of size 7 by capping a rhombic site. Surprisingly, the octahedral dianion is less stable than the anion. While Ge_8 prefers a capped pentagonal shape, the Ge_8^{2-} dianion is expected to adopt a tetracapped tetragonal shape, in agreement with the structure of Ge_8Li_2. Both low lying isomers are different from the open structure Ge_8^{4-} which has a hexagonal face. Ge_9^{x-} (x = 2-4) all form a tricapped trigonal prism (TTP), while the capped square antiprism (CSA) appears as an alternative for the ground state of Ge_9^{4-}. The TTP and the CSA are closely related by a single diamond-square process involving rupture of an edge connecting two degree 5 vertices of the TTP. For the lithium doped clusters the CSA motif already appears for three lithium dopants as the ground state, but the agreement with the anions is overall very strong. The anion and the dianion for Ge_{10} are both bicapped square antiprism (BSA) structures. While $Ge_{10}Li_2$ clearly has an identical shape, $Ge_{10}Li$ shows substitution of one capping atom by a lithium atom.

While the main structural features are the same for the lithium doped clusters S_nLi_m and the cluster anions S_n^{m-}, not all structures are identical. An obvious reason is that we might compare with structures that are not the global minimum structure: anions with more than one negative charge are not investigated very intense, and it is likely some of these structures are only local minima. However, the presence of the Li^+ counterions might very well have an effect on the shape of the structure and mix up the order of low lying isomers. Even in this case, the results of the lithium doped silicon clusters are very meaningfull with respect to bare silicon anions, as the latter never exist as such in a real environment.

6.3.2 Identification of stable systems

It is known for long time that medium-sized Si_n and Ge_n clusters dissociate into small fragments rather than monomers and dimers.[82,109,108] Zhang and coworkers performed mass selected laser photodissociation of silicon Si_n^+ ($n < 80$) and germanium Ge_n^+ ($n < 40$) cations.[110,111] For both silicon and germanium, the apparent positive ion fissioning process can better be explained by the loss of neutral fragments. The smaller Si_n^+ clusters preferentially lose Si_{10} and to a lesser extend Si_7. For the larger Si_n^+ clusters ($n > 30$) a subsidiary channel of monomer evaporation appears. The Ge_n^+ clusters lose Ge_7 fragments at smaller sizes and Ge_{10} at larger sizes, at least up to $n = 40$. Qin and coworkers investigated the stabilities and fragmentation energies of Si_n clusters ($n = 2$–33).[112] The relative stability of the clusters was estimated through the second order difference in energy, which shows distinct maxima for Si_7 and Si_{10}. Other maxima appear at $n = 4$, 12, and 14. The medium sized silicon clusters decompose preferably into Si_7 and Si_{10}: their fragmentation energies are smaller compared to other channels, showing that Si_7 and Si_{10} would appear frequently in fragmentation products. Zhao and coworkers investigated the fragmentation behaviour of Ge_n clusters ($n = 2$-33).[137] The second order difference in energy shows distinct maxima at Ge_7 and Ge_{10} and smaller maxima at $n = 4$, 12, and 14 as well. Maxima at higher sizes ($n = 20$, 23, 26, 29) are explained as each of these clusters contains two stable Ge_{10} subunits. In the fragmentation products, Ge_6, Ge_7 and Ge_{10} are obviously more abundant. The electronic stability of these sizes is supported by the low ionization energies of Si_7Li, $Si_{10}Li$ and Ge_7Li, $Ge_{10}Li$ as detailed in section 5.2.

Other stable silicon and germanium systems at other charge states were obtained in solution. Fässler and coworkers extensively reviewed the structure and charge state of silicon and germanium Zintl ions.[145,188] Many compounds containing homoatomic nine-atom clusters are characterised by single crystal X-ray diffraction. The proof that nine-atom germanium anions Ge_9^{4-} are also present in binary alloys was produced using Raman spectroscopy and X-ray diffraction methods in 1997 (Cs_4Ge_{36} and K_4Ge_{36}) and culminated in the structural characterization of the first Si_9^{4-} clusters in the binary phase $Rb_{12}Si_{17}$ one year later.[65,66,67] These compounds also contain Si_4^{4-} which has the same tetrahedral shape as Ge_4^{4-} for germanium.[68,69] Liquid ammonia was used as a solvent to extract nine- and five-atom naked clusters of silicon in solution and allowed for the structural characterization of Si_9^{3-} and Si_5^{2-} in compounds crystallized from such solutions.[70] Crystalline materials containing Ge_5^{2-} are obtained as well.[71,72] Recently, a Ge_{10}^{2-} cluster was characterized as a fragment in $[Ge_{10}Mn(CO)_4]^{3-}$.[73] Homoatomic ligand-free Group 14 clusters with six, seven, eight, or more than ten vertices have not yet been detected in solution. The fragmentation spectra for lithium doped germanium and silicon clusters confirm the stability of these anions. $Ge_5Li_3^+$ and $Si_5Li_3^+$ as well as $Ge_9Li_5^+$ and $Si_9Li_5^+$ show enhanced abundances. They correspond to anions Ge_5^{2-} and Si_5^{2-} as well as Ge_9^{4-} and Si_9^{4-} which were synthesized in solution. For the smallest sizes, both silicon and germanium clusters always show distinct maxima for $S_2Li_3^{(+)}$, $S_3Li_3^{(+)}$ and $S_4Li_5^{(+)}$ (S = Si, Ge). At larger sizes compound structures appear in two main series: $Ge_{9x}Li_m^{(+)}$ and to a lesser extend $Ge_{9x+6}Li_m^{(+)}$. Its members can be identified best as $Ge_9Li_5^+$, $Ge_{15}Li_1^+$, $Ge_{18}Li_7^+$, $Ge_{24}Li_1^+$, $Ge_{27}Li_{11}^+$, $Ge_{33}Li_4^+$, $Ge_{36}Li_{14}^+$, $Ge_{42}Li_4^+$, … and its neutral counterparts. For silicon these compound structures are limited to the first two species.

Combining these experimental results indicates enhanced stabilities for: S_4^{4-}, S_5^{2-}, S_7, S_9^{4-}, S_{10} and S_{10}^{2-} (S = Si, Ge). To check this assumption we will compare the

experimental results with calculations on lithium doped silicon and germanium clusters. To probe the stability we introduce a stability index $S_{n,m}$, based on the binding energy of the clusters:

$$S_{n,m} = -\frac{nE(S) + mE(\mathrm{Li}) - E(S_n\mathrm{Li}_m)}{nE(S) + mE(Li)}$$
$$S^{+}_{n,m} = -\frac{nE(S) + (m-1)E(\mathrm{Li}) + E(\mathrm{Li}^{+}) - E(S_n\mathrm{Li}_m)}{nE(S) + (m-1)E(\mathrm{Li}) + E(\mathrm{Li}^{+})} \quad (6.2)$$

The stability index becomes negative when the binding energy becomes negative. A higher value of the stability index means a higher binding energy. By normalizing with the energies of the constituents, a stability map can be created, which directly compares the stability fluctuations upon changing the number of host and dopant atoms.

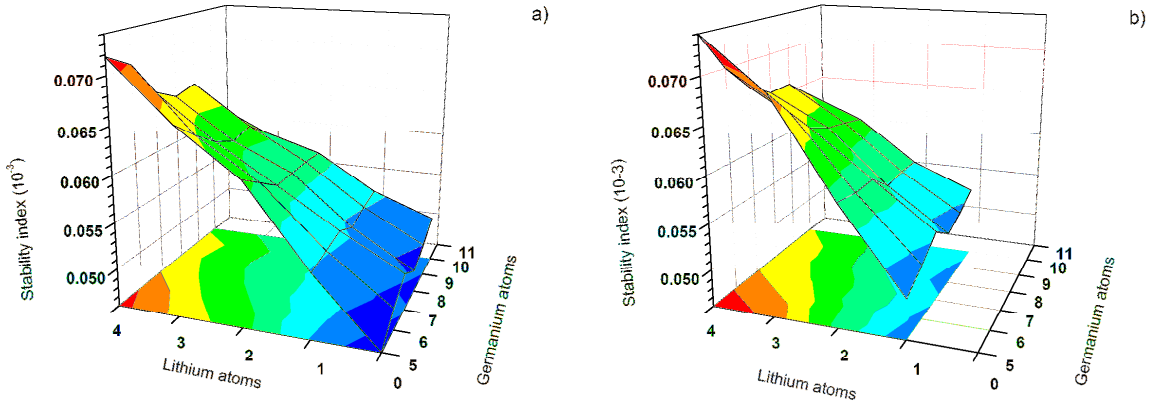

Figure 6-4: Stability map for lithium doped germanium clusters in neutral (a) and cationic (b) state showing the stability index $S_{n,m}$ in function of the number of lithium (n) and germanium (m) atoms. The colour scale goes from blue over green and yellow to red. Red indicates the most stable species, while blue shows the least stable species.

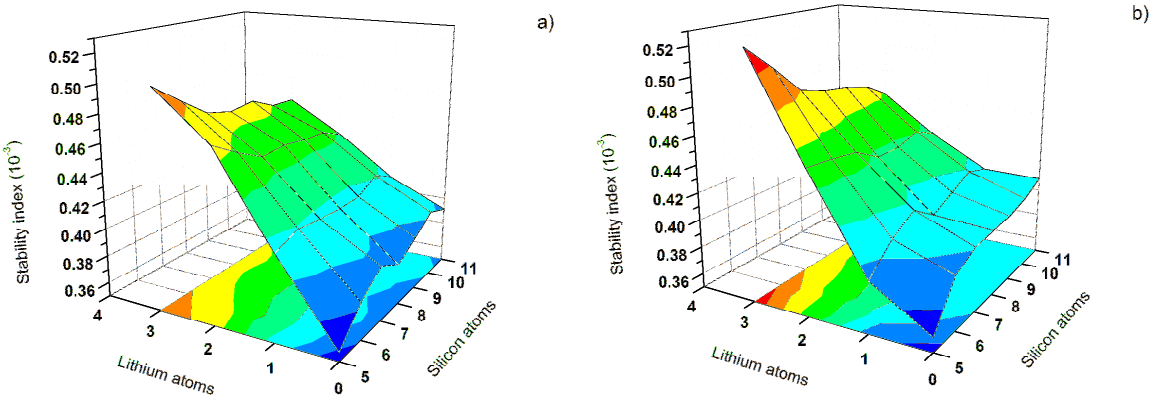

Figure 6-5: Stability map for lithium doped silicon clusters in neutral (a) and cationic (b) state showing the stability index $S_{n,m}$ in function of the number of lithium (n) and silicon (m) atoms. The colour scale goes from blue over green and yellow to red. Red indicates the most stable species, while blue shows the least stable species.

Figure 6-4 shows the results for neutral and cationic lithium doped germanium clusters. In general the stability index increases going from 0 to 4 lithium atoms. For the bare clusters there is an increase going from 5 to 10 atoms. The stability index of the closed shell systems Ge_nLi_2 and Ge_nLi_4 tends to rise sharper than the one of the open-shell systems Ge_nLi and Ge_nLi_3. This trend is less clear for the cations. Superposed on the

general trends some specific species stick out. For the neutral clusters these are: Ge_5Li_2, Ge_6Li_4, Ge_7, Ge_8Li_2, Ge_9Li_4, Ge_{10}, and $Ge_{10}Li_2$. For the cations there are equivalent species: $Ge_5Li_3^+$, $Ge_6Li_3^+$, Ge_7Li^+, $Ge_8Li_3^+$, $Ge_9Li_4^+$, $Ge_{10}Li^+$, and $Ge_{10}Li_3^+$. An analysis of natural populations points out that each of the lithium atoms transfers its valence electron to the Ge_n background. Consequently, the higher stabilities of these systems Ge_nLi_m can be understood from an enhanced stabilization of their hosts Ge_n^{m-}. The electrostatic interaction seemingly contributes to their thermodynamic stability.

Figure 6-5 shows the results for neutral and cationic lithium doped silicon clusters. It confirms the general trend in the case of germanium where the stability index increases going from 5 to 10 germanium atoms and from 0 to 3 lithium atoms. It seems stability starts to drop after size 10. The stability index of the closed shell systems Si_nLi_2 tends to rise sharper than the one of the open-shell system Si_nLi_3, but other trends found for germanium cannot be confirmed. Superposed on the general trends some specific species stick out. For the neutral clusters these are: Si_5Li_2, Si_7 and Si_{10}. For the cations there are equivalent species: $Si_5Li_3^+$, Si_7Li^+ and $Si_{10}Li^+$. This confirms the experimental results indicating enhanced stabilities for: S_4^{4-}, S_5^{2-}, S_7, S_9^{4-}, S_{10} and S_{10}^{2-} (S = Si, Ge).

6.3.3 Overview of some stable systems

For each size of host atoms we will now discuss the most stable stoichiometry S_nLi_m (S = Si, Ge) with respect to their electronic and geometric structure.

S_5^{2-}

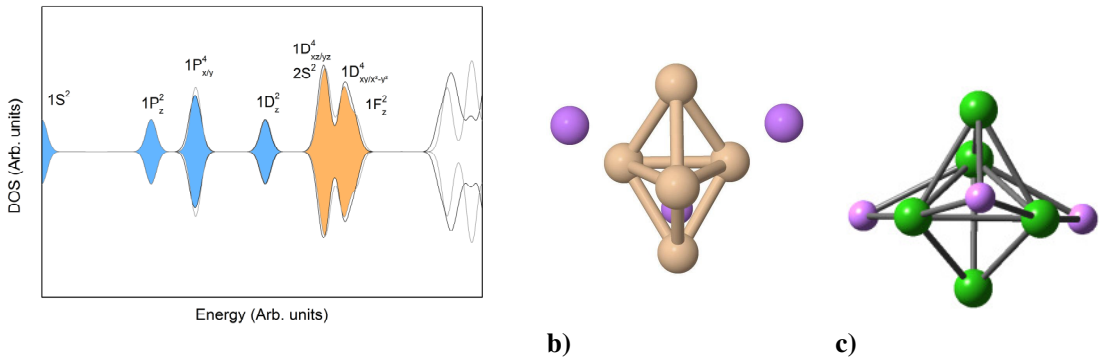

Figure 6-6: (a) DOS of $Si_5Li_3^+$ (grey line) and Si_5Li_2 (black line). Blue orbitals mainly consist of s electrons of silicon, while orange orbitals mainly consist of p electrons of silicon and s electrons of lithium. (b) The ground state structure of $Si_5Li_3^+$. (b) The ground state structure of $Ge_5Li_3^+$.

Figure 6-6 (a) shows the DOS of Si_5Li_2 and $Si_5Li_3^+$. The blue orbitals mainly consist of s electrons and show a 10 electron shell closing (1S, $1P_z$, $1P_x$, $1P_y$, $1D_{z^2}$). The remaining orange orbitals close a 22 electron shell (… 2S, $1D_{xz}$, $1D_{yz}$, $1D_{xy}$, $1D_{x^2-y^2}$, $1F_{z^3}$). Figure 6-6 (b) shows the ground state geometry of $Si_5Li_3^+$: a prolate trigonal bipyramid surrounded by lithium atoms. A trigonal bipyramidal crystal field induces lowering of the $1D_{z^2}$ and $1F_{z^3}$ orbitals, matching the electronic shell closings.[237]

S_6

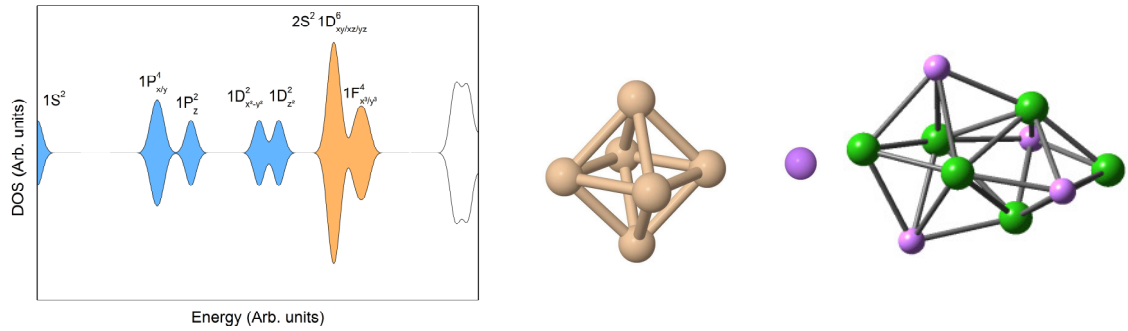

a) b) c)

Figure 6-7: (a) DOS of Si_6Li^+. Blue orbitals mainly consist of s electrons of silicon, while orange orbitals mainly consist of p electrons of silicon and s electrons of lithium. (b) The ground state structure of Si_6Li^+. (c) The ground state structure of Ge_6Li_4.

Figure 6-7 (a) shows the DOS of Si_6Li^+. The blue orbitals mainly consist of s electrons and show a 12 electron shell closing (1S, $1P_x$, $1P_y$, $1P_z$, $1D_{z^2}$, $1D_{x^2-y^2}$). The remaining orange orbitals close a 24 electron shell (… 2S, $1D_{xy}$, $1D_{xz}$, $1D_{yz}$, $1F_{x^3}$, $1F_y$). Figure 6-7 (b) shows the ground state geometry of Si_6Li^+: an oblate octahedron with a satellite lithium atom. An octahedral crystal field clearly promotes the $1D_{z^2}$, $1D_{x^2-y^2}$ and $1F_{x^3}$, $1F_{y^3}$, $1F_{z^3}$ orbitals.[238,237] As this would result in a 26 electron shell closing the cluster undergoes a distortion breaking the degeneracy of these two 1D and three 1F orbitals. With one of the 1F orbitals now higher in energy this matches the calculated 24 electron shell closing. Unfortunately, the symmetry breaking is limited by the 12 electron shell closing, and we end up with a compromise structure which doesn't show particular enhanced stability as confirmed from the experimental output. The 26 electron shell closing would suggest the observation of very stable Si_6Li_2 and Ge_6Li_2 octahedrons. This is also not the case. DFT calculations show an enhanced stability of the anion over the dianion in the case of a bare silicon octahedron. The mass spectrum shows an increase for Si_6Li_2 and Ge_6Li_2 but no more than the bare cluster and well below many other peaks. Moreover, these structures are not octahedral. To find the most stable charge state for S_6, the best candidate might be the structure of Ge_6Li_4 (Figure 6-7 (c)). It is a symmetric structure with an enhanced stability index.

S_7

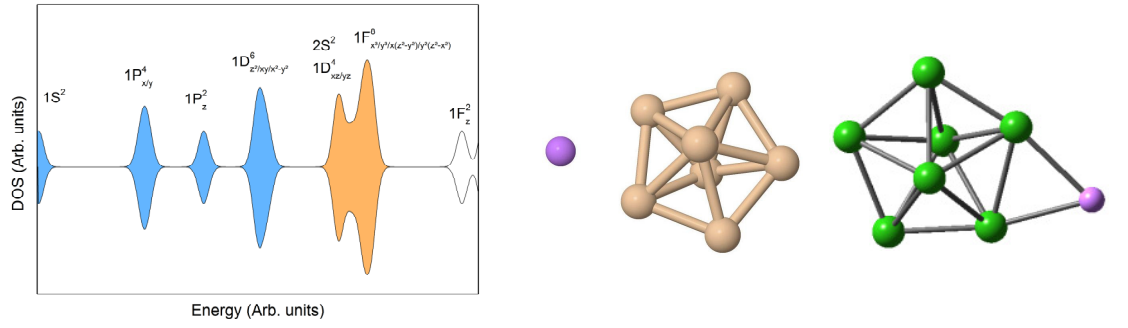

a) b) c)

Figure 6-8: (a) DOS of Si_7Li^+. Blue orbitals mainly consist of s electrons of silicon, while orange orbitals mainly consist of p electrons of silicon and s electrons of lithium. (b) The ground state structure of Si_7Li^+. (c) The ground state structure of Ge_7Li^+.

Figure 6-8 (a) shows the DOS of Si_7Li and $Si_7Li_1^+$. The blue orbitals mainly consist of s electrons and show a 14 electron shell closing (1S, $1P_x$, $1P_y$, $1P_z$, $1D_{xy}$, $1D_{x^2-y^2}$, $1D_{z^2}$). The remaining orange orbitals close a 28 electron shell (… 2S, $1D_{xz}$, $1D_{yz}$, $1F_{y(z^2-x^2)}$, $1F_{x(z^2-y^2)}$, $1F_{x^3}$, $1F_{y^3}$). Figure 6-8 (b) shows the ground state geometry of Si_7Li^+: an oblate trigonal bipyramid with a satellite lithium atom. A pentagonal bipyramidal crystal field favors the in plane orbitals, matching the electronic shell closings.[237]

S_9^{4-}

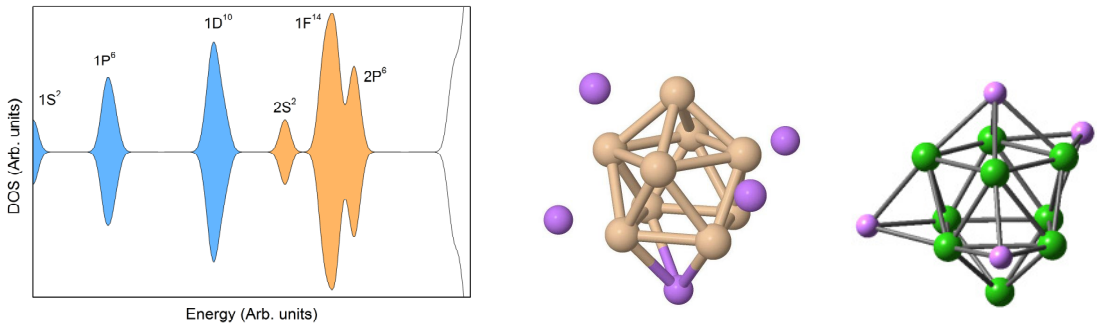

a) **b)** **c)**

Figure 6-9: (a) DOS of $Si_9Li_5^+$. Blue orbitals mainly consist of s electrons of silicon, while orange orbitals mainly consist of p electrons of silicon and s electrons of lithium. (b) The ground state structure of $Si_9Li_5^+$. (c) The ground state structure of $Ge_9Li_5^+$.

Figure 6-9 (a) shows the DOS of $Si_9Li_5^+$. The blue orbitals mainly consist of s electrons and show an 18 electron shell closing (1S, $1P_x$, $1P_y$, $1P_z$, $1D_{xy}$, $1D_{xz}$, $1D_{yz}$, $1D_{x^2-y^2}$, $1D_{z^2}$). The remaining orange orbitals close a 40 electron shell (… 2S, $1F_{xyz}$, $1F_{x(z^2-y^2)}$, $1F_{y(z^2-x^2)}$, $1F_{z(x^2-y^2)}$, $1F_{z^3}$, $1F_{x^3}$, $1F_{y^3}$, $2P_x$, $2P_y$, $2P_y$). Figure 6-9 (b) shows the ground state geometry of $Si_9Li_5^+$: a capped square antiprism with one capping the square face and four more capping non adjacent triangular faces. One can clearly recognize the spherical symmetry of this system. The clusters form a cage with no positive charge in the center, giving rise to a winebottle potential. As described in section 6.1 this lifts the 2S and 2P levels, which matches the electronic shell closings.

S_{10}

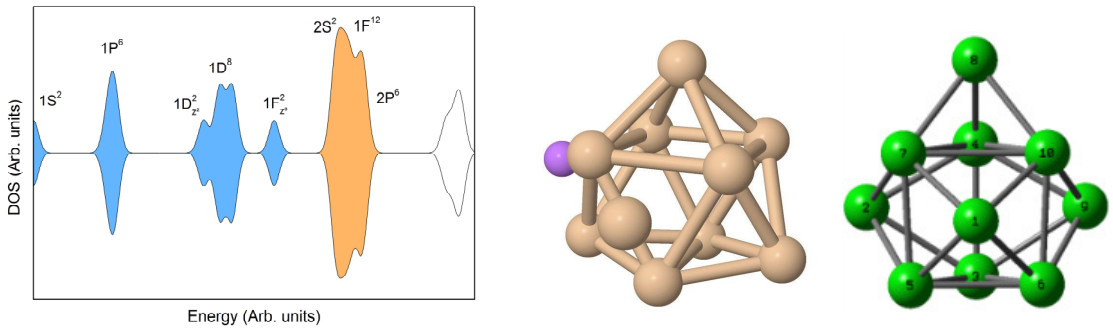

a) **b)** **c)**

Figure 6-10: (a) DOS of $Si_{10}Li^+$. Blue orbitals mainly consist of s electrons of silicon, while orange orbitals mainly consist of p electrons of silicon and s electrons of lithium. (b) The ground state structure of $Si_{10}Li^+$. (c) The ground state structure of Ge_{10}.

Figure 6-10 (a) shows the DOS of $Si_{10}Li^+$. The blue orbitals mainly consist of s electrons and show a 20 electron shell closing (1S, $1P_x$, $1P_y$, $1P_z$, $1D_{xy}$, $1D_{xz}$, $1D_{yz}$, $1D_{x^2-y^2}$, $1D_{z^2}$, $1F_{z^3}$). The remaining orange orbitals close a 40 electron shell (… 2S, $1F_{xyz}$, $1F_{x(z^2-y^2)}$,

$1F_{y(z^2-x^2)}$, $1F_{z(x^2-y^2)}$, $1F_{x^3}$, $1F_{y^3}$, $2P_x$, $2P_y$, $2P_y$). Figure 6-10 (b) shows the ground state geometry of $Si_{10}Li^+$: a silicon atom is capping the tricapped trigonal prism (TTP) isomer of $Si_9Li_5^+$. The TTP and CSA structures are very similar, but TTP symmetry matches better the current capping position of the tenth silicon atom. The capping along the z-axis lowers the $1D_{z^2}$ and $1F_{z^3}$ orbitals, changing the 18 into a 20 electron shell closing.

6.4 Stability model for semiconductor clusters

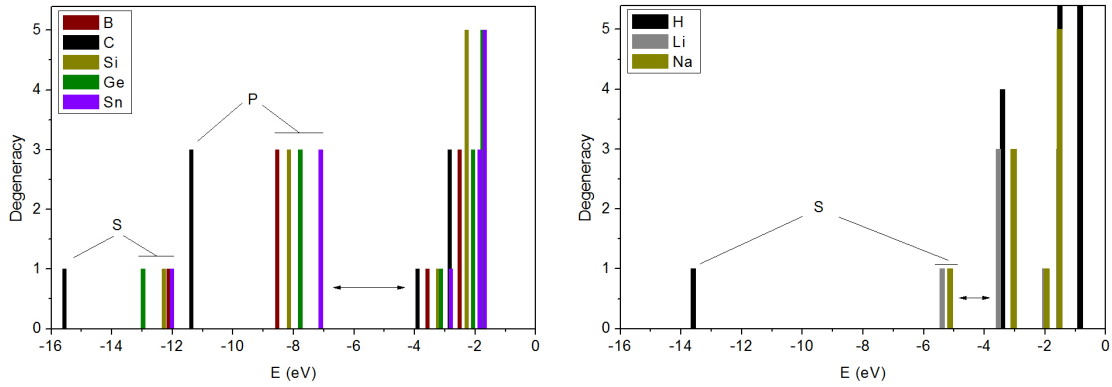

Figure 6-11: Atomic energy levels around the HOMO-LUMO gap for (a) a number of group IV elements: carbon, silicon, germanium and tin ($s^2p^2s^0p^0$…), as well as boron ($s^2p^1\ s^0p^0$…), and (b) a number of group I elements: hydrogen, lithium and sodium (s^1p^0…).[239]

While clusters are determined by both their geometrical and electronical configuration, there tends to be a fixation on the geometrical structure in literature: artfully illustrations of fascinating symmetric structures overshadow attempts to describe their electronic structure. However, density of states combined with orbital plots offers the same level of intuitive insight as the drawing of the core atoms.

To understand the position of the final cluster orbitals in the DOS it is important to know the relative energies of the atomic orbitals (see also section 6.2). Figure 6-11 gives an overview of the energetic levels of the orbitals around the HOMO-LUMO gap for (a) a number of group IV elements: carbon, silicon, germanium and tin ($s^2p^2s^0p^0$…), as well as boron ($s^2p^1\ s^0p^0$…), and (b) a number of alkali metals: hydrogen, lithium, and sodium (s^1p^0…). It is clear that the energy gaps between the occupied s orbital, the half occupied p orbitals and the higher lying unoccupied orbitals are similar for silicon, germanium, tin, and boron and in contrast to carbon. This is also clear from the experimental values of the ionization energy, which is much higher for carbon (C = 11.26 eV, Si = 8.15 eV, Ge = 7.90 eV, B = 8.30 eV, Sn = 7.34 eV). These differences will have distinct effects on the bonding with same and with different elements. We will give a few examples.

Arguing that silicon and germanium are isoelectronic with carbon and lithium with hydrogen, one could expect similar structures for all combinations. This is not the case. Looking at the energy levels of carbon and hydrogen we see that the hybridization of carbon 2s and 2p orbitals would result in an orbital exactly matching the hydrogen 1s level. If we assume sp^3 hybridization this would result in a tetragonal symmetry, and methane (CH_4) indeed has a tetragonal structure. This explains also the strong carbon-hydrogen covalent bond in methane, which is among the strongest in all hydrocarbons. Silane (SiH_4) and germane (GeH_4) are well known analogous of methane. Indeed, both structures also have the tetragonal structure, but they are more reactive and less stable: as an indication, the standard enthalpy of formation is 34.3 kJ/mol for silane and 90.8

kJ/mol for germane as compared to -74.87 kJ/mol for methane. The hydrogen 1s orbital now lies below the sp^3 hybrid and the bond will be less strong.

Already in section 5.1 it became clear that the tetragonal shape is no longer the global minimum for $SiLi_4$ and $GeLi_4$. The reason is clear as well. The lithium 2s orbital is much higher in energy (IE = 5.39 eV) than the 1s orbital of hydrogen (IE = 13.60 eV). It will not make covalent bonds, but rather ionic bonds, where the electrons are dropped in the lower laying unoccupied p orbitals of germanium (or silicon). The energy distance with the s orbital is too high to have a bond with a tetragonal hybridized system. The fact that CLi_4 does have a tetragonal shape is in fact more surprising than not, but as outlined before, the small size of the carbon atom brings the lithium atoms in a bonding distance among each other, which offsets the difficult bonding with the carbon, as compared to silicon and germanium.

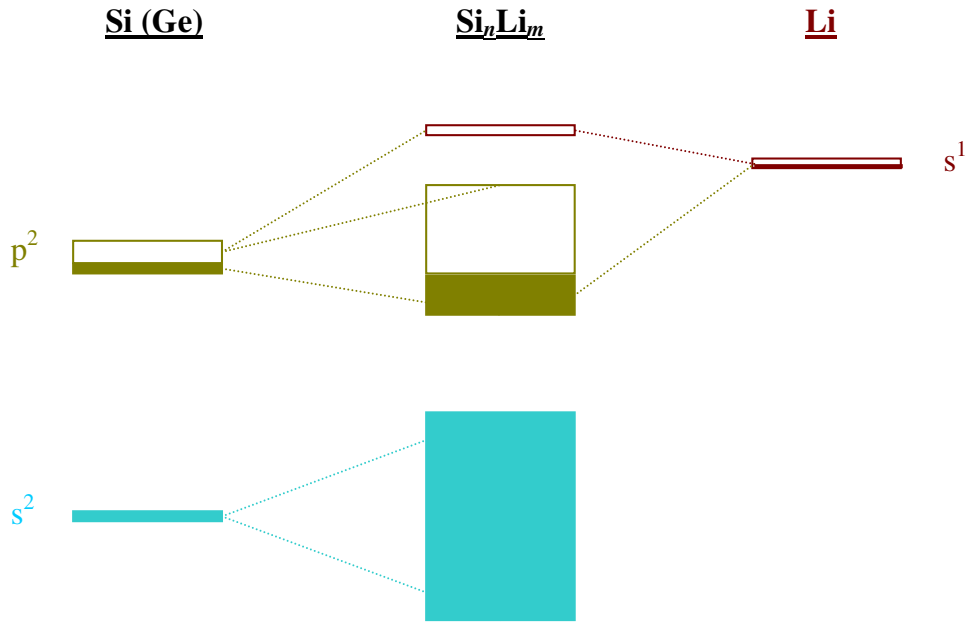

Figure 6-12: Bonding diagram showing the atomic energy levels of silicon (germanium) and lithium and their interaction to form a cluster s-band (blue) and p-band (yellow).

The experimental dissociation spectra show a clear increase for $Ge_5Li_3^+$ ($Si_5Li_3^+$) and $Ge_9Li_5^+$ ($Si_9Li_5^+$). These species correspond to the well known anions Ge_5^{2-} (Si_5^{2-}) and Ge_9^{4-} (Si_9^{4-}), synthesized in solution. Other stable species are Ge_7 (Si_7) and Ge_{10} (Si_{10}) which often appear as main fragments in collision induced dissociation experiments.

The electronic structure of silicon and germanium clusters is often discussed in terms of sp^3 hybridization. This is in analogy with the boranes where dangling bonds are passivated with hydrogen. However, no evidence of this kind of hybridization is apparent from the density of states (DOS) of these clusters. In fact, there appears to be little bonding between s and p electrons and they form two rather isolated s-bands and p-bands. This is similar to coinage metal clusters where there are independent s and d-bands. The characteristics of these two bands can easily be explained by a simple molecular orbital bonding model illustrated in Figure 6-12. Because there is a significant energy gap between the 3s (4s) and the 3p (4p) electrons in the silicon (germanium) atom there is little bonding between s and p type electrons upon cluster formation. The 3s (4s) electrons from the different silicon atoms in the cluster bind among each other forming bonding and antibonding combinations. Because all participating orbitals are filled the resulting band has its center at the 3s (4s) atomic energy and no energy can be gained.

The width of the band depends on the overlap of the individual atomic orbitals, which can directly be related to their bond length (see section 6.2). Similar, the 3p (4p) electrons of the individual silicon (germanium) atoms bind with each other forming the p-band. As the 3p orbitals are only occupied by two out of six electrons the total energy of the cluster can be lowered if these electrons only fill low lying orbitals in the cluster p-band, in essence: a shell closing. The width of the p-band is smaller than the s-band, because the overlap of s orbitals is in general larger compared to p orbitals. The lithium 2s electron is more than 2 eV above the p orbitals of silicon (germanium), and it will basically dump its electron into the partially filled cluster p-band: in essence forming an ionic bond.

In the case of small silicon and germanium clusters (<10), there remains a gap between the s-band and the p-band, which implies that the s-band de facto shows a shell closing. With a given number of electrons in this s-band, the number of electrons for that shell closing is set and the structure is forced into a geometry which field induces the given shell closing. As the geometry is determined by the s-band, the total electronic structure will try to lower its energy by filling a closed shell. In some cases, the total number of electrons (s and p) of all silicon (germanium) atoms fill a closed shell, as in the case of Si_7 and Si_{10}. However, in general, this number doesn't match a shell closing and a more stable system can be reached by adding or removing additional electrons, as in the case of Si_5 and Si_9.

When the number of neighbors starts to increase the splitting of the bands becomes larger because of the larger overlap. As the s-band and the p-band start to overlap, this will favor sp^3 hybridization and along with it the tetragonal packing from the bulk insulators. At that point, 4 degenerate sp^3 electrons for each atom start to fill spherical shell closings in a spherical potential. Because the energy difference between the 3s and 3p levels of silicon is smaller than the energy difference between the 4s and 4p levels of germanium, the critical size where the two bands start to overlap is larger for germanium. This explains the difference in the transition from elongated to spherical structures for silicon and germanium. In the intermediate region, elongated and stacked structures appear.

7 General conclusions and perspectives

Part I: High resolution tandem time-of-flight mass spectrometer

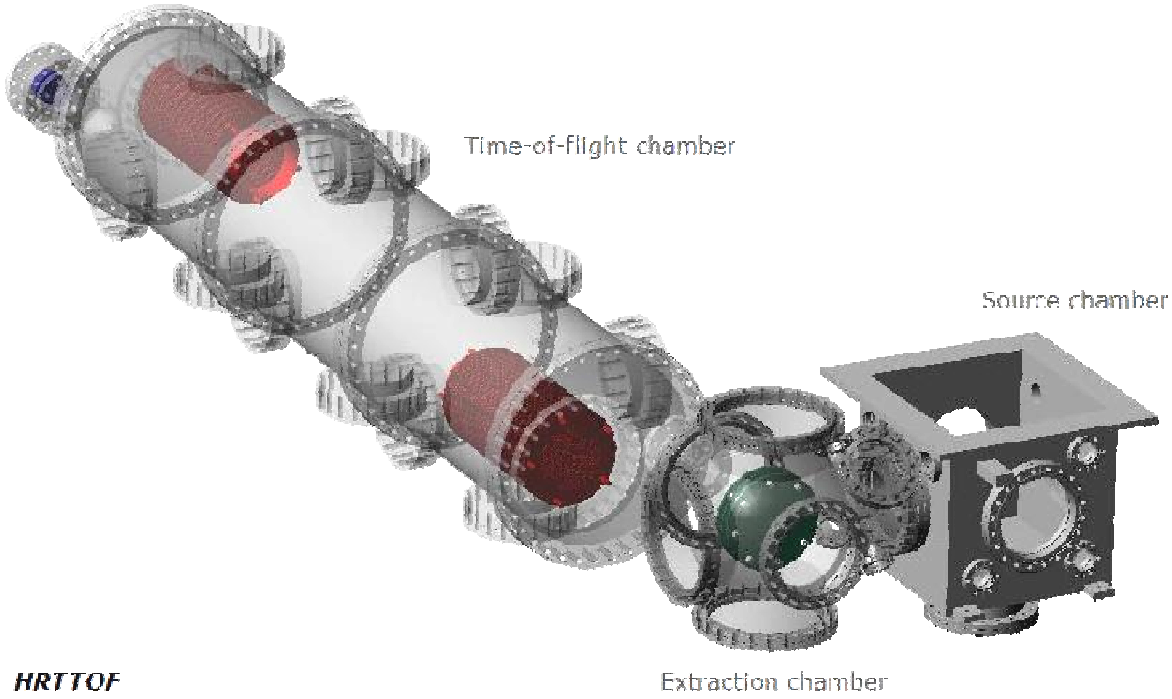

One of the problems with the mass spectrometric investigation of binary clusters is the need of a resolution high enough to identify clusters unambiguously. Therefore a novel instrument was constructed which consists of a binary cluster source and a high resolution tandem time-of-flight mass spectrometer (HRTTOF). Formation of clusters is a spontaneous process and this type of source is capable of producing clusters of up to several hundreds of atoms large. By using a time-of-flight mass spectrometer it is possible to probe the full mass range at once. But the specifications of the cluster beam after leaving the source limit the design possibilities of a high resolution instrument significantly.

A first option is to position the time-of-flight mass spectrometer along the flight direction of the cluster beam (linear extraction). The mass resolution is now limited by the spread in the position and the spread in the velocity of the extracted clusters along this direction. One of these two can be compensated, the most practical way is by using a reflectron. In our case, compensating for the spread in position is the most effective. The spread in velocity can still be large and the resulting resolution might be disappointing. The second option is to position the time-of-flight mass spectrometer on a 90° angle with respect to the cluster beam (orthogonal extraction). The velocity spread of the clusters along this

direction now depends on the cone angle of the cluster beam, which can be made very small. Unfortunately, different masses will enter the TOF in different angles depending on the magnitude of their initial velocity. The rather high and mass independent velocity of the clusters after leaving the source makes this a problematic restriction on the mass range and it is highly necessary to deflect different masses along the same path into the TOF. If the cluster beam inside the TOF would only be one dimenstional that would be fine, however the clusters also have a spread in the position and a spread in the velocity perpendicular to the flight axis. Now, any component in the TOF that is not on the same angle as the extraction will induce another limitation on the mass resolution. In the case of linear extraction the spread in the velocities and the positions perpendicular to the flight axis are strongly correlated as all clusters originate from a single point, which is the nozzle aperture. By tilting the angle of the detector the whole problem can be negated at once. In the case of orthogonal extraction there is no such correlation and the deflection angle can only be optimized to minimize the effect on the resolution. Where deflection electrodes are able to completely mess up high resolution, reflectrons also induce a significant decrease. An improved extraction optic is designed to obtain both high resolution and maintain a high mass range. It deflects a broad mass range of clusters because the deflection takes place inside the extraction optics and not after. While the appearance of a spacial focal point correlates the spread of the positions and the spread of the velocities perpendicular to the flight path, it is also very bad for the efficiency (yield at the detector). In reality, the cluster beam is not two but three dimensionally. Since all electrostatic components only act on one or two dimensions the third dimension is not influenced and will not hamper resolution in any way. Until now we only discussed limitations on the resolution determined by the properties of the cluster beam. There are also other sources of limitation. One of them is the use of grids. Grids are a convenient way to separate different electrostatic fields. But the small square or rectangular openings of the grid act as little lenses, which muddles up both the parallel and perpendicular velocity components. Depending on the precise position of the grid in the instrument, an optimal grid pitch can be derived which is small enough to have high enough resolution and big enough to have high enough efficiency. From the above it is clear that reaching, and maintaining, high resolution is not a straightforward task. This justifies the mathematical approach needed to quantify the problem for a given set of requirements. For this project also extensive simulations were used and they confirm the applicability of the derived formulas in a three dimensional setting.

While the high resolution is a safe-keep for the future to maintain a high level of academic research in binary clusters, the new instrument also holds a second key feature: to be able to perform mass selection an intermediate focal point is implemented by the use of a tandem reflectron TOF design. This design allows for a very high mass selectivity (up to 1/1000). By using two reflectrons and increasing the flight path the resolution is certainly not compromised, but the efficiency will be lowered even more. The background philosophy of the design is to simplify wherever possible to facilitate daily operation and maintance of the instrument as well as keeping many options open for future modifications.

The physical system can be separated in three vessels: source chamber, extraction chamber and the flight chamber, vacated by a total of four turbo molecular pumps. In the first, cubic vacuum chamber the dual-laser dual-target vaporization cluster source is installed. Though a number of variables can be changed, basically they all probe the (partial) gas pressure which determines the clustering process. The internal energy of the clusters is determined by the source cooling. The mixture of atoms, clusters, and inert gas

undergoes a supersonic expansion into the vacuum chamber through a suitable nozzle. The isentropic expansion reduces the density of the cluster beam and ends the cluster-growth process. The velocity after the supersonic expansion saturates almost immediatelly and depends on the source temperature. A conical skimmer with an aperture of 3 mm selects the central part of the cluster beam. Both ionic and neutral clusters are produced. The cationic clusters (direct ions) are studied directly by the HRTTOF, while for the study of neutral clusters, additional laser ionization is needed. Excimer lasers (6.42 eV and 7.89 eV) or a tunable laser provide the necessary laser light.

In the extraction chamber the clusters are accelerated perpendicular to their initial velocity into the dual reflectron mass spectrometer through a 'curved field' extraction optic. This novel extraction optic implements a new design with incorporated deflection which offers an extended mass range for simultaneous detection and which leaves the vertical velocity component of the incoming ions unaltered.

The extraction chamber is coupled to a large cylindrical flight chamber, which contains two dual stage reflectrons. Alongside the reflectrons are cylindrical liners to screen the cluster beam from the high voltage. In the center of the chamber a retractable wire type mass gate is installed for mass selection in the intermediate focal point. At each side of the mass gate there is a glass window to enable mass selected photofragmentation. The clusters are reflected twice before hitting a chevron type MCP detector. The detector is coupled capacitively to a fast preamplifier. A single ion counter and an oscilloscope can be used simultaneously for data collection. Due to the tandem design an intermediate time focal point can be accessed, which is required for mass selected photofragmentation spectroscopy. It is well known that the velocity and position spread along the beam strongly influence the mass resolution at the detector. Here we also introduced the effect of the velocity and position spread in the horizontal direction on the resolution. These contributions, as well as the effect of grids need to be balanced for each individual design not to jeopardize the resolution.

We performed a number of test experiments to initiate and optimize the instrument. Three out of four objectives of the new instrument are already realized:

- An enhanced resolution (> 10 000)
- A secondary focal point (1/400) for mass selected experiments
- Compatible with the K.U.Leuven binary cluster source

The requirement for a broad mass range (up to 100 000 amu) has not been met. This is as likely related to problems with the production in the cluster source as to the new design of 'curved field' extraction: it is unclear whether the source actually produced larger clusters than measured. Our results also demonstrate that a straightforward extraction design consisting of only a plate, a plate with a rectangular cut and a grid is able to extend the mass range of orthogonal extraction compared to conventional tilting of the extraction plates and using a standard set of deflection electrodes after the extraction optic. But mass resolution will always be a trade off against efficiency and mass range. While the results regarding resolution probably can be improved, the efficiency of this configuration is rather low. It is more than sufficient for the single ion count regime, which itself is however very slow: it takes more than 10 minutes to collect a meaningful and trustable mass spectrum, due to the 10 Hz duty cycle. A future effort will be to check whether the mass resolution can be increased as predicted by the simulations. This will require careful tuning of the mechanics and electronics of the system. The long detection times however constitute a major obstacle. For this reason, the analogue detection system

has been upgraded offering the possibility to work at higher detection rates. In experiments were very high mass resolution is not vital, using a linear extraction configuration might be more practical. There is also room for improvement on the mass selectivity either by calibrating the system or by improving the mechanics of the mass gate. There is no urgent need to perform these upgrades as the instrument is already providing interesting new experimental output in the field of mass selected photofragmentation.

The next project will be the investigation of the magnetic properties of clusters, making use of the fact that this instrument leaves the third dimension of the cluster beam unaltered and the modular character of the system. An instrument similar to HRTTOF will be implemented in the Atomic & Molecular Physics Division of the Bhabha Atomic Research Centre (Mumbai, India).

Part II: Stability of (lithium doped) silicon and germanium clusters

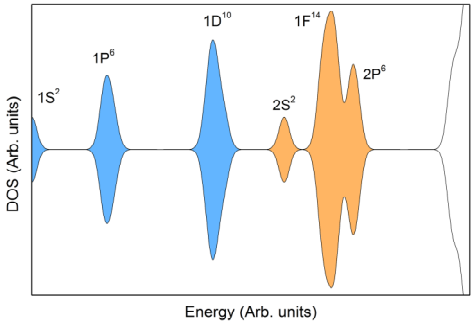

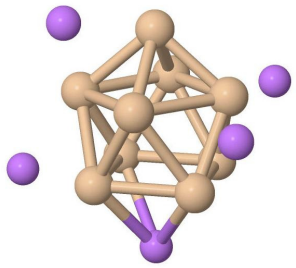

Unlike most other clusters, silicon and germanium clusters dissociate by fragmentation instead of dimer and monomer evaporation. Moreover, medium sized silicon clusters up to size 28 and germanium clusters up to size 70 have elongated shapes. It is likely that these clusters consist of stable building blocks. Mass spectra for smaller sized doped silicon and doped germanium clusters reveal a striking similarity and show enhanced abundances for particular sizes that relate to these building blocks. One of these building blocks consists of nine atoms: K_4Ge_9 is a wellknown Zintl complex which is extensively studied in solution.

We report on a combined experimental and theoretical study of the structure, stability, and ionization potentials of lithium doped silicon and germanium clusters. The main conclusions of this research project are:

- Silicon and germanium clusters have identical to similar properties. The similarities and differences can be traced back to the atomic energy levels.
- Lithium can be used as a charge probe for silicon and germanium clusters.
- The stability of the silicon and germanium clusters is determined by a double set of electronic shell closures: one for the s electrons and one for the p electrons.

Binary Si_nLi_m and Ge_nLi_m clusters were produced in a pulsed (10 Hz) dual-target dual-laser vaporization source. The cluster source was cooled by a regulated flow of liquid nitrogen to a temperature of 140 K. Neutral clusters were skimmed and ionized inside the extraction region of a reflectron time-of-flight mass spectrometer (not HRTTOF). By variation of the ablation lasers energies and the ion extraction timing, clusters with various amounts of lithium doping could be sampled. To determine photoionization efficiency (PIE) curves, mass spectra were recorded at different photon energies in the 4.68 - 5.72 and 5.84 - 6.24 eV range with a 0.04 eV step size using a dye laser. In order to limit the influence of source production fluctuations, reference spectra were taken with 6.42 eV photons from an excimer laser. An electronic device was designed for this experiment containing an analog controller that switched alternatively between the tunable dye laser and the reference laser and drove the recorded signal in two different channels of the oscilloscope. A program was written in Java to facilitate the data analysis, which was necessary to cover the large amount of data needed to extract PIE curves. The newest algorithm uses relative peak identification, which lowers the demands on the mass calibration and gives optimal peak assignment. By using a discrete deconvolution scheme also lithium doped germanium clusters could be analyzed, which are otherwise a meaningless hump due to large peak overlap.

Plotting the ionization efficiency as function of the photon energy yielded the PIE curves for Si_nLi_m (n = 5-11, m = 1-6) and Ge_nLi_m (n = 5-10, m = 1-6). Assuming that photoionization is a step function transition from a specific initial electronic state to a specific final electronic state, PIE curves can be represented by a sum of error functions, one for each electronic transition. The start of the step function is the ionization threshold, the measurable property most closely related to the AIE, and the inflection point is the VIE. The VIE is the energy difference between the ground state of the neutral and the cation in the neutral cluster's geometry. The AIE corresponds to the energy difference of the neutral and cationic cluster, both in their relaxed ground states. The reference isomer for the cationic cluster can be the isomer with the same structure as the neutral ground state or the cation ground state. The difference between the AIE and the VIE can be large, especially for small clusters when the geometric relaxation can be considerable.

Although knowledge of the ionization efficiencies is vital for the interpretation of mass abundance spectra, the PIE curves were mainly used as a fingerprint to compare with results from density functional theory. Ground state structures were determined for Si_nLi_m (n = 2-11, m = 1-3) and Ge_nLi_m (n = 5-10, m = 1-4). Not for all size there were PIE curves available to compare with, but for most sizes where comparison was possible there is a satisfactory match. The calculated structures are good candidates for the actual ground states. When interpreting the results it is immediately apparent that lithium doped silicon and germanium clusters often have identical structures and in all cases follow similar structural motives. Sometimes silicon or germanium favors a different ordering of low lying isomers. Due to the highly ionic character of the lithium bond towards the cluster, the lithium atom acts as a charge donor, and by investigating lithium doped silicon and germanium clusters different charge states of the bare silicon and germanium clusters can be compared experimentally. Already in the case of the lithium doped silicon and germanium monomer it was clear that lithium behaves as a strong electron donor. Moreover, the electron from the lithium atoms starts filling the atomic orbitals of silicon and germanium atoms. The closing of electronic shells of silicon and germanium atoms by doping with lithium results in enhanced stability. The stability is improved if a spherical shell closing coincides with a spherical symmetric geometry. Differences

between carbon and germanium (silicon) can be explained by differences in atom size and bond lengths but also by the relative position of the energy levels of the participating orbitals. Maybe some of these elements can also be applied to investigate the stability model for the larger lithium doped silicon and germanium clusters. To identify the most stable systems, additional photofragmentation mass abundance spectra of lithium doped silicon and germanium cations were derived. They clearly confirm the high stability of Ge_5^{2-}, Si_5^{2-}, Ge_9^{4-} and Si_9^{4-} units, previously synthesized in solution. Together with neutral Si_7, Ge_7, Si_{10}, and Ge_{10}, which are favoured in dissociation experiments, they form a set of highly stable structures. Each structure has deltahedral geometry with highly regular bond lengths and an associated optimal charge state.

The electronic structure of silicon and germanium clusters is often discussed in terms of sp^3 hybridization. This is in analogy with the boranes where dangling bonds are passivated with hydrogen. However, no evidence of this kind of hybridization is apparent from the density of states (DOS) of these clusters. In fact, there appears to be little bonding between s and p electrons and they form two rather isolated s-bands and p-bands. This is similar to coinage metal clusters where there are independent s and d-bands. Because there is a significant energy gap between the s and the p electrons in the silicon (germanium) atom there is little bonding between them upon cluster formation. The s electrons from the different silicon (germanium) atoms in the cluster bind among each other forming bonding and antibonding combinations. Because all participating orbitals are filled the resulting band has its center at the 3s (4s) atomic energy and no energy can be gained. Similarly, the p electrons of the individual silicon (germanium) atoms bind with each other forming the p-band. As the 3p (4p) orbitals are only occupied by two out of six electrons the total energy of the cluster can be lowered if these electrons only fill low lying orbitals in the cluster p-band, which occurs at a shell closing. The width of the p-band is smaller than the s-band, because the overlap of s orbitals is in general larger compared to p orbitals. The lithium 2s electron is more than 2 eV above the p orbitals of silicon (germanium), and it will basically dump its electron into the partially filled cluster p-band, in essence forming an ionic bond. In the case of small silicon and germanium clusters (<10), there remains a gap between the s-band and the p-band, which implies that the s-band de facto shows a shell closing. With a given number of electrons in this s-band, the number of electrons for that shell closing is set and the structure is forced into a geometry which field induces the given shell closing. As the geometry is determined by the s-band, the total electronic structure will try to lower its energy by filling a closed shell. In some cases, the total number of electrons (s and p) of all silicon (germanium) atoms fill a closed shell, as in the case of Si_7 and Si_{10}. However, in general, this number doesn't match a shell closing and a more stable system can be reached by adding or removing additional electrons, as in the case of Si_5 and Si_9. When the number of neighbors starts to increase the splitting of the bands becomes larger because of the larger overlap. As the s-band and the p-band start to overlap, this will favor sp^3 hybridization and along with it the tetragonal packing from the bulk insulators. At that point, 4 degenerate sp^3 electrons for each atom start to fill spherical shell closings in a spherical potential. Because the energy difference between the 3s and 3p levels of silicon is smaller than the energy difference between the 4s and the 4p levels of germanium, the critical size where the two bands start to overlap is larger for germanium. This explains the different size range of the transition from elongated to spherical structures for silicon and germanium often noticed before.

A future effort will be to do mass selected photofragmentation on lithium doped silicon and germanium clusters. This will complement results from collision induced

dissociation experiments on bare clusters and open up the possibility to get quantitative binding energies. The applicability of the proposed stability model can further be explored by density functional theory on specific cluster sizes and extended towards tin and lead clusters, which are closely related to silicon and germanium clusters. One of the aims of this work is to put a stronger emphasis on DOS plots as a means of understanding a cluster, while in literature the emphasis tends to go to geometrical structure. The DOS illustrates the different energies the electrons have, while the structure shows the position of the atomic cores. The next goal would be to visualize the location of the electrons in a convenient way as well. This is often done by showing plots of individual oribitals. Unfortunately for larger clusters, this becomes a blur of many (spherical) orbitals with seemingly meaningless geometries. It would be very helpful to draw all (near) degenerate orbitals as one large orbital, without making the artificial differentiation. By doing that one gets a good insight in the location of the electron cloud at a given energy (range) and how this matches the geometry of the atomic cores.

I would like to end this chapter with emphasizing the unique character of Ge_9^{4-} and Si_9^{4-}. Without any doubt these are one of the most interesting clusters available. These species have an appealing symmetric structure and a text book electronic structure. Multiple units can be synthezed in solution, stacked, functionalized with organo-metallic groups, or doped with interstitial atoms to tailor the chemical and physical properties of what can be conceived as promising nanomaterials.

Appendix

A.1 Analytical formulas

General formulas for kinetic energy focusing

For infinite order, kinetic energy focusing the following equation has to be solved:

$$\frac{d^i t}{dE_k^i} = \sum_j \frac{d^i t_j}{dE_k^i} = 0, \quad i = 1...\infty \tag{A.1}$$

The solutions for field free regions are given by:

$$\frac{d^i t_j}{dE_k^i} = \left[\prod_1^i \left(\frac{1}{2} - l\right)\right] \left(E_{k,j-1}\right)^{\left(-\frac{1}{2}-i\right)} \sqrt{\frac{m}{2}} L_j, \quad i = 1...\infty \tag{A.2}$$

For any non-zero, linear field region this becomes:

$$\frac{d^i t_j}{dE_k^i} = \left[\prod_1^i \left(\frac{3}{2} - l\right)\right] \frac{\sqrt{2m}}{q} \frac{l_j}{\Delta V_j} \left(\left(E_{k,j-1}\right)^{\frac{1}{2}-i} - \left(E_{k,j}\right)^{\frac{1}{2}-i} \right)^*, \quad i = 1...\infty \tag{A.3}$$

The star (*) means that in the formula each term including $E_{k,j} = 0$ needs to be removed. This is the case for i=0 for zero starting velocity and for the terms corresponding to the final stage of a reflectron. For infinite order, kinetic energy focusing this yields the following equation:

$$\begin{aligned} &\left(i - \frac{1}{2}\right) q \sum_{j'} \left[\left(E_{k,j'-1}\right)^{\left(-\frac{1}{2}-i\right)} L_{j'} \right]^* \\ &= \sum_j \left[\frac{l_j}{\Delta V_j} \left(\left(E_{k,j-1}\right)^{\frac{1}{2}-i} - \left(E_{k,j}\right)^{\frac{1}{2}-i} \right) \right]^*, \quad i = 1...\infty \end{aligned} \tag{A.4}$$

The index j explicitly counts over the non-zero regions, and the index j' over the field free regions. If all field free regions are assumed to be at the same potential, $E_{k,ff}$ can be defined as the kinetic energy in the field free region and L_{ff} the combined length of all field free regions. For second order focusing, then the following set of equations has to be solved:

$$\begin{cases} \dfrac{q}{2}\dfrac{L_{ff}}{E_{k,ff}} = \displaystyle\sum_j \left[\frac{l_j}{\Delta V_j} \left(\left(\frac{E_{k,j-1}}{E_{k,ff}} \right)^{-\frac{1}{2}} - \left(\frac{E_{k,j}}{E_{k,ff}} \right)^{-\frac{1}{2}} \right) \right]^* \\ \dfrac{3q}{2}\dfrac{L_{ff}}{E_{k,ff}} = \displaystyle\sum_j \left[\frac{l_j}{\Delta V_j} \left(\left(\frac{E_{k,j-1}}{E_{k,ff}} \right)^{-\frac{3}{2}} - \left(\frac{E_{k,j}}{E_{k,ff}} \right)^{-\frac{3}{2}} \right) \right]^* \end{cases} \tag{A.5}$$

Based on these equations a number of practical equations for second order focusing can be derived. A similar strategy can be used for potential energy focusing.

Formulas for second order reflectron focusing

In the first general case the reflectron is used to achieve second order focusing. This will be realized by solving the equations (A.5) above for the values of ΔV_{R1} and ΔV_{R2}. Explicit solutions for any given combination of electronic components can be found. First, the contributions of ΔV_{R1} and ΔV_{R2} will be isolated to the left hand side of the equations. A factor of ½ is introduced because the reflectron fields are traversed twice:

$$\begin{cases} \dfrac{l_{R1}}{\Delta V_{R1}} + \left[\dfrac{l_{R2}}{\Delta V_{R2}} - \dfrac{l_{R1}}{\Delta V_{R1}} \right] \left(1 - \dfrac{q\Delta V_{R1}}{E_{k,ff}} \right)^{-\frac{1}{2}} = \dfrac{q}{4}\dfrac{L_{ff}}{E_{k,ff}} - \dfrac{1}{2}\displaystyle\sum_j \left[\frac{l_j}{\Delta V_j} \left(\left(\frac{E_{k,j-1}}{E_{k,ff}} \right)^{-\frac{1}{2}} - \left(\frac{E_{k,j}}{E_{k,ff}} \right)^{-\frac{1}{2}} \right) \right]^* \\ \dfrac{l_{R1}}{\Delta V_{R1}} + \left[\dfrac{l_{R2}}{\Delta V_{R2}} - \dfrac{l_{R1}}{\Delta V_{R1}} \right] \left(1 - \dfrac{q\Delta V_{R1}}{E_{k,ff}} \right)^{-\frac{3}{2}} = \dfrac{3q}{4}\dfrac{L_{ff}}{E_{k,ff}} - \dfrac{1}{2}\displaystyle\sum_j \left[\frac{l_j}{\Delta V_j} \left(\left(\frac{E_{k,j-1}}{E_{k,ff}} \right)^{-\frac{3}{2}} - \left(\frac{E_{k,j}}{E_{k,ff}} \right)^{-\frac{3}{2}} \right) \right]^* \end{cases} \tag{A.6}$$

The index j now sums over all regions except for the reflectron stages. Both equations can be solved towards ΔV_{R2} immediately:

$$\begin{cases} \dfrac{l_{R2}}{\Delta V_{R2}} = \left[\dfrac{q}{4}\dfrac{L_{ff}}{E_{k,ff}} - \dfrac{1}{2}\displaystyle\sum_j \left[\frac{l_j}{\Delta V_j} \left(\left(\frac{E_{k,j-1}}{E_{k,ff}} \right)^{-\frac{1}{2}} - \left(\frac{E_{k,j}}{E_{k,ff}} \right)^{-\frac{1}{2}} \right) \right] - \dfrac{l_{R1}}{\Delta V_{R1}} \right]^* \left(1 - \dfrac{q\Delta V_{R1}}{E_{k,ff}} \right)^{\frac{1}{2}} + \dfrac{l_{R1}}{\Delta V_{R1}} \\ \dfrac{l_{R2}}{\Delta V_{R2}} = \left[\dfrac{3q}{4}\dfrac{L_{ff}}{E_{k,ff}} - \dfrac{1}{2}\displaystyle\sum_j \left[\frac{l_j}{\Delta V_j} \left(\left(\frac{E_{k,j-1}}{E_{k,ff}} \right)^{-\frac{3}{2}} - \left(\frac{E_{k,j}}{E_{k,ff}} \right)^{-\frac{3}{2}} \right) \right] - \dfrac{l_{R1}}{\Delta V_{R1}} \right]^* \left(1 - \dfrac{q\Delta V_{R1}}{E_{k,ff}} \right)^{\frac{3}{2}} + \dfrac{l_{R1}}{\Delta V_{R1}} \end{cases} \tag{A.7}$$

The first equation now gives the solution for first order focusing. In practice this means that by either changing ΔV_{R2} or ΔV_{R1} first order focusing can be achieved. By elimination of ΔV_{R2} we can also solve the equations towards ΔV_{R1}, and after some rewriting we find the following general solution:

$$\begin{cases} \Delta V_{R1} = \dfrac{2E_{k,ff}}{3q} \dfrac{\left(L_{ff} + \sum_j \lambda_j \right) + 2l_{R1}}{\left(L_{ff} + \sum_j \kappa_j \right)} \\ \Delta V_{R2} = \Delta V_{R1} \dfrac{2l_{R2}}{2l_{R1} + \left(L_{ff} + \sum_j \lambda_j \right) \left(1 - \dfrac{q\Delta V_{R1}}{E_{k,ff}} \right)^{\frac{3}{2}}} \end{cases} \tag{A.8}$$

While using the following abbreviations for clarity:

$$\begin{cases} \lambda_j = \dfrac{l_j}{q\Delta V_j} \left(\left(E_{k,ff} - E_{k,j} \right) \left(\dfrac{E_{k,j}}{E_{k,ff}} \right)^{-\frac{3}{2}} - \left(E_{k,ff} - E_{k,j-1} \right) \left(\dfrac{E_{k,j-1}}{E_{k,ff}} \right)^{-\frac{3}{2}} \right)^* \\ \kappa_j = \dfrac{2l_j}{3q\Delta V_j} \left(E_{k,ff} \left(\dfrac{E_{k,j}}{E_{k,ff}} \right)^{-\frac{3}{2}} - E_{k,ff} \left(\dfrac{E_{k,j-1}}{E_{k,ff}} \right)^{-\frac{3}{2}} \right)^* \end{cases} \tag{A.9}$$

It is sometimes useful to solve equations (A.9) for L_{ff}:

$$\begin{cases} L_{ff} = \dfrac{3q\Delta V_{R1} \sum_j \kappa_j - 2E_{k,ff} \left(\sum_j \lambda_j + 2l_{R1} \right)}{2E_{k,ff} - 3q\Delta V_{R1}} \\ L_{ff} = 2\Delta V_{R1} \left(\dfrac{l_{R2}}{\Delta V_{R2}} - \dfrac{l_{R1}}{\Delta V_{R1}} \right) \left(1 - \dfrac{q\Delta V_{R1}}{E_{k,ff}} \right)^{-\frac{3}{2}} - \sum_j \lambda_j \end{cases} \tag{A.10}$$

Through the parameters λ_i and κ_i as many components as necessary can be introduced. If we assume the starting velocity to be equal to zero, which is the case for orthogonal extraction, the following formulas apply for a double stage extraction:

$$\begin{cases} \lambda_{EXT} = \lambda_{E1} + \lambda_{E2} = \Delta V_{E2} \left(\dfrac{l_{E1}}{\Delta V_{E1}} - \dfrac{l_{E2}}{\Delta V_{E2}} \right) \left(1 + \dfrac{q\Delta V_{E2}}{E_{k,ff}} \right)^{-\frac{3}{2}} \\ \kappa_{EXT} = \kappa_{E1} + \kappa_{E2} = \dfrac{2E_{k,ff}}{3q} \dfrac{\left(l_{E2} + \lambda_{EXT} \right)}{\Delta V_{E2}} \end{cases} \tag{A.11}$$

To go from a double to a single stage extraction we can consider the field in both stages of the double stage extraction to be equal to the field in the single stage extraction:

$$\frac{l_{E2}}{\Delta V_{E2}} = \frac{l_{E1}}{\Delta V_{E1}} = \frac{l_E}{\Delta V_E} \tag{A.12}$$

This immediately leads to the following results for single stage extraction:

$$\begin{cases} \lambda_{EXT} = 0 \\ \kappa_{EXT} = \dfrac{2E_{k,ff}}{3q}\dfrac{l_E}{\Delta V_E} \end{cases} \tag{A.13}$$

This result can also be found by applying equations (A.11) directly. Another equivalent approach is to set ΔV_{E2} to zero:

$$\begin{cases} \lambda_{EXT} = l_{E2} \\ \kappa_{EXT} = \dfrac{2E_{k,ff}}{3q}\dfrac{l_{E1}}{\Delta V_{E1}} \end{cases} \tag{A.14}$$

The field of the single stage extraction now equals the field of the first stage of the double stage extraction and the length of the field free path has been extended by the length of the second stage. Moving further down to 'zero stage extraction' corresponds to the constraint $l_E = 0$, which gives the following trivial result:

$$\begin{cases} \lambda_{EXT} = 0 \\ \kappa_{EXT} = 0 \end{cases} \tag{A.15}$$

To incorporate the acceleration just in front of a detector, the following parameters can be used:

$$\begin{cases} \lambda_D = l_D\left(1 - \dfrac{q\Delta V_D}{E_{k,ff}}\right)^{-\frac{3}{2}} \\ \kappa_D = -\dfrac{2E_{k,ff}}{3q}\dfrac{\left(l_D + \lambda_D\right)}{\Delta V_D} \end{cases} \tag{A.16}$$

Formulas for second order extraction focusing

While in the previous paragraph a reflectron was used for focusing, in this paragraph the use of Wiley-McLaren extraction optics for focusing is investigated. This will be realized by solving the equations (A.5) for the values of ΔV_{E2} and ΔV_{E1} following similar calculation steps as in the case of reflectron focusing:

$$\begin{cases} \Delta V_{E2} = -\dfrac{2E_{k,ff}}{3q}\dfrac{L_{ff}+\sum_j \lambda_j + l_{E2}}{L_{ff}+\sum_j \kappa_j} \\ \Delta V_{E1} = \Delta V_{E2}\dfrac{l_{E1}}{l_{E2}+\left[L_{ff}+\sum_j \lambda_j\right]\left(1+\dfrac{q\Delta V_{E2}}{E_{k,ff}}\right)^{\frac{3}{2}}} \end{cases} \tag{A.17}$$

However, the field free kinetic energy in this case is not a free parameter as it is also a function of ΔV_{E2} and ΔV_{E1} through:

$$E_{k,ff} = E_{k,0} - q\Delta V_{E1}\frac{s_0}{l_{E1}} - q\Delta V_{E2} \tag{A.18}$$

If no other component is present and the initial velocity is zero, incorporating this equation into (A.17) yields:

$$\begin{cases} \dfrac{q\Delta V_{E2}}{E_{k,ff}} = -\dfrac{2L_{ff}+2l_{E2}}{3L_{ff}} \\ \dfrac{E_{k,ff}}{q\Delta V_{E2}} + 1 = -\dfrac{s_0}{l_{E2}}\dfrac{1}{1+\dfrac{L_{ff}}{l_{E2}}\left(1+\dfrac{q\Delta V_{E2}}{E_{k,ff}}\right)^{\frac{3}{2}}} \end{cases} \tag{A.19}$$

By combining the two equations, all energies can be eliminated:

$$\left(\frac{L_{ff}-2l_{E2}}{2L_{ff}+2l_{E2}}\right)\left[1+\frac{L_{ff}}{l_{E2}}\left(\frac{L_{ff}-2l_{E2}}{3L_{ff}}\right)^{\frac{3}{2}}\right] = \frac{s_0}{l_{E2}} \tag{A.20}$$

Formulas for deconvolution of the mass spectrum

The Gaussian curve for a peak at t_i, with $\sigma_i = \dfrac{FWHM_i}{2\sqrt{2\ln 2}}$ is given by:

$$f(t) = A_i e^{-\frac{(t-t_i)^2}{2\sigma_i^2}} \tag{A.21}$$

The integral over the whole peak is then:

$$I_{i,\infty} = \int_{-\infty}^{+\infty} f(t)\,dt = A_i\sigma_i\sqrt{2\pi} \tag{A.22}$$

To resemble the convolution of many peaks, the Gaussian functions for the individual peaks are added:

$$f(t) = \sum_i A_i e^{-\frac{(t-t_i)^2}{2\sigma_i^2}} \tag{A.23}$$

For each peak j in the convoluted spectrum the integral over a given interval is:

$$I_j = \int_{t_j-\Delta t}^{t_j+\Delta t} f(t)\,dt = \sum_i A_i \int_{t_j-\Delta t}^{t_j+\Delta t} e^{-\frac{(t-t_i)^2}{2\sigma_i^2}}\,dt = \sqrt{2}\sum_i \sigma_i A_i \int_{\frac{t_j-t_i-\Delta t}{\sqrt{2}\sigma_i}}^{\frac{t_j-t_i+\Delta t}{\sqrt{2}\sigma_i}} e^{-t^2}\,dt \tag{A.24}$$

using the substitution: $t \to \left(t\sqrt{2}\sigma_i + t_i\right)$.

This connects the convoluted integrals and the amplitudes through the following matrix equation:

$$I_j = \sum_i A_i C_{ij} \tag{A.25}$$

The coefficient matrix C is defined by:

$$C_{ij} = 2\sqrt{2\ln 2}\sigma_i \left[erf\left(\frac{t_j - t_i + \Delta t}{\sqrt{2}\sigma_i}\right) - erf\left(\frac{t_j - t_i - \Delta t}{\sqrt{2}\sigma_i}\right)\right] \tag{A.26}$$

where the error function is defined by:

$$erf(x) = \frac{2}{\sqrt{\pi}} \int_0^x e^{-t^2}\,dt \tag{A.27}$$

The integral of the deconvoluted peak j can be written as:

$$I_j^d = A_j C_{jj} \tag{A.28}$$

This can be connected to the convoluted integrals by rewriting the amplitude by inverting the coefficient matrix:

$$A_j = \sum_i I_i C'_{ij} \tag{A.29}$$

C'_{ij} are the coefficients of the inverse coefficient matrix. This immediately results in:

$$I_j^d = C_{jj} \sum_i I_i C_{ij}^{'} \tag{A.30}$$

With:

$$C_{ij} = FWHM_i \left[erf\left(2\sqrt{\ln 2}\, \frac{t_j - t_i + \Delta t}{FWHM_i} \right) - erf\left(2\sqrt{\ln 2}\, \frac{t_j - t_i - \Delta t}{FWHM_i} \right) \right] \tag{A.31}$$

or

$$C_{ij} = FWHM_i \left[erf\left(2\sqrt{\ln 2}\, \frac{m_j - m_i + \Delta m_i}{FWHM_i} \right) - erf\left(2\sqrt{\ln 2}\, \frac{t_j - t_i - \Delta m_i}{FWHM_i} \right) \right] \tag{A.32}$$

A.2 Numerical calculations

Position and velocity spread parallel to the TOF axis:

- RTOF

$$MR_p = \frac{t}{2\Delta t_p} = \frac{a_0 t}{2\Delta v_0} < \frac{50 \frac{mm}{\mu s^2} \cdot 45 \mu s}{2 \cdot 0.060 \frac{mm}{\mu s}} \frac{1}{\sqrt{n_{Au}}} \approx \frac{19 \cdot 10^3}{\sqrt{n_{Au}}}$$

$$MR_k = \frac{t}{2\Delta t_k} = \frac{v_0 t}{2\Delta s_0} \approx \frac{1.0 \frac{mm}{\mu s} \cdot 45 \mu s}{2 \cdot 10 mm} \sqrt{n_{Au}} \approx 2.3 \sqrt{n_{Au}}$$

- HRTTOF – orthogonal extraction

$$MR_p = \frac{t}{2\Delta t_p} = \frac{a_0 t}{2\Delta v_0} > \frac{136 \frac{mm}{\mu s^2} \cdot 100 \mu s}{2 \cdot 0.025 \frac{mm}{\mu s}} \frac{1}{\sqrt{n_{Au}}} \approx \frac{270 \cdot 10^3}{\sqrt{n_{Au}}}$$

$$MR_k = \frac{t}{2\Delta t_k} = \frac{v_0 t}{2\Delta s_0} < \frac{0.0125 \frac{mm}{\mu s} \cdot 100 \mu s}{2 \cdot 10 mm} \sqrt{n_{Au}} \approx 0.063 \sqrt{n_{Au}}$$

- HRTTOF – linear extraction

$$MR_p = \frac{t}{2\Delta t_p} = \frac{a_0 t}{2\Delta v_0} < \frac{136 \frac{mm}{\mu s^2} \cdot 100 \mu s}{2 \cdot 0.060 \frac{mm}{\mu s}} \frac{1}{\sqrt{n_{Au}}} \approx \frac{110 \cdot 10^3}{\sqrt{n_{Au}}}$$

$$MR_k = \frac{t}{2\Delta t_k} = \frac{v_0 t}{2\Delta s_0} \approx \frac{1.0 \frac{mm}{\mu s} \cdot 100 \mu s}{2 \cdot 10 mm} \sqrt{n_{Au}} \approx 5.0 \sqrt{n_{Au}}$$

Position and velocity spread perpendicular to the TOF axis:

- HRTTOF –fixed detector angle

$$MR_{\varphi} = \frac{t}{2\Delta t_{\varphi}} = \frac{t^2 v}{2t \sin\alpha_D d_D} = \frac{100\mu s \cdot 75\frac{mm}{\mu s}}{2 \cdot \sin(1.64°) \cdot 40mm} \approx 3.3 \cdot 10^3$$

$$MR_{y} = \frac{t}{2\Delta t_{y}} = \frac{vt}{2\Delta y \cdot tg\left(\left|\alpha_D - \alpha_E\right|\right)} = \frac{75\frac{mm}{\mu s} \cdot 100\mu s}{2 \cdot 0.25mm \cdot tg\left(0°\right)} \approx \infty$$

- HRTTOF – optimized detector angle

$$MR_{\varphi} = \frac{t}{2\Delta t_{\varphi}} = \frac{t^2 v}{2t_{Ref} \sin\alpha_D d_D} = \frac{3 \cdot 100\mu s \cdot 75\frac{mm}{\mu s}}{2 \cdot \sin(0.030°) \cdot 40mm} \approx 540 \cdot 10^3$$

$$MR_{y} = \frac{t}{2\Delta t_{y}} = \frac{vt}{2\Delta y \cdot tg\left(\left|\alpha_D - \alpha_E\right|\right)} = \frac{75\frac{mm}{\mu s} \cdot 100\mu s}{2 \cdot 0.25mm \cdot tg\left(1.61°\right)} \approx 540 \cdot 10^3$$

Grids

- Extraction

$$MR_{g} = \frac{v_{//} t}{2G_{rms} g \left|q\Delta E\right| \frac{\partial t}{\partial E_{k,//}} v_{\perp}}$$

$$= \frac{28\frac{mm}{\mu s} \cdot 284\mu s}{2 \cdot 0.144 \cdot 0.112mm \cdot 333\frac{eV}{mm} \cdot 0.00030\frac{\mu s}{eV} \cdot 0.40\frac{mm}{\mu s}} \approx 1900 \cdot 10^3$$

$$MR_{g'} \approx \frac{E_k t}{G_{rms} g \left|q\Delta E\right| t_{Ref} \sin\alpha_D} \approx \frac{3 \cdot 5000eV}{0.144 \cdot 0.122mm \cdot 333\frac{eV}{mm} \cdot \sin(1.64°)} \approx 97 \cdot 10^3$$

- Reflectron, entrance grid

$$MR_{g} = \frac{v_{//} t}{2G_{rms} g \left|q\Delta E\right| \frac{\partial t}{\partial E_{k,//}} v_{\perp}}$$

$$= \frac{28\frac{mm}{\mu s} \cdot 284\mu s}{2 \cdot 0.144 \cdot 0.23mm \cdot 55\frac{eV}{mm} \cdot 0.0046\frac{\mu s}{eV} \cdot 0.50\frac{mm}{\mu s}} \approx 300 \cdot 10^3$$

$$MR_{g'} \approx \frac{E_k t}{G_{rms} g \left|q\Delta E\right| t_{Ref} \sin\alpha_D} = \frac{3 \cdot 5000eV}{0.144 \cdot 0.23mm \cdot 55\frac{eV}{mm} \cdot \sin(1.64°)} \approx 286 \cdot 10^3$$

- Reflectron, middle grid

$$MR_g = \frac{v_{//}t}{2G_{rms}g\left|q\Delta E\right|\frac{\partial t}{\partial E_{k,//}}v_\perp}$$

$$= \frac{14\frac{mm}{\mu s}\cdot 284\mu s}{2\cdot 0.144\cdot 0.23mm\cdot 44\frac{eV}{mm}\cdot 0.0052\frac{\mu s}{eV}\cdot 0.90\frac{mm}{\mu s}} \approx 92.10^3$$

$$MR_{g'} \approx \frac{E_k t}{G_{rms}g\left|q\Delta E\right|t_{Ref}\sin\alpha_D} = \frac{3\cdot 5000eV}{0.144\cdot 0.23mm\cdot 44\frac{eV}{mm}\cdot\sin(1.64°)} \approx 357.10^3$$

Electronics

- Extraction

$$MR_{ext} = \frac{t}{2\Delta t_{ext}} = \frac{100\mu s}{2\cdot 1.0ns} \approx 25\cdot 10^3\sqrt{n_{Au}}$$

- Detector + amplifier

$$MR_{\det} = \frac{t}{2\Delta t_{\det}} = \frac{100\mu s}{2\cdot 2.0ns} \approx 50\cdot 10^3\sqrt{n_{Au}}$$

Source cooling

- Radiation:

$$P = \sigma A(T_{sc}^4 - T_{sb}^4)$$

$$= 5.670\,400\cdot 10^{-8}\frac{\mathrm{W}}{\mathrm{m}^2K^4}\cdot 0.00825m^2\cdot\left((300K)^4 - (200K)^4\right) = 3.04W$$

- Convection:

$$P = \frac{C_{mol}n\Delta T}{t} = 20.786\frac{\mathrm{J}}{\mathrm{mol}K}\cdot 1.52\cdot 10^{-7}\mathrm{mol}\cdot\frac{300K}{0.10s} = 9.5mW$$

- Conduction, configuration 1, 2 and 3 (see Figure 2-3):

$$P_1 = \left[\frac{A_{SS}k_{SS}}{l_{SS}} + \frac{A_M k_M}{l_M}\right]\Delta T = \left[\frac{7.1\cdot10^{-6}m^2\cdot14\dfrac{W}{mK}}{0.010m} + \frac{1.3\cdot10^{-5}m^2\cdot1.46\dfrac{W}{mK}}{0.010m}\right]250K = 14W$$

$$P_2 = 4\left[\left(\frac{l_M}{A_M k_M} + \frac{l_{SS}}{A_{SS}k_{SS}}\right)^{-1} + \frac{A_M k_M}{l_M}\right]\Delta T$$

$$= 4\left[\left(\frac{0.0010}{2.5\cdot10^{-4}\cdot1.46} + \frac{0.011}{7.1\cdot10^{-6}\cdot14}\right)^{-1} + \frac{1.3\cdot10^{-5}\cdot1.46}{0.010}\right]\frac{W}{K}300K = 13W$$

$$P_3 = \left[8\left(\frac{l_T}{A_T k_T} + \frac{l_{SS}}{A_{SS}k_{SS}}\right)^{-1} + \frac{A_T k_T}{l_T}\right]\Delta T$$

$$= \left[8\left(\frac{0.0050}{1.3\cdot10^{-5}\cdot0.25} + \frac{0.010}{1.3\cdot10^{-5}\cdot14}\right)^{-1} + \frac{1.7^{-3}\cdot0.25}{0.015}\right]\frac{W}{K}300K = 10W$$

A.3 Custom vacuum components

Source chamber (SS 316L)

- Box chamber in Stainless Steel:

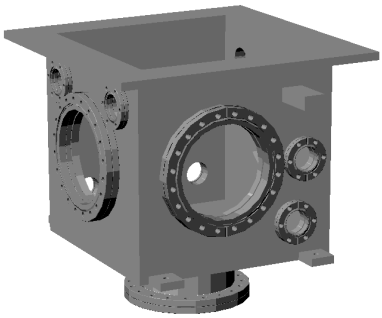

Not shown: hinged lid with DN-160 viewport and handles, O-ring sealed.

- Double sided flange DN-160, with 100 mm aperture and tapped holes

Extraction chamber (SS 304)

- DN-200 6-way cross:

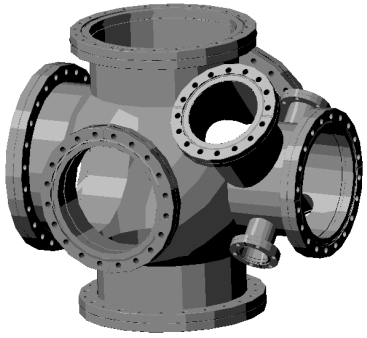

- Reducer flange DN-200/DN-63:

Flight chamber (SS 304)

- 3x DN-350 cylindrical tube (l = 600 mm):

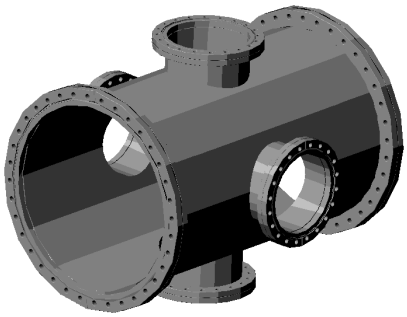

- 2x Custom DN-350 flange:

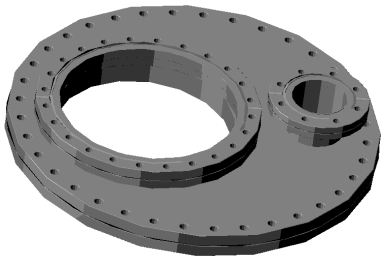

The DN-200 port is on an angle of 1°

- Reducer flange DN-160/DN-40:

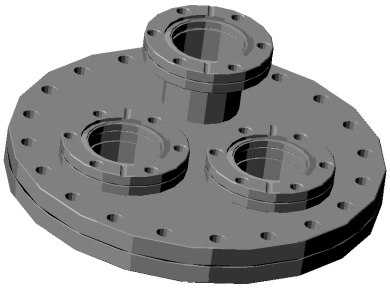

- 2x Cylindrical liner (l = 600 mm, d = 60 mm) with suspension rings

A.4 Overview of cluster structures

Deltahedral structures

Tabel 1: Overview of deltahedra that are found in borane chemistry along with their number of vertices, faces, edges and their symmetry.

Name		Vertices	Faces	Edges	Vertex configurations	Symmetry group
Tetrahedron		4	4	6	4 × 3	T_d
Trigonal bipyramid		5	6	9	2 × 3 3 × 4	D_{3h}
Octahedron	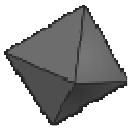	6	8	12	6 × 4	O_h
Pentagonal bipyramid		7	10	15	5 × 4 2 x 5	D_{5h}

Bisdisphenoid		8	12	18	4 × 4 4 x 5	D_{2d}
Tricapped trigonal prism		9	14	21	3 × 4 6 x 5	D_{3h}
Bicapped square antiprism		10	16	24	2 × 4 8 x 5	D_{4d}
Icosahedron		12	20	30	12 × 5	I_h

Bare and lithium doped silicon structures

Quantum chemical computations were carried out by Minh Tam Nguyen and coworkers at the K.U.Leuven Chemistry department with the Gaussian 03 suite of programs.[217] Geometry optimizations were performed for all studied clusters, both in the neutral and the cationic charge state, using the pure B3LYP hybrid functional in conjunction with the 6-311+G(d,p) basis sets. Vibrational frequency analyses characterized all optimized structures as minima and gave zero point vibrational energies.

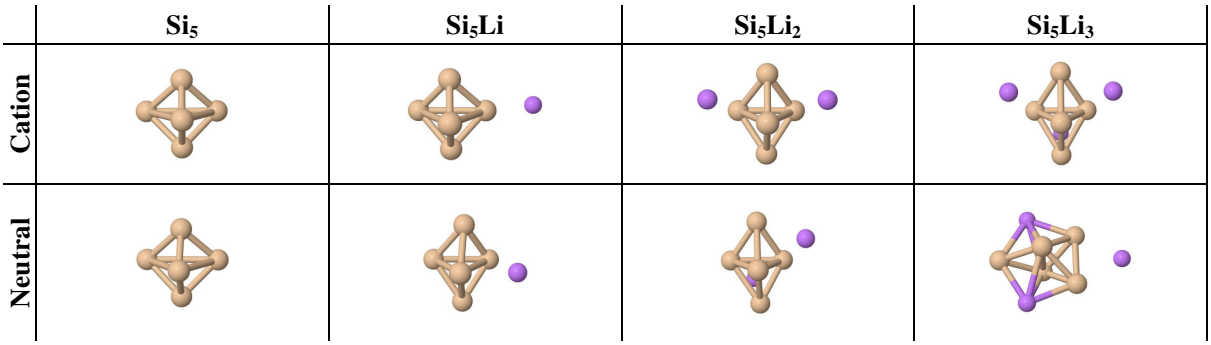

Figure A-1: The shapes of the Si_5Li_{1-3} clusters in both neutral and cationic ground states.

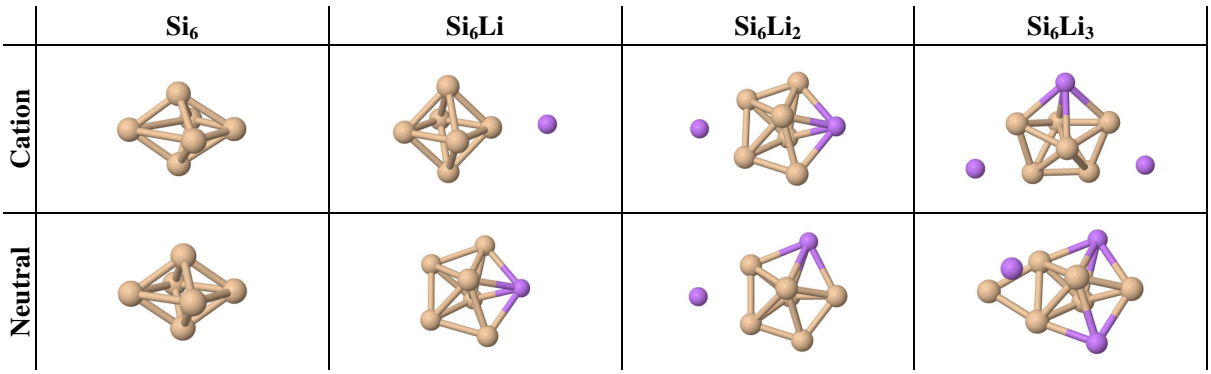

Figure A-2: The shapes of the Si_6Li_{1-3} clusters in both neutral and cationic ground states.

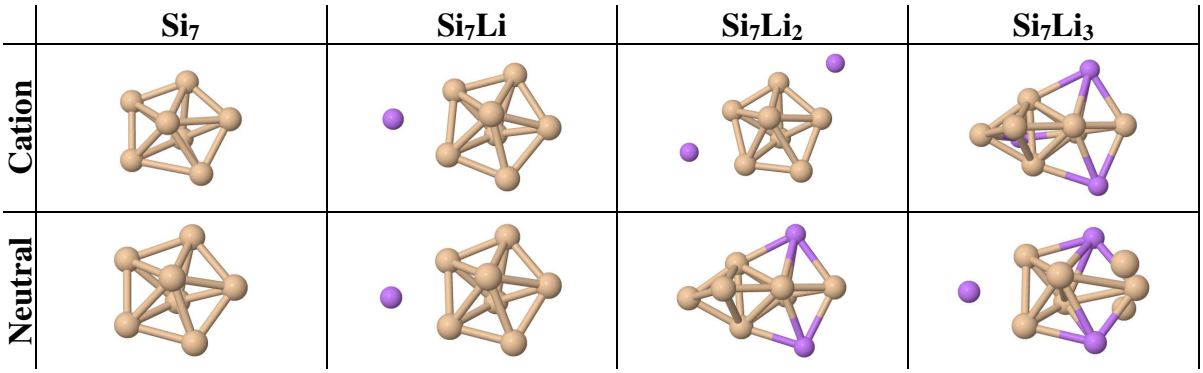

Figure A-3: The shapes of the $Si_7Li_{1\text{-}3}$ clusters in both neutral and cationic ground states.

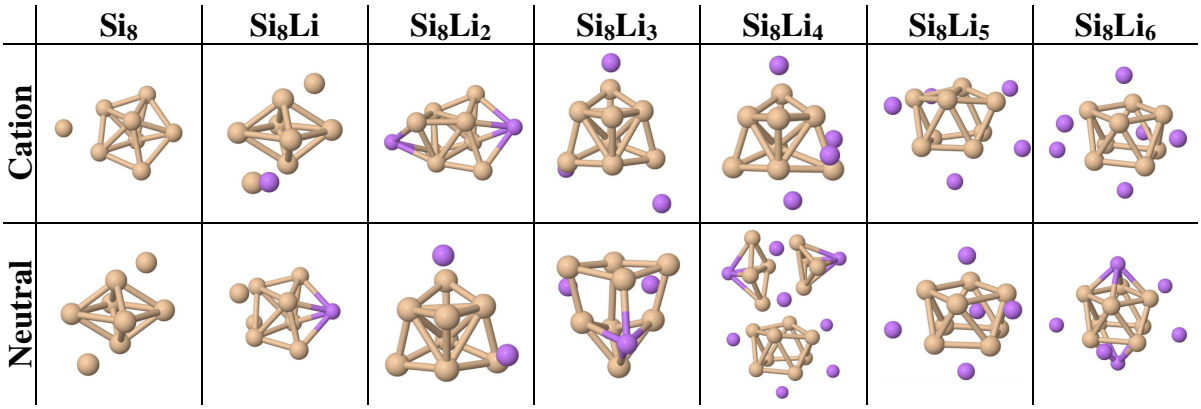

Figure A-4: The shapes of the $Si_8Li_{1\text{-}6}$ clusters in both neutral and cationic ground states.

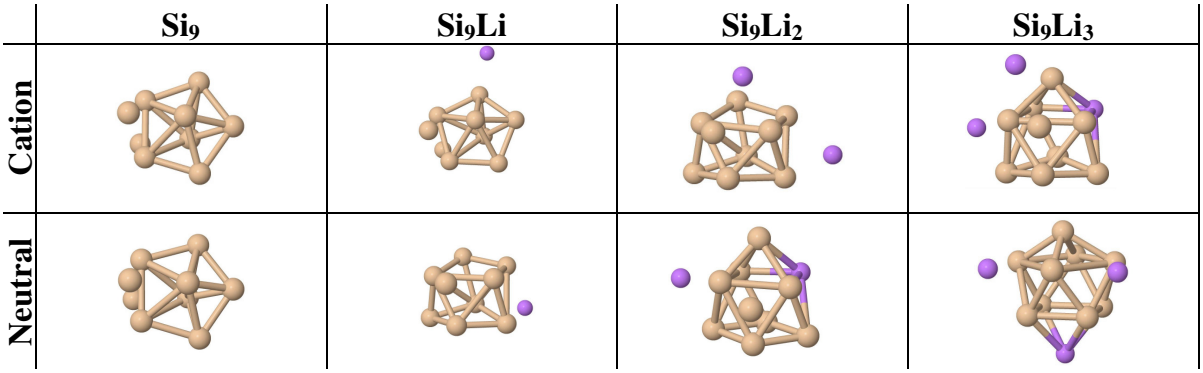

Figure A-5: The shapes of the $Si_9Li_{1\text{-}3}$ clusters in both neutral and cationic ground states.

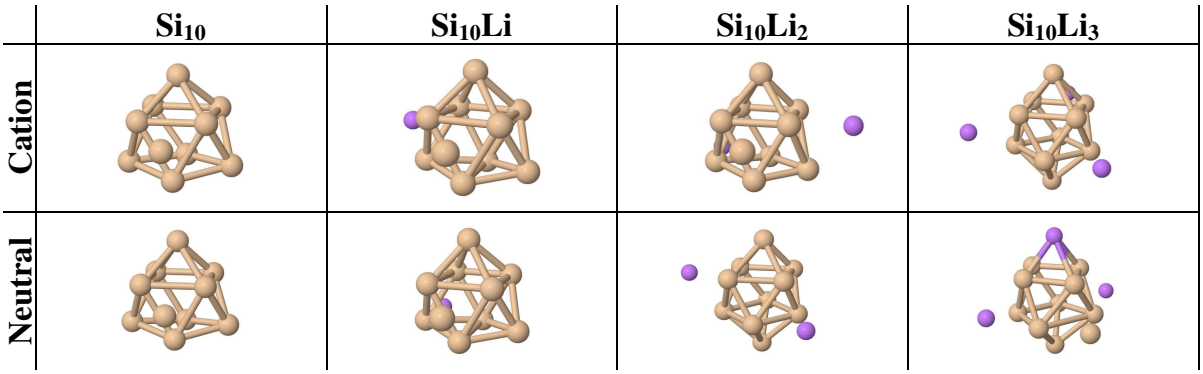

Figure A-6: The shapes of the $Si_{10}Li_{1\text{-}3}$ clusters in both neutral and cationic ground states.

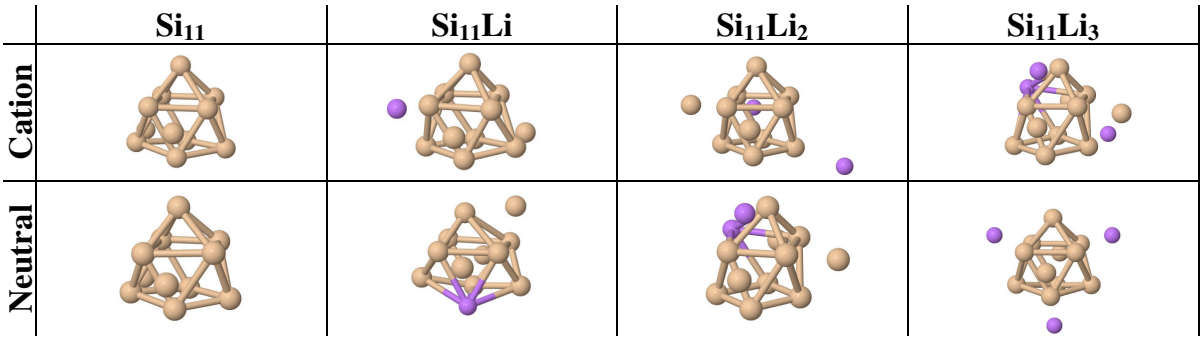

Figure A-7: The shapes of the $Si_{11}Li_{1-3}$ clusters in both neutral and cationic ground states.

Bare and lithium doped germanium structures

Quantum chemical computations were carried out by Truong Ba Tai and coworkers at the K.U.Leuven Chemistry department with the Gaussian 03 suite of programs. The relative energies are determined at the B3LYP/6-311+G(d) level and are corrected for zero point energies.

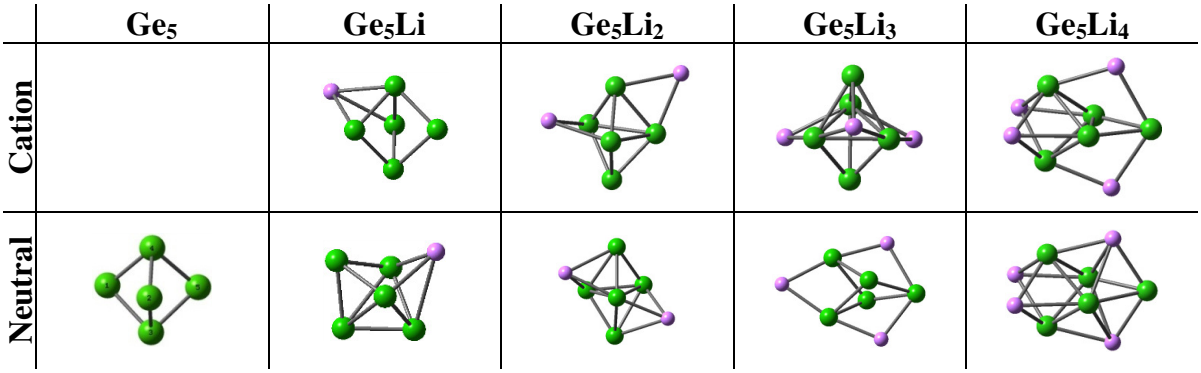

Figure A-8: The shapes of the Ge_5Li_{1-4} clusters in both neutral and cationic ground states.

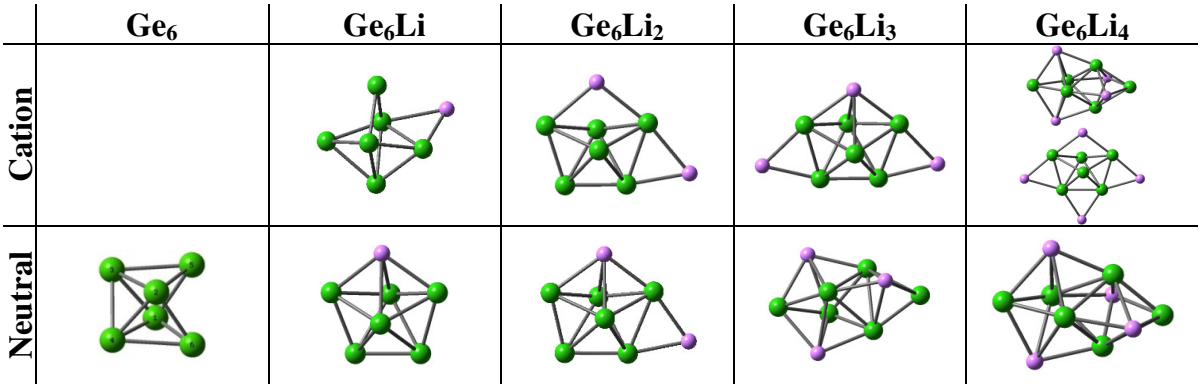

Figure A-9: The shapes of the Ge_6Li_{1-4} clusters in both neutral and cationic ground states.

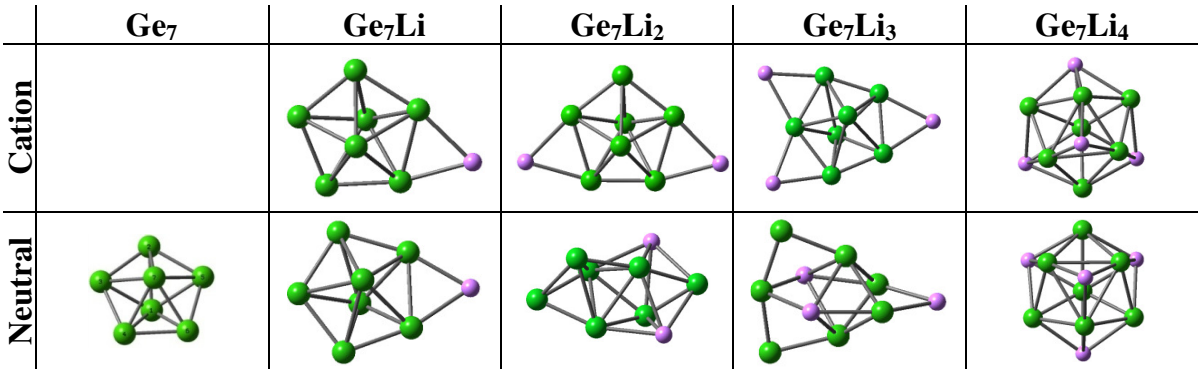

Figure A-10: The shapes of the $Ge_7Li_{1\text{-}4}$ clusters in both neutral and cationic ground states.

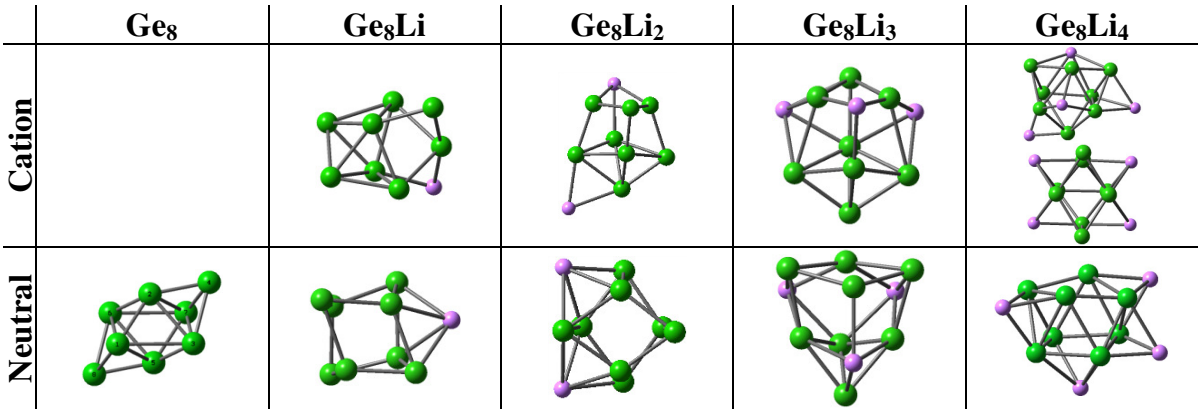

Figure A-11: The shapes of the $Ge_8Li_{1\text{-}4}$ clusters in both neutral and cationic ground states.

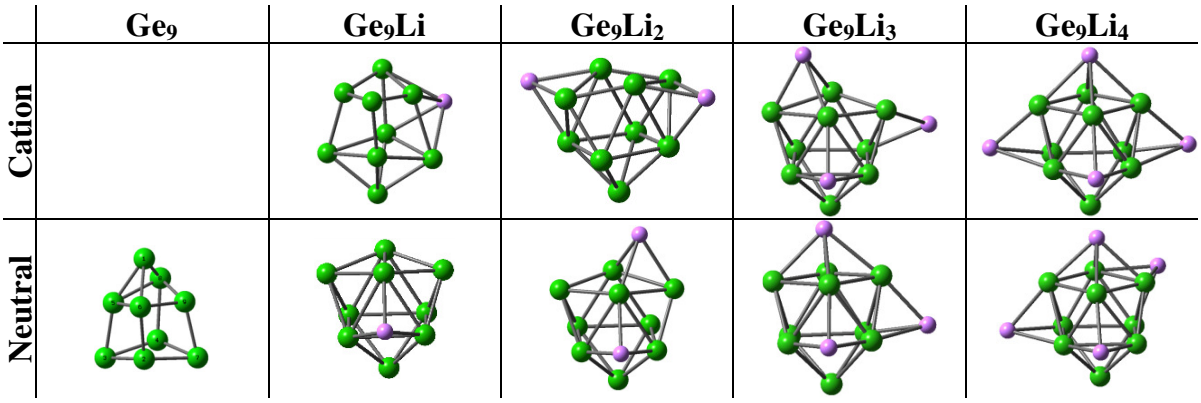

Figure A-12: The shapes of the $Ge_9Li_{1\text{-}4}$ clusters in both neutral and cationic ground states.

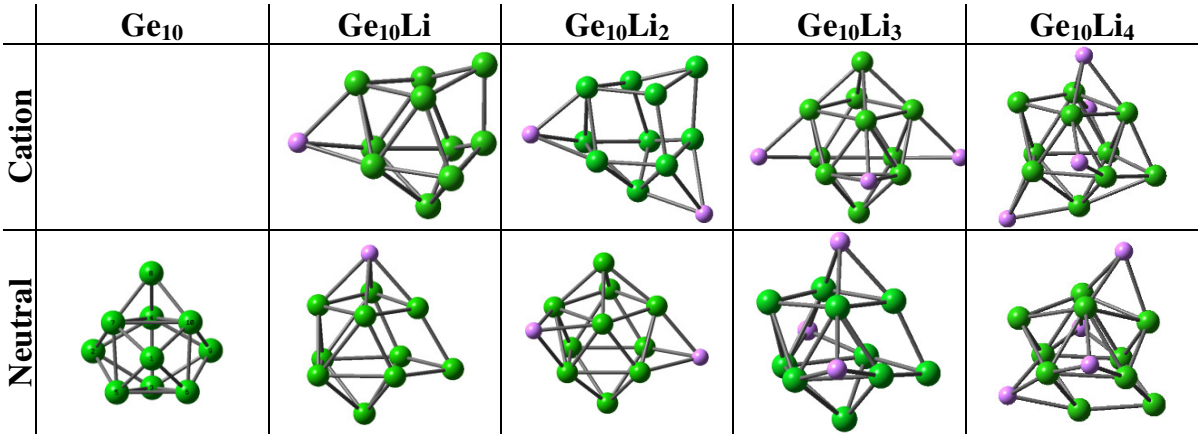

Figure A-13: The shapes of the $Ge_{10}Li_{1\text{-}4}$ clusters in both neutral and cationic ground states.

A.5 Overview of cluster DOS

Bare and lithium doped silicon structures

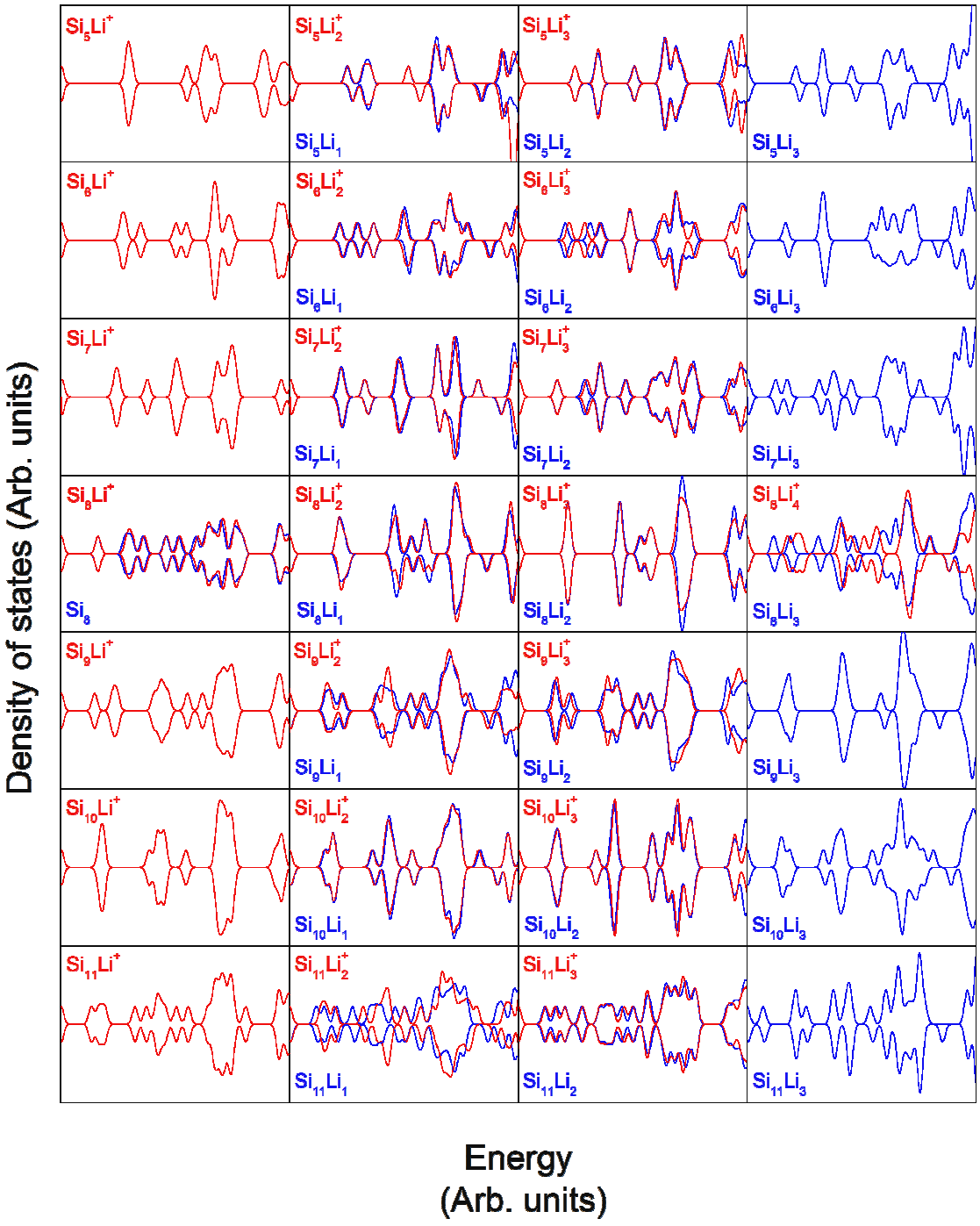

Figure A-14: Comparison of the shape of the density of states (DOS) of isoelectronic $Si_nLi_m^{(+)}$ (n = 6-11; m = 1-3). The energy scale of both systems is calibrated by matching the energetic position of their lowest cluster orbital.

References

1 P. Thoen, 'Lithium monoxide and lithium monocarbide clusters: production by a laser vaporization source and measurement of the ionization', Phd. Thesis, K.U.Leuven (1998)

2 W. Bouwen, 'Productie, stabiliteit en depositie van homo- en hetero-atomaire metallische clusters', Phd. Thesis, K.U.Leuven (2000)

3 J. De Haeck, N. Veldeman, P. Claes, E. Janssens, M. Andersson, and P. Lievens, *J. Phys. Chem. A* **115**, 2103-2109 (2011)

4 G. Gopakumar, X. Wang, L. Lin, J. De Haeck, P. Lievens, and M.T. Nguyen, *J. Phys. Chem. C* **103**, 10858-10867 (2009)

5 N. Veldeman, E. Janssens, K. Hansen, J. De Haeck, R.E. Silverans, and P. Lievens, *Faraday Discuss.* **138**, 147 (2008)

6 J.B. Fenn, M. Mann, C.K. Meng, S.F. Wong, and C.M. Whitehouse, *Science* **246**, 64 (1989)

7 K. Tanaka, *Rapid Commun. Mass Spectrom.* **2**, 151-153 (1988)

8 S.A. McLuckey and J.M. Wells, *Chem. Rev.* **101**, 571-606 (2001)

9 W. Bouwen, P. Thoen, F. Vanhoutte, S. Bouckaert, F. Despa, H. Weidele, R.E. Silverans, and P. Lievens, *Rev. Sc. Instr.* **71**, 54 (2000)

10 R.A. Yost and C.G. Enke, *J. Am. Chem. Soc.***100**, 2274–2275 (1978)

11 M.B. Comisarow and A.G. Marshall, *Chem. Phys. Lett.* **25**, 282-283 (1974)

12 Orbitrap™ is a trademark of Thermo Fisher Scientific, Inc. in the United States and other countries.

13 M. Makarov, *Anal. Chem.* **72**, 1156–1162 (2000)

14 B.A. Mamyrin, V.I. Karataev, D.V. Shmikk, and V.A. Zagulin, *Sov. Phys. JETP* **37**, 45-48 (1973)

15 C.K.G. Piyadasa, P. Hakansson, and T.R. Ariyaratne, *Rapid Commun. Mass Spectrom.* **13**, 620-624 (1999)

16 D. Okumura, M. Toyoda, M. Ishihara, and I. Katakuse, *J. Mass Spectrom.* **39**, 86-90 (2004)

17 M. Guilhaus, D. Selby, and V. Mlynski, *Mass Spec. Rev.* **19**, 65-107 (2000)

18 M. Guilhaus, J. Am. Soc. *Mass Spectrom.* **5**, 588-595 (1994)

19 T. Bergmann, T.P. Martin, and H. Schaber, *Rev. Sci. Instrum.* **60**, 792 (1989)

20 T. Bergmann, T.P. Martin, and H. Schaber, *Rev. Sci. Instrum.* **60**, 347 (1989)

21 T. Bergmann, H. Goehlich, T.P. Martin , H. Schaber, and G. Malegiannakis, *Rev. Sci. Instrum.* **61**, 2585 (1990)

22 T. Bergmann, T.P. Martin, and H. Schaber, *Rev. Sci. Instrum.* **61**, 2592 (1990)

23 T. Bergmann, T.P. Martin, *Int. J. Mass Spectrom. Ion Processes* **131**, 21 (1994)

24 W.A. de Heer and P. Milani, *Rev. Sci. Instrum.* **62(3)**, 670-677 (1991)

25 B. von Issendorff and R. Palmer, *Rev. Sci. Instrum.* **70**, 4497 (1999)

26 P.R. Vlasak, D.J. Beussman, Q. Ji, and C.G. Enke, *J. Am. Soc. Mass Spectrom.* **7**, 1002-1008 (1996)

27 R.J. Cotter, S. Iltchenko, D. Wang, and R. Gundry, *J. Mass Spectrom. Soc. Jpn.* **53(1)**, 7-17 (2005)

28 K. LaiHing, P.Y. Cheng, T.G. Taylor, K.F. Willey, M. Peschke, and M.A. Duncan, *Anal. Chem.* **61**, 1460-1465 (1989)

29 U. Boesl, H.J. Neusser, R. Weinkauf, E.W. Schlag, *J. Phys. Chem.* **86**, 4857 (1992)

30 T.J. Cornish and R.J. Cotter, ACS Symp. Ser. **549,** 95 (1994)

31 H. Nagao, S. Shimma, S. Hayakawa, K. Awazu, and M. Toyoda, *J. Mass. Spectrom.* **45**, 937–943 (2010)

32 D.J. Beussman, P.R. Vlasak, R.D. McLane, M.A. Seeterlin, and C.G. Enke, *Anal. Chem.* **67**, 3952-3957 (1995)

33 S.C. O'Brien, J.R. Heath, R.F. Curl, and R.E. Smalley, *J. Chem. Phys.* **88**, 220 (1988)

34 M.L. Quiniou, A.J. Yates, and P.R.R. Langridge-Smith, *Rapid Commun. Mass Spectrom.* **14**, 361–367 (2002)

35 T.H. Bergmann, 'Entwurf eines Flugzeit-Massenspektrometers und Messungen an Cäsiumoxidclustern', Inaugural-Dissertation, Max-Planck-Institut für Festkörperforschung Stuttgartt (1988)

36 V.M. Doroshenko and R.J. Cotter, *J. Am. Soc. Mass Spectrom.* **10**, 992–999 (1999)

37 C.A. Flory, R.C. Taber, and G.E. Yefchak, *Int. J. Mass Spectrom. Ion Processes* **152**, 177-184 (1996)

38 D.A. Dahl, *Int. J. Mass Spectrom.* **200**, 3 (2000)

39 Excel® and Windows® are registered trademarks of Microsoft Corporation in the United States and other countries.

40 Origin® is a registered trademark of OriginLab Corporation.

41 D.L. Williams, F.H. Read, and N.J. Bowring, *Nucl. Instr. and Meth. in Phys. Res. A* **363**, 120-123 (1995)

42 S.M. Colby and J.J. Manura, Proc. 42nd ASMS Conf. (1997). (Available at www.sisweb.com application note #59)

43 F.H. Read, N.J. Bowring, P.D. Bullivant, and R.R.A. Ward, *Nucl. Instr. and Meth. in Phys. Res. A* **427**, 363-367 (1999)

44 S.M. Colby, C.W. Baker, and J.J. Manura , Proc. 41st ASMS Conf. 1996. (Available at www.sisweb.com application note #47)

45 M. Guilhaus, J. *Am. Soc. Mass Spectrom.* **5**, 588-595 (1994)

46 M. Guilhaus, V. Mlynski, and D. Selby, *Rapid Commun. Mass Spectrom.* **11**, 951–962 (1997)

47 Alibre Design is a Registered Trademark of Alibre, Inc. in the United States and other countries

48 NASA; http://www.grc.nasa.gov/WWW/K-12/airplane/ „isentropic flow”

49 NASA; http://www.grc.nasa.gov/WWW/K-12/airplane/ „mass flow choking”

50 Wikipedia; http://en.wikipedia.org/ „choked flow”

51 Wikipedia; http://en.wikipedia.org/ „de Laval nozzle”

52 http://www.atomox.com/gas_graphs.html

53 G. Scoles, Atomic and molecular beam methods, Oxford university press (1988)

54 Kore Technology Ltd offers products and services in the fields of ultra-high-vacuum design (UHV), surface analysis and time-of-flight mass spectrometry (TOF-MS); http://www.kore.co.uk/index.html

55 C.W.S. Conover, Y.J. Twu, Y.A. Yang, and L.A. Bloomfield, *Rev. Sci. Instum.* **60(6)**, 1065-1070 (1989)

56 D.S. Selby, V. Mlynski, and M. Guilhaus, *Int. J. Mass Spectrom.* **206**, 201–210 (2001)

57 P.R. Vlasak, D.J. Beussman, M.R. Davenport, and C.G. Enke, *Rev. Sci. Instr.* **67**, 68 (1996)

58 JavaTM is a trademark of Sun Microsystems, Inc. in the United States and other countries.

59 Borland® and JBuilder® are registered trademarks of Borland Software Corporation in the United States and other countries.

60 D. Debruyne, 'Drempelfotoionisatie van lithium-gedopeerde siliciumclusters', Master Thesis K.U.Leuven (2010)

61 E.C. Honea, A. Ogura, C.A. Murray, K. Raghavachari, W.O. Sprenger, M.F. Jarrold, and W.L. Brown, *Nature* **366**, 42 (1993)

62 E.C. Honea, A. Ogura, D.R. Peale, C. Félix, C.A. Murray, K. Raghavachari, W.O. Sprenger, M.F. Jarrold, W.L. Brown, *J. Chem. Phys.* **110**, 12161 (1999)

63 S. Li, R.J. Van Zee, J.W. Weltner, and K. Raghavachari, *Chem. Phys.Lett.* **243**, 275 (1995)

64 K.D. Rinnen and M.L. Mandich, *Phys. Rev. Lett.* **69**, 1823 (1992)

65 V. Quéneau, S.C. Sevov, *Angew. Chem. Int. Ed. Engl.* **36**, 1754 (1997)

66 H.G. von Schnering, M. Baitinger, U. Bolle, W. Carrillo-Cabrera, J. Curda, Y. Grin, F. Heinemann, J. Llanos, K. Peters, A. Schmeding and M. Somer, *Z. Anorg. Allg. Chem.* **623**, 1037 (1997)

67 V. Quéneau, E. Todorov, and S.C. Sevov, *J. Am. Chem. Soc.* **120**, 3263 (1998)

68 R.E. Marsh and D.P. Shoemaker, *Acta Crystallogr.* **6**, 197 (1952)

69 H. Schäfer, *Annu. Rev. Mater. Sci*, **15**, 1 (1985)

70 J.M. Goicoechea and S.C. Sevov, *J. Am. Chem. Soc.* **126(22)**, 6860-686 (2004)

71 J. Campbell and G.J. Schrobilgen, *Inorg. Chem.* **36**, 4078 (1997)

72 C. Suchentrunk and N. Korber, *New J. Chem.* **30**, 1737 (2006)

73 D. Rios and S.C. Sevov, *Inorg. Chem.* **49**, 6396 (2010)

74 A. Fielicke, J.T. Lyon, M. Haertelt, G. Meijer, P. Claes, J. De Haeck, and P. Lievens, *J. Chem. Phys.* **131**, 171105 (2009)

75 J.T. Lyon, P. Gruene, A. Fielicke, G. Meijer, E. Janssens, P. Claes, and P. Lievens, *J. Am. Chem. Soc.* **131**, 1115 (2009)

76 O. Cheshnovsky, S. H. Yang, C. L. Pettiette, M. J. Craycraft, Y. Liu, and R. E. Smalley, *Chem. Phys. Lett.* **138**, 119 (1987)

77 J. Müller, B. Liu, A. A. Shvartsburg, S. Ogut, J. R. Chelikowsky, K. W. M. Siu, K.-M. Ho and G. Gantefor, *Phys. Rev. Lett.* **85**, 1666 (2000)

78 M. Astruc Hoffmann, G. Wrigge, B. v. Issendorff, J. Müller, G. Ganteför, and H. Haberland, *Eur. Phys. J. D* **16**, 9 (2001)

79 J. Bai, L.F. Cui, J. Wang, S. Yoo, X. Li, J. Jellinek, C. Koehler, T.Frauenheim, L.S. Wang, and X.C. Zeng, *J. Phys. Chem. A* **110**, 908 (2006)

80 G. Meloni, M. J. Ferguson, S. M. Sheehan, and D. M. Neumark, *Chem. Phys. Lett.* **399**, 389 (2004)

81 D.Y. Zubarev, A.I. Boldyrev, X. Li, L.F. Cui, and L.S. Wang, *J. Phys.Chem. A* **109**, 11385 (2005)

82 G.R. Burton, C.S. Xu, C.C. Arnold, and D.M. Neumark, *J. Chem. Phys.* **104**, 2757 (1996)

83 Y. Negishi, H. Kawamata, F. Hayakawa, A. Nakajima, and K. Kaya, *Chem. Phys. Lett.* **294**, 370-376 (1998)

84 C. Xu, T.R. Taylor, G.R. Burton, and D.M. Neumark, *J. Chem. Phys.* 108, 1395 (1998)

85 G.S. Icking-Konert, H. Handschuh, P.S. Bechthold, G. Ganteför, B.Kessler, and W. Eberhardt, *Surf. Rev. Lett.* **3**, 483 (1996)

86 D.J. Trevor, D.M. Cox, K.C. Reichmann, R.O. Brickman, and A. Kaldor, *J. Phys. Chem.* **91**, 2598 (1987)

87 K. Fuke, K. Tsukamoto, F. Misaizu, and M.J. Sanekata, *Chem. Phys.* **99**, 7807 (1993)

88 C.B. Winstead, S.J. Paukstis, and J.L. Gole, *J. Mol. Spectrosc.* **173**, 311 (1995)

89 A. Marijnissen and J.J. ter Meulen, *J. Chem. Phys. Lett.* **263**, 803 (1996)

90 B.H. Boo and P.B. Armentrout, *J. Am. Chem. Soc.* **109**, 3549 (1987)

91 D.A. Dixon, D. Feller, K.A. Peterson, and J.L. Gole, *J. Phys. Chem. A* **104**, 2326-2332 (2000)

92 J.B. Jaeger, T.D. Jaeger, and M.A. Duncan, *J. Phys. Chem. A* **110**, 9310 (2006)

93 O. Kostko, S.R. Leone, M.A. Duncan, and M. Ahmed, *J. Phys. Chem. A* **114**, 3176–3181 (2010)

94 W. Vonniessen and V.G. Zakrzewski, *J. Chem. Phys.* **98**, 1271 (1993)

95 J.J. Zhao, X.S. Chen, Q. Sun, F.Q. Liu, and G.H. Wang, *Phys. Lett. A* **198**, 243 (1995)

96 S.Q. Wei, R.N. Barnett, and U. Landman, *Phys. Rev. B* **55**, 7935 (1997)

97 S. Nigam, C. Majumder, and S.K. Kulshreshtha, *J. Chem. Phys.* **121**, 7756 (2004)

98 B. Liu, Z.Y. Lu, B.C. Pan, C.Z. Wang, K.M. Ho, A.A. Shvartsburg, and M.F. Jarrold, *J. Chem. Phys.* **109**, 9401 (1998)

99 C. Jo and K. Lee, *Phys. Lett. A* **263**, 376 (1999)

100 S. Ishii, K. Ohno, V. Kumar, and Y. Kawazoe, *Phys. Rev. B* **68**, 5 (2003)

101 S. Yoshida and K. Fuke, *J. Chem. Phys.* **111**, 3880 (1999)

102 K. Fuke and S. Yoshida, *Eur. Phys. J. D* **9**, 123-126 (1999)

103 A.A. Shvartsburg, R.R. Hudgins, P. Dugourd, and M.F. Jarrold, *Chem.Soc. Rev.* **30**, 26 (2001)

104 R.R. Hudgins, M. Imai, M.F. Jarrold, and P. Dugourd, *J. Chem. Phys.* **111**, 7865 (1999)

105 M.F. Jarrold and V.A. Constant, *Phys. Rev. Lett.* **67**, 2994 (1991)

106 M.F.Jarrold and J.E. Bower, *J. Chem. Phys.* **96**, 9180 (1992)

107 A.A. Shvartsburg, B. Liu, Z.Y. Lu, C.Z. Wang, M.F. Jarrold, and K.M. Ho, *Phys. Rev. Lett.* **83(11)**, 2167-2170 (1999)

108 J.M. Hunter, J.L. Fye, M.F. Jarrold, and J.E. Bower, *Phys. Rev. Lett.* **73**, 2063 (1994)

109 J.R. Heath, Y. Liu, S.C. OBrien, Q.L. Zhang, R.F. Curl, F.K. Tittel, and R.E. Smalley, *J. Chem. Phys.* **83**, 5520 (1985)

110 Q.L. Zhang, Y. Liu, R.F. Curl, F.K. Tittel, and R.E. Smalley, *J. Chem. Phys.* **88**, 1670-1677 (1988)

111 Y. Liu, Q.L. Zhang, F.K. Tittel, R.F. Curl, and R.E. Smalley, *J. Chem. Phys.* **85**, 7434-7441 (1986)

112 W. Qin, W.C. Lu, L.Z. Zhao, Q.J. Zang, C.Z. Wang, and K.M. Ho, *J. Phys. Condens. Matter* **21**, 455501 (2009)

113 A.D. Zdetsis, *J. Chem. Phys.* **127**, 244308 (2007)

114 A.D. Zdetsis, *J. Chem. Phys.* **127**, 014314 (2007)

115 W. Xu, Y. Zhao, Q. Li, Y. Xie, and H.F. Schaefer III, *Mol. Phys.* **102**, 579 (2004)

116 R.B. King, I. Silaghi-Dumitrescu, and A. Kun, *Dalton Trans.,* 3999 (2002)

117 R.B. King and I. Silaghi-Dumitrescu, *Inorg. Chem.* **42**, 6701 (2003)

118 R.B. King, I. Silaghi-Dumitrescu, and A. Lupan, *Inorg. Chem.* **44**, 3579 (2005)

119 R.B. King, I. Silaghi-Dumitrescu, and A. Lupan, *Dalton Trans.,* 1858 (2005)

120 R.B. King, I. Silaghi-Dumitrescu, and A. Lupan, *Chem. Phys.* **327**, 344 (2006)

121 R.B. King, I. Silaghi-Dumitrescu, and M.M. Uta, *Inorg. Chem.* **45**, 4974–4981 (2006)

122 R.B. King, I. Silaghi-Dumitrescu, and M.M. Uta, *Dalton Trans.,* 364 (2007)

123 R.B. King, I. Silaghi-Dumitrescu, and M.M. Uta, *Eur. J. Inorg. Chem.* **2008**, 3996–4003 (2008)

124 R.B. King, I. Silaghi-Dumitrescu, and M.M. Uta, *J. Chem. Theory Comput.* **4**, 209-215 (2008)

125 R.B. King and I. Silaghi-Dumitrescu, *Dalton Trans.,* 6083 (2008)

126 F.S. Liang and B.X. Li, *Phys. Lett. A* **328**, 407 (2004)

127 S. Bulusu, S. Yoo, and X.C. Zeng, *J. Chem. Phys.* **122**, 164305 (2005)

128 S. Yoo and X.C. Zeng, *J. Chem. Phys.* **124**, 184309 (2006)

129 S. Yoo and X.C. Zeng, *Angew. Chem. Int. Ed.* **44**, 1491 (2005)

130 S. Yoo, N. Shao, and X.C. Zeng, *J. Chem. Phys.* **128**, 104316 (2008)

131 J.L. Wang, G.H. Wang, and J.J. Zhao, *Phys. Rev. B* **64**, 205411 (2001)

132 L. Wang and J. Zhao, *J. Chem. Phys.* **128**, 024302 (2008)

133 J. Wang, J. Zhao, L. Ma, and G. Wang, *Eur. Phys. J. D* **45**, 289–294 (2007)

134 L. Ma, J. Zhao, J. Wang, B. Wang, and G. Wang, *Phys. Rev. A* **73**, 063203 (2006)

135 O. Oña, V. Bazterra, M. Caputo, J. Facelli, P. Fuentealba, and M. Ferraro, *Phys. Rev. A* **73**, 053203 (2006)

136 K.M. Ho, A.A. Shvartsburg, B.C. Pan, Z.Y. Lu, C.Z. Wang, J. Wacker, J.L. Fye, and M.F. Jarrold, *Nature* **392**, 582 (1998)

137 L.Z. Zhao, W.C. Lu, W. Qin, Q.J. Zang, C.Z. Wang, and K.M. Hoc, *Chem. Phys. Lett.* **455**, 225–231 (2008)

138 W. Qin, W.C. Lu, Q.J. Zang, L.Z. Zhao, G.J. Chen, C.Z. Wang, and K.M. Ho, *J. Chem. Phys.* **132**, 214509 (2010)

139 W. Qin, W.C. Lu, L.Z. Zhao, Q.J. Zang, G.J. Chen, C.Z. Wang, and K.M. Ho, *J. Chem. Phys.* **131(12)**, 124507 (2009)

140 K. Jackson, M. Horoi, I. Chaudhuri, T. Frauenheim, and A. Shvartsburg, *Phys. Rev. Lett.* **93**, 013401 (2004)

141 R.L. Zhou and B.C. Pan, *J. Chem. Phys.* **128**, 234302 (2008)

142 P.A. Edwards and J.D. Corbett, *Inorg. Chem.* **16**, 903 (1977)

143 E.F. Archibong and A. St-Amant, *J. Chem. Phys.* **109**, 962 (1998)

144 P. Kircher, G. Huttner, K. Heinze, and G. Renner, *Angew. Chem. Int. Ed.* **37**, 1664 (1998)

145 T.F. Fässler, *Coord. Chem. Rev.* **215**, 347-377 (2001)

146 R.W. Rudolph, W.L. Wilson, F. Parker, R.C. Taylor, and D.C. Young, *J. Am. Chem. Soc.* **100**, 4629 (1978)

147 R.W. Rudolph, W.L. Wilson, and R.C. Taylor, *J. Am. Chem. Soc.* **103**, 2480 (1981)

148 T.F. Fässler and M. Hunziker, *Inorg. Chem.* **33**, 5380 (1994)

149 S. Ögüt and J.R. Chelikowsky, *Phys. Rev. B* **55**, 4914 (1997)

150 B.X. Li and P.L. Cao, *Phys. Stat. Sol. (b)* **218**, 399 (2000)

151 T.B. Tai and M.T. Nguyen, *Chem. Phys. Lett.* **492**, 290–296 (2010)

152 V.T. Ngan, 'Transition Metal Doped Silicon Clusters: Structural, Electronic and Spectroscopic Properties', Phd. Thesis, K.U.Leuven (2011)

153 P. Claes, Phd. Thesis, K.U.Leuven (expected 2012)

154 S.D. Li, Q.L. Guo, X.F. Zhao, H.S. Wu, and Z.H. Jin, *J. Chem. Phys.* **117**, 606 (2002)

155 S.D. Li, G.M. Ren, and Z.H. Jin, *J. Chem. Phys.* **119**, 10063 (2003)

156 R. Kishi, S. Iwata, A. Nakajima, and K. Kaya, *J. Chem. Phys.* **107**, 3056 (1997)

157 R. Kishi, H. Kawamata, Y. Negishi, S. Iwata, A. Nakajima, and K. Kaya, *J. Chem. Phys.* **107**, 10029 (1997)

158 G. Gopakumar, P. Lievens, and M. T. Nguyen, *J. Chem. Phys.* **124**, 214312 (2006)

159 G. Gopakumar, P. Lievens, and M. T. Nguyen, *J. Phys. Chem. A* **111**, 4353 (2007)

160 X. Wang, 'Mass spectrometric study of metal-doped group IV clusters', Phd. Thesis, K.U.Leuven (2006)

161 S. Neukermans, X. Wang, N. Veldeman, E. Janssens, R.E. Silverans, and P. Lievens, *Int. J. Mass Spectrom.* **252**, 145–150 (2006)

162 S.M. Beck, *J. Chem. Phys.* **90**, 6306 (1989)

163 V.T. Ngan, P. Gruene, P. Claes, E. Janssens, A. Fielicke, M.T. Nguyen, and P. Lievens, *J. Am. Chem. Soc.* **132** (44), 15589–15602 (2010)

164 X.J. Li and K.H Su, *Theor. Chem. Acc.* **124**, 345–354 (2009)

165 J. Wang, Y. Liu, and Y.C. Li, *Phys. Lett. A* **374**, 2736–2742 (2010)

166 A. Spiekermann, S.D. Hoffmann, F. Kraus, and T.F. Fässler, *Angew. Chem. Int. Ed.* **46**, 1638 (2007)

167 K. Koch, A. Schnepf, and H. Schnöckel, *Z. Anorg. Allg. Chem.* **632**, 1710-1716 (2006)

168 C. Schenk and A. Schnepf, Angew. *Chem. Int. Ed.* **46**, 5315 (2007)

169 A. Ugrinov and S.C. Sevov, *J. Am. Chem. Soc.* **125**, 14059–14064 (2003)

170 L. Xu, S.C. Sevov, *J. Am. Chem. Soc.* **121**, 9245–9246 (1999)

171 A. Ugrinov and S.C. Sevov, *J. Am. Chem. Soc.* **124**, 10990–10991 (2002)

172 C. Downie, Z. Tang, and A.M. Guloy, *Angew. Chem. Int. Ed.* **39**, 337–340 (2000)

173 A. Ugrinov and S.C. Sevov, *Inorg. Chem.* **42**, 5789 (2003)

174 A. Ugrinov and S.C. Sevov, *C. R. Chimie* **8**, 1878 (2005)

175 P.D. Pancharatna and R. Hoffmann, *Inorg. Chem. Acta* **359**, 3776 (2006)

176 G.S. Armatas and M.G. Kanatzidis, *Nature* **441**, 1122–1125 (2006)

177 D. Sun, A.E. Riley, A.J. Cadby, E.K. Richman, S.D. Korlann, and S.H. Tolbert, *Nature* **441**, 1126–1130 (2006)

178 G.S. Armatas and M.G. Kanatzidis, *Science* **313**, 817–820 (2006)

179 G.S. Armatas and M.G. Kanatzidis, *Adv. Mater.* **20**, 546–550 (2008)

180 G.S. Armatas and M.G. Kanatzidis, *J. Am. Chem. Soc.* **130**, 11430–11436 (2008)

181 J.M. Goicoechea and S.C. Sevov, *J. Am. Chem. Soc.* **128**, 4155–4161 (2006)

182 J.M. Goicoechea and S.C. Sevov, *Organometallics* **25**, 4530–4536 (2006)

183 A. Spiekermann, S.D. Hoffmann, T.F. Fässler, I. Krossing, and U. Preiss, *Angew. Chem. Int. Ed.* **46**, 5310–5313 (2007)

184 A. Nienhaus, R. Hauptmann, and T.F. Fässler, *Angew. Chem. Int. Ed.* **41**, 3213–3215 (2002)

185 M.B. Boeddinghaus, S.D. Hoffmann, and T.F. Fässler, *Z. Anorg. Allg. Chem.* **633**, 2338–2341 (2007)

186 A. Ugrinov and S.C. Sevov, *Chem. Eur. J.* **10**, 3727 (2004)

187 J.M. Goicoechea and S.C. Sevov, *Angew. Chem. Int. Ed.* **44**, 4026 (2005)

188 S. Scharfe, F. Kraus, S. Stegmaier, A. Schier, and T.F. Fässler, *Angew. Chem. Int. Ed.* **50**, 3630–3670 (2011)

189 C.H. Wu, H. Kudo, and H.R. Ihle, *J. Chem. Phys.* **70**, 1534 (1979)

190 C.H. Wu, *Chem. Phys. Let.* **139**, 357 (1987)

191 H.I. Kudo, *Nature* **355**, 432 (1992)

192 Y. Li, D. Wu, Z.R. Li, and C.C. Sun, *J. Comput. Chem.* **28**, 1677 (2007)

193 R.O. Jones, A.I. Lichtenstein, and J.J. Hutter, *Chem. Phys.* **106**, 4566 (1997)

194 M.S. Lee, S. Gowtham, H. He, K.C. Lau, L. Pan, and D.G. Kanhere, *Phys. Rev. B* **74**, 245412 (2006)

195 P. Lievens, P. Thoen, S. Bouckaert, W. Bouwen, F. Vanhoutte, H. Weidele, R.E. Silverans, A. Navarro-Vazquez, and P.v.R. Schleyer, *Eur. Phys. J. D* **9**, 289 (1999)

196 K. Joshi and D.G. Kanhere, *Phys. Rev. A* **65**, 043203 (2002)

197 S. Shetty, S. Pal, and D.G. Kanhere, *J. Chem. Phys.* **118**, 7288 (2003)

198 P. Lievens, P. Thoen, S. Bouckaert, W. Bouwen, F. Vanhoutte, H. Weidele, R.E. Silverans, A. Navarro-Vazquez, and P.v.R. Schleyer, *J. Chem. Phys.* **110**, 10316 (1999)

199 P. Lievens, P. Thoen, S. Bouckaert, W. Bouwen, F. Vanhoutte, H. Weidele, and R.E. Silverans, *Chem. Phys. Let.* **302**, 571 (1999)

200 V.T. Ngan, J. De Haeck, H.T. Le, G. Gopakumar, P. Lievens, and M.T. Nguyen, *J. Phys. Chem. A* **113**, 9080–9091 (2009)

201 C. Yannouleas and U. Landman, *Phys. Rev. B* **51**, 1902 (1995)

202 S. Neukermans, E. Janssens, H. Tanaka, R.E. Silverans, P. Lievens, K. Yokoyama, and H. Kudo, *J. Chem. Phys.* **119**, 14 (2003)

203 A.D. Becke, *J. Chem. Phys.* **104**, 1040 (1996)

204 C.T. Lee, W.T. Yang, and R.G. Parr, *Phys. Rev. B* **37**, 785 (1988)

205 T.H. Dunning Jr., *J. Chem. Phys.* **90**, 1007 (1989)

206 R.A. Kendall, T.H. Dunning Jr., and R.J. Harrison, *J. Chem. Phys.* **96**, 6796 (1992)

207 C.J. Marsden, Chem. *Phys. Lett.* **245**, 475 (1995)

208 P.v.R. Schleyer and J. Kapp, *Chem. Phys. Lett.* **255**, 363 (1996)

209 N. He, H.B. Xie, and Y.H. Ding, *J. Comput. Chem.* **29**, 1850–1858 (2008)

210 P.v.R. Schleyer, New Horizons of Quantum Chemistry (Reidel Dordrecht), 95 (1983)

211 A. Dhavale, V. Shah, and D.G. Kanhere, *Phys Rev A* **57**, 4522 (1998)

212 E. Janssens, S. Neukermans, F. Vanhoutte, R. E. Silverans, P. Lievens, A. Navarro-Vázquez, and P.v.R. Schleyer, *J. Chem. Phys.* **118**, 5862 (2003)

213 P.M. Guyon, and J. Berkowitz, *J. Chem. Phys.* **54**, 1814 (1971)

214 J. Akola, H. Häkkinen, and M. Manninen, *Eur. Phys. J. D* **9**, 179 (1999)

215 W.A. Saunders, K. Clemenger, W.A. de Heer, and W.D. Knight, *Phys. Rev. B* **32**, 1366 (1985)

216 T. Bergmann and T.P. Martin, *J. Chem. Phys.* **90**, 2848 (1989)

217 Gaussian 03, Revision A.1, M.J. Frisch, G.W. Trucks, H.B. Schlegel, and coworkers, Gaussian, Inc., Pittsburgh PA (2003)

218 A.D. Becke, *Phys. Rev. A* **38**, 3098 (1988)

219 Gaussian 03, Revision D.02, M. J. Frisch and coworkers, Gaussian, Inc., Wallingford CT (2004)

220 Molpro, version 2008.1, H. J. Werner and coworkers

221 A.D. Becke, *J. Chem. Phys.* **98**, 5648 (1993)

222 T.M. Tai and M.T. Nguyen, *J. Chem. Theory. Comput.* **7(4)**, 1119-1130 (2011)

223 P. Lievens, P. Thoen, S. Bouckaert, W.Bouwen, F. Vanhoutte, H.Weidele, R.E. Silverans, A. Navarro-Vazquez, and P.v.R. Schleyer, *Eur. Phys. J. D* **9**, 289 (1999)

224 W. de Heer, *Rev. Mod. Phys.* **65**, 611-676 (1993)

225 W.D. Knight, K. Clemenger, W.A. de Heer, W.A. Saunders, M.Y. Chou, and M.L. Cohen, *Phys. Rev. Lett.* **52**, 2141 (1984)

226 K. Clemenger, *Phys. Rev. B* **32**, 1359-1362 (1985)

227 S.G. Nilsson, *K. Dan. Vidensk. Selsk. Mat. Fys. Medd.* **29**, 16 (1955)

228 G. Wrigge, M.A. Hoffmann, and B. von Issendorff, *Phys. Rev. A* **65**, 063201 (2002)

229 C. Bartels, C. Hock, J. Huwer, R. Kuhnen, J. Schwöbel, and B. von Issendorff, *Science* **323**, 1323 (2009)

230 E. Janssens, S. Neukermans, and P. Lievens, *Curr. Opin. Solid State Mat. Sci.* **8**, 185–193 (2004)

231 J. Daintith, Oxford Dictionary of Chemistry, Oxford University Press NY (ISBN 0-19-860918-3, 2004)

232 M.J. Licker, McGraw-Hill Concise Encyclopedia of Chemistry, McGraw-Hill NY (ISBN 0-07-143953-6, 2004)

233 J. Clayden, N. Greeves, S. Warren, and P. Wothers, Organic Chemistry (1st ed.), Oxford University Press. 96–103 (ISBN 978-0-19-850346-0, 2000)

234 M.A. Fox and J.K. Whitesell, Organic Chemistry (3th ed.), (ISBN 978-0-7637-3586-9, 2003)

235 P.Y. Bruice, Organic Chemistry (3rd ed.), (ISBN 0-13-017858-6, 2001)

236 K. Wade, *Chem. Commun.* 792 (1971)

237 Wikipedia; http://en.wikipedia.org/wiki/Crystal_field_theory

238 Scienceworld (http://scienceworld.wolfram.com/chemistry/CrystalFieldTheory.html)

239 J.E. Sansonetti, W.C. Martin, and S.L. Young, Handbook of Basic Atomic Spectroscopic Data (version 1.1.2), National Institute of Standards and Technology, Gaithersburg MD (2005), [Online: http://physics.nist.gov/Handbook (2011, February 15)]

Curriculum vitae

Jorg De Haeck

1978, July 17 Born in Borgerhout, Belgium

1990-1996 Latin-Greek
Onze-Lieve-Vrouw van Lourdescollege Edegem

1996-1997 1st bachelor in Mathematics (with distinction)
Universiteit Antwerpen

1998-1999 Bachelor in Physics (with distinction)
Universiteit Gent

1999-2001 Master in Physics (with great distinction)
Universiteit Gent
Dissertation: 'Fysica leren en begrijpen: begripsvorming bij golfverschijnselen'

2001-2002 Teaching degree in Physics (with great distinction)
Universiteit Gent

2001-2005 Teacher in secondary school
Sint-Janscollege (Gent)
Berthout Instituut-Klein Seminarie (Mechelen)
Instituut Heilig Hart van Maria (Berlaar)

2004-2005 Parttime teaching assistant
Universiteit Antwerpen

2005-2010 Ph.D. candidate in Physics
K.U.Leuven

List of publications

1. Stability and dissociation pathways of doped Au_nX^+ clusters (X = Y, Er, Nb)
   N.Veldeman, E. Janssens, K. Hansen, J. De Haeck, R.E. Silverans and P. Lievens, *Faraday Discuss.* **138**, 147 (2008)

2. Growth Mechanism and Chemical Bonding in Scandium-Doped Copper Clusters: Experimental and Theoretical Study in Concert
   T. Holtzl, N. Veldeman, J. De Haeck, T. Veszpremi, P. Lievens and M.T. Nguyen, *Chem. Eur. J.* **15**, 3970 (2009)

3. Experimental Detection and Theoretical Characterization of Germanium-Doped Lithium Clusters Li_nGe (n=1-7)
   V.T. Ngan, J. De Haeck, H.T. Le, G. Gopakumar, P. Lievens and M.T. Nguyen, *J. Phys. Chem. A* **113**, 9080 (2009)

4. Lithium-Doped Germanium Nanowire? Experimental and Theoretical Indication
   G. Gopakumar, X. Wang, L. Lin, J. De Haeck, P. Lievens and M.T. Nguyen, *J. Phys. Chem. C* **103**, 10858 (2009)

5. Vibrational spectroscopy of neutral silicon clusters via far-IR-VUV two color ionization
   A. Fielicke, J.T. Lyon, M. Haertelt, G. Meijer, P. Claes, J. De Haeck and P. Lievens, *J. Chem. Phys.* **131**, 171105 (2009)

6. Carbon monoxide adsorption on neutral silver doped gold clusters
   J. De Haeck, N. Veldeman, P. Claes, E. Janssens, M. Andersson and P. Lievens, *J. Phys. Chem. A* **115**, 2103-2109 (2011)

7. Singly and Doubly Lithium-Doped Silicon Clusters: Geometrical and Electronic Structures and Ionization Energy
   T.M. Nguyen, V.T. Ngan, J. De Haeck, S. Bhattacharyya, H.T. Le, E. Janssens, P. Lievens and M.T. Nguyen, Manuscript to be submitted to *J. Chem. Phys.*, October 2011

8. Ionization energies of lithium doped silicon clusters
   J. De Haeck, S. Bhattacharyya, H.T. Le, D. Debruyne, T.M. Nguyen, V.T. Ngan, E. Janssens, M.T. Nguyen and P. Lievens, Manuscript to be submitted to *J. Chem. Phys.*, October 2011

9. Structures and Ionization Energies of Small Lithium-Doped Germanium Clusters
   J. De Haeck, T.B. Tai, S. Bhattacharyya, H.T. Le, E. Janssens, M.T. Nguyen and P. Lievens, Manuscript to be submitted to *Chem.Eur. J.*, November 2011

10. Dual reflectron high-resolution time-of-flight mass spectrometer for binary cluster research
    J. De Haeck, S. Bhattacharyya, H.T. Le, P. Claes, E. Janssens and P. Lievens, Manuscript to be submitted to *Rev. Sci. Instrum.*, November 2011

11. Carbon monoxide adsorption on neutral and cationic vanadium doped gold clusters
    H.T. Le, J. De Haeck, E. Janssens, S. Lang and P. Lievens, Manuscript in preparation

12. Stable structural motifs of bare and lithium doped silicon and germanium clusters
    J. De Haeck, T.M. Nguyen, T.B. Tai, H.T. Le, M.T.Nguyen and P. Lievens, Manuscript in preparation

Acknowledgments

First of all I would like to thank my promotor Prof. Dr. Peter Lievens for his guidance, inspiration, knowledge and encouragement. Expermental research is a rough journey, but with beautiful sights. Many good memories will remain from that. Knowing that others will continue on the same road is maybe even more rewarding. Every new thesis student you accept will make a small but irreversible step forward in science.

With a feeling of honour and gratitude I would like to mention the members of my exam committee: Prof. Dr. R. Silverans (K.U.Leuven), Prof. Dr. N. Severijns (K.U.Leuven), Prof. Dr. M. Nguyen (K.U.Leuven), Prof. Dr. S. Bals (Universiteit Antwerpen), Dr. Martin Schmidt (Laboratoire Aimé Cotton, CNRS), Dr. E. Janssens (K.U.Leuven), and Prof. Dr. P. Lievens (K.U.Leuven).

Parts of this thesis are in close collaboration with the Quantum Chemistry group of Prof. Dr. M. Nguyen. It was a great benefit working together. Special thanks to Gopa, Ling, Tibor, Ngan, Tam and Tai for the nice work you did and the many conversations.

For part I of this thesis I found much inspiration in the work of Dr. T. Bergmann and Dr. A. Makarov: true masters of mass spectrometry. I found much inspiration for part II in the work of Prof. Dr. P. Lievens, Dr. E. Janssens, Dr. M. Schmidt, Dr. A. Fielicke and Prof. Dr. B. von Issendorff: great experimental cluster physicists. Longer ago, I received excellent guidance from Dr. B. Coquyt and Prof. Dr. J. Lenaers: great teachers of physics.

'You never walk alone…' so I would like to extend my gratitude to all present and former members of the CLASS laboratory. Thuy and Soumen: you are the most excellent team members and larger than friends. Thanks for the great times together. Thanks also to Nele, Pieterjan, Tung, Dries and Nico for sharing the pleasures of our lab. I'm happy to mention 'the people from CDA', who I believe still have some of our tools … I'll miss you (not the tools). I will also miss Dmitrij, Kenneth and Milan, who are such nice people. Special thanks go to

Lucien and Philippe. You are exemplary, not only in your technical skills but also in your demeanour. Many thanks as well to the other members of the technical staff: Erik, Johan, Philippe, Patrick, Tony, Bas, Bart, Mark, Eddy, Jeroen … And of course to Liliane, Monique, Steven and Stijn. Your support is priceless for the lab. Not only for keeping the lab running, but also for making it progress. All of you: keep up the good work!

Last but not least I want to thank my family. I especially thank my parents, for their unconditinal love and support during all these years.

Not everyone can be mentioned in this short space. Doubtless I had to omit the names of many good friends and colleagues. Every one of you I would like to thank here as well.

[1] P. Thoen, 'Lithium monoxide and lithium monocarbide clusters: production by a laser vaporization source and measurement of the ionization', Phd. Thesis, K.U.Leuven (1998)
[2] W. Bouwen, 'Productie, stabiliteit en depositie van homo- en hetero-atomaire metallische clusters', Phd. Thesis, K.U.Leuven (2000)
[3] J. De Haeck, N. Veldeman, P. Claes, E. Janssens, M. Andersson, and P. Lievens, *J. Phys. Chem. A* **115**, 2103-2109 (2011)
[4] G. Gopakumar, X. Wang, L. Lin, J. De Haeck, P. Lievens, and M.T. Nguyen, *J. Phys. Chem. C* **103**, 10858-10867 (2009)
[5] N. Veldeman, E. Janssens, K. Hansen, J. De Haeck, R.E. Silverans, and P. Lievens, *Faraday Discuss.* **138**, 147 (2008)
[6] J.B. Fenn, M. Mann, C.K. Meng, S.F. Wong, and C.M. Whitehouse, *Science* **246**, 64 (1989)
[7] K. Tanaka, *Rapid Commun. Mass Spectrom.* **2**, 151-153 (1988)
[8] S.A. McLuckey and J.M. Wells, *Chem. Rev.* **101**, 571-606 (2001)
[9] W. Bouwen, P. Thoen, F. Vanhoutte, S. Bouckaert, F. Despa, H. Weidele, R.E. Silverans, and P. Lievens, *Rev. Sc. Instr.* **71**, 54 (2000)
[10] R.A. Yost and C.G. Enke, *J. Am. Chem. Soc.***100**, 2274–2275 (1978)
[11] M.B. Comisarow and A.G. Marshall, *Chem. Phys. Lett.* **25**, 282-283 (1974)
[12] Orbitrap™ is a trademark of Thermo Fisher Scientific, Inc. in the United States and other countries.
[13] M. Makarov, *Anal. Chem.* **72**, 1156–1162 (2000)
[14] B.A. Mamyrin, V.I. Karataev, D.V. Shmikk, and V.A. Zagulin, *Sov. Phys. JETP* **37**, 45-48 (1973)
[15] C.K.G. Piyadasa, P. Hakansson, and T.R. Ariyaratne, *Rapid Commun. Mass Spectrom.* **13**, 620-624 (1999)
[16] D. Okumura, M. Toyoda, M. Ishihara, and I. Katakuse, *J. Mass Spectrom.* **39**, 86-90 (2004)
[17] M. Guilhaus, D. Selby, and V. Mlynski, *Mass Spec. Rev.* **19**, 65-107 (2000)
[18] M. Guilhaus, J. Am. Soc. *Mass Spectrom.* **5**, 588-595 (1994)
[19] T. Bergmann, T.P. Martin, and H. Schaber, *Rev. Sci. Instrum.* **60**, 792 (1989)
[20] T. Bergmann, T.P. Martin, and H. Schaber, *Rev. Sci. Instrum.* **60**, 347 (1989)
[21] T. Bergmann, H. Goehlich, T.P. Martin , H. Schaber, and G. Malegiannakis, *Rev. Sci. Instrum.* **61**, 2585 (1990)
[22] T. Bergmann, T.P. Martin, and H. Schaber, *Rev. Sci. Instrum.* **61**, 2592 (1990)
[23] T. Bergmann, T.P. Martin, *Int. J. Mass Spectrom. Ion Processes* **131**, 21 (1994)
[24] W.A. de Heer and P. Milani, *Rev. Sci. Instrum.* **62(3)**, 670-677 (1991)
[25] B. von Issendorff and R. Palmer, *Rev. Sci. Instrum.* **70**, 4497 (1999)
[26] P.R. Vlasak, D.J. Beussman, Q. Ji, and C.G. Enke, *J. Am. Soc. Mass Spectrom.* **7**, 1002-1008 (1996)
[27] R.J. Cotter, S. Iltchenko, D. Wang, and R. Gundry, *J. Mass Spectrom. Soc. Jpn.* **53(1)**, 7-17 (2005)
[28] K. LaiHing, P.Y. Cheng, T.G. Taylor, K.F. Willey, M. Peschke, and M.A. Duncan, *Anal. Chem.* **61**, 1460-1465 (1989)
[29] U. Boesl, H.J. Neusser, R. Weinkauf, E.W. Schlag, *J. Phys. Chem.* **86**, 4857 (1992)
[30] T.J. Cornish and R.J. Cotter, ACS Symp. Ser. **549,** 95 (1994)
[31] H. Nagao, S. Shimma, S. Hayakawa, K. Awazu, and M. Toyoda, *J. Mass. Spectrom.* **45**, 937–943 (2010)
[32] D.J. Beussman, P.R. Vlasak, R.D. McLane, M.A. Seeterlin, and C.G. Enke, *Anal. Chem.* **67**, 3952-3957 (1995)
[33] S.C. O'Brien, J.R. Heath, R.F. Curl, and R.E. Smalley, *J. Chem. Phys.* **88**, 220 (1988)
[34] M.L. Quiniou, A.J. Yates, and P.R.R. Langridge-Smith, *Rapid Commun. Mass Spectrom.* **14**, 361–367 (2002)
[35] T.H. Bergmann, 'Entwurf eines Flugzeit-Massenspektrometers und Messungen an Cäsiumoxidclustern', Inaugural-Dissertation, Max-Planck-Institut für Festkörperforschung Stuttgartt (1988)
[36] V.M. Doroshenko and R.J. Cotter, *J. Am. Soc. Mass Spectrom.* **10**, 992–999 (1999)
[37] C.A. Flory, R.C. Taber, and G.E. Yefchak, *Int. J. Mass Spectrom. Ion Processes* **152**, 177-184 (1996)
[38] D.A. Dahl, *Int. J. Mass Spectrom.* **200**, 3 (2000)
[39] Excel® and Windows® are registered trademarks of Microsoft Corporation in the United States and other countries.
[40] Origin® is a registered trademark of OriginLab Corporation.
[41] D.L. Williams, F.H. Read, and N.J. Bowring, *Nucl. Instr. and Meth. in Phys. Res. A* **363**, 120-123 (1995)
[42] S.M. Colby and J.J. Manura, Proc. 42nd ASMS Conf. (1997). (Available at www.sisweb.com application note #59)
[43] F.H. Read, N.J. Bowring, P.D. Bullivant, and R.R.A. Ward, *Nucl. Instr. and Meth. in Phys. Res. A* **427**, 363-367 (1999)

[44] S.M. Colby, C.W. Baker, and J.J. Manura , Proc. 41st ASMS Conf. 1996. (Available at www.sisweb.com application note #47)
[45] M. Guilhaus, J. *Am. Soc. Mass Spectrom.* **5**, 588-595 (1994)
[46] M. Guilhaus, V. Mlynski, and D. Selby, *Rapid Commun. Mass Spectrom.* **11**, 951–962 (1997)
[47] Alibre Design is a Registered Trademark of Alibre, Inc. in the United States and other countries
[48] NASA; http://www.grc.nasa.gov/WWW/K-12/airplane/ „isentropic flow"
[49] NASA; http://www.grc.nasa.gov/WWW/K-12/airplane/ „mass flow choking"
[50] Wikipedia; http://en.wikipedia.org/ „choked flow"
[51] Wikipedia; http://en.wikipedia.org/ „de Laval nozzle"
[52] http://www.atomox.com/gas_graphs.html
[53] G. Scoles, Atomic and molecular beam methods, Oxford university press (1988)
[54] Kore Technology Ltd offers products and services in the fields of ultra-high-vacuum design (UHV), surface analysis and time-of-flight mass spectrometry (TOF-MS); http://www.kore.co.uk/index.html
[55] C.W.S. Conover, Y.J. Twu, Y.A. Yang, and L.A. Bloomfield, *Rev. Sci. Instum.* **60(6)**, 1065-1070 (1989)
[56] D.S. Selby, V. Mlynski, and M. Guilhaus*, Int. J. Mass Spectrom.* **206**, 201–210 (2001)
[57] P.R. Vlasak, D.J. Beussman, M.R. Davenport, and C.G. Enke, *Rev. Sci. Instr.* **67**, 68 (1996)
[58] JavaTM is a trademark of Sun Microsystems, Inc. in the United States and other countries.
[59] Borland® and JBuilder® are registered trademarks of Borland Software Corporation in the United States and other countries.
[60] D. Debruyne, 'Drempelfotoionisatie van lithium-gedopeerde siliciumclusters', Master Thesis K.U.Leuven (2010)
[61] E.C. Honea, A. Ogura, C.A. Murray, K. Raghavachari, W.O. Sprenger, M.F. Jarrold, and W.L. Brown, *Nature* **366**, 42 (1993)
[62] E.C. Honea, A. Ogura, D.R. Peale, C. Félix, C.A. Murray, K. Raghavachari, W.O. Sprenger, M.F. Jarrold, W.L. Brown, *J. Chem. Phys.* **110**, 12161 (1999)
[63] S. Li, R.J. Van Zee, J.W. Weltner, and K. Raghavachari, *Chem. Phys.Lett.* **243**, 275 (1995)
[64] K.D. Rinnen and M.L. Mandich, *Phys. Rev. Lett.* **69**, 1823 (1992)
[65] V. Quéneau, S.C. Sevov, *Angew. Chem. Int. Ed. Engl.* **36**, 1754 (1997)
[66] H.G. von Schnering, M. Baitinger, U. Bolle, W. Carrillo-Cabrera, J. Curda, Y. Grin, F. Heinemann, J. Llanos, K. Peters, A. Schmeding and M. Somer, *Z. Anorg. Allg. Chem.* **623**, 1037 (1997)
[67] V. Quéneau, E. Todorov, and S.C. Sevov, *J. Am. Chem. Soc.* **120**, 3263 (1998)
[68] R.E. Marsh and D.P. Shoemaker, *Acta Crystallogr.* **6**, 197 (1952)
[69] H. Schäfer, *Annu. Rev. Mater. Sci*, **15**, 1 (1985)
[70] J.M. Goicoechea and S.C. Sevov, *J. Am. Chem. Soc.* **126(22)**, 6860-686 (2004)
[71] J. Campbell and G.J. Schrobilgen, *Inorg. Chem.* **36**, 4078 (1997)
[72] C. Suchentrunk and N. Korber, *New J. Chem.* **30**, 1737 (2006)
[73] D. Rios and S.C. Sevov, *Inorg. Chem.* **49**, 6396 (2010)
[74] A. Fielicke, J.T. Lyon, M. Haertelt, G. Meijer, P. Claes, J. De Haeck, and P. Lievens, *J. Chem. Phys.* **131**, 171105 (2009)
[75] J.T. Lyon, P. Gruene, A. Fielicke, G. Meijer, E. Janssens, P. Claes, and P. Lievens, *J. Am. Chem. Soc.* **131**, 1115 (2009)
[76] O. Cheshnovsky, S. H. Yang, C. L. Pettiette, M. J. Craycraft, Y. Liu, and R. E. Smalley, *Chem. Phys. Lett.* **138**, 119 (1987)
[77] J. Müller, B. Liu, A. A. Shvartsburg, S. Ogut, J. R. Chelikowsky, K. W. M. Siu, K.-M. Ho and G. Gantefor, *Phys. Rev. Lett.* **85**, 1666 (2000)
[78] M. Astruc Hoffmann, G. Wrigge, B. v. Issendorff, J. Müller, G. Ganteför, and H. Haberland, *Eur. Phys. J. D* **16**, 9 (2001)
[79] J. Bai, L.F. Cui, J. Wang, S. Yoo, X. Li, J. Jellinek, C. Koehler, T.Frauenheim, L.S. Wang, and X.C. Zeng, *J. Phys. Chem. A* **110**, 908 (2006)
[80] G. Meloni, M. J. Ferguson, S. M. Sheehan, and D. M. Neumark, *Chem. Phys. Lett.* **399**, 389 (2004)
[81] D.Y. Zubarev, A.I. Boldyrev, X. Li, L.F. Cui, and L.S. Wang, *J. Phys.Chem. A* **109**, 11385 (2005)
[82] G.R. Burton, C.S. Xu, C.C. Arnold, and D.M. Neumark, *J. Chem. Phys.* **104**, 2757 (1996)
[83] Y. Negishi, H. Kawamata, F. Hayakawa, A. Nakajima, and K. Kaya, *Chem. Phys. Lett.* **294**, 370-376 (1998)
[84] C. Xu, T.R. Taylor, G.R. Burton, and D.M. Neumark, *J. Chem. Phys.* 108, 1395 (1998)
[85] G.S. Icking-Konert, H. Handschuh, P.S. Bechthold, G. Ganteför, B.Kessler, and W. Eberhardt, *Surf. Rev. Lett.* **3**, 483 (1996)
[86] D.J. Trevor, D.M. Cox, K.C. Reichmann, R.O. Brickman, and A. Kaldor, *J. Phys. Chem.* **91**, 2598 (1987)

[87] K. Fuke, K. Tsukamoto, F. Misaizu, and M.J. Sanekata, *Chem. Phys.* **99**, 7807 (1993)
[88] C.B. Winstead, S.J. Paukstis, and J.L. Gole, *J. Mol. Spectrosc.* **173**, 311 (1995)
[89] A. Marijnissen and J.J. ter Meulen, *J. Chem. Phys. Lett.* **263**, 803 (1996)
[90] B.H. Boo and P.B. Armentrout, *J. Am. Chem. Soc.* **109**, 3549 (1987)
[91] D.A. Dixon, D. Feller, K.A. Peterson, and J.L. Gole, *J. Phys. Chem. A* **104**, 2326-2332 (2000)
[92] J.B. Jaeger, T.D. Jaeger, and M.A. Duncan, *J. Phys. Chem. A* **110**, 9310 (2006)
[93] O. Kostko, S.R. Leone, M.A. Duncan, and M. Ahmed, *J. Phys. Chem. A* **114**, 3176–3181 (2010)
[94] W. Vonniessen and V.G. Zakrzewski, *J. Chem. Phys.* **98**, 1271 (1993)
[95] J.J. Zhao, X.S. Chen, Q. Sun, F.Q. Liu, and G.H. Wang, *Phys. Lett. A* **198**, 243 (1995)
[96] S.Q. Wei, R.N. Barnett, and U. Landman, *Phys. Rev. B* **55**, 7935 (1997)
[97] S. Nigam, C. Majumder, and S.K. Kulshreshtha, *J. Chem. Phys.* **121**, 7756 (2004)
[98] B. Liu, Z.Y. Lu, B.C. Pan, C.Z. Wang, K.M. Ho, A.A. Shvartsburg, and M.F. Jarrold, *J. Chem. Phys.* **109**, 9401 (1998)
[99] C. Jo and K. Lee, *Phys. Lett. A* **263**, 376 (1999)
[100] S. Ishii, K. Ohno, V. Kumar, and Y. Kawazoe, *Phys. Rev. B* **68**, 5 (2003)
[101] S. Yoshida and K. Fuke, *J. Chem. Phys.* **111**, 3880 (1999)
[102] K. Fuke and S. Yoshida, *Eur. Phys. J. D* **9**, 123-126 (1999)
[103] A.A. Shvartsburg, R.R. Hudgins, P. Dugourd, and M.F. Jarrold, *Chem.Soc. Rev.* **30**, 26 (2001)
[104] R.R. Hudgins, M. Imai, M.F. Jarrold, and P. Dugourd, *J. Chem. Phys.* **111**, 7865 (1999)
[105] M.F. Jarrold and V.A. Constant, *Phys. Rev. Lett.* **67**, 2994 (1991)
[106] M.F.Jarrold and J.E. Bower, *J. Chem. Phys.* **96**, 9180 (1992)
[107] A.A. Shvartsburg, B. Liu, Z.Y. Lu, C.Z. Wang, M.F. Jarrold, and K.M. Ho, *Phys. Rev. Lett.* **83(11)**, 2167-2170 (1999)
[108] J.M. Hunter, J.L. Fye, M.F. Jarrold, and J.E. Bower, *Phys. Rev. Lett.* **73**, 2063 (1994)
[109] J.R. Heath, Y. Liu, S.C. OBrien, Q.L. Zhang, R.F. Curl, F.K. Tittel, and R.E. Smalley, *J. Chem. Phys.* **83**, 5520 (1985)
[110] Q.L. Zhang, Y. Liu, R.F. Curl, F.K. Tittel, and R.E. Smalley, *J. Chem. Phys.* **88**, 1670-1677 (1988)
[111] Y. Liu, Q.L. Zhang, F.K. Tittel, R.F. Curl, and R.E. Smalley, *J. Chem. Phys.* **85**, 7434-7441 (1986)
[112] W. Qin, W.C. Lu, L.Z. Zhao, Q.J. Zang, C.Z. Wang, and K.M. Ho, *J. Phys. Condens. Matter* **21**, 455501 (2009)
[113] A.D. Zdetsis, *J. Chem. Phys.* **127**, 244308 (2007)
[114] A.D. Zdetsis, *J. Chem. Phys.* **127**, 014314 (2007)
[115] W. Xu, Y. Zhao, Q. Li, Y. Xie, and H.F. Schaefer III, *Mol. Phys.* **102**, 579 (2004)
[116] R.B. King, I. Silaghi-Dumitrescu, and A. Kun, *Dalton Trans.,* 3999 (2002)
[117] R.B. King and I. Silaghi-Dumitrescu, *Inorg. Chem.* **42**, 6701 (2003)
[118] R.B. King, I. Silaghi-Dumitrescu, and A. Lupan, *Inorg. Chem.* **44**, 3579 (2005)
[119] R.B. King, I. Silaghi-Dumitrescu, and A. Lupan, *Dalton Trans.,* 1858 (2005)
[120] R.B. King, I. Silaghi-Dumitrescu, and A. Lupan, *Chem. Phys.* **327**, 344 (2006)
[121] R.B. King, I. Silaghi-Dumitrescu, and M.M. Uta, *Inorg. Chem.* **45**, 4974–4981 (2006)
[122] R.B. King, I. Silaghi-Dumitrescu, and M.M. Uta, *Dalton Trans.,* 364 (2007)
[123] R.B. King, I. Silaghi-Dumitrescu, and M.M. Uta, *Eur. J. Inorg. Chem.* **2008**, 3996–4003 (2008)
[124] R.B. King, I. Silaghi-Dumitrescu, and M.M. Uta, *J. Chem. Theory Comput.* **4**, 209-215 (2008)
[125] R.B. King and I. Silaghi-Dumitrescu, *Dalton Trans.,* 6083 (2008)
[126] F.S. Liang and B.X. Li, *Phys. Lett. A* **328**, 407 (2004)
[127] S. Bulusu, S. Yoo, and X.C. Zeng, *J. Chem. Phys.* **122**, 164305 (2005)
[128] S. Yoo and X.C. Zeng, *J. Chem. Phys.* **124**, 184309 (2006)
[129] S. Yoo and X.C. Zeng, *Angew. Chem. Int. Ed.* **44**, 1491 (2005)
[130] S. Yoo, N. Shao, and X.C. Zeng, *J. Chem. Phys.* **128**, 104316 (2008)
[131] J.L. Wang, G.H. Wang, and J.J. Zhao, *Phys. Rev. B* **64**, 205411 (2001)
[132] L. Wang and J. Zhao, *J. Chem. Phys.* **128**, 024302 (2008)
[133] J. Wang, J. Zhao, L. Ma, and G. Wang, *Eur. Phys. J. D* **45**, 289–294 (2007)
[134] L. Ma, J. Zhao, J. Wang, B. Wang, and G. Wang, *Phys. Rev. A* **73**, 063203 (2006)
[135] O. Oña, V. Bazterra, M. Caputo, J. Facelli, P. Fuentealba, and M. Ferraro, *Phys. Rev. A* **73**, 053203 (2006)
[136] K.M. Ho, A.A. Shvartsburg, B.C. Pan, Z.Y. Lu, C.Z. Wang, J. Wacker, J.L. Fye, and M.F. Jarrold, *Nature* **392**, 582 (1998)
[137] L.Z. Zhao, W.C. Lu, W. Qin, Q.J. Zang, C.Z. Wang, and K.M. Hoc, *Chem. Phys. Lett.* **455**, 225–231 (2008)

[138] W. Qin, W.C. Lu, Q.J. Zang, L.Z. Zhao, G.J. Chen, C.Z. Wang, and K.M. Ho, *J. Chem. Phys.* **132**, 214509 (2010)
[139] W. Qin, W.C. Lu, L.Z. Zhao, Q.J. Zang, G.J. Chen, C.Z. Wang, and K.M. Ho, *J. Chem. Phys.* **131(12)**, 124507 (2009)
[140] K. Jackson, M. Horoi, I. Chaudhuri, T. Frauenheim, and A. Shvartsburg, *Phys. Rev. Lett.* **93**, 013401 (2004)
[141] R.L. Zhou and B.C. Pan, *J. Chem. Phys.* **128**, 234302 (2008)
[142] P.A. Edwards and J.D. Corbett, *Inorg. Chem.* **16**, 903 (1977)
[143] E.F. Archibong and A. St-Amant, *J. Chem. Phys.* **109**, 962 (1998)
[144] P. Kircher, G. Huttner, K. Heinze, and G. Renner, *Angew. Chem. Int. Ed.* **37**, 1664 (1998)
[145] T.F. Fässler, *Coord. Chem. Rev.* **215**, 347-377 (2001)
[146] R.W. Rudolph, W.L. Wilson, F. Parker, R.C. Taylor, and D.C. Young, *J. Am. Chem. Soc.* **100**, 4629 (1978)
[147] R.W. Rudolph, W.L. Wilson, and R.C. Taylor, *J. Am. Chem. Soc.* **103**, 2480 (1981)
[148] T.F. Fässler and M. Hunziker, *Inorg. Chem.* **33**, 5380 (1994)
[149] S. Ögüt and J.R. Chelikowsky, *Phys. Rev. B* **55**, 4914 (1997)
[150] B.X. Li and P.L. Cao, *Phys. Stat. Sol. (b)* **218**, 399 (2000)
[151] T.B. Tai and M.T. Nguyen, *Chem. Phys. Lett.* **492**, 290–296 (2010)
[152] V.T. Ngan, 'Transition Metal Doped Silicon Clusters: Structural, Electronic and Spectroscopic Properties', Phd. Thesis, K.U.Leuven (2011)
[153] P. Claes, Phd. Thesis, K.U.Leuven (expected 2012)
[154] S.D. Li, Q.L. Guo, X.F. Zhao, H.S. Wu, and Z.H. Jin, *J. Chem. Phys.* **117**, 606 (2002)
[155] S.D. Li, G.M. Ren, and Z.H. Jin, *J. Chem. Phys.* **119**, 10063 (2003)
[156] R. Kishi, S. Iwata, A. Nakajima, and K. Kaya, *J. Chem. Phys.* **107**, 3056 (1997)
[157] R. Kishi, H. Kawamata, Y. Negishi, S. Iwata, A. Nakajima, and K. Kaya, *J. Chem. Phys.* **107**, 10029 (1997)
[158] G. Gopakumar, P. Lievens, and M. T. Nguyen, *J. Chem. Phys.* **124**, 214312 (2006)
[159] G. Gopakumar, P. Lievens, and M. T. Nguyen, *J. Phys. Chem. A* **111**, 4353 (2007)
[160] X. Wang, 'Mass spectrometric study of metal-doped group IV clusters', Phd. Thesis, K.U.Leuven (2006)
[161] S. Neukermans, X. Wang, N. Veldeman, E. Janssens, R.E. Silverans, and P. Lievens, *Int. J. Mass Spectrom.* **252**, 145–150 (2006)
[162] S.M. Beck, *J. Chem. Phys.* **90**, 6306 (1989)
[163] V.T. Ngan, P. Gruene, P. Claes, E. Janssens, A. Fielicke, M.T. Nguyen, and P. Lievens, *J. Am. Chem. Soc.* **132** (44), 15589–15602 (2010)
[164] X.J. Li and K.H Su, *Theor. Chem. Acc.* **124**, 345–354 (2009)
[165] J. Wang, Y. Liu, and Y.C. Li, *Phys. Lett. A* **374**, 2736–2742 (2010)
[166] A. Spiekermann, S.D. Hoffmann, F. Kraus, and T.F. Fässler, *Angew. Chem. Int. Ed.* **46**, 1638 (2007)
[167] K. Koch, A. Schnepf, and H. Schnöckel, *Z. Anorg. Allg. Chem.* **632**, 1710-1716 (2006)
[168] C. Schenk and A. Schnepf, Angew. *Chem. Int. Ed.* **46**, 5315 (2007)
[169] A. Ugrinov and S.C. Sevov, *J. Am. Chem. Soc.* **125**, 14059–14064 (2003)
[170] L. Xu, S.C. Sevov, *J. Am. Chem. Soc.* **121**, 9245–9246 (1999)
[171] A. Ugrinov and S.C. Sevov, *J. Am. Chem. Soc.* **124**, 10990–10991 (2002)
[172] C. Downie, Z. Tang, and A.M. Guloy, *Angew. Chem. Int. Ed.* **39**, 337–340 (2000)
[173] A. Ugrinov and S.C. Sevov, *Inorg. Chem.* **42**, 5789 (2003)
[174] A. Ugrinov and S.C. Sevov, *C. R. Chimie* **8**, 1878 (2005)
[175] P.D. Pancharatna and R. Hoffmann, *Inorg. Chem. Acta* **359**, 3776 (2006)
[176] G.S. Armatas and M.G. Kanatzidis, *Nature* **441**, 1122–1125 (2006)
[177] D. Sun, A.E. Riley, A.J. Cadby, E.K. Richman, S.D. Korlann, and S.H. Tolbert, *Nature* **441**, 1126–1130 (2006)
[178] G.S. Armatas and M.G. Kanatzidis, *Science* **313**, 817–820 (2006)
[179] G.S. Armatas and M.G. Kanatzidis, *Adv. Mater.* **20**, 546–550 (2008)
[180] G.S. Armatas and M.G. Kanatzidis, *J. Am. Chem. Soc.* **130**, 11430–11436 (2008)
[181] J.M. Goicoechea and S.C. Sevov, *J. Am. Chem. Soc.* **128**, 4155–4161 (2006)
[182] J.M. Goicoechea and S.C. Sevov, *Organometallics* **25**, 4530–4536 (2006)
[183] A. Spiekermann, S.D. Hoffmann, T.F. Fässler, I. Krossing, and U. Preiss, *Angew. Chem. Int. Ed.* **46**, 5310–5313 (2007)
[184] A. Nienhaus, R. Hauptmann, and T.F. Fässler, *Angew. Chem. Int. Ed.* **41**, 3213–3215 (2002)
[185] M.B. Boeddinghaus, S.D. Hoffmann, and T.F. Fässler, *Z. Anorg. Allg. Chem.* **633**, 2338–2341 (2007)

[186] A. Ugrinov and S.C. Sevov, *Chem. Eur. J.* **10**, 3727 (2004)
[187] J.M. Goicoechea and S.C. Sevov, *Angew. Chem. Int. Ed.* **44**, 4026 (2005)
[188] S. Scharfe, F. Kraus, S. Stegmaier, A. Schier, and T.F. Fässler, *Angew. Chem. Int. Ed.* **50**, 3630–3670 (2011)
[189] C.H. Wu, H. Kudo, and H.R. Ihle, *J. Chem. Phys.* **70**, 1534 (1979)
[190] C.H. Wu, *Chem. Phys. Let.* **139**, 357 (1987)
[191] H.I. Kudo, *Nature* **355**, 432 (1992)
[192] Y. Li, D. Wu, Z.R. Li, and C.C. Sun, *J. Comput. Chem.* **28**, 1677 (2007)
[193] R.O. Jones, A.I. Lichtenstein, and J.J. Hutter, *Chem. Phys.* **106**, 4566 (1997)
[194] M.S. Lee, S. Gowtham, H. He, K.C. Lau, L. Pan, and D.G. Kanhere, *Phys. Rev. B* **74**, 245412 (2006)
[195] P. Lievens, P. Thoen, S. Bouckaert, W. Bouwen, F. Vanhoutte, H. Weidele, R.E. Silverans, A. Navarro-Vazquez, and P.v.R. Schleyer, *Eur. Phys. J. D* **9**, 289 (1999)
[196] K. Joshi and D.G. Kanhere, *Phys. Rev. A* **65**, 043203 (2002)
[197] S. Shetty, S. Pal, and D.G. Kanhere, *J. Chem. Phys.* **118**, 7288 (2003)
[198] P. Lievens, P. Thoen, S. Bouckaert, W. Bouwen, F. Vanhoutte, H. Weidele, R.E. Silverans, A. Navarro-Vazquez, and P.v.R. Schleyer, *J. Chem. Phys.* **110**, 10316 (1999)
[199] P. Lievens, P. Thoen, S. Bouckaert, W. Bouwen, F. Vanhoutte, H. Weidele, and R.E. Silverans, *Chem. Phys. Let.* **302**, 571 (1999)
[200] V.T. Ngan, J. De Haeck, H.T. Le, G. Gopakumar, P. Lievens, and M.T. Nguyen, *J. Phys. Chem. A* **113**, 9080–9091 (2009)
[201] C. Yannouleas and U. Landman, *Phys. Rev. B* **51**, 1902 (1995)
[202] S. Neukermans, E. Janssens, H. Tanaka, R.E. Silverans, P. Lievens, K. Yokoyama, and H. Kudo, *J. Chem. Phys.* **119**, 14 (2003)
[203] A.D. Becke, *J. Chem. Phys.* **104**, 1040 (1996)
[204] C.T. Lee, W.T. Yang, and R.G. Parr, *Phys. Rev. B* **37**, 785 (1988)
[205] T.H. Dunning Jr., *J. Chem. Phys.* **90**, 1007 (1989)
[206] R.A. Kendall, T.H. Dunning Jr., and R.J. Harrison, *J. Chem. Phys.* **96**, 6796 (1992)
[207] C.J. Marsden, Chem. *Phys. Lett.* **245**, 475 (1995)
[208] P.v.R. Schleyer and J. Kapp, *Chem. Phys. Lett.* **255**, 363 (1996)
[209] N. He, H.B. Xie, and Y.H. Ding, *J. Comput. Chem.* **29**, 1850–1858 (2008)
[210] P.v.R. Schleyer, New Horizons of Quantum Chemistry (Reidel Dordrecht), 95 (1983)
[211] A. Dhavale, V. Shah, and D.G. Kanhere, *Phys Rev A* **57**, 4522 (1998)
[212] E. Janssens, S. Neukermans, F. Vanhoutte, R. E. Silverans, P. Lievens, A. Navarro-Vázquez, and P.v.R. Schleyer, *J. Chem. Phys.* **118**, 5862 (2003)
[213] P.M. Guyon, and J. Berkowitz, *J. Chem. Phys.* **54**, 1814 (1971)
[214] J. Akola, H. Häkkinen, and M. Manninen, *Eur. Phys. J. D* **9**, 179 (1999)
[215] W.A. Saunders, K. Clemenger, W.A. de Heer, and W.D. Knight, *Phys. Rev. B* **32**, 1366 (1985)
[216] T. Bergmann and T.P. Martin, *J. Chem. Phys.* **90**, 2848 (1989)
[217] Gaussian 03, Revision A.1, M.J. Frisch, G.W. Trucks, H.B. Schlegel, and coworkers, Gaussian, Inc., Pittsburgh PA (2003)
[218] A.D. Becke, *Phys. Rev. A* **38**, 3098 (1988)
[219] Gaussian 03, Revision D.02, M. J. Frisch and coworkers, Gaussian, Inc., Wallingford CT (2004)
[220] Molpro, version 2008.1, H. J. Werner and coworkers
[221] A.D. Becke, *J. Chem. Phys.* **98**, 5648 (1993)
[222] T.M. Tai and M.T. Nguyen, *J. Chem. Theory. Comput.* **7(4)**, 1119-1130 (2011)
[223] P. Lievens, P. Thoen, S. Bouckaert, W.Bouwen, F. Vanhoutte, H.Weidele, R.E. Silverans, A. Navarro-Vazquez, and P.v.R. Schleyer, *Eur. Phys. J. D* **9**, 289 (1999)
[224] W. de Heer, *Rev. Mod. Phys.* **65**, 611-676 (1993)
[225] W.D. Knight, K. Clemenger, W.A. de Heer, W.A. Saunders, M.Y. Chou, and M.L. Cohen, *Phys. Rev. Lett.* **52**, 2141 (1984)
[226] K. Clemenger, *Phys. Rev. B* **32**, 1359-1362 (1985)
[227] S.G. Nilsson, *K. Dan. Vidensk. Selsk. Mat. Fys. Medd.* **29**, 16 (1955)
[228] G. Wrigge, M.A. Hoffmann, and B. von Issendorff, *Phys. Rev. A* **65**, 063201 (2002)
[229] C. Bartels, C. Hock, J. Huwer, R. Kuhnen, J. Schwöbel, and B. von Issendorff, *Science* **323**, 1323 (2009)
[230] E. Janssens, S. Neukermans, and P. Lievens, *Curr. Opin. Solid State Mat. Sci.* **8**, 185–193 (2004)
[231] K. Wade, *Chem. Commun.* 792 (1971)
[232] J. Daintith, Oxford Dictionary of Chemistry, Oxford University Press NY (ISBN 0-19-860918-3, 2004)

[233] M.J. Licker, McGraw-Hill Concise Encyclopedia of Chemistry, McGraw-Hill NY (ISBN 0-07-143953-6, 2004)
[234] J. Clayden, N. Greeves, S. Warren, and P. Wothers, Organic Chemistry (1st ed.), Oxford University Press. 96–103 (ISBN 978-0-19-850346-0, 2000)
[235] M.A. Fox and J.K. Whitesell, Organic Chemistry (3th ed.), (ISBN 978-0-7637-3586-9, 2003)
[236] P.Y. Bruice, Organic Chemistry (3rd ed.), (ISBN 0-13-017858-6, 2001)
[237] Wikipedia; http://en.wikipedia.org/wiki/Crystal_field_theory
[238] Scienceworld (http://scienceworld.wolfram.com/chemistry/CrystalFieldTheory.html)
[239] J.E. Sansonetti, W.C. Martin, and S.L. Young, Handbook of Basic Atomic Spectroscopic Data (version 1.1.2), National Institute of Standards and Technology, Gaithersburg MD (2005), [Online: http://physics.nist.gov/Handbook (2011, February 15)]